Semiconductor-Superconductor Josephson Junctions in the Presence of Zeeman and Spin-Orbit Fields

vorgelegt von

Christian Baumgartner
aus Landau a. d. Isar

im Jahr 2022

Abstract

Epitaxially grown Al-InAs hybrids have a great potential for future applications. The most prominent incentive in this regard are potential Majorana zero modes, which are to be believed ideal candidates for fault-tolerant quantum computers. However, with the recent access to these novel materials, it is furthermore possible to conduct experiments on a wide range of generic phenomena. With the help of top-down fabrication, individual designed Josephson junctions offer an unprecedented playground for experimentalists due to the unique combination of the two-dimensional electron gas (2DEG) and the superconductor.

This dissertation is about examining of the fundamental building blocks of single Josephson junctions built on such a heterostructure. For this purpose, we elaborated a fabrication process and installed a measurement technique based on a cold RLC resonator in the low MHz regime that is placed in series to the sample. In contrast to the normal resistance, the resonator is a tool which allows us to access the inductance of a superconducting system and thus to probe the supercurrent-carrying Andreev bound states (ABS).

The main discoveries of this work include a complete picture of the ABS dependency on various parameters, such as the charge carrier density, the dc current, the magnetic fields, the temperature, or the transparency of the junction, which is close to unity. In the heterostructure, we can break inversion and time-reversal symmetry simultaneously with the interaction of spin-orbit and Zeeman fields. This, in combination with the ballistic character of the Josephson device, leads to a non-reciprocal current that depends on the cross product of current and Zeeman field. Furthermore, we report a rectification effect of the supercurrent even far below the critical temperature of the superconductor. The observed non-reciprocal current is a consequence of a distorted current-phase relation (CPR). Using the inductance, we can display this distortion and derive the novel magnetochiral anisotropy (MCA) coefficient γ_L for supercurrents.

Moreover, with the MCA coefficient γ_L we extract the Dresselhaus com-

ponent and witness furthermore a peculiar sign change of the MCA at the point where the Zeeman energy is as large as the induced gap.

Finally, with the gained understanding and experience of single superconductor-semiconductor Josephson junctions, we create the basis for more complex devices, e.g. multiterminal Josephson junctions (MTJJs). Such junctions with multiple superconducting leads are predicted to host synthetic Weyl singularities in their ABS spectrum. In this work, we present first results of this new topic and show that it is possible to fabricate such MTJJs and to measure their inductance.

Acknowledgements

At this point I would like to express my gratitude to all those who have supported and assisted me during this thesis.

In particular, I would like to express my sincere thanks to my supervisor **Prof. Dr. Christoph Strunk**. Christoph was very interested in my work from the beginning and was always there. I often confronted him with simple and naïve, but also with extremely complicated and unanswerable questions, to which I nevertheless always got a good answer. We always have coordinated closely and Christoph gave me and the work the right direction. He was eminent important for the success of this thesis.

I'm very grateful to **Dr. Nicola Paradiso** for the support and close cooperation, when it was about questions in the lab, about the evaluation of the experiments or about the writing of the publications.

Thanks to **PD Dr. Denis Kochan** for the theoretical support and for being the second referee.

Many thanks goes to **Prof. Dr. Jaroslav Fabian** and his group. In particular to **Dr. Andreas Costa** and **Dr. Paulo E. De Faria Junior** for their theoretical cooperation and the discussions we had.

This work would not have been possible without the material from **Michael J. Manfra's group** from Purdue University. Many thanks for providing it.

I want to thank **Prof. Dr. D. Bougeard** and **Michael Prager** for their support, especially at the beginning of my PhD.

It was always nice to have a talk with **M. Kronseder**, whether it was about physics, teaching or something else, thanks.

very reliable, which makes me feel lucky.

A collective thanks goes out to my (former) colleauges **Dr. Christian Bäuml**, **Dr. Stefan Blien**, **Dr. Klaus Kronfellner**, **Paul Linsmaier**, **Lorenz Bauriedl**, **Jay Schmidt**, **Alexander Weitzel**, **Lea Pfaffinger**, **Simon Feyrer** and all those ones I forgot to mention, for ensuring a pleasant and collegial atmosphere.

However I should express it, I am very grateful to my parents **Herbert** and **Renate** for their endless support throughout my life. I am also thankful to my siblings **Carolin** and **Andreas** for being such a nice family and supporting me everytime.

And of course I am extremely grateful to my girlfriend **Anna**, who listens to me sincerely, even if there is no chance of understanding anything. She is always there for me and enriches my life very much with her love and positive attitude.

Contents

Contents

1 Introduction

1.1 Motivation

In our daily lives, we are confronted with more and more technological revolutions in shorter periods of time. But with increasing prosperity and technical progress, new problems such as climate change, financial crisis or deseases like Covid-19 emerge and affect everyone on our planet. The solution to solve these problems are supposed to be new technologies. Technologies such as quantum computing (QC). A quantum computer promises to process data at an exponential rate and to perform large-scale simulations that are unthinkable in any supercomputer [1].

Due to this capability, in addition to the above-mentioned problems, applications in the most diverse areas of industry and research and development are conceivable, such as in chemical and pharma industry (e.g. simulation of molecules or pattern finding in genomics and DNA classification), finance (risk analysis etc.), technology (i.e. machine learning, cryptography etc.), industrial good (e.g. logistics, energy flow in power networks etc.) or for many-body simulations in physics [2]. Because of these far-reaching and enticing applications, many companies and start-ups are now researching alongside government institutions. Figure 1.1 lists some of the companies with significant research activities on the field of quantum computing. However, in addition to the competition between companies, there is also a competition between the respective technological approaches.
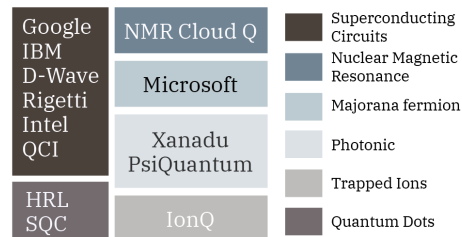
Figure 1.1
Overview of leading institutions, sorted by the respective hardware technology. Image taken from [2].

The leading technology for quantum computing hardware today is based on superconducting circuits [3]. With this approach, google declared quantum supremacy 2019 [4]. In other words, the group led by J. Martinis claimed to solve a task in 200 s, whereas a modern supercomputer would need 10,000 years to do so. The current stage is called noisy intermediate-scale quantum (NISQ) era. In this era, quantum computers with 50 to 100 qubits[1] will surpass the computing power of classical computers, but the number of reliable controlled qubits is limited and therefore NISQ devices will not fundamentally change the world [5].

The reason why it is so difficult to develope the necessary hardware is decoherence. The qubits interact with the environment and can collapse at the slightest disturbance or measurement. But on the other hand, the qubits need to communicate with each other very strongly. A way to overcome this contradiction is either by quantum error correction (very cumbersome) or by storing the quantum information in a topological state[2], where the underlying wavefunction is decoupled from the environment.

1.2 Why Coupling a Superconductor to a Semiconductor?

Topological superconductors have the potential to possess so-called Majorana fermions, which were theoretically predicted in 1937 and named after the physicist E. Majorana [6]. These novel particles are neither bosons nor fermions [7][8] and follow the non-abelian anyon statistics, which, according to Alexei Kitaev's theoretical report in 2001 [9], holds out the prospect of use for fault-tolerant quantum computers. In 2008, Fu and Kane enriched the research field with their proposal to use the proximity effect between an s-wave superconductor and a 3D topological insulator for the creation of Majorana bound states [10]. Later followed the realisation that a 2D metal with Rashba spin-orbit coupling in combination with the Zeeman effect can replace the topological insulator [11][12][13][14].

Since these proposals and the first promising experiment by Mourik et al. in 2012 [15], the effort put into the search of this new kind of particle is steadily increasing.

---

[1]A **qu**antum **bit** (qubit) is a two-state quantum-mechanical system.

[2]Topology is a mathematical concept. A geometric object belongs to the same class if it preserves its properties under continuous deformation.

Among the variety of other materials [16][17][18][19], the idea of using a super-semi plattform has several advantages. One is the large number of control parameters such as the gate voltage, magnetic field orientation and magnitude, device geometry, materials, interface tailoring and the phase difference of superconductors in the case of Josephson junctions. Another advantage is the benefit of historically well known materials in terms of crystal growth and top-down fabrication [20]. To date, one of the best developed semiconductors, say a two dimensional electron gas (2DEG), are InAs and InSb and they are commonly used in combination with aluminium as the superconductor. The first kind of these hybrid materials were one-dimensional nanowires [21]. In 2016, Shabani et al. [22] set a new benchmark with the report of *in-situ* MBE grown two-dimensional heterostructures.

In such heterostructures, the semiconductor inherits certain superconducting properties due to proximitisation, but it can maintain its characteristics like long mean free path, spin-orbit interaction, *g*-factor or the tunability of the charge carrier density.

The aluminium can be removed in a predefined area in order to form a nanowire-like device. The exposed 2DEG with its two superconducting leads is called Josephson junction. The supercurrent, carried by electrons and holes, is dissipationless due to the so-called Andreev bound states (ABS) and arise from coherent back and forth bouncing between the superconductors [23]. Topological states can emerge due to the absence of inversion symmetry and broken time-reversal symmetry which are caused by intrinsic crystal structure and external magnetic fields, respectively.

In the past years, many different kinds of experiments were made in order to find signatures of topological superconductivity in a 2D system [24][25]. Consequently, in 2019 Fornieri et al.[26] and Ren et al.[18] demonstrated this nature in planar Josephson junctions. However, the evidence of Majorana bound states is still to come. The zero-bias peaks (ZBP)[3] are qualitatively similar to those in the 1D nanowire-based devices, where Majorana zero modes (MZM) are indistinguishable from Andreev bound states [27][28]. Moreover, according to theory these ZBPs must be quantized by $2e^2/h$ and appear on both ends of the nanowire at the same time. Neither of these conditions has yet been confirmed experimentally. So far, even the opposite has been observed [29]. Therefore, the attempt of addressing the MZMs directly appears to have failed. New spectroscopy tools beyond electron transport are necessary and the

---

[3]ZBP can be a signature of Majorana zero modes

scientific focus should be extended to indirect signatures of topological properties, to deepen the overall knowledge of this material class.

The specific aim of this thesis was therefore to study the effect of Rashba- and Dresselhaus spin-orbit interactions in combination with external magnetic fields on the nature of Andreev bound states in Josephson junctions. Our approach was to obtain the inductance of superconducting devices directly as a widely unused quantity. We achieved this through embedding our sample in series to a cold RLC-circuit. Thus, a change of the inductance of our device leads to a resonance shift of the center frequency of the circuit, which then can be calculated in absolute inductance values. We stress that this technique allows us to access the current-phase relation (CPR) directly and hence the ABS-spectrum. In addition, it is possible to apply large external fields and to perform DC transport measurement simultaneously.

We demonstrate the functionality of this method on one-dimensional Josephson junction arrays and on multiterminal Josephson junction arrays, where the junctions consist of at least three superconducting leads. Arrays are necessary to guarantee a sizeable inductance which must be large enough for a decent resonant shift of the center frequency in the resonator. Furthermore, serial arrays have the advantage that they compensate for the effects of individual defect configurations of a single Josephson junction.

Among other things, this work contributes several achievements to the research community of topological superconductivity. First of all, we show the feasibility of the described methodology and the preparation of the appropriate samples. From the current dependent Josephson inductance, we extract the average ABS transparency $\overline{\tau}$, which is 0.94. This high value substantiates the quality of the material and the ballistic character of the devices. In addition, we can use the Josephson inductance to determine some other parameters, such as the number of ABS channels, the induced gap, or the fraction of the Dresselhaus parameter [30].

By applying a magnetic field in-plane, our devices exhibit a superconducting diode effect (SDE). This diode effect depends on the cross product between the current $\vec{I}$ and the in-plane magnetic field $\vec{B}_{\mathrm{ip}}$. In other words, the orientation and sign of the field determine whether there is a difference between positive and negative critical currents and the sign and magnitude of that difference.

Moreover, we studied the magnetochiral anisotropy (MCA) in the fluctuation and in the non-resistive regime. For latter case, we defined a new coefficient: the magnetochiral anisotropy for supercurrents γ_L to which we can assign the value $0.77{\cdot}10^6\mathrm{T}^{-1}\mathrm{A}^{-1}$ for our one-dimensional Josephson junction array.

The origin of the diode effect is a cosine contribution to the sinusoidal current-phase relation. In non-ballistic devices, this was observed by other groups as a shift in the phase of the CPR by a finite φ_0 [31]. However, with the help of the group of Prof. Jaroslav Fabian from the University of Regensburg, we can provide a full story and describe the physics of the superconducting diode effect qualitatively [32].

Besides these findings, we made some further observations in the presence of a Zeeman field. For instance, a peculiar sign change of the newly defined magnetochiral anisotropy coefficient γ_L. This change occurs, when the Zeeman energy and the size of the induced gap coincide. This robust feature, which we measured in two samples independently, is anisotropic with respect to the in-plane field orientation.

At the end, we make a detour into the world of multiterminal Josephson junctions (MTJJs). With an additional superconducting lead, time-reversal symmetry can be broken despite the absence of a Zeeman field and the spectrum of the Andreev bound states take peculiar shapes. Theory predicts the emergency of topological protected states such as Weyl singularities [33]. We show, that it is possible to fabricate and to obtain the inductance of these new kind of devices.

1.3 Organisation of this Thesis

This thesis gives an overview what was established and achieved in our group with regard to Josephon junctions based on epitaxial Al-InAs heterostructures. This work can serve as a guide for a successor or researchers from other groups in terms of fabrication, measurement methodology, and theory.
This thesis is subdivided into eight chapters and organized as follows:

- Chapter 1 - Introduction
  This chapter introduces the subject. What is the motivation? What does this work contribute to the research community? Why is it relevant to do this kind

of research? All important questions that have to be answered to justify the resources spent on this PhD thesis.

- Chapter 2 - Theory
  First, the respective physics behind the semiconductor and the superconductor are discussed. The third section in this chapter is dedicated to the description of Josephson junctions. Finally, the physics related to the super-semi interface of this material is discussed.

- Chapter 3 - Material, Methods & Characterisation
  Here, the introduction of the heterostructure, the precharacterisation tools for a new wafer, the description for the fabrication of devices and the methodology of our measurement setup can be found.

- Chapter 4 - Josephson Inductance of One-Dimensional Josephson Junction Arrays
  The Josephson inductance allows us here to get an insight to the Josephson junctions deep in the superconducting state. We describe the observations we made in the absence of any in-plane magnetic field.

- Chapter 5 - Superconducting Diode Effect (SDE)
  When we activate the Zeeman field in the plane, we observe due to the interplay with the spin-orbit interaction a supercurrent rectification and magnetochiral effect. This chapter is devoted to the experimental part of the study.

- Chapter 6 - Further Observations in One-Dimensional Josephson Junction Arrays
  In addition to the diode behaviour, we also see other effects. Such as the difference of the Dresselhaus component or a peculiar sign change of the MCA γ_{L}.

- Chapter 7 - Multiterminal Josephson Junction Array (MTJJA)
  This chapter is about the first steps into the world of MTJJAs. In DC transport we see an enhancement and the counterpart with a deduction of the critical current for finite magnetic fields in-plane and out-of plane applied simultaneously.

- Chapter 8 - Summary

2 Theory

There are essentially two categories of topological superconductors. They are either intrinsic or artificially produced [34]. Candidates for the intrinsic approach are for instance Sr_2RuO_4 [35][36], $Cu_xBi_2Se_3$ [37] or nodal superconductors like YPtBi [38][39].

Artificial topological supercondcutors are commonly made of a combination between InAs/InSb and Al/Pb/Sn etc. and must fulfil basically two requirements, superconductivity and strong spin-orbit interaction (SOI).

Other requirements may also include high quality interface, robustness to external fields, control of fabrication, low quasiparticle poisoning, intrinsic magnetic fields (e.g. realized by ferromagnets), scalability for devices and other individual reasons. In our case, the material of choice is a two dimensional superconductor which proximitises a shallow quantum well (QW) underneath.

The heterostructure (sketched in figure 2.1) consists of a 7 nm thick epitaxial aluminium film. The film induces superconductivity into the also 7 nm thick two-dimensional electron gas (2DEG) made of InAs and is separated by a 10 nm InGaAs barrier and 2 monolayer GaAs (made for fabrication purposes). Increasing the thickness or the Ga concentration of the InGaAs barrier enhances the mobility, but at the price of a lower proximity effect. The barrier height between the InAs and the Al layer is thus important for the quality of the heterostructure and a key challenge of the MBE growth.

For our studies we were supplied with material from

| Al (7 nm) |
| $In_{0.8}Ga_{0.2}As$ (10 nm) |
| InAs (7 nm) |
| $In_{0.81}Ga_{0.19}As$ (4 nm) |
| $In_{0.81}Al_{0.19}As$ (25 nm) |
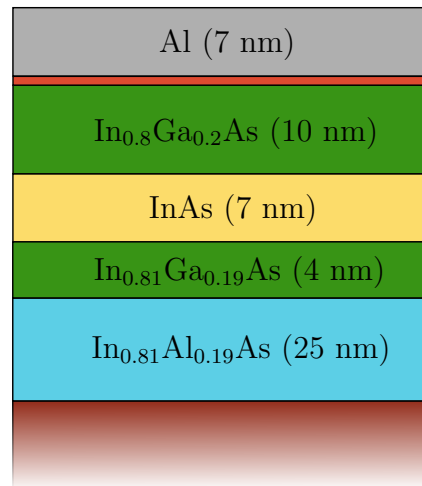
Figure 2.1

Layer stack of the heterostructure. The orange layer between the aluminium and the InGaAs denotes two monolayer of GaAs.

Prof. Dr. M. Manfra and his group from Purdue University, New Lafayette. This material has the necessary properties to fabricate and perform experiments on extended Josephson junction arrays. The most important features of the heterostructure are the possibility of top-down fabrication, large SOI ($\approx$ 15 meV nm), high *g*-factor ($\approx$ 10), sufficient mean free path l_{el} ($\approx$ 200 nm) for ballistic junctions, adequate proximity effect (induced gap $\Delta^* \simeq$ 130 μeV), sustainability against external magnetic fields ($B_{\text{c},\parallel}^{\text{Al}} \approx$ 2.7 T) in the plane and the potential for low-resistive ohmic contacts ($R_{\text{contact}} <$ 1 Ω).

Before the discussion of the methods and the experimental results, a fundamental theoretical background is provided in this chapter. First, the basic properties of the 2DEG, the spin-orbit interaction and the Zeeman effect are described, followed by an insight into the physics of superconductors. Subsequently, the physics of Josephson contacts including the RSCJ model is discussed, passing over to interface phenomena which are described by the Andreev process, BTK formalism and the proximity effect.

2.1 The Semiconductor

2.1.1 Two Dimensional Electron Gas

When semiconductors are arranged in a subtle way, a 2DEG can be formed, where the motion of electrons is free in the plane and confined in z-direction. This confinement leads to a quantisation and is essential for the observation of several effects such as the Quantum Hall Effect [40] or the quantised conductance [41]. In our case, we use the shallow 2DEG to benefit from its unique properties that allow us to manipulate the Andreev bound states. The following pages give a quick overview of the underlying physics. For a deeper understanding, solid state physics books with the following references are recommended [42][43][44][45].

The density of states (DOS) in a quantum well differs significantly from the three, one or zero-dimensional case. The spin-degenerate dispersion relation in two dimensions has a parabolic shape and can be described by

$$E_n(k_{||}) = E_n + \frac{\hbar^2 k_{||}^2}{2m^*}, \tag{2.1}$$
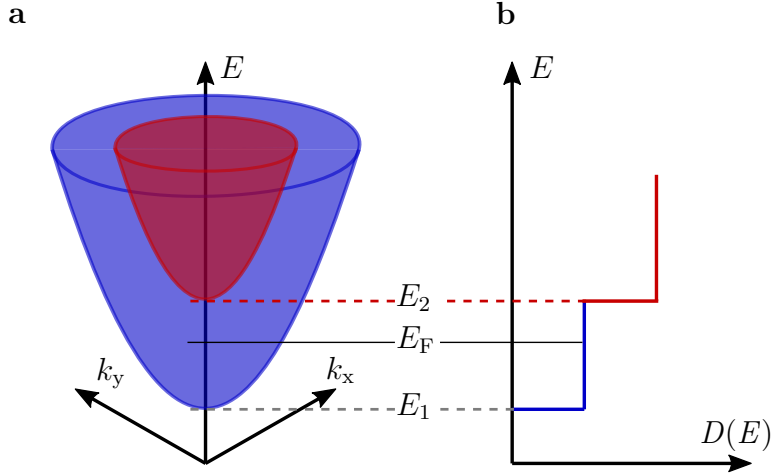
Figure 2.2: **Confinement in z: a)** Parabolic dispersion relation for the first and second sub-band. In between lies the Fermi energy E_F. **b)** Density of states as a function of energy.

with $k_{||} = \sqrt{k_x^2 + k_y^2}$ and m^* being the effective mass. Because the integrated density of states is energy independent, the carrier density n in the case of the first sub-band is given by

$$n = \frac{m^*}{\pi\hbar^2} \int_{E_1}^{E_F} dE' = \frac{m^*}{\pi\hbar^2}(E_F - E_1) \tag{2.2}$$

and the resulting DOS is therefore

$$D(E) = \frac{dN(E)}{dE} = \frac{m^*}{\pi\hbar^2}. \tag{2.3}$$

It is constant and shows a step for each corresponding parabolic sub-band, as illustrated in Fig. 2.2. The Fermi wavevector k_F given from Eq. 2.1 as $(E_F - E_1) = \frac{\hbar^2 k_F^2}{2m^*}$ leads to

$$k_F = \sqrt{2\pi n}, \tag{2.4}$$

when inserted into Eq. 2.2. This relation allows us to calculate a few mesoscopic parameters of the 2DEG, which are key in evaluating our S-N-S devices. Parameters such as

$$\lambda_F = \frac{2\pi}{k_F}, \qquad v_F = \frac{\hbar k_F}{m^*}, \qquad l_e = \frac{\hbar}{e}\mu\sqrt{2\pi n}, \tag{2.5}$$

where λ_F is the Fermi wavelength, v_F the Fermi velocity and l_e the mean free path. The needed value n and the charge carrier mobility μ can be measured by using a

hallbar geometry, where the quantities are extracted via the following relations:

$$n = \frac{1}{|e|d\rho_{xy}(B=0)/dB}, \qquad \mu = \frac{1}{en\rho_{xx}(B=0)} \qquad (2.6)$$

How we characterised our 2DEG is described in section 3.4.2. There one can find the gate voltage dependent parameters of our heterostructure.
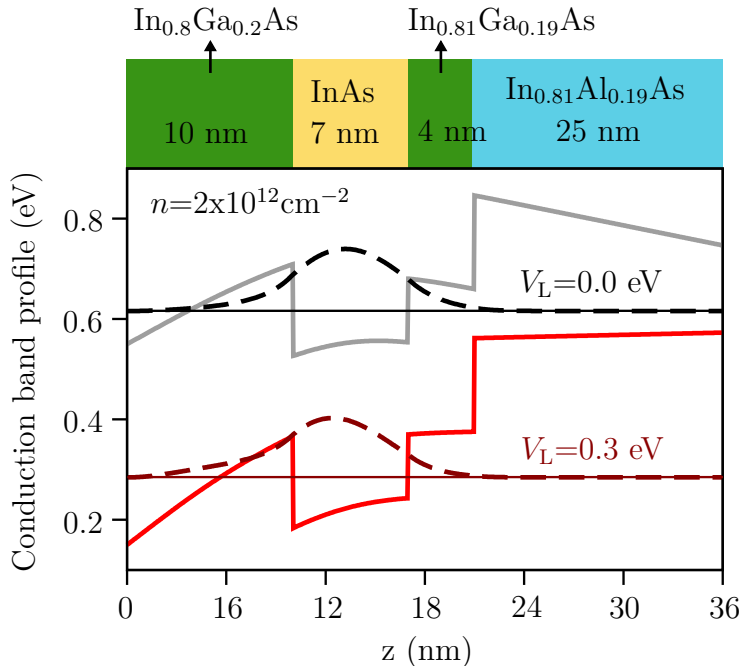
Figure 2.3: **Shallow quantum well:** Illustration of the conduction band profiles of the InAs quantum well for two different surface potentials V_L (=left interface) with an electron density of $n = 2 \cdot 10^{12} \text{cm}^{-2}$. The Fermi energy, corresponding to the energy of the lowest sub-band, is indicated by the horizontal thin line, whereas the probability density of the wavefunction is displayed by the dashed line. Original figure made by P.E. Faria Junior.

In order to create a confinement in one direction, the InAs layer with a lower band gap ($E_g = 0.417$ eV [46]) is sandwiched between layers of $In_{1-x}Ga_xAs$ and $In_{1-x}Al_xAs$, which have a higher band gap. The Fermi energies from the layers align and cuts the conduction band of the InAs layer. The wave function distribution therefore localises in the InAs QW and becomes asymmetric due to the broken inversion symmetry of the heterostructure. Figure 2.3 shows the conduction band profile and the Fermi energy of our near surface quantum well. Increasing the surface potential V_L leads to a further asymmetric shape, which in turn increases the Rashba spin-orbit coupling strength. But what that actually is will be described in the next section.

2.1.2 Spin-Orbit Interaction

As we know from the famous Stern-Gerlach experiment [47], the spin of an electron determines whether the electron experiences a force in one or the other direction in a magnetic field gradient. The same applies in an electric field which can originate from an atom or a lattice. As requested by Lorentz invariance, an electron moving in an electric field with a certain velocity v feels a magnetic field in its rest frame according to

$$B_{\text{eff}} = \frac{v}{c^2} \times E, \tag{2.7}$$

where c is the velocity of light. It is called spin-orbit coupling due to the interaction of the electron's spin and the orbital motion. In atoms this effect manifests itself in the splitting of the energy levels known as the fine structure. In 2D systems such as in our 2DEG, the spin-orbit interaction is responsible for linear spin dependent shifts of the momentum dependent energy $E(k)$. Hence, the spin degeneracy of the dispersion relation is lifted.

In our system we can distinguish between two spin-orbit-related influences. One stems from the Zincblende structure of the InAs. Here, the lack of inversion symmetry of the crystal lattice (**b**ulk **i**nversion **a**symmetry = BIA) causes the so-called Dresselhaus term [48].

The other influence comes from the 2D crystal growth and the parabolic confinement potential, where spatial inversion symmetry (**s**tructure **i**nversion **a**symmetry = SIA) is absent and gives rise to the Rashba term [49][50]. Taking both effects into account, the Hamiltonian for a Zincblende structure in two-dimensional electron gases is given by

$$H = H_0 + \alpha_{\text{R}}(\sigma_x k_y - \sigma_y k_x) + \beta_{\text{D}}(\sigma_x k_x - \sigma_y k_y), \tag{2.8}$$

where σ_x and σ_y describe the Pauli spin matrices[1] in the plane of the 2DEG and H_0 the energy of the electrons without spin-orbit interaction [51].

The Rashba coefficient

$$\alpha_{\text{R}} = \alpha \langle E_{\text{Z}} \rangle \tag{2.9}$$

depends on the material specific constant α and on the external electric field E_{Z} normal to the plane. In practice, a gate electrode can be used as a capacitor to tune α_{R}. The Dresselhaus coefficient β_{D} is determined by the thickness of the quantum

---

[1]the pauli matrices are: $\sigma_x = \begin{pmatrix} 0 & 1 \\ 1 & 0 \end{pmatrix}, \sigma_y = \begin{pmatrix} 0 & -i \\ i & 0 \end{pmatrix}, \sigma_z = \begin{pmatrix} 1 & 0 \\ 0 & -1 \end{pmatrix}$
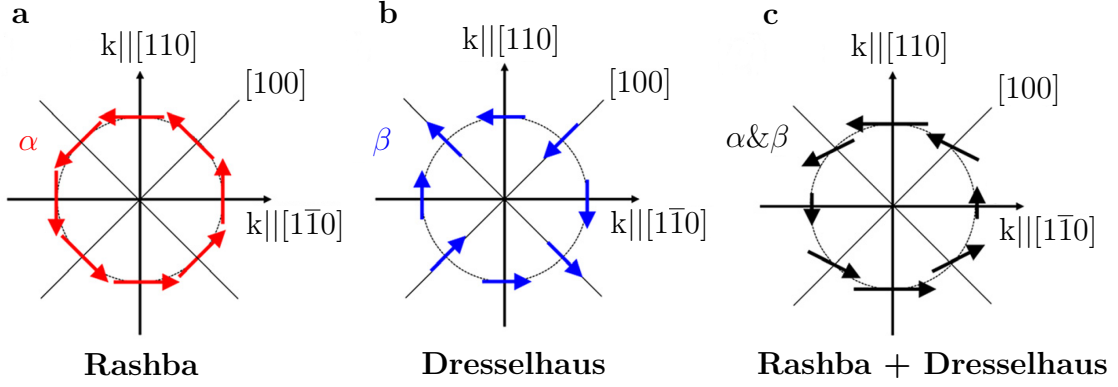
Figure 2.4: **SOI:** Fermi circles and spin-orbit interaction fields for different k-space directions in our InAs quantum well for **a,** the Rashba term, **b,** the Dresselhaus term, and the sum of both **c,** showing the resulting asymmetric SOI strength. Figures adapted from Ref. [52].

well in the growth direction and by the band structure parameters of the material. In contrast to the isotropic Rasbha SOI fields (Fig. 2.4**a**), the Dresselhaus field (Fig. 2.4**b**) is highly anisotropic and thus, the total spin-orbit field (Fig. 2.4**c**) is weaker in k-direction $[1\bar{1}0]$ than in $[110]$. As we know from the bulk [53] and from previous experiments [51], the Dresselhaus coefficient is expected to be much smaller. Does it then still play a decisive role in experiments? This question will be answered in chapter 6.1.

For the theoretical explanation of our observed diode effect (see chapter 5), P. E. Faria Junior and the group of J. Fabian made self-consistent $k \cdot p$ calculations for the estimation of realistic SOI values in our heterostructure (see the supplement of Ref. [32]). The summarised result in figure 2.5 shows in panel **a** the Rashba- and in panel **b** the Dresselhaus coefficient as a function of the charge carrier density n and the surface potential V_{L}. This potential is a representative of an electric field in growth direction. In order to get an idea of the total SOI energy ($E_{\mathrm{SO}} = 2\alpha_{\mathrm{R/D}}k_{\mathrm{F}}$) in relation to the Fermi energy ($E_{\mathrm{F}} = \hbar^2 k_{\mathrm{F}}^2/2m^*$), the following ratio can be set up:

$$\frac{\Delta E_{\mathrm{SO}}}{E_{\mathrm{F}}} = \frac{4\alpha_{\mathrm{R/D}}m^*}{\hbar^2 k_{\mathrm{F}}(n)} \tag{2.10}$$

In general, this relation points out, that apart from the Rashba and Dresselhaus coefficients, a big effective mass m^* and a smaller charge carrier density (i.e. small k_{F}) enhance the SOI effect.

a

b
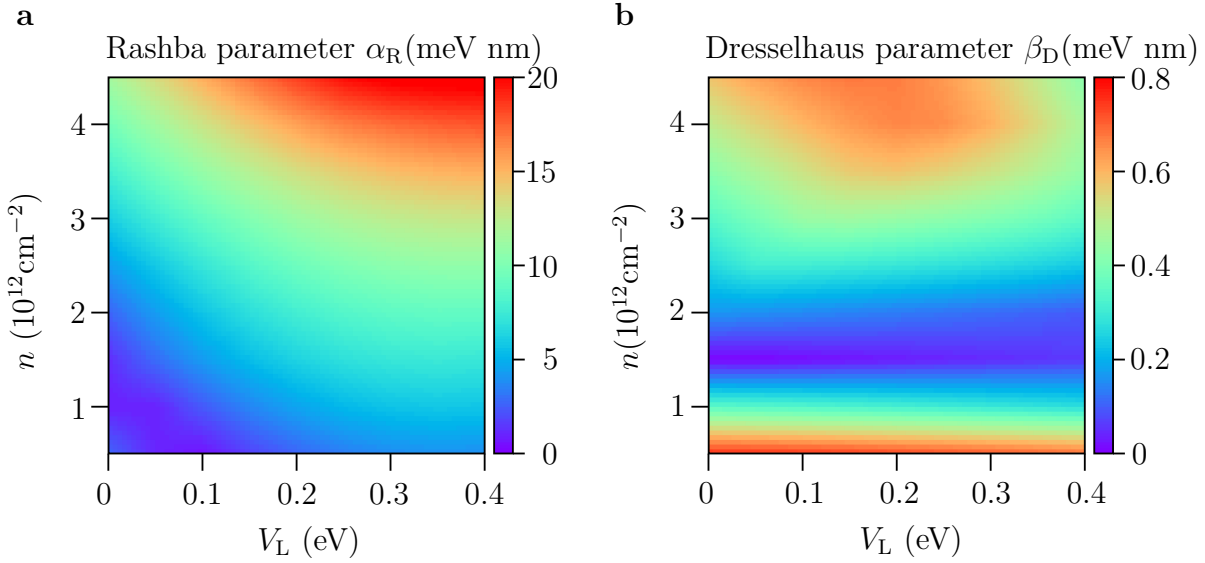
Figure 2.5: **SOI: a,** Rashba and **b,** Dresselhaus coefficients α_R and β_D for different n and V_L. Figure provided by P.E. Faria Junior.

2.1.3 Zeeman Effect

Each electron possesses an additional degree of freedom, namely the electronic spin. It is a magnetic dipole moment which is related to the spin angular momentum according to [42]

$$\mu = -\frac{1}{2}g\mu_B\sigma, \tag{2.11}$$

with $\mu_B = |e|\hbar/2m_e$ being the Bohr's magneton. The Landé g-factor is $\simeq 2$ for free electrons. In bulk InAs, the g-factor is $\simeq 15$ and becomes smaller with decreasing thickness of the quantum well [54]. A magnetic field can couple to the magnetic dipole moment, with the energy described by the Hamiltonian

$$H = -\mu B = \frac{1}{2}g\mu_B\sigma B. \tag{2.12}$$

The Zeeman energy can therefore be written as follows:

$$E_{z,\pm} = \pm\frac{1}{2}g\mu_B B \tag{2.13}$$

The applied field opens a gap of $2E_z$ at k=0. This spin splitting leads to a spin polarisation of the energy bands. Furthermore, the Zeeman field breaks the time-reversal symmetry giving rise to different phenomena, such as the non-reciprocal current discussed in chapter 5.

13

2.2 The Superconductor

Superconductors are metals that lose their electrical resistance below a certain critical temperature T_c. It was discovered by H. Kamerlingh Onnes in 1911 in Leiden, when he studied the electrical behaviour of mercury [55]. Three years earlier, in 1908, he had been the first person to succeed in liquefying helium giving him the ability to reach temperatures of a few Kelvin. From then on, superconductor research expanded, more and more materials were discovered, cooling techniques improved and the first applications developed. A major leap for the theoretical description was made with the publication of the macroscopic Ginzburg-Landau theory in 1950 [56] and the microscopic BCS theory from Bardeen, Cooper and Schrieffer in 1957 [57]. To date, superconductity is a huge field of research with much unknown land. Unlike other quantum phenomena, it does not disappear when the system size is increased [44].

2.2.1 BCS Theory

According to BCS theory, two electrons with opposite momentum and spin $(k \downarrow, -k \uparrow)$ feel an attractive interaction and form pairs, resulting in bosonic particles called Cooper pairs. These Cooper pairs have zero spin, form a macroscopic phase ϕ and condensate to a single ground state. Due to the lower ground state the kinetic energy of the electrons is increased compared to a non-interacting Fermi gas and thus overcompensated by the pairing energy $\Delta(r)$. If $\Delta(r)$ is present, excited particles are described by the Bogoliubov-de-Gennes equations [45]

$$\begin{pmatrix} H(r) & \Delta(r) \\ \Delta^*(r) & -H(r) \end{pmatrix} \begin{pmatrix} u_k(r) \\ v_k(r) \end{pmatrix} = E \begin{pmatrix} u_k(r) \\ v_k(r) \end{pmatrix}, \tag{2.14}$$

where the solutions are either electron-like or hole-like quasiparticles and are represented by the vector (u_k, v_k). The single-electron Hamiltonian $H(r)$ is defined as

$$H(r) = -\frac{\hbar^2}{2}\nabla^2 \frac{1}{m^*} + U(r) - \mu, \tag{2.15}$$

with m^* as the effective mass, μ as the chemical potential and $U(r)$ as a scalar potential. The superconducting pair potential $\Delta(r)$ is responsible for the coupling of the electron and hole content u_k and v_k. The character of the quasiparticles is electron-like for $|u_k|^2 > |v_k|^2$ and hole-like for the opposite case. The electron or hole-like components decay into single-particle states when $\Delta(r)$ disappears. The spatial
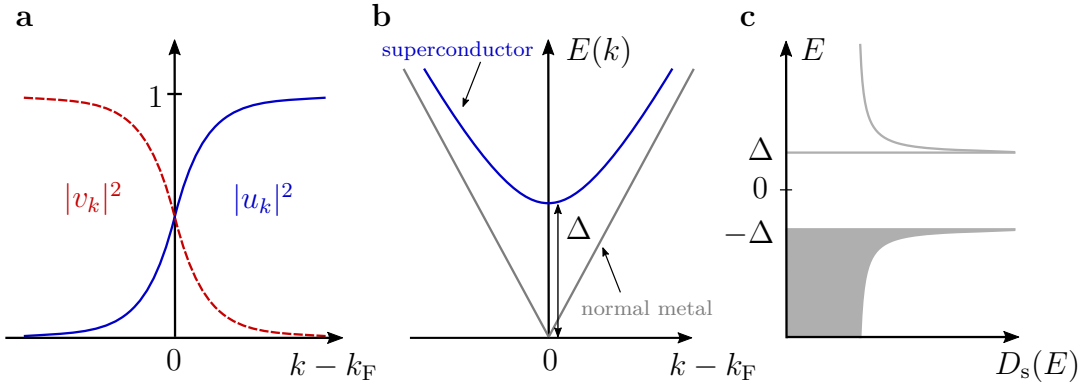
Figure 2.6: **Quasiparticle spectrum and superconducting gap: a,** Coherence factors v_k and u_k of quasiparticles near k_{F}. **b,** Excitation energy of quasiparticles in a superconductor compared to a normal metal close to k_{F}. **c,** Quasiparticle density of states as a function of excitation energy in a superconductor. A gap of the size Δ opens around E_{F} in which states are non-existent. Figure inspired by [58].

component $g(r)$ can be neglected in many cases and decoupled in the following way:

$$
\begin{pmatrix} u_k(r) \\ v_k(r) \end{pmatrix} = g(r) \begin{pmatrix} u_0 \\ v_0 \end{pmatrix}
\tag{2.16}
$$

The assumption for a homogeneous superconductor $\Delta(r) = \Delta_0$ and that the scalar potential $U(r)$ is zero facilitates the solution of equation 2.14 and yields u_0 and v_0 according to

$$
u_0^2 = \frac{1}{2}\left(1 + \frac{\sqrt{E^2 - \Delta_0^2}}{E}\right),
\tag{2.17}
$$

$$
v_0^2 = 1 - u_0^2,
\tag{2.18}
$$

where the eigenvalues of the energy are given by

$$
E = \pm\sqrt{\xi^2 + |\Delta_0|^2},
\tag{2.19}
$$

with $\xi = \left(\frac{\hbar^2 k^2}{2m^*} - \mu\right)$. As illustrated in figure 2.6**a**, excitations with $k > k_{\text{F}}$ are electron-like, while excitations with $k < k_{\text{F}}$ are hole-like.

The superconducting density of states $N_{\text{s}}(E)$ can be obtained by taking into account, that a superconductor is a metal with a gap around E_{F}, which leads us to the

assumption

$$N_{\text{s}}(E)dE = N_{\text{n}}(\xi)d\xi. \tag{2.20}$$

Since we are interested in energies ξ close to E_{F}, we can equate $N_{\text{n}}(\xi) = N_{\text{n}}(0)$ and treat it as a constant. This leads to the result

$$\frac{D_{\text{s}}(E)}{D_{\text{n}}(E)} = \frac{N_{\text{s}}(E)}{N(0)} = \frac{d\xi}{dE} = \begin{cases} \frac{E}{(E^2-\Delta^2)^{1/2}} & (E > \Delta) \\ 0 & (E < \Delta) \end{cases}. \tag{2.21}$$

We see that the pairing potential Δ opens a gap around the Fermi energy, where no fermionic states exist. This signature is illustrated in figure 2.6**b** for the dispersion relation and in figure 2.6**c** for the density of states. The latter figure further indicates the raised energy above Δ for excitations with momentum k, whose ξ falls into the gap. The density $N_{\text{s}}(E)$ diverges for $E = \Delta$, as the denominator in Eq. 2.21 becomes zero [23].

Since the group velocity of a particle is described by

$$v_k = \frac{1}{\hbar}\nabla_k E \tag{2.22}$$

and the energy is positive for electrons with the momentum $k > k_{\text{F}}$, it is evident that the group velocity v_k and the wave vector k have the same sign, whereas for a hole it is the opposite situation. This foreshadows the application of the Bogoliubov equation for inhomogeneous systems, like a superconductor/normal conductor interface. At such an interface, the Andreev process and the proximity effect play a crucial role, as we will see in section 2.4.

2.2.2 Ginzburg-Landau Theory

In 1950, Ginzburg and Landau proposed a phenomenological macroscopic description of superconductivity. The theory indroduces a complex pseudowavefunction ψ as an order parameter within treating superconductivity as a second-order transition. The order parameter is related to the local density of superconducting electrons by

$$n_s = |\psi(x)|^2. \tag{2.23}$$

In the normal phase, ψ is equal to zero and can be used at the phase transition to describe the free energy of the system which is

$$F = F_{\mathrm{n}} + \alpha|\psi|^2 + \frac{\beta}{2}|\psi|^4 + \frac{1}{2m^*}\left|\left(-i\hbar\vec{\nabla} + 2e\vec{A}\right)\psi\right|^2 + \frac{|\vec{B}|^2}{2\mu_0}, \qquad (2.24)$$

where F_{n} is the free energy in the normal state and α and β are phenomological parameters. The minimisation of the free energy with respect to the fluctuations of the order parameter ψ and the vector potential A leads to the two Ginzburg-Landau equations: [23]

$$\alpha\psi + \beta|\psi|^2\psi + \frac{1}{2m^*}\left(-i\hbar\vec{\nabla} + 2e\vec{A}\right)^2\psi = 0 \qquad (2.25)$$

and

$$j_{\mathrm{s}} = -\frac{2e}{m^*}\mathrm{Re}\left\{\psi^*\left(-i\hbar\vec{\nabla} + 2e\vec{A}\right)\psi\right\}. \qquad (2.26)$$

From these equations we can derive the London penetration depth λ, which is a measure of the depth an external magnetic field can penetrate the superconductor. To derive the London penetration depth λ, we assume that the superconductor is homogeneous and contains no magnetic fields, so that ψ becomes constant. Therefore, Eq. 2.25 reduces to the first two terms, leading to $|\psi|^2 = -\alpha/\beta$. Inserting this expression into Eq. 2.26 gives the supercurrent density [59]

$$j_{\mathrm{s}} = \frac{4e^2}{2m}\frac{|\alpha|}{\beta}A. \qquad (2.27)$$

This equation is equal to the *second London equation*

$$\mathrm{curl}\, j_{\mathrm{s}} = -\frac{n_{\mathrm{s}}e_{\mathrm{s}}^2}{m_{\mathrm{s}}}B \qquad (2.28)$$

and as a result the Ginzburg-Landau expression for the penetration depth λ_{L} is

$$\lambda_{\mathrm{L}} = \sqrt{\frac{m\beta}{4\mu_0 e^2|\alpha|}}. \qquad (2.29)$$

Since the density of Cooper pairs n_s varies with temperature, the penetration depth depends on the temperature according to

$$\lambda_L(T) = \frac{\lambda_{\mathrm{L}}(0)}{\sqrt{1 - (T/T_{\mathrm{c}})^4}}. \qquad (2.30)$$

The second parameter derived from the Ginzburg-Landau equation is the coherence length

$$\xi_{\mathrm{GL}}(T) = \frac{\hbar}{\sqrt{|2m^*\alpha(T)|}}, \tag{2.31}$$

and characterises the lengthscale over which the Cooper pair density n_{s} can vary.

The ratio $\frac{\lambda_{\mathrm{L}}}{\xi_{\mathrm{GL}}}$ is the Ginzburg-Landau parameter κ which discriminates two scenarios:

$$\kappa < 1/\sqrt{2} \quad \text{for type 1 superconductors}$$
$$\kappa > 1/\sqrt{2} \quad \text{for type 2 superconductors}$$

Later in 1959, the GL-theory gain appreciation after Gor'kov showed that it was actually a limiting form of the BCS-theory near T_{c}, where ψ is directly proportional to the BCS gap Δ [23][60].

2.2.3 Coherence Length

The *Pippard coherence length* ξ_0 is another important characteristic. It describes the length over which Cooper pairs are correlated to each other. In a pure superconductor, when ξ is much smaller than the mean free path of electrons in the normal state l_{el}, it is given by [44]

$$\xi_0^{\mathrm{clean}} = \frac{\hbar v_{\mathrm{F}}}{\pi |\Delta|}. \tag{2.32}$$

In the dirty case, $\xi_0 \gg l_{\mathrm{el}}$, it is described by

$$\xi_0^{\mathrm{dirty}} = \sqrt{\frac{\hbar D}{2\Delta}} \quad \text{with} \quad D = \frac{1}{2} v_{\mathrm{F}} l_{\mathrm{el}}, \tag{2.33}$$

where D is the *diffusion constant*. In the pure case far below T_c, ξ approaches $\xi_{\mathrm{GL}}(T)$, whereas near T_c, $\xi_{GL}(T)$ diverges. These two parameter are thus related, but nevertheless different quantities [23].

2.2.4 Why Aluminium?

Why is aluminium chosen over other materials such as niobium or lead, which are more robust superconductors? Well, the most obvious reason is that up to now it has only been possible to grow two-dimensional heterostructures with aluminium. Among other things, this is due to the similar lattice constant to InAs and thus aluminium

shows good growth properties. However, there are also physical reasons that make aluminium interesting. One reason is the Fermi velocities of Al ($v_\mathrm{F} \simeq 2.0 \cdot 10^6$ m/s for bulk Al [61]) and InAs ($v_\mathrm{F} \simeq 1.2 \cdot 10^6$ m/s in our 2DEG system). The smaller the Fermi velocity mismatch, the higher are the probabilites for Andreev reflections and thus favors a strong proximity effect (discussed in section 2.4). Another property that favours the proximity effect is the relatively high coherence length ξ_0 of aluminium. Furthermore, in order to perform operations with Majorana qubits it is essential to prevent dephasing of the topological states. Unpaired electrons from the superconductor can disturb and scramble up the states, known as quasiparticle poisening [62]. Aluminium seems to be more robust against this poisening than other materials. Aluminium shows $2e$-periodic transport in Coulomb-blockaded devices without changing the charge parity [63][20][64].

2.3 S-N-S Devices

In this section we cover the main and most important physics behind S-N-S weak links. By removing the aluminium in a predefined area, the result is an overdamped Josephson junction in the short-ballistic regime, as sketched in Fig. 2.7. The devices discussed in this work are based on such junctions, where most of the general mechanisms can be described and understood by the Josephson equations and the RCSJ-model. The superconducting banks with their own Ginzburg-Landau phase and BCS-gap proximitise the 2DEG underneath, inducing a non-BCS like gap Δ^*, whose quantity depends on the transparency of the interface between the aluminium and the InAs.
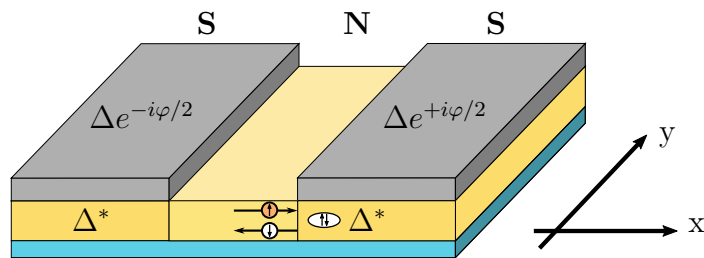
Figure 2.7: Schematic setup of a **Josephson junction**. The supercurrent is carried by the Andreev bound states between the proximitised 2DEG areas.

The supercurrent between the proximitized 2DEG areas is carried by Andreev bound states (ABS). Those can be manipulated via external magnetic fields, spin-orbit interaction, gate voltages and other external or intrinsic parameters. Due to the dominant part of the ABS in the measurement signal compared to other sources (e.g. the superconducting film or vortex contributions), it is a subtle way to investigate the nature of ABS to gain more insight into the properties of the underlying heterostructure and associated devices. The ABS can be phase or current controlled and, therefore, they are interesting in terms of topological aspects. Theoretically, this system has all the ingredients that are required to tune it into a topological state, depending on the magnitude and the orientation of the magnetic field. The phase difference between the superconducting banks can function as an additional knob.

2.3.1 Josephson Effect

Superconducting junctions are rich of many unique physical phenomena and are thus the basis for several applications nowadays, such as highly accurate voltmeters, single-

photon detectors [65][66], magnetometers [67] or radiation meters just to mention a few [68][44]. Josephson junctions can also be the basis of various future components, e.g. superconducting diodes [69][70][32], quantum computers based on Andreev qubits, transmon qubits or fault-tolerant topological qubits [71].

In general, the Josephson effect describes the current flowing between two weakly coupled superconducting banks at zero voltage. In 1962, B. D. Josephson [72] predicted the 1st Josephson equation according to

$$I_\mathrm{s} = I_\mathrm{c} \sin(\Delta\varphi) \tag{2.34}$$

for a thin insulating weak link. The supercurrent I_s depends on the phase difference $\varphi_2 - \varphi_1$ of the macroscopic Ginzburg-Landau wavefunctions of the banks and on the critical current I_c, the maximum current the weak link can sustain. This relation, also known as the current-phase relation (CPR), is sinusoidal in the general case. But its shape can change for highly transparent S-N-S junctions (chapter 4), can have cosine contributions (chapter 5) or can take many other forms [73]. Moreover, B. D. Josephson made a further prediction for finite voltages V across the junction, where the phase difference $\Delta\varphi$ evolves as

$$d(\Delta\varphi)/dt = 2eV/\hbar. \tag{2.35}$$

In other words, a finite voltage causes an alternating current with the amplitude I_c and the Josephson frequency $\nu = 2eV/h \approx 484\frac{\mathrm{MHz}}{\mu\mathrm{V}}$. Thus, such a Josephson device can be used as a voltage controlled oscillator and this behaviour is so fundamental that it is even used to define the volt.

In the superconducting state, no energy will be dissipated in the junction. However, we can define a Josephson coupling energy:

$$E_\mathrm{J} = \frac{\hbar I_\mathrm{c}}{2e} \tag{2.36}$$

The overlap of the macroscopic wavefunctions of the superconducting leads are responsible for a binding energy in analogy to molecules and covalent bonds. The coupling energy is the maximal potential energy ($E_\mathrm{pot}(\varphi) = E_\mathrm{J}(1 - \cos\varphi)$) which can be stored in a junction. The potential energy depends on the magnitude of the critical current and on the phase of the banks. In order to change the phase difference, energy

has to be supplied externally. Once the critical current is reached, the stored energy E_{pot} is converted to a kinetic energy E_{kin}. To better understand what this actually means, we need to look at the following model.

2.3.2 RCSJ Model

The **resistively and capacitively shunted junction** (RCSJ) model is an electrotechnical way to describe an ideal Josephson junction at finite voltages. In partic-
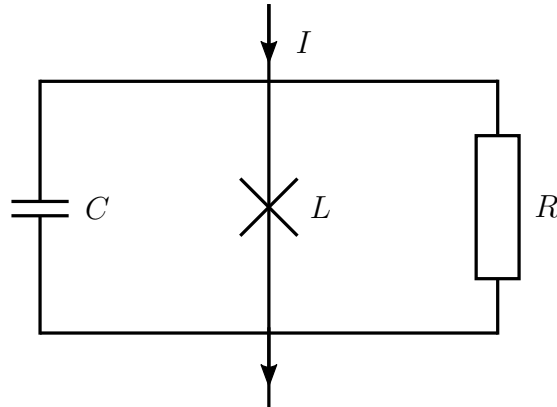
Figure 2.8: **Circuit diagramm** of the RCSJ model.

ular, it is a model to describe the dynamic state of the junction for currents larger than the critical current by including a resistor and a capacitor in parallel to our Josephson inductor (illustrated in scheme 2.8). Here, we neglect noise currents that can stem from thermal noise in the resistor. The total current for these three components according to Kirchhoff's law is therefore

$$I = I_{\text{c}} \sin \varphi + \frac{V}{R} + C \frac{\partial V}{\partial t}. \tag{2.37}$$

By eliminating the voltage $V = \dot{\varphi} \frac{\hbar}{2e} = \dot{\varphi} \Phi_0{}^2 / 2\pi$ and the substitution of $L_{\text{c}} = \Phi_0 / I_{\text{c}} 2\pi$, we can write the equation as:

$$I \frac{2\pi}{\Phi_0 C} = \frac{1}{L_{\text{c}} C} \sin \varphi + \frac{1}{RC} \frac{\partial \varphi}{\partial t} + \frac{\partial^2 \varphi}{\partial t^2}. \tag{2.38}$$

This differential equation reveals a circuit that behaves as a non-linear LC-oscillator. Therefore, we can introduce new parameters such as the Josephson plasma frequency

---

[2]$\Phi_0 = \frac{h}{2e} \approx 2 \cdot 10^{-15}$ T·m^2

$$w_{\mathrm{p}}^2 = \frac{1}{L_{\mathrm{c}}C} = \frac{I_{\mathrm{c}}2\pi}{\Phi_0 C} = \frac{2eI_{\mathrm{c}}}{\hbar C} \tag{2.39}$$

and the quality factor [74][75]

$$Q = w_{\mathrm{p}}RC = R\sqrt{\frac{C}{L_c}} = \sqrt{\frac{2eI_cR^2C}{\hbar}}. \tag{2.40}$$

By introducing the normalised time $\tau = w_{\mathrm{p}}t$ and using the Eqs. 2.39 and 2.40, we can write equation 2.38 as

$$Q^2\frac{\partial^2\varphi}{\partial\tau^2} + \frac{\partial\varphi}{\partial\tau} + \sin\varphi - \frac{I}{I_{\mathrm{c}}} = 0. \tag{2.41}$$

This is recognised as an equation of motion by a "classical" particle in a so-called tilted washboard potential (visualised in Fig. 2.9). The background slope of the corrugated
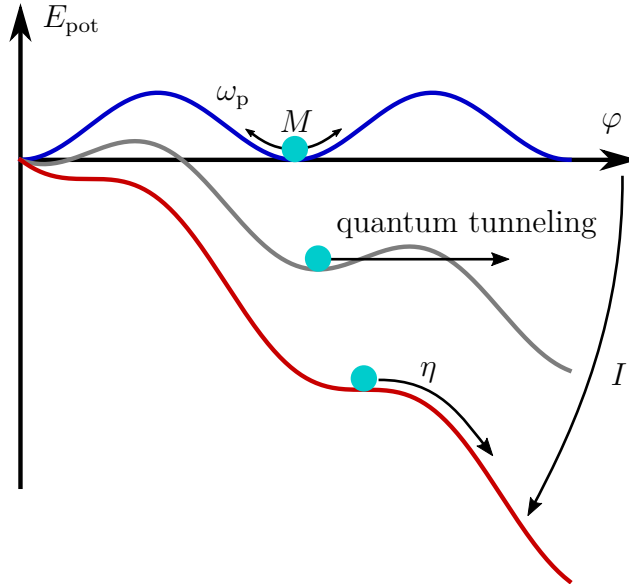
Figure 2.9: **Washboard potential:** The current can modify the tilt in both directions and bring the particle into motion. Potential energy converts to kinetic energy and the point mass moves along the phase axis φ. Figure inspired by [43].

potential

$$E_{\mathrm{pot}} = E_{\mathrm{J}}(1 - \cos\varphi) - (\hbar I/2e)\varphi \tag{2.42}$$

is tuned by the applied current I. As long as the current I is smaller than the critical current I_{c}, the particle is trapped in one of the minima and oscillates locally with the Josephson frequency w_{p}. Upon reaching the critical current, the point mass

starts to slide over the barrier and the potential energy converts into a kinetic energy ($E_{\text{kin}} = \frac{1}{2}m(\frac{\partial \varphi}{\partial t})^2$). Now, the particle with the mass $M = (\hbar/2e)^2 C$ and the damping $\eta = (\hbar/2e)^2 1/R$ moves along the φ axis and causes a finite voltage. In analogy to a physical pendulum we can draw the following comparisons [76]:

Josephson Analog		Mechanical Analog
Phase Difference φ	<=>	Angle Position θ
$\dot{\varphi}$	<=>	Angle Velocity $\dot{\theta}$
Capacitance C	<=>	Mass M
Direct Current I	<=>	Applied Torque $\vec{M}$
Conductance $1/R$	<=>	Damping Coefficient η

Note that quantum uncertainty or thermal fluctuations can assist quantum tunneling through the barrier and bring the particle into motion. Thus, the observed critical current is lower than the actual one. A particle with high mass and low damping continues its ride down the potential. In our case, however, the opposite is valid.

2.3.3 Overdamped Junctions

We can discriminate between underdamped ($Q \gg 1$) and overdamped ($Q \ll 1$) Josephson junctions. In our two-dimensional S-N-S devices, the capacitance and the resistance are small and, hence, $Q = (2eI_{\text{c}}R^2C/\hbar)^{1/2}$ is much smaller than 1. Starting from the zero voltage state, the particle in our RCSJ model has no kinetic energy until the critical current is reached.

In the strongly damped case, the particle starts moving slowly, corresponding to small voltages. Whereas in the underdamped case, the particle accelerates immediatly to an average velocity given by the background slope. However, reducing the current and thus the tilt again, the barely damped particle has a sufficient high inertia to continue its motion until the slope of the potential is almost zero. In contrast, the strongly damped particle will stop its motion abruptly for $I < I_{\text{c}}$ and the $I - V$ characteristicts follows:

$$V = R(I^2 - I_{\text{c}}^2)^{1/2} \qquad \text{for} \quad T = 0 \tag{2.43}$$

In the underdamped case the $I - V$ curve shows a hysteretic behaviour.

2.3.4 Activation Energy

Ambegaokar and Halperin [77] showed in the late 60s that the kink in the $I - V$ relation 2.43 for an overdamped junction is smeared when thermal noise is considered and thus they included an extra term in equation 2.38. In our washboard model, the particle diffuses over the barriers and the strong damping brings it back into an equilibrium distribution, where it can again diffuse into the next minimum. This non-linear process increases towards $I \to I_{c}$ and, hence, a finite resistance is present throughout. There exists a non-zero limiting value R_0 for $I \to 0$ which is related to the normal resistance R_N of the junction by

$$R_0/R_N = [I_0(u/2)]^{-2} \propto u e^{-u}, \tag{2.44}$$

with $u = \hbar I_c / e k_B T$ as the normalised activation energy and I_0 as a modified Bessel function. This equation is true for $u \gg 1$. The activation energy reveals how much energy is needed to lift the particle above the barrier at zero temperature.

2.3.5 Thouless Energy

The *Thouless Energy* E_{Th} characterises an energy scale sensitive to the boundary conditions in diffusive disordered conductors [78]. This energy is defined as [79]

$$E_{Th} = \frac{\hbar D}{L^2}, \tag{2.45}$$

with L being the size of the system and D the diffusion constant. If we consider $D/L^2 = 1/\tau_{Th}$, we see an inversely proportional relation to the diffusion time τ_{Th}. It tells us how long it takes on average for an electron to explore the area L^2 within the given boundaries.
Strongly localized states (E_{Th} small) are hardly influenced by a change of the system edges, whereas it is the case for extended states (E_{Th} large) [42].

For a ballistic system, the Thouless energy changes to [80]

$$E_{Th} = \frac{\hbar v_F}{L}, \tag{2.46}$$

with v_F as the Fermi velocity. Although the Thouless energy describes numerous quantities, it is not clearly defined for the ballistic regime [81][82][79].

2.4 Interfaces of Hybrid Materials

In this section, we address the transport mechanism through a superconductor-2DEG-superconductor junction, where the interface plays a crucial role. After introducing Andreev reflection and BTK-theory, we will look into the nature of Andreev bound states that form the supercurrent carrying states in the normal region. Finally, we will discuss the proximity effect.

2.4.1 Andreev Reflection

When an electron in a normal conductor (metal or semiconductor) impinges on a superconductor, it will undergo an unique reflection process called *Andreev reflection* [83]. Since there are no quasiparticle states in the superconductor, transmission will not take place for $E < \Delta_0$. Moreover, at an ideal interface, normal reflection is also excluded, due to the lack of a barrier which can absorb the momentum difference. However, an electron with an energy slightly above the Fermi energy μ forms a Cooper pair with a second electron from the Fermi sea. As a consequence, a hole with opposite momentum and spin is *retroreflected*, see figure 2.10. The hole carries furthermore information of the phase of the electron state and of the macroscopic phase φ of the BCS superconductor. The transfer of $2e$ into the superconductor increases the conductance by a factor of two below the superconducting gap at zero temperature.
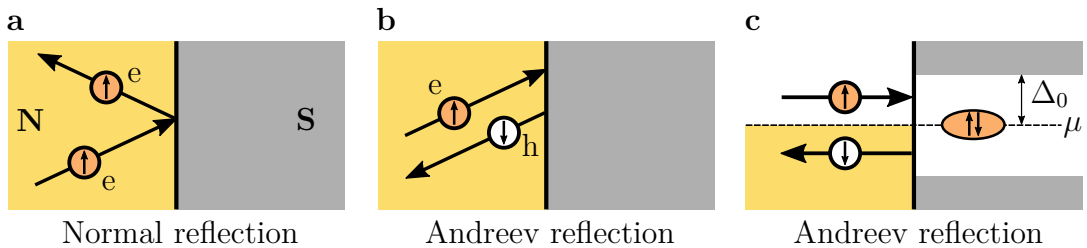
Figure 2.10: **Andreev reflection: a,** Schematic of normal reflection in real space. **b,** Andreev reflection in real space and in **c,** energy space. The incident electron is retroreflected as a hole for energys below Δ. Images inspired by [45] and [84].

2.4.2 BTK Theory

In reality, no interface is perfect and thus not every electron is retroreflected as a hole. In 1982, Blonder, Tinkham and Klapwijk presented a theory describing the

probabilites of Andreev reflection (A), normal reflection (B) and transmission (T) with and without branch crossing (C/D) [85]. For an approaching carrier counts:

$$A(E) + B(E) + T(E) = 1 \qquad (2.47)$$

Disorder, remaining oxides etc. lead to a non-ideal interface which is modeled by a δ-shaped barrier, located at the S-N interface. For semiconductor/superconductor systems, an additional potential stage U_0 must be taken into account, which is assumed to increase in a step-like manner, as schematically shown in Fig. 2.11**a**. The cause of U_0 is the difference in the respective charge carrier densities, which is responsible for a considerable difference in the Fermi energies. Accordingly, the potential $U(x)$ of a S/2DEG junction is [45]

$$U(x) = U_0 \Theta(-x) + \frac{\hbar^2 k_{\mathrm{FS}}}{m_{\mathrm{e}}} Z \delta(x), \qquad (2.48)$$

with $k_{\mathrm{FS}} = \sqrt{2m_{\mathrm{e}}\mu/\hbar^2}$ being the Fermi wave number in the superconductor. The dimensionless parameter Z expresses the coefficient H of the δ-shaped barrier and is therefore

$$Z = H \frac{m_{\mathrm{e}}}{\hbar^2 k_{\mathrm{FS}}}, \qquad (2.49)$$

whereas $Z = 0$ corresponds to an ideal interface and thus to perfect Andreev reflection.

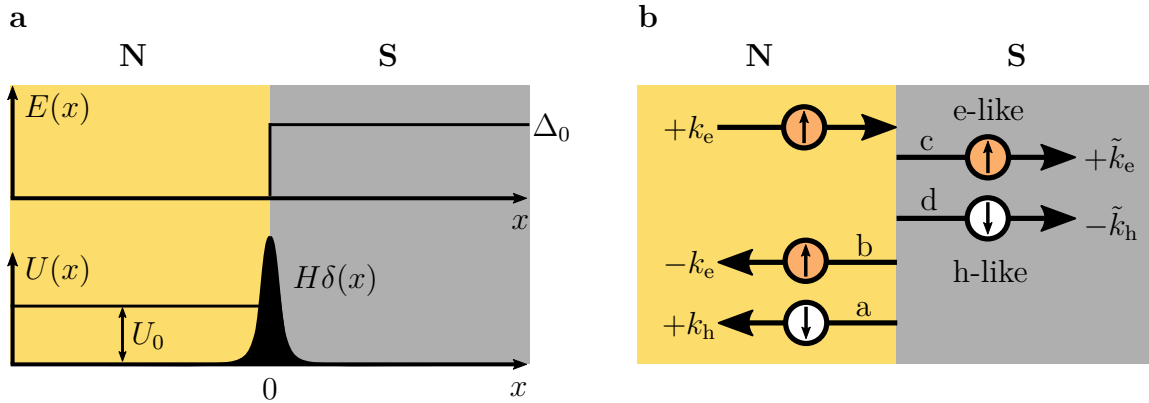Figure 2.11: **BTK theory: a,** S-N junction modeled with a δ-function at the interface in order to describe a realistic barrier. A step-like increase of the potential by U_0 is included due to Fermi velocity mismatch. **b,** Schematic representation of the possible reflection or transmission effects that an electron impinging on the superconductor from the semiconductor can experience.

An incoming electron from the normal side with the wavefunction [45]

$$\Psi_{\text{incoming}} = \begin{pmatrix} 1 \\ 0 \end{pmatrix} e^{ik_{\text{e}}x} \tag{2.50}$$

has overall four options, which are sketched in Fig. 2.11**b**. It can either be reflected as a hole or electron

$$\Psi_{\text{reflected}}(x) = a \begin{pmatrix} 0 \\ 1 \end{pmatrix} e^{+ik_{\text{h}}x} + b \begin{pmatrix} 1 \\ 0 \end{pmatrix} e^{-ik_{\text{e}}x} \tag{2.51}$$

or be transmitted as an electron-like or hole-like quasiparticle into the superconductor:

$$\Psi_{\text{transmitted}}(x) = c \begin{pmatrix} u_0 \\ v_0 \end{pmatrix} e^{+i\tilde{k}_{\text{e}}x} + d \begin{pmatrix} v_0 \\ u_0 \end{pmatrix} e^{-i\tilde{k}_{\text{h}}x} \tag{2.52}$$

The wavenumbers can be derived from the eigenenergies of the BdG equation, introduced in section 2.14. The resulting planewaves are

$$k_{\text{e}} = \sqrt{k_{\text{FN}}^2 + (2m^*/\hbar^2)E}, \tag{2.53a}$$

$$k_{\text{h}} = \sqrt{k_{\text{FN}}^2 - (2m^*/\hbar^2)E}, \tag{2.53b}$$

$$\tilde{k}_{\text{e}} = \sqrt{k_{\text{FS}}^2 + (2m_{\text{e}}/\hbar^2)(E^2 - \Delta_0^2)^{1/2}}, \tag{2.53c}$$

$$\tilde{k}_{\text{h}} = \sqrt{k_{\text{FS}}^2 - (2m_{\text{e}}/\hbar^2)(E^2 - \Delta_0^2)^{1/2}}, \tag{2.53d}$$

with $k_{\text{FN}} = \sqrt{(2m^*/\hbar^2)(\mu - U_0)}$ as the Fermi wave number in the normal region.

By applying appropriate boundary conditions on the wavefunctions 2.51 and 2.52 at $x = 0$, it is possible to derive the probability coefficients for the Andreev reflection $A = a^*a$, for the normal reflection $B = b^*b$ and for the transmission $T = c^*c + d^*d$.

The corresponding probability amplitudes are listed in table 2.1. The parameter Z is adjusted to $Z_{\text{eff}} = \sqrt{Z^2 + (1-r)^2/4r}$ to include the Fermi velocity mismatch

	A	B	T
$Z > 0$			
$E < \Delta$:	$\frac{\Delta^2}{E^2+(\Delta^2-E^2)(1+2Z_{\mathrm{eff}}^2)^2}$	$1 - A$	0
$E > \Delta$:	$\frac{u_0^2 v_0^2}{\gamma^2}$	$\frac{(u_0^2-v_0^2)^2 Z_{\mathrm{eff}}^2(1+Z_{\mathrm{eff}}^2)}{\gamma^2}$	$1 - A - B$
$Z = 0$			
$E < \Delta$:	1	0	0
$E > \Delta$:	$\frac{v_0^2}{u_0^2}$	0	$1 - A$

Table 2.1: **Reflection and transmission coefficients:** Probabilites for Andreev reflection (A), normal reflection (B) and transmission ($T = C + D$) for a perfect ($Z = 0$) and a non-perfect ($Z > 0$) interface. Taken from [85].

$r = v_{\mathrm{FN}}/v_{\mathrm{FS}}$, and γ corresponds to

$$\gamma = u_0^2 + (u_0^2 - v_0^2)Z_{\mathrm{eff}}^2, \tag{2.54}$$

with the factors u_0 and v_0 given by the Eqs. 2.17 and 2.18. How the coefficients $A(E)$, $B(E)$ and $T(E)$ change for different Z_{eff} shows figure 2.12.
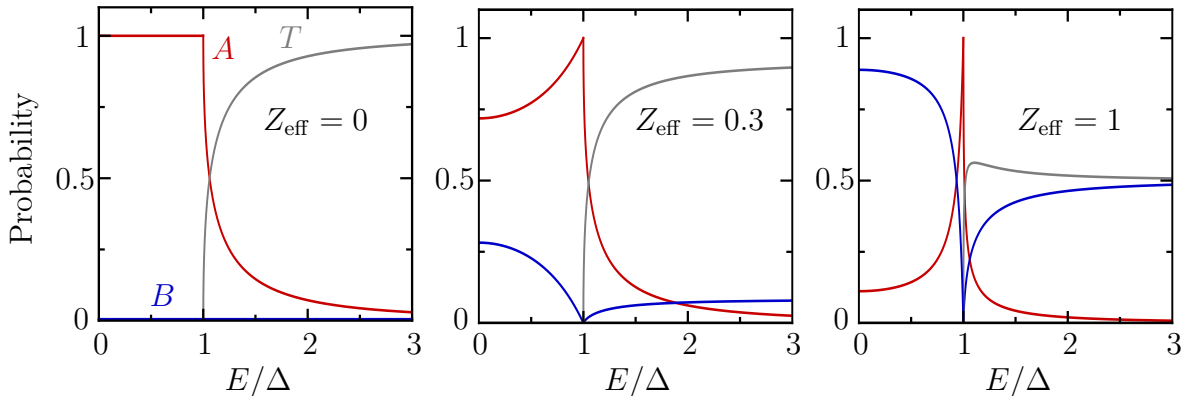
Figure 2.12: **BTK theory:** Probabilites of Andreev reflection A, normal reflection B and transimission T for Z_{eff}=0, 0.3 and 1.

2.4.3 Andreev Bound States

In our S-N-S junction, which we regard without barriers at the S-N and N-S interfaces for a moment, the electron is retroreflected as a hole on the right N-S interface. This hole moves along the same path in opposite direction and is in turn reflected at the S-N interface as an electron again, destroying a Cooper pair in the first superconducting

lead. This cycle continues and is called Andreev bound state, if a full cycle picks up a phase multiple of 2π. The formation of these Andreev levels in Josephson junctions is depicted in figure 2.13. The phases encountered of an electron at the retroreflection
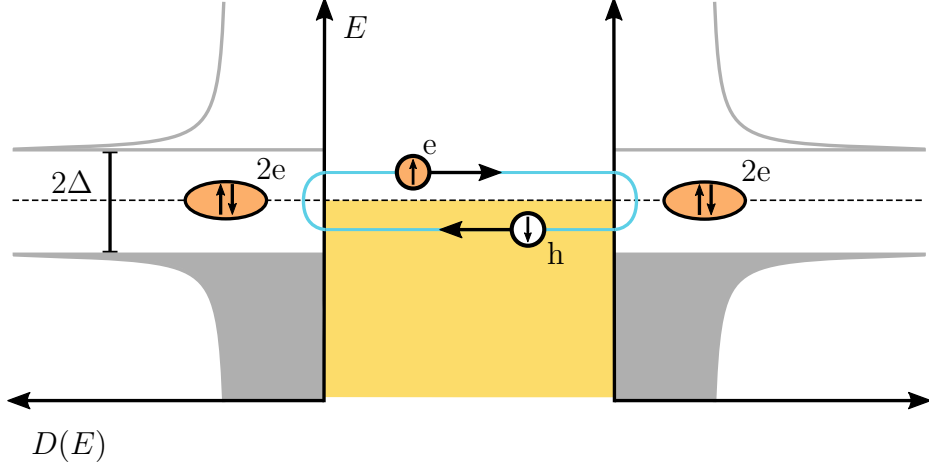
Figure 2.13: **Andreev bound state** in the 2DEG between two superconducting leads.

into a hole (φ_{eh}) and of a hole into an electron (φ_{he}) are [44]

$$\varphi_{\text{eh}} = -\arccos(E/\Delta) + \phi_{\text{s}}, \quad \varphi_{\text{he}} = -\arccos(E/\Delta) - \phi_{\text{s}}, \tag{2.55}$$

with ϕ_{s} being the phase of the superconductor. The accumulated phase of a full cycle is

$$\phi_{\text{tot}}^{(1)} = (k_{\text{h}} + k_{\text{e}})L + \phi + 2\arccos(E/\Delta) \tag{2.56}$$

and for the opposite case the total phase is

$$\phi_{\text{tot}}^{(2)} = (k_{\text{e}} + k_{\text{h}})L - \phi + 2\arccos(E/\Delta). \tag{2.57}$$

In the normal metal a total dynamical phase of $(k_{\text{h}} + k_{\text{e}})L \simeq 2EL/v_{\text{F}}\hbar$ is aquired. As discussed, the confined bound states must fulfil the condition $\phi_{\text{tot}}^{(1/2)} = 2n\pi$ and discrete energies are given.

As the Thouless energy $E_{\text{Th}} = \hbar v_{\text{F}}/L$ is much larger than the superconducting gap $\Delta(T)$, our junctions are in the short limit and the dynamical phase contribution can be neglected. Therefore the energies of the Andreev bound states are

$$E_{\text{ABS}} = \pm\Delta\cos(\varphi/2) \tag{2.58}$$

in the case of clean interfaces. In the presence of impurities, however, avoided crossing

Figure 2.14: **a,** The **Andreev bound state** energies and **b,** the **current-phase relation** for different transmission probabilities.
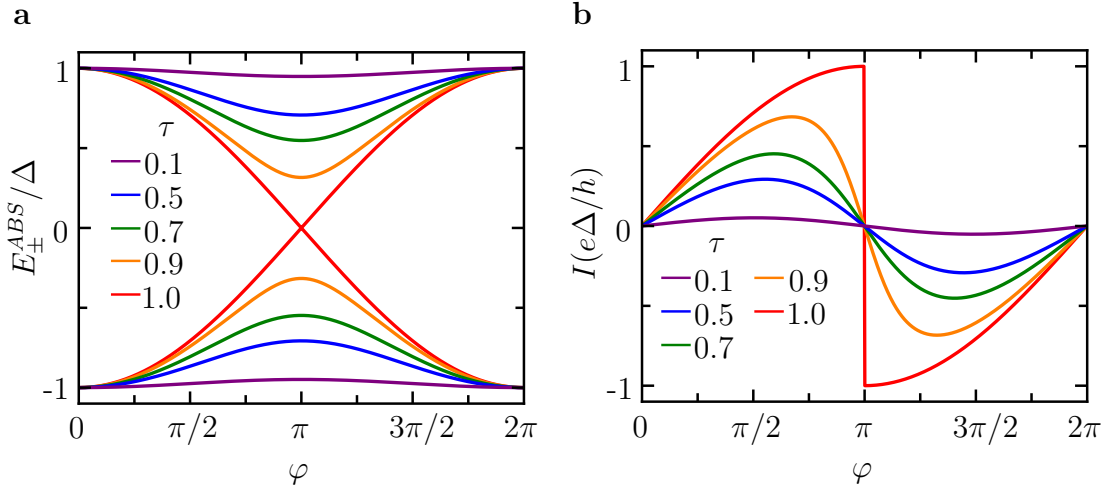
appears at $\varphi = \pi$ and the bound state energies are described by [86][87]

$$E_{\pm}^{\mathrm{ABS}} = \pm\Delta\sqrt{1 - \tau_n \sin^2(\varphi/2)} \qquad 0 < \tau_n < 1, \qquad (2.59)$$

where $n(= 1, 2...m)$ is the number of all ABS modes and τ_n is the transmission probability through the system per mode. The energy-phase relation for different τ is shown in 2.14**a**. Each bound state transfers a Cooper pair through the normal region and thus the supercurrent carried by each state is [88][89]

$$I_{\pm}^{\mathrm{ABS}} = \frac{2e}{\hbar}\frac{dE}{d\varphi}. \qquad (2.60)$$

The total supercurrent of a S-N-S junction is the sum of all ABS modes. For finite temperatures the supercurrent is given by [90][91][44]

$$I_{\mathrm{s}} = \frac{2e}{\hbar}\sum_{\pm}\frac{dE_{\pm}^{\mathrm{ABS}}}{d\varphi}\tanh\left(\frac{E^{\mathrm{ABS}}}{2k_{\mathrm{B}}T}\right) = \frac{e\Delta^2}{2\hbar}\frac{\tau\sin(\varphi)}{E_{+}^{\mathrm{ABS}}}\tanh\left[\frac{E_{+}^{\mathrm{ABS}}(\varphi)}{2k_{\mathrm{B}}T}\right]. \qquad (2.61)$$

The shape of the current-phase relation is basically given by the derivative of equation 2.59 and is plotted in figure 2.14**b**. The first Josephson equation $I_{\mathrm{s}} = I_{\mathrm{c}}\sin\Delta\varphi$ is valid only for the case of small transmission probabilities or high temperatures [44].

2.4.4 Josephson Inductance

How can the current-phase relation be determined experimentally? In chapter 4 we will see, that the CPR and the transmission probability can be obtained with the direct current dependent Josephson inductance $L(I)$.

In general, the inductance L is defined as the voltage divided by the time derivative of the current. Together with the first and second Josephson equations 2.34 and 2.35, the following equation can be established:

$$L(\varphi) = \frac{V}{\frac{dI}{dt}} = \frac{\Phi_0}{2\pi I_0 f'(\varphi)}.$$

(2.62)

Φ_0 is defined as the magnetic flux quantum and φ as the phase difference between the superconducting leads. The derivative $f'(\varphi)$ comes from a 2π-periodic dimensionless function. This function is part of the current-phase relation $I = I_0 f(\varphi)$ and is sinusoidal ($\sin\varphi$) in the case of tunnel junctions. By integrating $L\dot{I} = \Phi_0\dot{\varphi}/2\pi$, we can extract the inverse CPR according to

$$\varphi(I) = \varphi(0) + \frac{2\pi}{\Phi_0}\int_0^I L(I')dI'.$$

(2.63)

The function $L(I)$ is what we get from the resonator. What we cannot determine, however, is the integration constant $\varphi(0)$, corresponding to a φ_0-shift in the CPR.

In order to evaluate our data, we use the Beenakker-Furusaki formula to describe the CPR for short-ballistic junctions, which applies to arbitrary temperatures and is defined as follows [92][93][91][90]:

$$I(\varphi) = I_0 f(\varphi) = I_0 \frac{\overline{\tau}\sin\varphi\tanh\left[\frac{\Delta^*}{2k_\mathrm{B}T}\sqrt{1 - \overline{\tau}\sin^2(\frac{\varphi}{2})}\right]}{2\sqrt{1 - \overline{\tau}\sin^2(\frac{\varphi}{2})}},$$

(2.64)

where $\overline{\tau}$ is the average transmission coefficient, Δ^* the induced superconducting gap and I_0 the maximum critical current for $\overline{\tau} = 1$ and $T = 0$. An illustrative example of how the Eqs. 2.62 and 2.64 are applied together is shown in figure 4.2 in chapter 4.

2.4.5 Proximity Effect

In the context of hybrid S-N materials, the word *proximity effect* is part of the standard vocabulary. It labels the leakage of Cooper pairs from the superconductor through a good interface into the normal conducting part. This part inherits properties of the superconductor. In textbooks, this effect is rarely described in contrast to the Andreev process and is often treated as a separate phenomenon [94]. But this is actually not the case. With increasing amount of studies it became clear that these effects are intimately connected [89]. A fundamental reason for this discrepancy was the original overly simple theory of the proximity effect. The usage of the Gorkov equations or the simplified version of the Ginzburg-Landau theory, valid close to T_c, were insufficient.

Further theoretical developement lead to the quasi-classical equations by Eilenberger [95] and by Usadel [96] in the case of the dirty limit. Many experimental observations can be evaluated with the help of these quasi-classical equations, although the Bogoliubov-de-Gennes equations in addition with the concept of Andreev reflection give a better understanding in the case for ballistic electron transport [87].

Nowadays, the proximity effect can be understood as follows. Andreev reflection causes a phase correlation between the incident electron and retroreflected hole. The correlated phase decays over a distance of $\simeq \hbar v_{\rm F}/2E$ $(= \xi_{\rm N})$ from the interface, with E being the energy difference of the electron and hole. The proximity effect also works the other way round. Excited quasiparticles can diffuse into the superconductor and suppress superconductivity near the interface on the length scale of $\xi_{\rm s}$ [90][97].

The BTK model, described in section 2.4.2, assumes a step-like pair potential $\Delta(x)$ at the S-N interface and is therefore oversimplified in the context of the proximity effect. In Ref [45] and the authors cited therein, the application of the Green's function on the BTK model is discussed. They introduce the normal angle-averaged Green's function $G(E, x)$ and the anomalous angle-averaged Green's function $F(E, x)$. The real part of $G(E, x)$ represents the quasiparticle density of states, $DOS(E, x) = Re[G(E, x)]$, whereas $Re[F(E, x)]$ stands for the density of states of the correlated particles.

In their superconductor-semiconductor system, the authors include an additional layer N, which represents a few degraded layers of atoms originating from the deposition of the corresponding material. Hence, the layer sequence S-Sm extends to S-N-Sm.

We look at the S-N boundary in the *dirty limit*, since the superconductor is a metal which contains many scattering points. In the dirty limit, the coherence lengths $\xi_{\mathrm{S,N}} = \sqrt{\frac{\hbar D_{\mathrm{S,N}}}{2\pi k_{\mathrm{B}} T_{\mathrm{c}}}}$ are much larger than the corresponding mean free paths $l_{\mathrm{el,S}}$ and $l_{\mathrm{el,N}}$. The attached semiconductor can be either in the clean or in the dirty limit.

Because the Usadel equations are [96] not applicable for distances of the order of $l_{\mathrm{el,S}}$ and $l_{\mathrm{el,N}}$ from the interface, the Eilenberger [95] equations must be used to derive the boundary conditions, yielding two parameters. The first parameter is the barrier strength

$$\gamma_{\mathrm{B}} = \frac{2}{3} \frac{l_{\mathrm{el,N}}}{\xi_{\mathrm{N}}} \left\langle \frac{1-t}{t} \right\rangle, \tag{2.65}$$

where t is the interface transmission probability and related to the Z parameter from the BTK model via $t = \frac{1}{1+Z^2}$ and the parantheses $<...>$ denote angle averaging. The second parameter

$$\gamma = \frac{\varrho_{\mathrm{S}} \xi_{\mathrm{S}}}{\varrho_{\mathrm{N}} \xi_{\mathrm{N}}} \tag{2.66}$$

is a measure of the proximity strength and marks the suppression of the order parameter in the superconductor. It depends on the resistivities and coherence lengths $\varrho_{\mathrm{N,S}}$ and $\xi_{\mathrm{N,S}}$ of the N and S material, respectively. What the Cooper pair density,
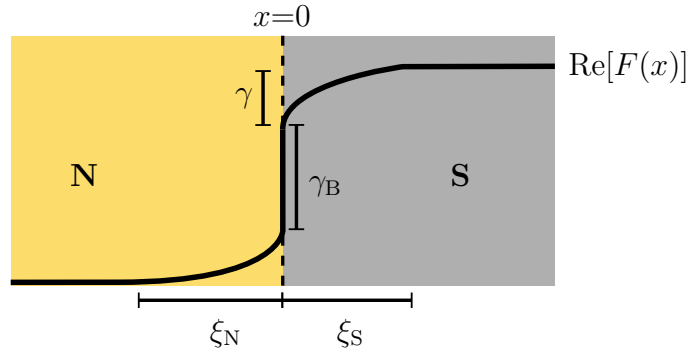
Figure 2.15: **Superconducting proximity effect:** $Re[F(x)]$ represents the spatial density of states of Cooper pairs. The amount of leaking correlated particles into the normal region depends on the proximity strength γ and the barrier strength γ_{B}. The coherence lengths $\xi_{\mathrm{N,S}}$ determine the characteristic length scale for this effect. Figure adapted from [45].

expressed by $Re[F(x)]$ near the interface, looks like is shown in figure 2.15. We can see an *inverse proximity effect* in the superconductor, where the density of the Cooper pairs decreases gradually towards the interface and is determined by γ. At the tran-

sition to the normal-conducting part (i.e. $x = 0$), the parameter γ_B represents the step in the pair density and thus the boundary transparency, while further on in the normal conductor, $Re[F(x)]$ decreases again gradually.

For a thin N layer with thickness d_N, γ can be replaced by $\gamma_m = \gamma \frac{d_N}{\xi_N}$, if $d_N/\xi_N \ll 1$ is fulfilled, as reported by Aminov et al. in Ref. [98]. Due to the reduced amount of parameters, Aminov et al. could calculate and plot the density of states at different locations for various γ_B for a fixed γ_m, as shown in figure 2.16. At the S-N interface,
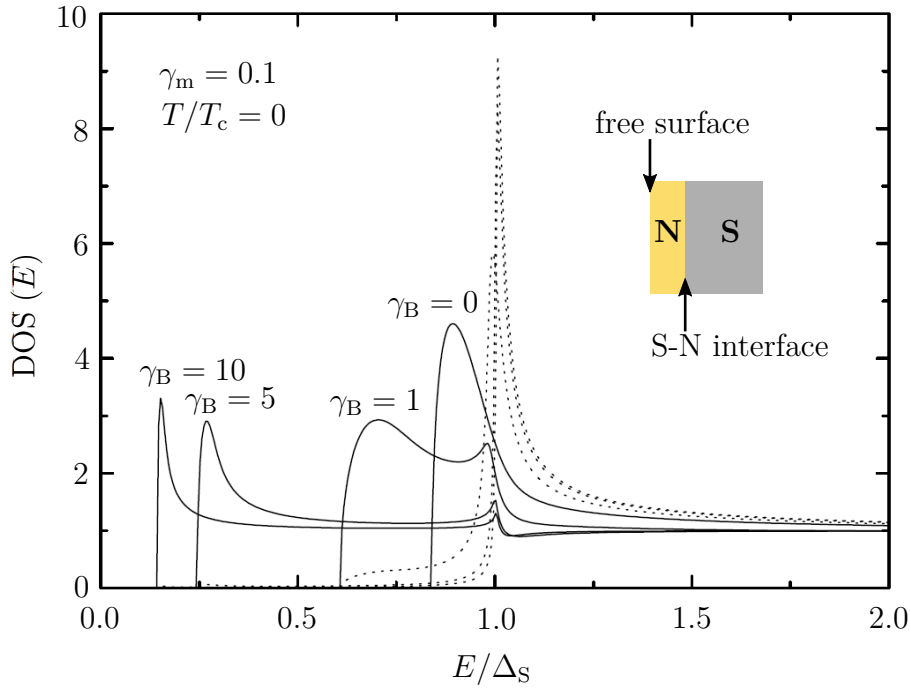

Figure 2.16: **Induced gap:** Density of states for different barrier strenghts γ_B of a S-N device with a thin N-layer ($d_N \ll \xi_N$) and constant proximity strength $\gamma_m = 1$. Dashed and grey lines denote the location at the S-N interface and at the free surface, respectively. Energy is normalized by the bulk superconducting gap Δ_S, while the DOS is normalised to their normal-state values. Figure adapted from [45][98].

the superconducting gap Δ_S is hardly affected, whereas at the free surface of the N layer ($x = +d_N$), Δ_N highly depends on barrier strength γ_B. An increase of γ_B results in the reduction of Δ_N.

This theory does not include impurities and, so far, finite temperatures. If the ratio γ_m/γ_B is small one can neglect the spatial gradients in the superconductor and $\Delta_S(x)$ becomes equal to the BCS value $\Delta_0(T)$. The temperature dependence for the energy

gap Δ_N in the normal layer is then given by [98][45]

$$\Delta_N(T) = \frac{\Delta_0(T)}{1 + \gamma_B \sqrt{\Delta_0^2(T) - \Delta_N^2(T)}/\pi T_c}.$$ (2.67)

This equation becomes invalid for temperatures close to T_c, where $\Delta_0(T)$ is small and moreover, the two gaps Δ_N and Δ_0 merge for temperature towards T_c.

Besides theory, there are also great experimental reports, such as from Chrestin et al. [99] or from Cherkez et al. [100], who visualised the proximity effect with spatially resolved scanning tunneling spectroscopy. Another experiment that is definetely worth to be mentioned is the work from le Sueur et al. [101]. Le Sueur et al. used a dual-mode STM-AFM microscope to study the phase controlled proximity effect.

Despite these experiments, it is still unknown how magnetic fields influence the proximity effect. In section 6.3, we present measurements of the proximity induced gap Δ^* in the presence of in-plane magnetic fields.

2.5 φ_0-Junction

A normal metal sandwiched in two conventional superconductors forms a Josephson junction. The corresponding current-phase relation is sinusoidal near the critical temperature, while at lower temperatures, higher harmonics $I_n \sin(n\varphi)$ may contribute to the CPR. If both time-reversal symmetry and inversion symmetry are broken, the CPR is no longer antisymmetric $I(-\varphi) \neq -I(\varphi)$ and the ground state of the junction shifts by a finite phase φ_0 according to [102][103][104]

$$I_J = I_c \sin(\varphi + \varphi_0).$$ (2.68)

The phase offset φ_0 is proportional to the spin-orbit parameter and magnetic field as the following equation shows [105]:

$$\varphi_0 = \frac{4\alpha d |g^*| \mu_B B}{\hbar v_{F,N}}$$ (2.69)

Here, $v_{F,N}$ is the Fermi velocity and g^* the g-factor in the normal metal. A. Buzdin [105] predicted the existence of such φ_0-junctions with the help of the phenomenolog-

ical Ginzburg-Landau theory and the quasi-classical Eilenberger approach. Very important for the occurence of this anomalous effect is the mixing of the spin-dependent channels due to the SOI [106]. In other words, several transverse modes are necessary to observe a finite current at zero phase difference.

In 2016, Szombati et. al [31] reported a finite current at zero phase difference on gate-controlled nanowire quantum dots, demonstrating the existence of a φ_0-junction. In 2019 and 2020, the observation of the φ_0 effect in planar Josephson junctions made of Bi_2Se_3 and InAs, each with aluminium electrodes, was reported by Assouline et al. [16], by W. Mayer et al. [107] and 2020 again by Strambini et al. [108].
However, in chapter 5 we will see, that the φ_0-shift alone is not the full story in order to explain the observations we made in our short-ballistic Josephson junctions.

3 Material, Methods & Characterisation

As part of this work, our group broke new ground with this novel material and resonator technique. This chapter describes in a compact way the foundation of this thesis - the methodology we elaborated in the past four years. Section 3.1 presents the material of choice and its specific properties. Next, section 3.2 describes the fabrication recipe, designed for the facilities in Regensburg. The following section 3.3 lists an overview of the most important samples. Section 3.4 is about how a new wafer can be characterised. The final section 3.5 describes our measurements setups with focus on the resonator technique.

3.1 Material

3.1.1 Introduction

A convenient way to create topological superconductors is to marry an s-wave superconductor with a Rashba semiconductor [11][22]. In the past, one common approach was to evaporate Al or Nb *ex-situ* to proximitise a nanowire or 2DEG [109]. However, the result in those days were low interface qualities.

In 2015, T.S. Jespersen and P. Krogstrup et al. [21] reported how to solve this problem. They evaporated aluminium epitaxially *in-situ* on the facets of Vapor-liquid-solid (VLS) grown InAs nanowires with a diameter of $\simeq 100$ nm. By finishing the evaporation process before breaking the vacuum of the growth chamber, the material characterisation showed high transparent and clean interfaces. Further tunnel experiments showed a hard-induced superconducting gap in the InAs regime, revealing a strong hybridisation [110]. Though, standard VLS nanowires are not suitable for complex quantum devices, because manual placement of the individual nanowires quickly reaches its limits. This approach does not allow scalability. Therefore, research interest is orientated towards other techniques such as the *Selective Area Growth* - a

bottom-up approach similar to nanowire growth. Instead of catalyst particles, a pre-fabricated SiO_x mask is used to grow planar hybrid Al/InAs nanowires [111].

After the success of the nanowire experiments, a new approach was reported for two-dimensional quantum wells proximitised by epitaxial Al [22]. Both techniques showed a hard induced superconducting gap in the semiconductor [112][24]. For our experiments, we use the latter case. Here, the devices are fabricated in a top-down procedure utilising selective wet etching. These materials offer the ideal playground for us to study the physics of planar Josephson junctions and more.

We work in close collaboration with the group of D. Bougeard in Regensburg in order to establish and improve the growing process of these hybrid materials. This working together was an ongoing side project during this thesis and will not be covered in this work. For this thesis we used material from the group of M. Manfra from Purdue University, West Lafayette, USA. They supplied our group with half a wafer of the epitaxial Al/InAs heterostructure. We carried out all the experiments discussed in this work on this batch. Therefore, we will take a closer look on this material composition.

3.1.2 Heterostructure

The heterostructure is grown layer-by-layer with molecular beam epitaxy (MBE). The result is crystal of high purity and homogeneity, where the atoms are precisely aligned in a known composition. The schematic of our heterostructure is shown in figure 3.1**a**. From bottom to top, the 500 μm thick indium phosphide (InP) is functioning as a substrate. Followed by 100 nm $In_{0.52}Al_{0.48}As$ matched buffer, 900 nm $In_{0.52}Al_{0.48}As$ to $In_{0.84}Al_{0.16}As$ graded buffer (18×50 nm steps), a reversed 33 nm graded buffer from $In_{0.84}Al_{0.16}As$ to $In_{0.81}Al_{0.19}As$ to compensate the overshoot[1] and a 25 nm thick $In_{0.81}Al_{0.19}As$ virtual substrate. The 7 nm InAs quantum well is sandwiched in a 4 nm $In_{0.81}Ga_{0.19}As$ bottom barrier and a 10 nm $In_{0.8}Ga_{0.2}As$ top barrier. The whole semiconducting wafer stack is capped with two monolayer GaAs, as the Al etchant we use is designed to etch Al on GaAs. Finally, the superconducting layer, namely 7 nm of epitaxial Al, covers the top. Figure 3.1**b** shows a top-side-view SEM[2] image of the surface.

---

[1]In our case overshoot means a higher concentration of indium in the graded buffer compared to the virtual substrate in order to adjust the lattice mismatch.

[2]**S**canning **E**lectron **M**icroscope

a

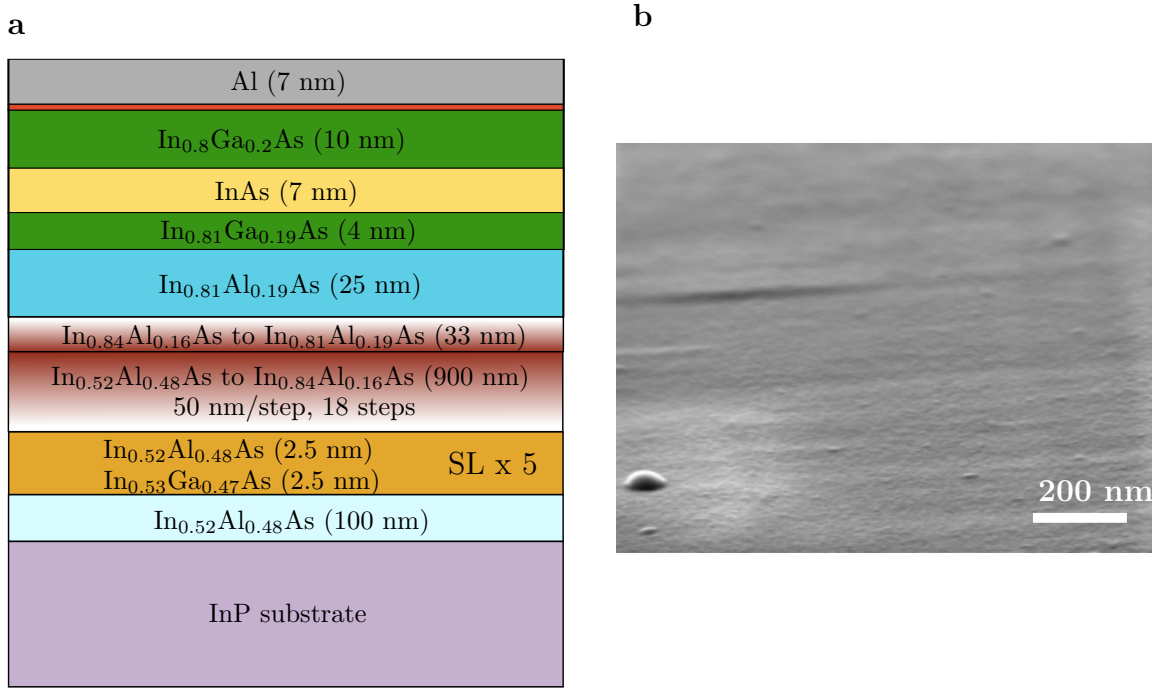| |
|---|
| Al (7 nm) |
| In$_{0.8}$Ga$_{0.2}$As (10 nm) |
| InAs (7 nm) |
| In$_{0.81}$Ga$_{0.19}$As (4 nm) |
| In$_{0.81}$Al$_{0.19}$As (25 nm) |
| In$_{0.84}$Al$_{0.16}$As to In$_{0.81}$Al$_{0.19}$As (33 nm) |
| In$_{0.52}$Al$_{0.48}$As to In$_{0.84}$Al$_{0.16}$As (900 nm) 50 nm/step, 18 steps |
| In$_{0.52}$Al$_{0.48}$As (2.5 nm) In$_{0.53}$Ga$_{0.47}$As (2.5 nm)   SL x 5 |
| In$_{0.52}$Al$_{0.48}$As (100 nm) |
| InP substrate |

b

200 nm

Figure 3.1: **Heterostructure: a,** Shows the layer stack, while **b,** shows a SEM image of the Al surface from a of 60° tilted side-view.

Aluminium

Bulk aluminium as a superconductor has a relatively small T_c ($\approx$ 1.2 K), a small superconducting gap Δ and a low critical field B_{c2} ($\approx$ 10.5 mT). These disadvantages are an incentive for the search for other superconductors. Recent reports showed, that other material compositions such as lead or vanadium on InAs [116][114] or tin on InSb [115] can be grown with an epitaxial match if applied to nanowires. Other candidates such as tantalum or niobium are up to debate, but do not yet have the quality [113]. TEM[3] images in figure 3.2 show the existing qualitative differences between Al, Ta and Nb, Pb and Sn in 2020/2021. However, for the case of 2D systems, aluminium seems to be the only material so far, as far as we know, that epitaxially conforms to the lattice periodicity of InAs.

A still inexplicable and peculiar property of aluminium is the increase of T_c and B_c by growing thinner films or in a disorderly manner [117]. But growing thin films is challenging. It requires a cooled substrate during the evaporation to avoid dewetting. Even with the use of liquid nitrogen cooling, the aluminium starts dewetting at a certain small film thickness, as long as the oxide layer is not formed. After the latter

---
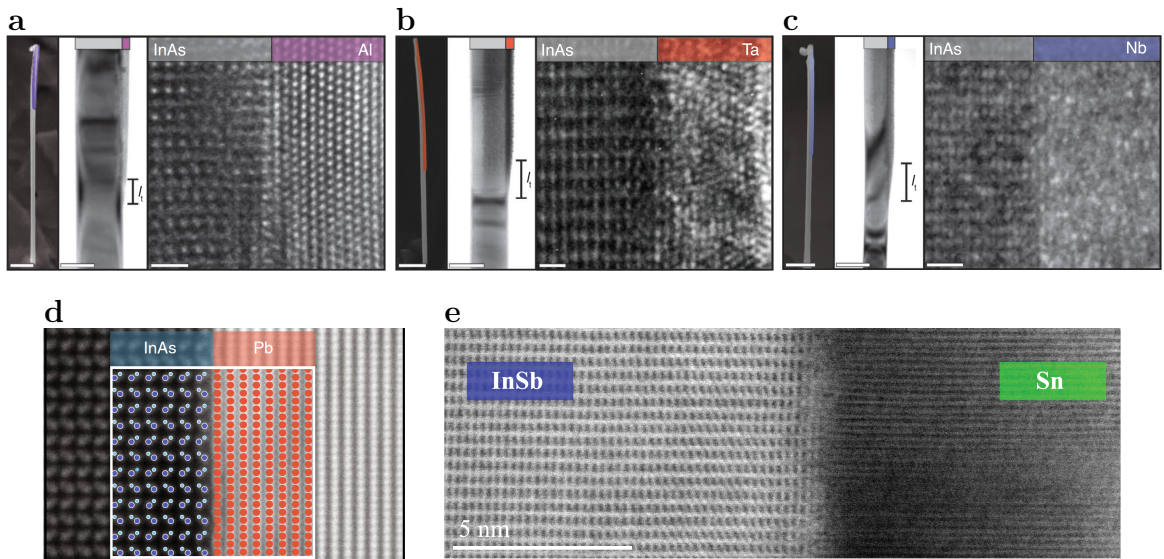
[3]**T**ransmission **E**lectron **M**icroscope

Figure 3.2: **TEM images** showing epitaxial match for **a,** aluminium, **d,** lead on InAs and **e,** tin on InSb in the case of nanowires. Tantalum **b,** or niobium **c,** are possible future candidates just like vanadium or indium, but the proof of their epitaxial capability for superconductor-semiconductor hybrids is still missing. Images taken from [113][114][115].

has happened, the film retains its epitaxial form [84][118].

Shallow 2DEG

The idea behind a near-surface QW is to let the electron wave function extend to the surface, where the Al is deposited (see Fig. 3.3**a**). The desired proximity effect is achieved in combination with a clean interface. For such an interface, the lattice periods of the different layers should match, whereby the atoms are aligned orderly. This is usually checked by using a TEM, as exemplified in figure 3.2**a**.

The price for a good proximity effect is a reduced mobility caused by the increased scattering of the charge carriers at the surface of the 2DEG. Therefore, disorders at the interface to the aluminium have a big impact on the materials properties and play a crucial role in the fabrication process. As reported in [22] and shown in Fig. 3.3**a**, the position of the wavefunction depends on the thickness of the InGaAs barrier and the size of its band gap and thus on the Ga concentration. In addition, a significant difference in mobility is observed for devices which have seen a wet etchant or not (compare Fig. 3.3**b**).

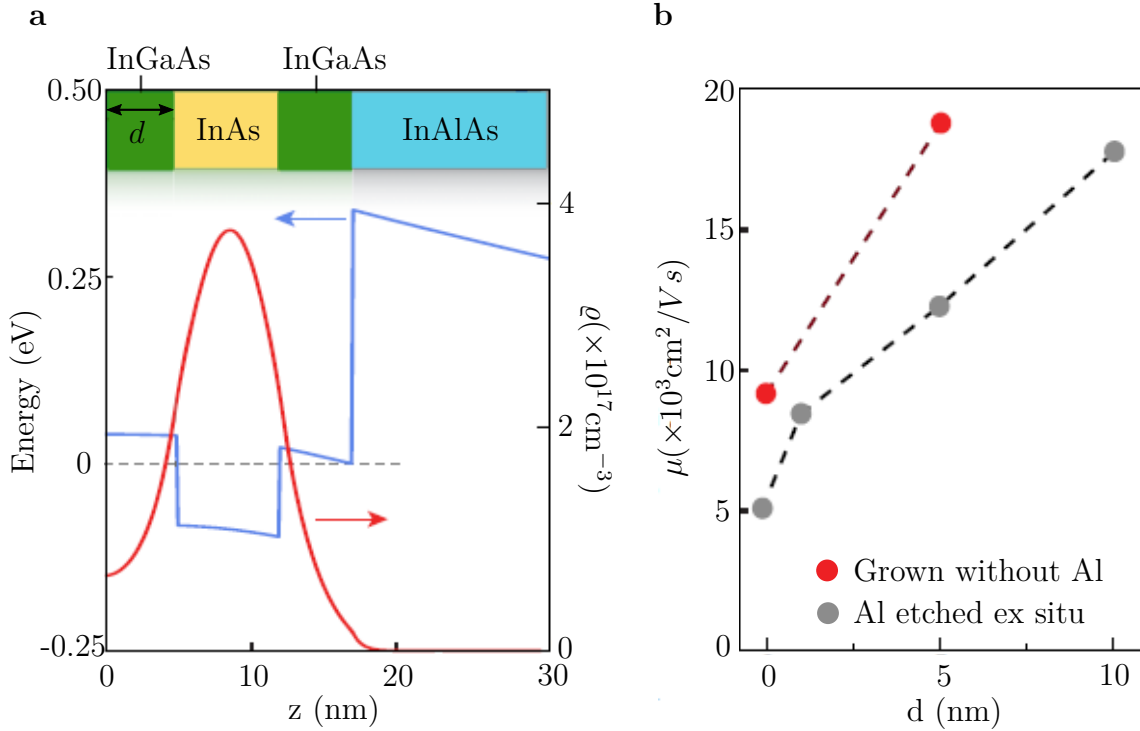This sensitivity to the 2DEG surface topography limits the amount of opportunities

a

b

Figure 3.3: **Near-surface InAs quantum well: a,** Conduction band and electron density distribution calculated by a self-consistent Schrödinger-Poisson solver for d=5 nm. **b,** 2DEG electron mobility μ as a function of InGaAs top barrier thickness. Red dots show the result for wafers grown without Al. Images adapted from [22].

how to strip off the aluminium. So far, Transene's phosporic acid-based wet etchant has become the standard and is used for most purposes. Despite of InAs surface repairing attempts with argon-hydrogen plasma [119], the future seems to be pre-growth fabrication to solve the obstacle of etched induced disorders. Utilising shadow masks [120][121], it is possible to grow devices *in-situ* yielding Josephson junctions with significantly higher quality than the etched junctions [122]. Other attemps were made by thinning the aluminium with anodic oxidation. In combination with lithography, anodic oxidation allows the fabrication of S-N-S junctions [123].

3.2 Fabrication

In order to study individual Josephson junction devices we had to structure, or in other words, fabricate them on the plain wafer. Because we started from scratch, we had to get access to a heterostructure. After this, we set up a fabrication recipe. The pioneering work in this regard was done by M. Kjaergaard and his colleague H. Suominen from the Niels-Bohr Institute in Copenhagen. A very well documented fabrication manual provides the PhD thesis from M. Kjaergaard [58].

However, our facility and experimental environment is different and therefore we had to adapt and elaborate new fabrication steps. The most crucial step is the wet etching of the aluminum and the semiconductor. The result of the etching steps gives already a hint about the quality of the wafer and it can differ immensely from wafer to wafer. But if the quality of the wafer is good and if the recipe is applied rigidly, the success of working devices is very high. In the case of our Josephson junction arrays, we faced the problem of single impurities while etching the mesa. The acquisition of own equipment (beakers, pipettes, chemicals, resist etc.) lead to substantial improvements but was nevertheless not perfect. Thereupon, it was tried to divide the array into small sections in order to connect the better parts and to omit the bad ones. This approach still offers room for improvement for the future.

Cleaving

First, we spin-coat a newly obtained wafer with optical resist to preserve the material and to wash off particles with the resist that originate from the scribing process. To maximise the amount of chips, we always cleave as needed, since the required sample size is experiment dependent. A common size is 4×4 mm.

For cutting the long edge, we scratch a marker with a fine diamond hand cleaver at the outer part of the wafer. To apply some force gently, we use two tweezers to break off a long piece. For the small edge, a high precision scriber is used to scratch the surface once. Using the tweezer method for the smaller edges resulted in damaged chips from time to time.

Cleaning

After cleaving, the chip is placed in two beakers with acetone for 1.5 minutes in each, exposed to sonication for a few seconds during the acetone bath, then put in isopropanol and blown dry with the nitrogen pistol. It is unclear whether the sonication

changes the material negatively or not. Therefore, sonication is avoided once fabrication started. Our master student Linus Frész tested Trichloroethene (TCE) for an additional cleaning step [124]. However, this step was abondonned, because we saw no advantage in it. The philosophy throughout the fabrication is: As few steps as necessary, but carried out very precisely and carefully.

Lithography

We use a 4 % PMMA 950 K (anisol) resist throughout the fabrication and spin-coat it with 4000 rpm[4] forming a pristine $\simeq$ 160 nm thick layer after a bakeout of 10 minutes at 120°C. We expose the sample to a maximum temperature of only 120°C. Higher temperatures increased the surface roughness, what we relate to a decrease of the aluminium quality [124].
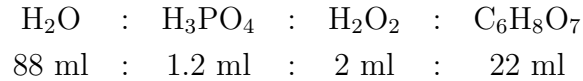
We write the predefined structures into the resist using our Auriga SEM system from Zeiss with the 30 μm aperture and 30 kV acceleration voltage. The sample is then developed in methylisobutylketone (MIBK) and isopropanol. It has proved useful to start by defining the mesa first, where the alignment markers can be easily etched into the chip for further fabrication steps. For certain devices, the proximity effect of the electron beam exposure poses an extremely great difficulty. This effect, not to be confused with the superconducting proximity effect discussed in chapter 2.4.5, results from scattered secondary electrons that still clearly expose the resist at distances greater than 2 μm.

Etching the Mesa

The removement of the aluminium and the 2DEG take place in two steps. What remains are bondpads, Al/InAs leads for the device, alignment markers and the sample name (very important). The mesa has to be etched deep enough to distinguish the markers in the SEM. Otherwise it is impossible to perform the SEM alignment, which is necessary for the exposure of the fine structures (e.g. the part where the Al should be removed for the Josephson junctions) at the right place.
Furthermore, we witnessed a mesa to mesa connection after the deployment of the AlOx dielectric. We have overcome this obstacle by etching deeper (>250 nm). After removing the aluminium layer (discussed below), we use the following solution

---

[4]**r**ounds **p**er **mi**nute

$$H_2O \quad : \quad H_3PO_4 \quad : \quad H_2O_2 \quad : \quad C_6H_8O_7$$
$$88 \text{ ml} \quad : \quad 1.2 \text{ ml} \quad : \quad 2 \text{ ml} \quad : \quad 22 \text{ ml}$$

with a etching rate of ≈ 0.95 nm/s to remove everything of the semiconducting layers homogeneously. The hydrogen peroxide H_2O_2 is responsible for oxidising the semiconducting material and the phoshporic acid H_3PO_4 binds on the oxidised components. Citric acid facilitates the replenish of fresh etch for the reaction process. After 5 minutes, the process is stopped by swirling the sample in distilled water.

Etching the Aluminium

This step is, besides the mesa etch, the most critical step in the fabrication process. The desired result should be a clean and an uncovered aluminium free 2DEG as unharmed as possible. As mentioned above in section 3.1.2, wet chemical etching deteriorates the transport properties, but to our knowledge, the etchant type D from Transene is up to date the best wet chemical to strip off the epitaxial aluminium. After lithography and developement of the resist, we expose the sample to an oxygen plasma to get rid of resist residues in the respective areas. At the beginning we used our RIE[5] system with the following parameters:

$$\text{flow} \quad : \quad \text{pressure} \quad : \quad \text{power} \quad : \quad \text{duration}$$
$$O_2 \text{ 20 sccm} \quad : \quad 100 \text{ mTorr} \quad : \quad 5 \text{ W} \quad : \quad 10 \text{ s}$$

Over time, we benefited from a new plasma asher (used for the multiterminal Josephson junctions), with which lower power could be set and a lot of time could be saved due to the easier handling.

After this step, the sample is ready for etching Josephson junctions or other types of device patterns. But before, the etchant has to be pipetted into a beaker and heated up to about 50°C ± 2°C on a hotplate. The etching time itself is short and takes about 2 to 2.2 s, varying from user to user. This short etch time is a reason why it is difficult to etch a Josephson junction with a higher precision than $\pm$ 20 nm. The process is again stopped for 20 s and 40 s in distilled water. The resist is then washed off in acetone and isopropanol and the result can be examined in the SEM.

---

[5]**R**eactive **I**on **E**tching

Insulator Deposition

The choice for the dielectric separating the topgate from the heterostructure is aluminium oxide (Al_2O_3). It is grown at 80 °C with our Cambridge Nanotech Savannah ALD[6] machine. A preconditioning step by placing the sample in the chamber at 80°C under low pressure for several hours might increase the quality. However, we produced not a significant amount of samples to make a statistic. In addition, it is recommended to start with the TMA (trimethylaluminium) cycle. This should passivate the surface and lower the amount of possible surface states.

Before the insulator is deposited, another EBL step is required to keep the bondpads free from the AlOx. The reason for this step are the low contact resistances we need for our inductance measurements (see chapter 4). Bonding directly to the bare aluminium achieves a contact resistance well below one ohm, while bonding through the dielectric leads to higher contact resistances.

Topgate Deposition

At the end, the Ti/Au topgate is deposited with an e-beam evaporator. The gate area, connected to a bondpad, is again defined by an EBL step. For fine structures, such as the gate finger of a quantum point contact, the deposition must be done in two steps. In this case, (Ti/Au) (5/20 nm) was deposited first for the inner part, followed by (Ti/Au) (5/100 nm) in a second step for the outer part.

Chip Carrier and Bonding

Finally, the fabricated devices are glued into a 20-pin chip carrier with PMMA. For bonding the sample it turned out that only our old aluminium bonding machine[7] can meet our requirements. It bonds on the plain aluminium film with a small contact resistance and a high success rate. The following settings have usually proved successful:

Gold bondpad on chip carrier:	180 (power)/ 100 (time)
Aluminium bondpad on sample:	120-140 (power)/ 100 (time)

The bondpads should be large enough so that each contact can be bonded at least twice. This can save unnecessary, troublesome cooldowns, as the likelihood of a

---

[6]**a**tomic **l**ayer **d**eposition
[7]from Westbond company - model 5400B

contact failing is greatly reduced.

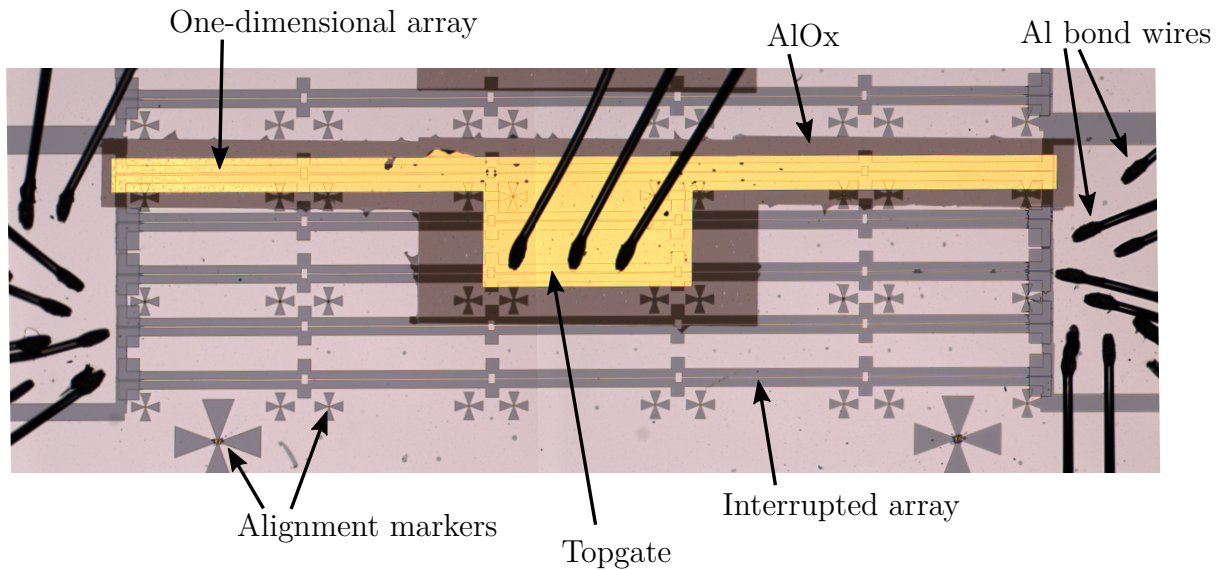Figure 3.4 shows an optical micrograph of sample 1 after bonding.

Figure 3.4: **Optical image from Sample 1.**

3.2.1 Notes on the Fabrication Process

Despite a quite good working recipe has been elaborated, there is always room for improvements. Because we had a small amount of material, we tried to get things working step by step. For tests, we used the outer parts of the wafer, which are not suitable and not worth for a characterisation. Mesa etching tests can be done only once per chip, since the result of a second test is totally different and not reproducable for an unknown reason. Solely aluminium etching tests can be carried out at least five times per chip.

So far, the greatest source of inaccuracy in removing the aluminium film is the time. With 2 to 2.2 s, it is hard to reproduce the etching process. That's why it might be worth a try on the long term to dilute the etchant type D solution with distilled water. This approach was avoided because it is not known what the solution would then do to the exposed 2DEG and how much the mobility might be degraded.

Reducing the temperature of the solution is not an option, since the result are aluminium residues or underetching if the etching time is increased.

Overall, the lithography gives the greatest opportunity for improvements. For our arrays, we need to expose the same fine structure several hundred or thousand times

per chip. Often we faced the problem, that the SEMs (Auriga or Supra) did not expose each fine structure equally. In this regard, we did not find any systematics behind this problem so far, as it occured irregularly and the number of samples in this respect was too small.

Dividing the array into smaller parts can improve the quality immensely, as it was the case for the multiterminal Josephson junction array, discussed in chapter 7. The fabrication of small segments, for instance with only 50 Josephson junctions, results in several defect free parts. After a further mesa etching step, the defect free segments stay connected.

3.3 Devices

Various samples have been fabricated in recent years. Besides normal Josephson junctions (JJ) and Quantum Point Contacts (QPC), the attention was drawn to different Josephson junction arrays (JJA). The most important samples are shown as SEM images in Fig. 3.5. Figure **a** and **b** show a JJ and a QPC, respectively. The first
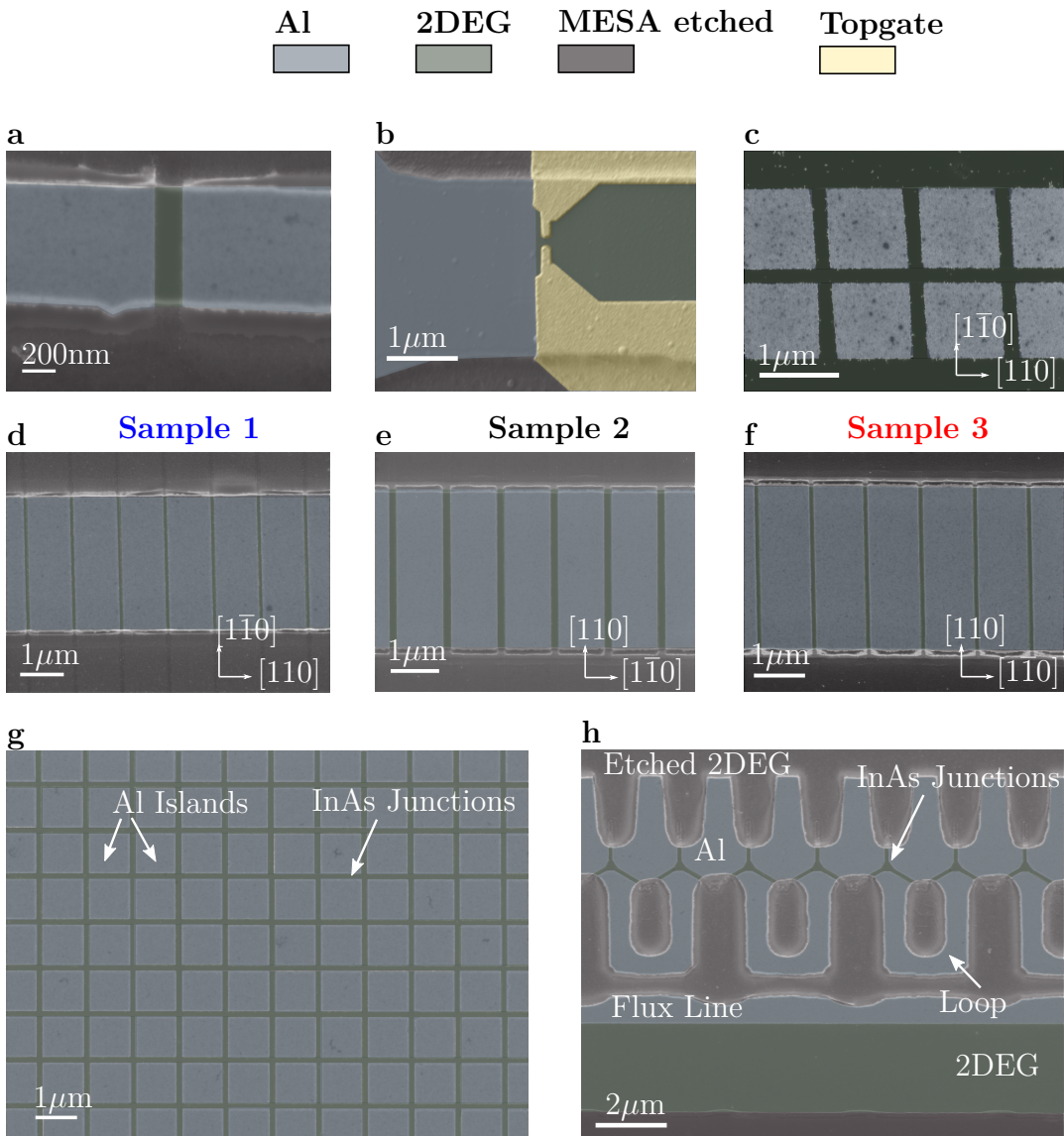

Figure 3.5: **Devices** with different layouts fabricated in the scope of this thesis. **a,** A single Josephson junction. **b,** Quantum point contact. **c,** One-dimensional SQUID array. **d-f,** One-dimensional Josephson junction array. **g,** Two-dimensional Josephson junction array. **h,** Multiterminal Josephson junction array.

inductance measurements were performed on a one-dimensional SQUID[8] array (Fig. **c**) and the results are presented in Ref. [124]. The figures **d-f** show one-dimensional Josephson junction arrays. Most of the results in this work are from the sample 1, with the current direction parallel to the [110] InAs crystallographic axis. The complementary array is sample 3, with the current direction parallel to [1-10]. Sample 2 was characterised prior to sample 3, but the Josephson junctions length of sample 2 ranges from 130 to 170 nm from one end to the other and has thus an average transparency $\overline{\tau}$ of only $\simeq 0.75$. Therefore, it was necessary to measure sample 3 afterwards for a quantitative analysis of the Dresselhaus component (see chapter 6.1).

Figure **g** shows a two-dimensional Josephson junction array with a junction length of $\simeq 100$ nm. This sample will be characterised by the colleague Simon Reinhardt in order to investigate the nature of frustration patterns. In addition to apply DC transport and the resonator technique, it is planned to use a scanning Hall microscope to spatially resolve the quantum patterns of the magnetic flux.

The last picture in **h** shows a multiterminal Josephson junction array. In this sample, each Josephson junction is connected to a third superconducting lead, whose phase difference can be controlled by an attached SQUID. The sample and the first experimental results are presented in chapter 7.

3.4 Characterisation Measurements

In order to execute experiments for the ongoing research, it is of significant advantage to know and determine several parameters of a new wafer. Furthermore, a quantitative feedback is essential for the growers. Hence, we use four different device geometries to perform a precharacterisation of each new wafer. The devices can be placed on a single chip, requiring a single fabrication and measurement session. Details of the fabrication are discussed above in section 3.2.

Each of this standard characterisation devices we use is described in the rest of this chapter. A hallbar with aluminium on top gives information about parameters such as the critical field or critical temperature. Standard hallbar measurement techniques applied on the 2DEG with stripped off aluminum reveals the mobility and the mean free

---

[8]**S**uperconducting **QU**antum **I**nterference **D**evice

path. A single superconductor-normal-superconductor (S-N-S) Josephson junction is a prerequisite for the functionality for more complex devices. Tunnel spectroscopy on a superconductor-quantum point contact-normal (S-QPC-N) device measures the induced gap Δ^* and thus provides information about the proximity effect.

3.4.1 Aluminium Hallbar

The hallbar for this wafer was a meander with 3074 squares and was characterised by the colleague Lorenz Fuchs. As he was investigating the physics of plain films, he was mounting the sample (top view shown in Fig. 3.6) into a dilution refrigerator, where he determined the following parameters listed in table 3.1.

Material parameter:	Value:	Formula:
Thickness (Al)	7 nm	
Fermi velocity	$2.0 \cdot 10^6$ m/s	[61]
Sheet resistance	9.22 Ω	$R_\square$
Mean free path	5 nm	$l_{\text{el}} = 4 \times 10^{-16} \Omega\text{m}^2 / R_\square d$ [125]
Critical Temperature	1.502 K	T_c defined at $R = 0.5R_\text{n}$
Energy gap	228 μeV	$\Delta(0) = 1.764 k_\text{B} T_\text{c}$
Sheet kinetic inductance	9.2 pH	$L_\square = \mu_0 \frac{\lambda_\text{s}^2}{d}$
London penetration depth	220 nm	$\lambda_\text{s} = \sqrt{\frac{L_\square d}{\mu_0}}$
Pearl penetration depth	19.8 μm	$\Lambda = 2\frac{\lambda_\text{s}^2}{d}$
GL coherence length	74 nm	$\xi_\text{GL} = \sqrt{\frac{\Phi_0}{2\pi B_\text{c2}}}$
Critical field out-of-plane	61 mT	$B_{\text{c},2}$ measured at low T
Critical field in-plane	2.8 T	$B_{\text{c},\|\|}$ measured at low T
Clogston-Chandrasekar limit	2.78 T	$B_\text{c} = \frac{\Delta}{\sqrt{2}\mu_\text{B}}$
Diffusion constant	$3.3 \cdot 10^{-3}$ m²/s	$D = \frac{1}{2} v_\text{F}^\text{s} l_{\text{el}}$

Table 3.1

Table with parameter obtained from the meander characterisation by Lorenz Fuchs [126].

Besides the sheet resistance $R_\square$, the critical temperature T_c and the Ginzburg-Landau coherence length ξ_Gl, the in-plane critical field $B_{\text{c},\|\|}$ is of particular interest. High values for the critical field $B_{\text{c},\|\|}$ are desired, so the superconducting condensate can sustain
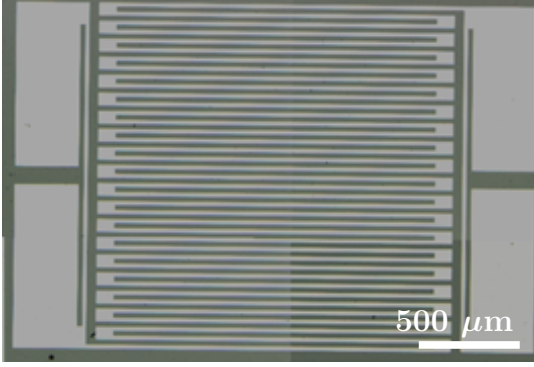
Figure 3.6
Optical image of a hallbar meander with 3074 squares. The light grey areas indicate the aluminium. The aluminium and the 2DEG are etched away in the dark grey areas.

high Zeeman fields. The robustness against fields in the plane increases with decreasing thickness of the aluminium film [117]. We can use the Clogston-Chandrasekhar limit $B_c = \frac{\Delta}{\sqrt{2}\mu_B}$ to calculate the critical magnetic field. The result of $B_{c,||}^{calc}$=2.78 T agrees with the measured $B_{c,||}^{meas} \simeq$2.7 T at low temperatures.

3.4.2 2DEG Hallbar

We performed hall measurements with standard lock-in techniques on the plain 2DEG, whereby the Al was etched away. Although it turned out that the obtained values for λ_F here are different from the case of etched Josephson junctions (see chapter 4.1.2), we get nonetheless important information of the gate electric behaviour of the near-surface quantum well. Quantum hall measurements on the hallbar (Fig.
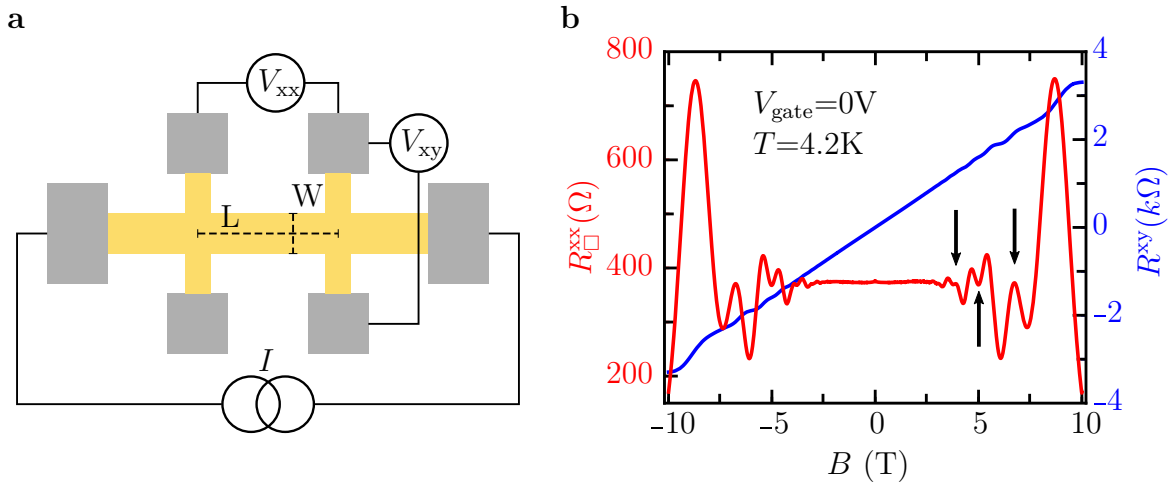
Figure 3.7: **Hallbar measurements: a,** Scheme of a hallbar. **b,** Longitudinal and transversal magnetoresistance. The Shubnikov-de-Haas oscillations show a second harmonic due to the occupation of the second sub-band at $V_{gate} = 0$ V (indicated by the black arrows).
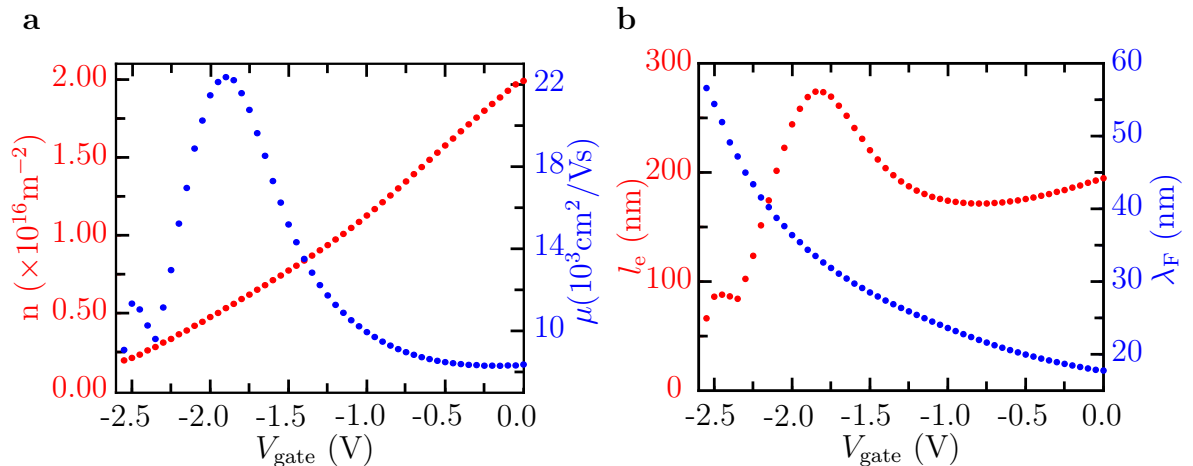
a

b

Figure 3.8: **2DEG characteristics: a,** Charge carrier density n and mobility μ. **b,** Mean free path l_e and Fermi wavelength λ_F.

3.7) showed higher harmonics in the Shubnikov-de-Haas oscillations, since a second oscillation pattern is recognisable in the red $R_\square^\mathrm{xx}$ curve in Fig. **b**. Consistent with other reports [127][128], we explain the higher harmonics with the occupation of the second sub-band, as it is vanishing for lower gate voltages. As elaborated in chapter 2.1.1, we can determine the carrier density n, mobility μ, mean free path l_e and the fermi wavelength λ_F as a function of gate voltage. Plotted in figure 3.8, the mobility reaches a maximum at 22000 cm^2/Vs for the charge carrier density $n = 0.5 \times 10^{16} \mathrm{m}^{-2}$ and so does the mean free path l_e at ≈ 270 nm, consequently. We relate the decrease of μ and l_e for increasing gate voltages to the above discussed occupation of the second sub-band, which enhances the probability of scattering of charge carriers at the coexisting sub-band.

3.4.3 S-N-S Josephson Junction

A fast and informative tool is the DC transport characterisation of a single Josephson junction. At the very beginning, we briefly measured a Josephson junction in a He3 setup with a base temperature of 330 mK. Soon it became clear that we were getting similar results to the pioneering experiments of M. Kjaergaard et al. [22][129] and we moved on to quantum point contact measurements. The graphs in figure 3.9 show current-voltage characteristics for different gate voltages and temperatures. The critical current is relatively small due to the junction's length of 180 nm. A distance of $\approx$100 nm between the superconducting leads proved to be more subtle resulting in ballistic junctions.
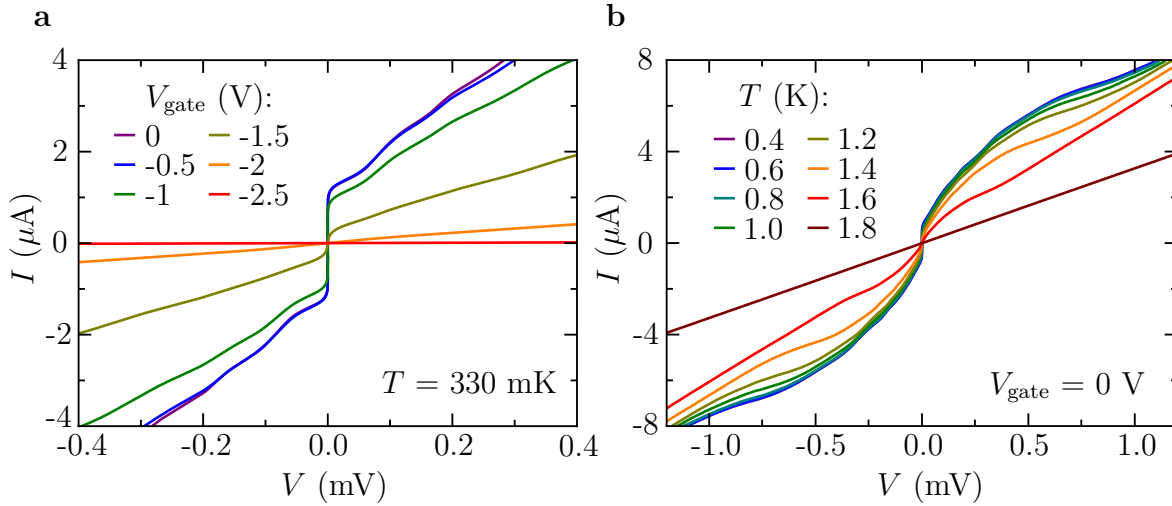
Figure 3.9: **IV curves: a,** Current bias measurements for different gate voltages and for **b,** different temperatures.

3.4.4 Quantum Point Contact

In 1988, Van Wees et al. [41] and Wharam et al. [130] reported about plateaus in the conductance of quantum point contacts (QPC) in ballistic GaAs/AlGaAs heterostructures. These plateaus depend on multiples of natural constants and are quantised in the form of

$$G = \frac{2e^2}{h} N, \tag{3.1}$$

where the factor two reflects the spin degeneracy and N the number of transmissive channels. The channel number N is controlled by the width of the constriction, which can be set by an applied voltage of the metallic split-gates. These split-gates deplete the semiconductor underneath and reduce the effective width $w(V_g)$ of the constriction with decreasing voltage. In order to observe a single mode, $w(V_g)$ has to be $\geq \lambda_F$ showing $\frac{2e^2}{h}$ conductance steps. However, if the QPC is placed next to a semiconductor-superconductor interface, Beenakker predicted in 1992 a doubling of the quantisation steps [131]. In 2016, this prediction was experimentally confirmed by Kjaergaard et al. [24] with the obervation of $\frac{4e^2}{h}$ conductance steps.

Furthermore, QPCs are used to measure the local density of states in the proximitised InAs and thus the induced gap Δ^*. Our main reason to perform a tunnel spectroscopy experiment was to measure Δ^*. In addition, it was intended to study the transport in the presence of an in-plane field.

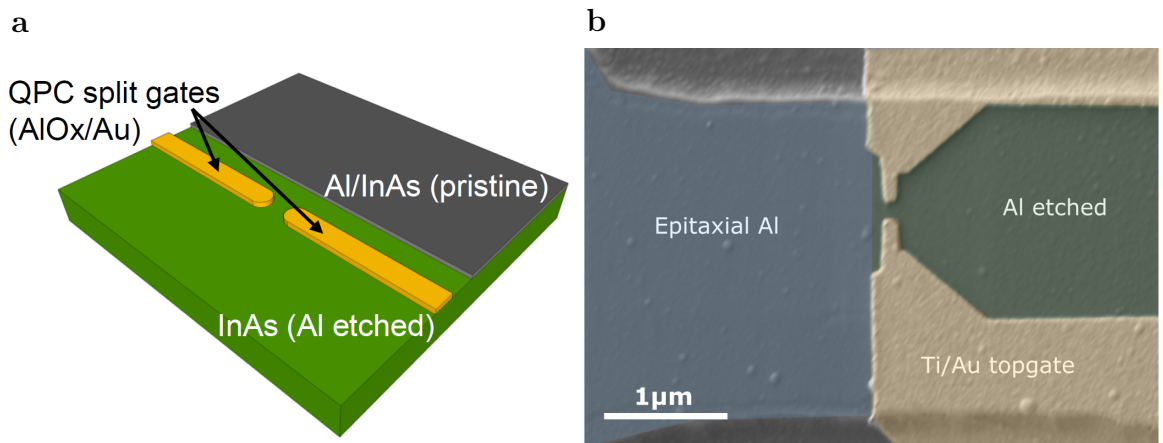The design of our sample is shown in Fig. 3.10 and was inspired by the experiment

Figure 3.10: **Quantum point contact: a,** Illustration of the QPC (made by Nicola Paradiso). **b,** False color SEM image of the QPC seen from above.

of Ref. [24]. The metallic split-gates with a thickness of 5 nm Ti and 20 nm Au were evaporated on top of a 40 nm thick AlOx dielectric. The gates are separated by $l_\mathrm{g} \simeq 200$ nm, have a width $w_\mathrm{g} \simeq 80$ nm and count $\simeq 100$ nm (d_g) in distance to the epitaxial aluminium. In total, two samples were fabricated. First, sample QPC1 was characterized in the a He3 setup at 330 mK, whereas sample QPC2 was mounted into a dilution refrigerator with $T_\mathrm{base} \approx 40$ mK.

Open-Channel Regime

The behaviour of the QPC in the open-channel regime is depicted in Fig. 3.11. The figure shows a blue curve with superconductivity present and two curves where superconductivity is absent due to temperature (grey) or to a perpendicular magnetic field (red). The blue curve shows conductances which are increased by a factor of roughly two compared to the red and grey curve. This increase is caused by the above mentioned Andreev process, where an impinging electron forms a Cooper pair with charge 2e with an electron from the Fermi sea. In order to align the first plateau to an integer of G at $\approx V_\mathrm{gate}$=-8V, a resistance of 3.5 kΩ is substracted, which stems from the semiconducting part in series to the QPC and is due to the topgate layout slightly gate dependent (see SEM image 3.10).

As we deal here with a near surface quantum well with a mean free path of $\approx$200 nm, we observe very unclear defined plateaus with many coexisting resonances in the conductance. Impurities, a not perfect electric potential landscape from the gates and trapped charges in the dielectric lead to a deterioration of the shape and reproducibility of the plateaus.
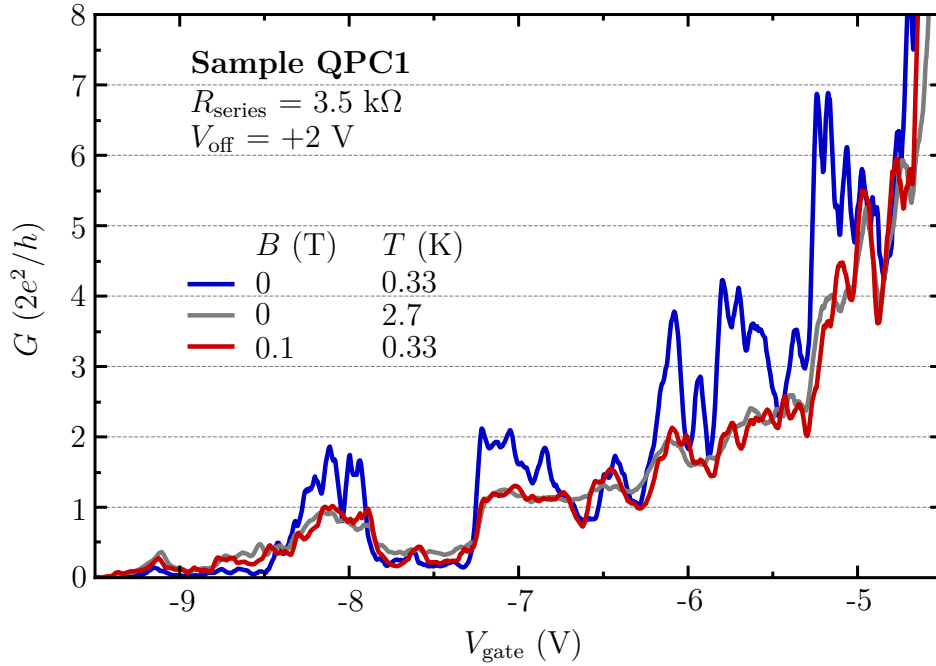
Figure 3.11: **Quantised conductance:** Enhancement of the conductance by factor of two due to the Andreev process at the S-N interface (blue curve). If superconductivity is suppressed (grey and red curves), the conductance plateaus take values of a multiple of $2e^2/h$.

A way to improve the conditions is to sweep the split-gates asymmetric with a certain offset to each other. In this way, it was tried to bypass impurities or other sources for scattering events. The result of this calibration step of the offset is shown in figure 3.12**a**. In this figure, the offset voltage V_{offset} between the left and right gate show an asymmetry between positive and negative values, in this case exemplified for sample QPC2. Figure 3.12**b** illustrates the given situation schematically. The top figure shows the S-N interface with the split-gates in the presence of impurities. If both gates are swept with V_{diag} equally with the potential difference V_{offset} to each other, the current can be directed along an impurity-free path.

A quite robust and peculiar feature is a dip between the first and second plateau. It was observed in previous experiments on 2D materials [24] and on nanowires [132][133]. It is presumably caused by mode mixing in presence of residual disorder.
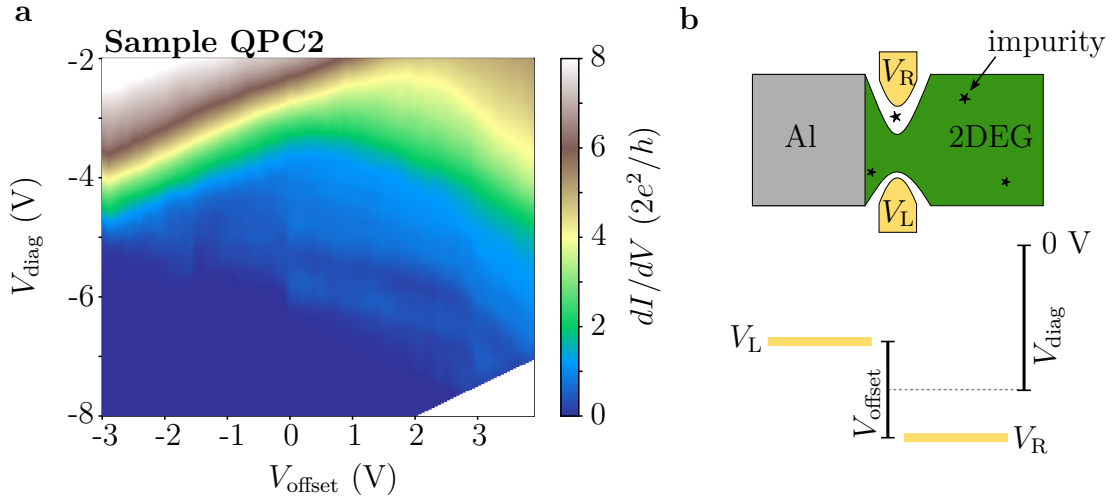
57

a

b

Figure 3.12: **Offset voltage: a,** Gates are sweept with a certain offset to each other in order to reduce the influence of scattering centers. **b,** Illustation and definition of V_{diag} and V_{off}.

Tunnel Regime

If the voltage of the split-gate is further reduced, the QPC will be pinched off and enter the tunnel regime. In this regime, the Andreev reflection is turned off by artificially increasing the Z parameter of the interface via the gates and normal reflection as well as transmission are the most likely events to take place. The Z parameter is

a

b
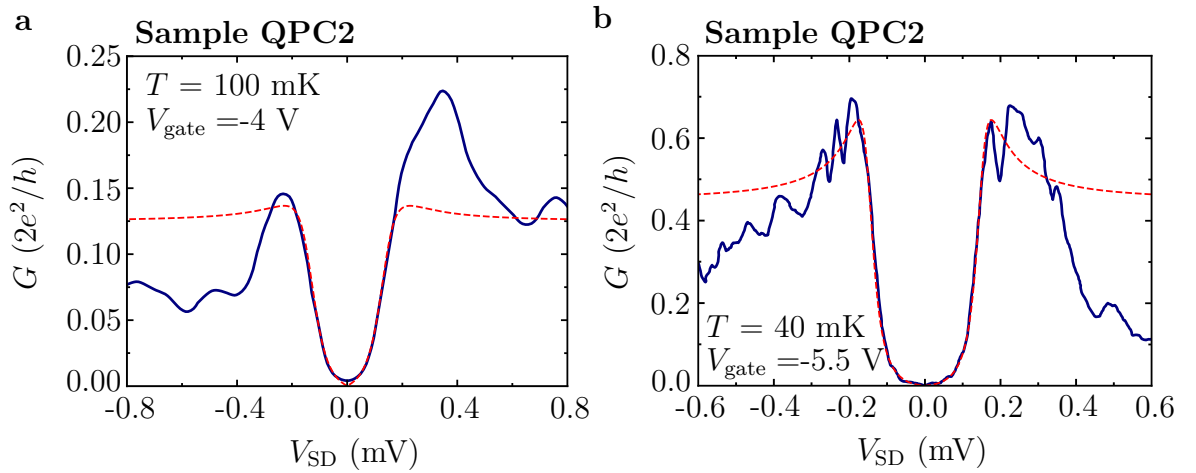
Figure 3.13: **Tunnel spectroscopy: a,** and **b,** show two distinct conductance curves in the tunnel regime and are fitted with the Dynes formula revealing a induced gap of 137 μeV and 150 μeV, respectively.

introduced by the BTK formalism and described in section 2.4.2. A charge carrier can

tunnel through the barrier and move on, only if there are states in the proximitised InAs, which is not the case for $eV_{SD} < \Delta^*$. Therefore, it is a tool that is used to detect states inside the superconducting gap. Such a state can be a Majorana zero mode which manifests itself with an emerging zero bias peak [15][26].

Figure 3.13**a** and **b** show the results of our tunnel spectroscopy measurements. The two curves, obtained at 40 and 100 mK, show the conductance with respect to the source-drain voltage V_{SD}. The red dashed lines are fits with the Dynes formula according to the following equation [134]:

$$N_S(E, \Gamma, \Delta^*) = \frac{(E - i\Gamma)}{[(E - i\Gamma)^2 - \Delta^{*2}]^{1/2}} \tag{3.2}$$

The resulting fit parameters are $\Delta^* = 137$ μeV and $\Gamma = 60$ μeV in Fig. 3.13**a** and $\Delta^* = 150$ μeV and $\Gamma = 28$ μeV in Fig. 3.13**b**. The evolution of the gap with decreasing gate voltage is presented in figure 3.14. Besides the induced gap a interference pattern is recognisable for $eV_{SD} > \Delta^*$. This pattern probably originates from Fabry-Pérot interferences, caused by scattering on the S-N interface and the depleted 2DEG area of the split-gates. However, the size of Δ^* appears to be unaffected. Although it
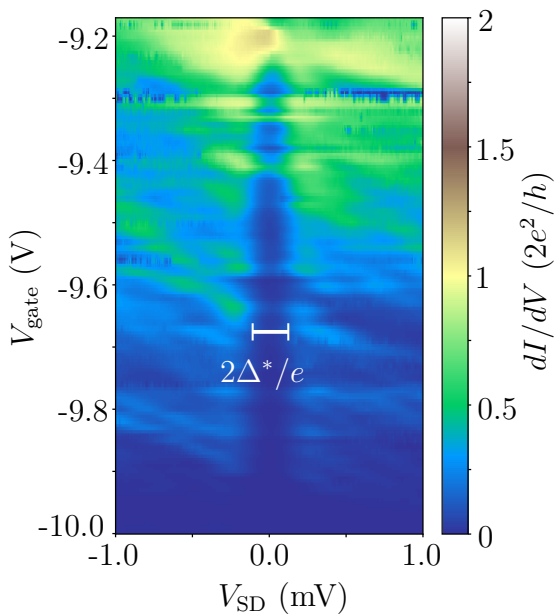

Figure 3.14
Induced gap: Differential conductance curves as a function of voltage bias for different gate voltages and at T=330 mK. A gap emerges for gate voltages below -9.25 V. The offset voltage V_{off} between left and right gate is +2 V. Data obtained from sample QPC1.

quickly became clear that a QPC system of this kind with such a shallow 2DEG is far too unreliable to achieve reproducible results, we continued to carry out tunnel spectroscopy measurements in the presence of an in-plane magnetic field orientated perpendicular to the current direction. The result, plotted in Fig. 3.15, shows an

induced superconducting gap which becomes smaller with increasing fields. However, at 0.7 T, the conductance at zero bias starts to decrease again. Because it was not possible to reproduce $G(V_{SD})$ curves, we stopped the experiment and moved on to the investigation of Josephson junction based samples.
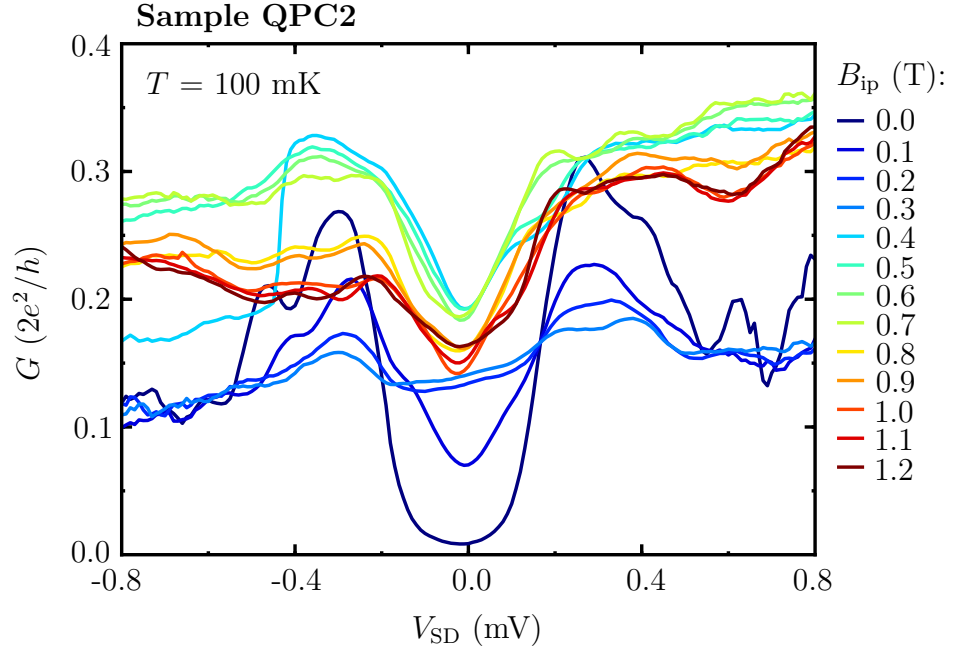

Figure 3.15: **Induced gap at finite B_{ip}:** Conductance versus voltage bias measurements at different in-plane magnetic fields at V_{gate}=-5.5 V and V_{off}=-2 V.

3.5 Measurement Techniques

This work is based on the dissipative and non-dissipative characterisation of Josephson junction devices. For this purpose, we use a RLC circuit in a special arrangement of the electronic components. This arrangement allows us to measure the DC behaviour of the sample in the resistive state and the Josephson inductance when no resistance is present. In this way, we can investigate the behaviour of a Josephson junction for any direct current, magnetic field, temperature and gate voltage in a single measurement session.

3.5.1 Cryostat

The measurements for this thesis were carried out in a dilution refrigerator with a base temperature of $\approx$30 mK. The cryostat is surrounded by a copper shield to screen external electrical fields. Throughout the measurements, a μ-metal shield was placed around the dewar to screen the influence of external magnetic fields. A superconducting magnet can produce magnetic fields from -8 T $\leq B \leq$ 8 T. Inside the magnet, two home-made NbTi coils are situated in opposite to each other. With the help of these coils, the mismatch between the sample and the 8 tesla magnet can be compensated. Moreover, the compensation coils can be used to apply fields orientated out-of-plane to the two-dimensional sample. The sample holder on the cold finger can be rotated *in-situ* via a piezo-rotator. This means that the device can be exposed to large magnetic fields for various angles in the 2D plane.

The importance of noise reduction cannot be overemphasised. Noise which reaches the sample can mess up the entire measurement. Part of the prevention are π-filters[9] at room temperature and cold copper-powder filters in the case of the DC lines. Another part is a decent grounding topology, choice of the measuring devices and the proper use of amplifiers. Many other things can have a significant impact on the quality of the signal. However, these things often depend on the individual setup.

3.5.2 DC Techniques

The dc current bias ranges of Josephson junction devices are in the order of a few μA. The voltage can be measured in parallel with the aid of two voltage lines. The circuit
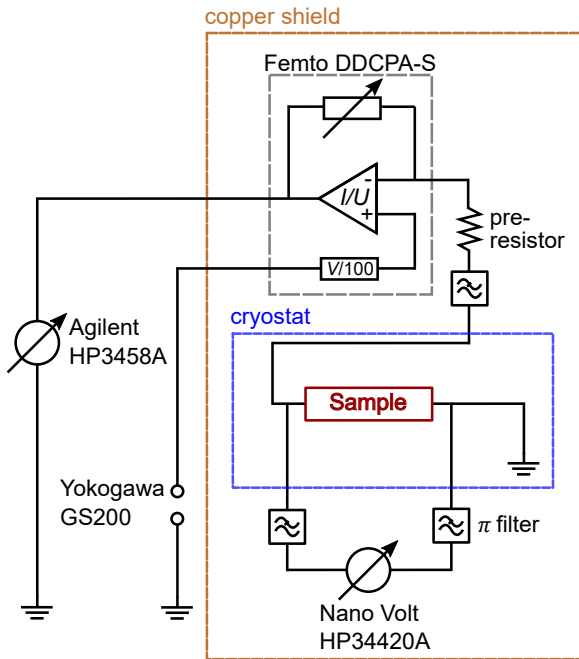
---

[9]π-filter Tusonix 4201-053LF

Figure 3.16
DC configuration: Two voltage probes make it possible to perform a four-terminal characterisation of the sample at finite resistances. In this case, the current is applied single ended, where one end is the cold ground of the resonator. The sample is mounted in the resonator, whose circuit diagramm is shown in Fig. 3.17.

digaramm is displayed in figure 3.16. In order to apply and measure a direct current bias single ended, we use the current preamplifier Femto DDCPA-S the other way round. With a Yokogawa GS200 voltage source we bias the offset of the DDCPA-S on the input with respect to ground. This offset voltage as a source defines together with a 10 or 100 kΩ preresistor the current bias on the sample and is drained by the cold ground of the resonator. The built-in voltage divider of the Femto reduces the input signal and noise coming from the Yokogawa voltage source. On the output of the Femto, we measure the corresponding offset voltage, amplified with a factor of 10^5, with the Agilent HP3458A multimeter.

3.5.3 Obtaining the Josephson Inductance

For the detection of the inductance we use the resonance frequency of a cold RLC circuit. Such attempts to study superconducting materials were reported by Meservey et al. in the late 60s [135], but this tool was to our knowledge rarely used in the past decades. With increasing importance of external magnetic fields and the search for different methods to study Josephson junctions and the nature of Andreev bound states, it became interesting for us to use this method to extract the inductance. Compared to other inductance measurement techniques, e.g. microwave experiments with superconducting stripline resonators in the GHz regime, the advantages are: Reliable results at high magnetic fields and the possibility to perform direct current

measurements simultaneously. The disadvantage is the requirement of sufficient high inductances. We solve this issue by using meander structures for plain films or in the case of Josephson junction arrays, with the fabrication of several hundred or thousand weak links in series. A low-transparent Josephson junction with 1 μA critical current has a inductance of $L(\varphi) = \Phi_0/2\pi I_c \cos(\varphi) \simeq 0.3$ nH.

In section 3.5.3, we will see that the center frequency of the resonance can be determined with an accuracy of $\simeq 0.1$ nH in the best condition. In order to detect small changes of the Josephson inductance by external parameters, e.g. direct current, we need to increase the total inductance of the device under investigation.
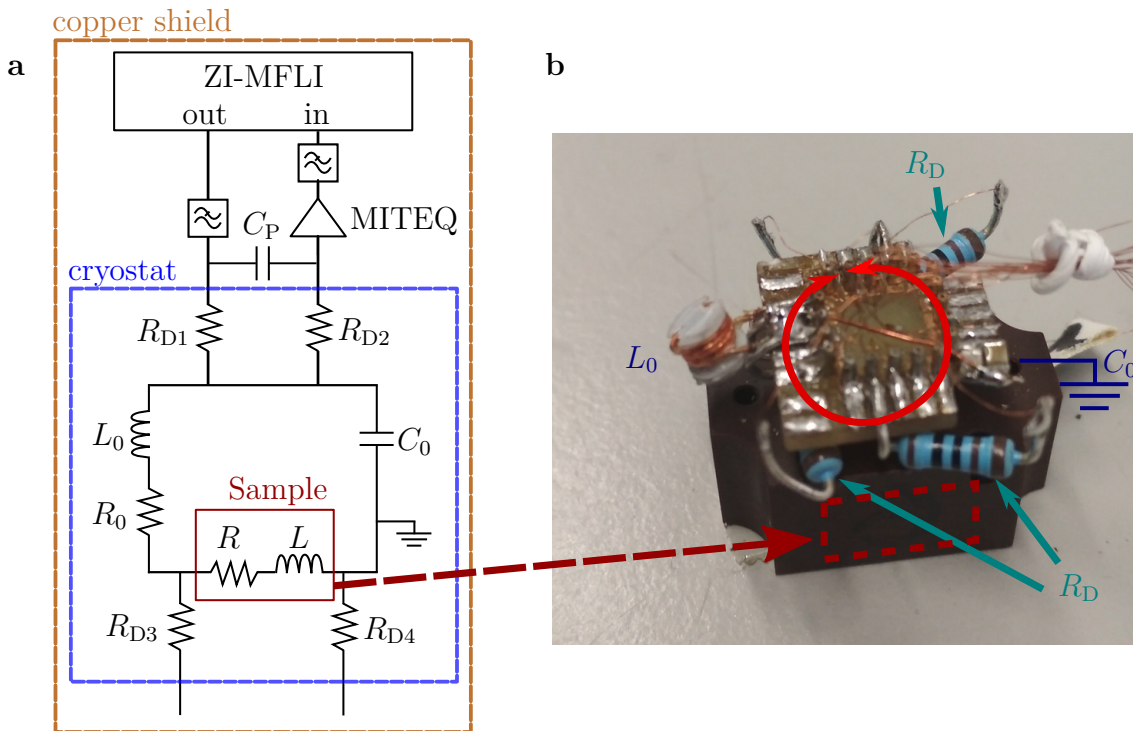
Figure 3.17: **The resonator: a,** Circuit diagramm of our cold RLC resonator. The sample is embedded in parallel to the capacitor C_0 and in series to the inductor L_0. The resistors R_{D1-4} decouple the resonator from the cryostat cables. The resonator is driven by a Zurich Instrument 5 MHz lock-in and reads out the returned signal, which is preamplified by 56 dB via the MITEQ amplifier. **b,** Photograph of the RLC setup. The sample is mounted with the chip carrier inside the brown element (indicated by the red dashed rectangular). The whole component is screwd on to the piezo-rotator, which is installed on the cold finger.

The Resonator

In general, a RLC circuit is an electrical device composed of a resistor, a capacitor and an inductor. These elements can be arranged in a parallel or in a serial configuration. Our series RLC circuit with the components $L_0 = 382$ nH, $C_0 = 4$ nF and $R_{Dj} = 1$ kΩ for j = 1,2,3,4 is shown in figure 3.17. The sample under investigation is mounted in series to the inductor L_0 and in parallel to the capacitor C_0. In addition, the capacitor C_0 disconnects the direct connection between the input lines and the cold ground, so that the direct current must flow through the sample.

The resistors R_{Dj} decouple the resonator from the external environment, i.e. mostly from the measuring cables. These cables have a capacitance in the order of a few hundreds of nF and would therefore hinder reasonable resonances in the MHz regime, if they wouldn't be disconnected from the resonator. R_{D3} and R_{D4} decouple the voltage probe lines, R_{D1} and R_{D2} do the same to the coaxial input and output cable of the lock-in. Thereby, the influence of the cryostat cables and of the π-filters on the center frequency becomes negligible. Figure 3.18**a** shows an example of resonance
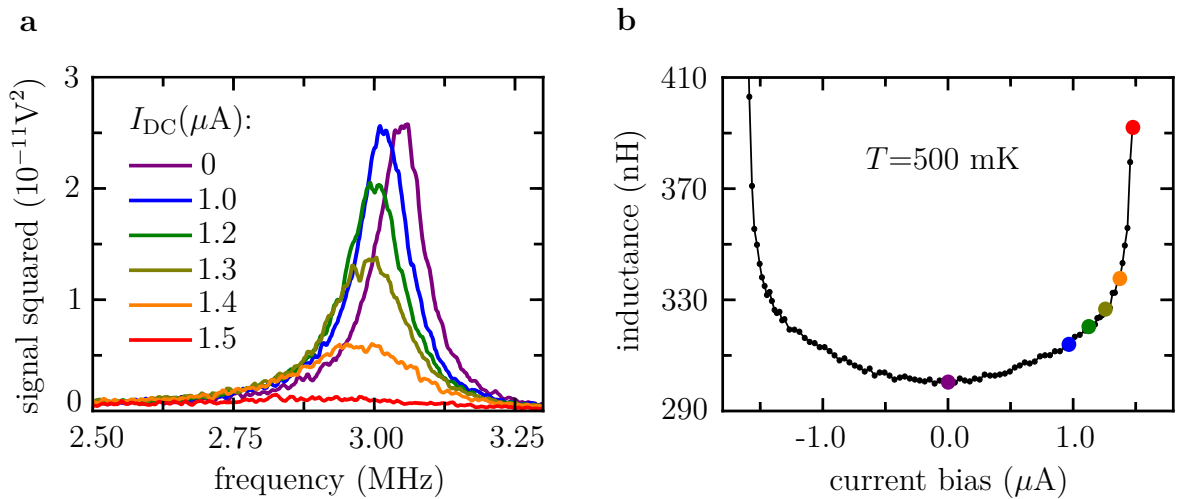
a

b

Figure 3.18: **Resonance curves: a,** Example of resonance spectra for different DC bias at $T = 500$ mK. The data was measured on Sample 1. **b,** Calculated inductance by the center frequency with respect to direct current bias. The colored dots correspond to the spectra in panel **a**.

spectra for different current bias of sample 1, an one-dimensional Josephson junction array. The resonator is driven and read out with a 5 MHz MFLI lock-in from Zurich Instruments. At the resonance, the resonator becomes resistive and a voltage builds up

at the readout line, which is amplified by 56 dB with a preamplifier[10]. The resonator is designed in such a way, that the resonances appear around 3 MHz and are thus in the range of our 5 MHz MFLI lock-in. The center frequency f_0 of the measured spectra are given by the following relation:

$$f_0 \equiv \frac{1}{2\pi\sqrt{L_\mathrm{T}C_0}} \tag{3.3}$$

The total inductance L_T is the sum of the external coil L_0 and the Josephson inductance L.

The quality factor Q is a measure how strong the damping and thus the energy loss of the resonator is. The lower the q-factor, the higher the loss. For a *series* RLC circuit the Q-factor is defined as

$$Q = \frac{f_0}{\Delta f} = \frac{1}{R_\mathrm{s}}\sqrt{\frac{L_\mathrm{T}}{C_0}} = 2\pi\frac{Lf_0}{R_\mathrm{s}}, \tag{3.4}$$

with R_s being the total normal resistance in the resonator.

We further define the sensitivity S according to

$$S \equiv \frac{\delta f}{\Delta f} = \frac{\partial f}{\partial L}\delta L\frac{1}{\Delta f} = \frac{\pi f_0}{R_\mathrm{s}}\delta L. \tag{3.5}$$

The sensitivity S is a tiny frequency shift δf caused by a change of the inductance δL. It depends for a given f_0 only on R_s. We see, that simply increasing the total inductance L_T does not increase the sensitivity. However, the series resistance R_s decreases S, which is why we try to minimise R_s in our setups. What can still significantly improve the sensitivity is the center frequency f_0. This means that at higher frequencies one can examine samples with a smaller Josephson inductance L_J.

Eqn. 3.4 is valid for a serial RLC circuit which in our case is true as long as the decoupling resistors R_D1 and R_D2 are much bigger than the maximum tank impedance. The maximum impedance at the resonance is given by

$$Z_\mathrm{m} = R_\mathrm{s}Q^2\frac{L}{R_\mathrm{S}C_0} = \frac{4\pi^2 f^2 L^2}{R_\mathrm{s}}. \tag{3.6}$$

The reason why we have chosen 1 kΩ decoupling resistors becomes clear if we calculate

---

[10]We use the MITEQ AU-1447 amplifier with a frequency range of 0.01-400 MHz.

Z_m. We obtain a maximum Z_m of about 400 Ω at the peak resonance, if we assume $L_\mathrm{T} = 600$ nH, $R_\mathrm{s} = 0.3$ Ω and $f_0 = 3$ MHz. Bigger decoupling resistors lower the input signal without improving the quality factor Q. Smaller decoupling resistors lead henceforth to a parallel configuration of the circuit and the Q-factor goes down. Consequently, a center frequency f_0 cannot be extracted anymore.

Inductance L_0

The external inductance L_0 is mostly determined by our home-made copper coil. As mentioned above, L_0 does not affect the sensitivity. However, the inductor is necessary to set the range of the center frequency f_0. We performed a calibration measurement at 4 K in our dilution refrigerator with a standard chip-carrier, whose source and drain contacts were shorted with aluminium bond wires. From the center frequency, we determined L_0 to be 382 nH. This L_0 is througout substracted from the total inductance L_T and the result is the Josephson inductance L_J.
Other sources to the total inductance are the kinetic inductance of the aluminium film or the geometric inductance. However, their value in summary are in the order of a few nH and thus within the scattering range. Therefore, the contribution to the inductance from other sources can be neglected.

Resistance and Quality-Factor

A finite resistance R_s of a few ohms suppresses the Q-factor and hence the resonance breaks down. In order to maintain the underdamped case ($Q > 1$), we have to eliminate or decrease possible sources for dissipation. The main contribution comes from the copper coil, that has to be without ferromagnetic oder superconducting materials, because those would perturb the measurements with magnetic fields. Further sources of resistance are the solder joints of the resonator, the sample itself, the bond wires and the contacts. We reduce the contact resistance to a minimum by bonding each bondpad $\simeq 5$ times. In the superconducting regime the dissipation of the sample is zero. Once the current of the weakest junction approaches its critical current, the inductance increases abruptly and the Q-factor drops down to zero. Figure 3.19**a** illustrates this on the spectra example from above. We determine R_s by using equation 3.4 according to $R_\mathrm{s} = Q^{-1}\sqrt{(L + L_0)/C_0}$. The corresponding resistances are presented in 3.19**b**.

a

b

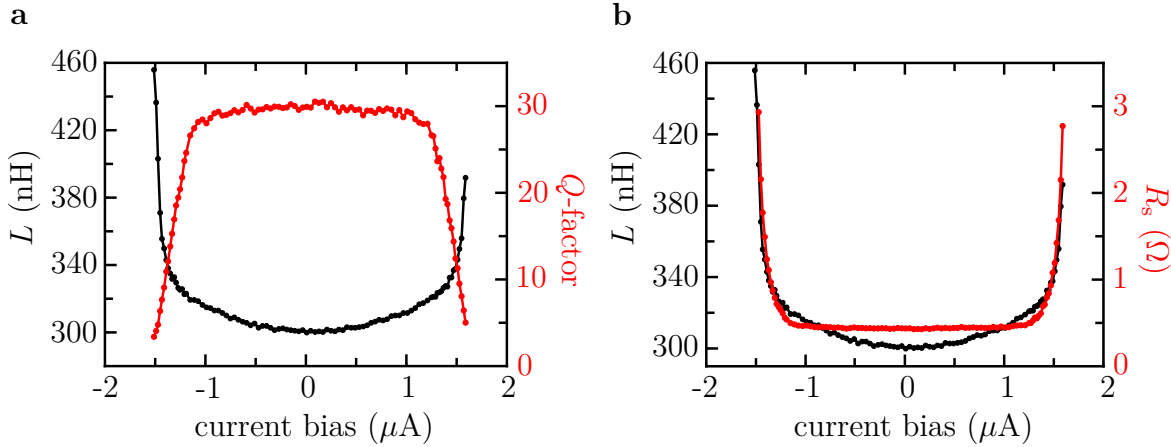
Figure 3.19: **Q-factor and serial resistance: a,** $L(I)$ curve together with the corresponding Q-factor values. **b,** From the Q-factor calculated series resistance R_s in our RLC circuit plus sample 1 at T=500 mK.

The Resonance Spectrum

In order to fit the spectra reliable, quick and automatically, we use a model based on the Breit-Wigner-Fano function to extract the parameter L from the center frequency f_0. Due to a stray capacitance C_P between the coaxial measurement leads (see circuit diagramm 3.17), we observe a low-pass behaviour as a continuous background signal in our spectra, which lead to an asymmetric line shape of the resonances. By using the Breit-Wigner-Fano function, we can neglect this background or other small continuous resonances, which interfere with the discrete resonance of the RLC. The Breit-Wigner-Fano function is defined as

$$f(x; A, \mu, \sigma, q) = \frac{A(q\sigma/2 + x - \mu)^2}{(\sigma/2)^2 + (x - \mu)^2}, \tag{3.7}$$

with μ being the center frequency, A the amplitude, σ the cross-section and x as the frequency. The Fano factor q is the ratio between the discrete resonance of our RLC and the above mentioned continuous background. However, if this background amplitude vanishes, q becomes zero and the Fano function boils down to a Lorentzian function. Lorenz Fuchs treats the influence of the continuous background resonances in his PhD thesis [126] in more detail and describes the corresponding scattering matrices.

In this thesis, the *BreitWignerModel* class of the *LMFIT* module [136] for the programming language *python* was used for the execution of the automated fits. The
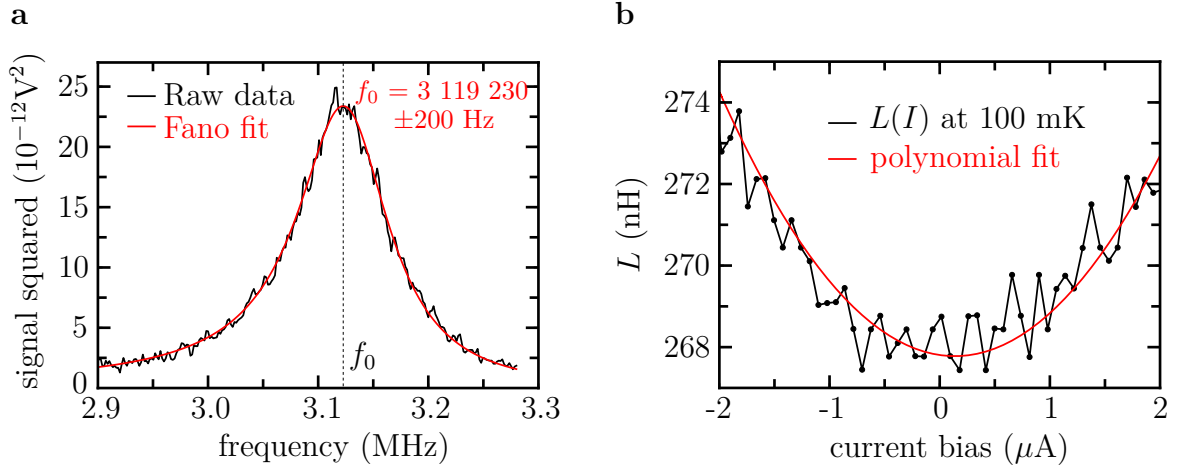
a

b

Figure 3.20: **Experimental uncertainty: a,** Resonance curve with Fano fit. **b,** Zoom-in on $L(I)$ curve with applied polynomial fit.

result of such an automated fit routine is illustrated in figure 3.20**a**. The center frequency f_0 of about 3 MHz is determined with an accuracy of 220 Hz. This corresponds to an error of less than 0.1 nH.

The graph in 3.20**b** shows a zoom-in of a $L(I)$ curve measured at 100 mK. The scattering of the inductance points ($\simeq$ center frequencies) is with 0.6 nH at least 5 times higher than the mentioned 0.1 nH standard deviation of the polynomial fit. We do not know where this discrepancy comes from. It might stem from the sum of fluctuations in the setup (e.g. gate voltage, current bias, temperature ...) or from instabilities in the eletrical environment of the substrate.

4 Josephson Inductance of One-Dimensional Josephson Junction Arrays

In this chapter, we focus on the results of DC transport and Josephson inductance measurements of sample 1, an one-dimensional Josephson junction array. This array consists of 2250 Josephson junctions in series, each with a length, width and spacing of 100 nm, 3.15 μm and 1 μm, respectively. The current direction in this sample is parallel to the InAs [110] crystallographic axis. A metal film of 5 nm Ti/ 120 nm Au serves as a global topgate and is separated by an insulator of 40 nm AlOx. Figure 4.1**a** shows a schematic of sample 1. The large number of Josephson junctions is
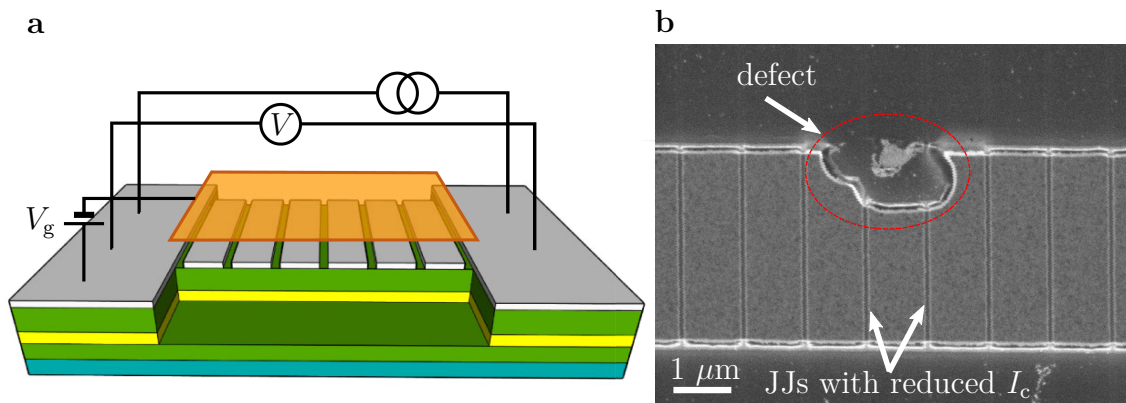
Figure 4.1: **One-dimensional Josephson junction array a,** depicted as a cartoon. **b,** SEM image of an array seen from the top before the deposition of the AlOx. The array shows a defect by what two Josephson junctions have a reduced critical current. Cartoon in panel **a** made by Nicola Paradiso.

necessary for a sizeable inductance in the order of a few hundred nH, which leads to a detectable resonance shift in our RLC circuit. Furthermore, individual junctions can be strongly affected by defects that blur the generic physics, as it was for instance

reported in Ref. [137]. These individual defects are averaged out in our array and become negligible.

One disadvantage of these large arrays is the high demands on the fabrication process. The fabrication requirements were chosen as simple as possible for the first sample. Surprisingly, the measurements on sample 1 were so productive that initially no improvements to the fabrication process were required. Therefore, the fabrication was not yet optimised and the arrays were not free from defects, as exemplified in Fig. 4.1**b**. Such defects are responsible for some weaker junctions whose critical currents are reduced. The accessible current range for the inductance is thus determined by the smallest critical current, since a finite resistance of a few ohms already completely damps our RLC circuit, causing the resonance to collapse.

In the following sections we show how we use the Josephson inductance to determine various parameter. Most of these parameters are listed in table 4.1, such as the average transpareny $\overline{\tau}$, the barrier parameter γ_B or the magnetochiral anisotropy coefficient γ_L are not accessible with ordinary DC transport measurements.

Parameter	Value	Remarks
$\overline{\tau}$	0.94	Average transmission coefficient
I_0	5.882 μA	Maximum current
I_C	4.41 μA	Critical current
Δ^*	130 μeV	Induced gap
Δ_{Al}	220 μeV	BCS gap of Al
γ_B	1.7	Barrier parameter
N	187	Number of channels
γ_L	$0.77 \cdot 10^{-6}$ T^{-1}A^{-1}	Magnetochiral anisotropy coefficient

Table 4.1: **List of parameters** of Sample 1 obtained with the help of the Josephson inductance.

4.1 Josephson Inductance

The Josephson inductance at finite current is a direct mirror of the CPR. Once one can access the CPR, one can gather information about the Andreev bound states energy spectrum, which in turn is the integration of the CPR, as described in chapter 2.4.3. To understand pictorially how we access the CPR, figure 4.2 shows descriptively what it means to apply the equations 2.62 and 2.63. A theoretical optimum is exemplified
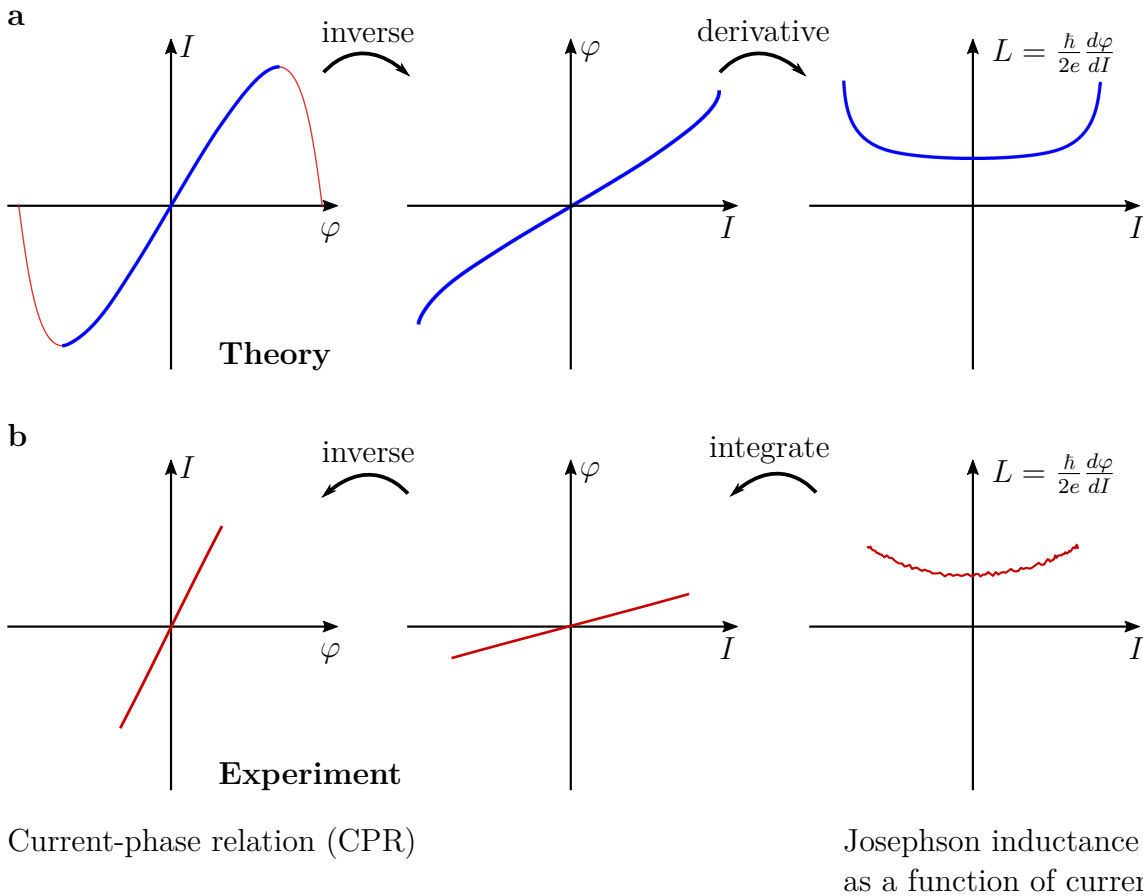
Current-phase relation (CPR)   Josephson inductance
                                                 as a function of current

Figure 4.2: **Relationship between CPR and Josephson inductance: a,** By taking the inverse and the derivative of the CPR (from left to right) leads to the $L(I)$ curve. **b,** In the experiment, however, weaker junctions in the array allow inductance values in a limited current range, so that the CPR is only partially probed (bottom right to left).

in panel **a**, while panel **b** shows the reality with the limited range in current due to defects in the array from the fabrication process.

4.1.1 Temperature Dependence

The temperature dependence of the Josephson inductance gives information about the induced gap Δ^*, the superconducting gap Δ_{Al} and about the barrier height γ_{B}. For low temperatures, when the induced gap becomes constant, it is possible to derive the average transmission coefficient $\bar{\tau}$ from the curvature of the $L(I)$ curve. In figure 4.3**a**, $L(I)$ curves are plotted for different temperatures. The inductance at zero current increases with temperature, as does the curvature. The dashed lines represent the

a

b
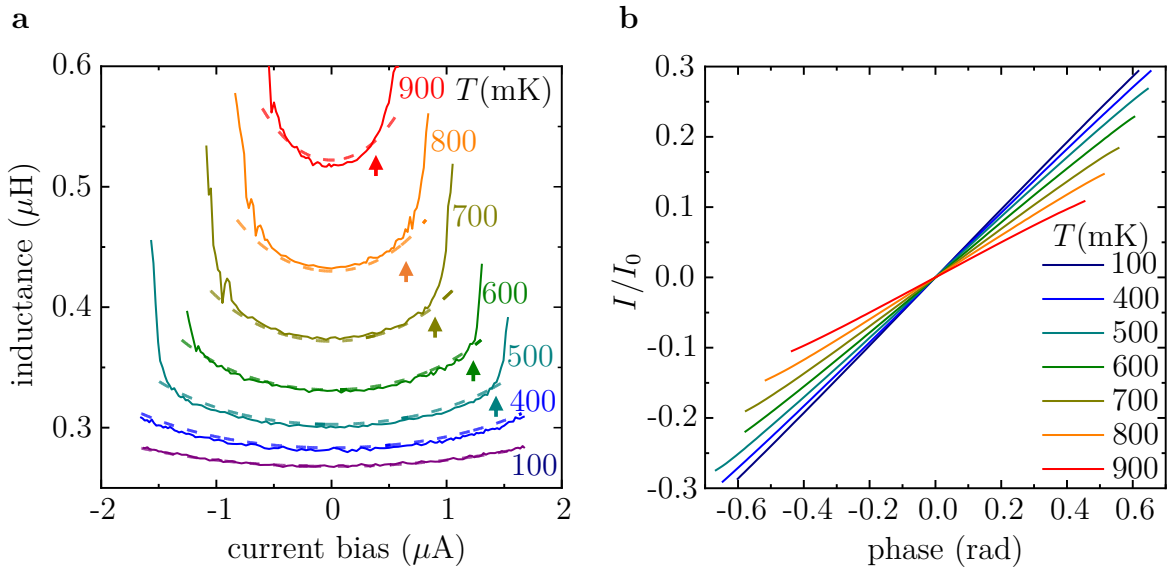
Figure 4.3: **Temperature dependent Josephson inductance** measured with respect to an applied direct current bias (solid lines). The dashed lines in **a,** show the calculated inductance. **b,** The corresponding CPR curves.

quantitative description using the Beenakker-Furusaki equation 2.64 with the determined parameters listed above in table 4.1. The data deviates from the dashed lines for a given current at finite temperatures, as indicated by the arrows. These *kinks* occur when the weakest junction reaches its critical current. In this condition, the inductance increases drastically and becomes dominant. At moderate bias, however, the inductance of such a junction with a reduced critical current is negligible in the ensemble of 2250 junctions. Figure 4.3**b** shows the accessible part of the CPR, which is the inverse integrated $L(I)$ data from figure 4.3**a**.

In order to extract $\bar{\tau}$ from the shape of the $L(I)$ curves, it is advantageous to get rid of the prefactor I_0 in the Beenakker-Furusaki equation 2.64. For this purpose, we plot the data in a normalised way - namely as $L(0)/L$ as a function of $2\pi L(0)I/\Phi_0$ - as it
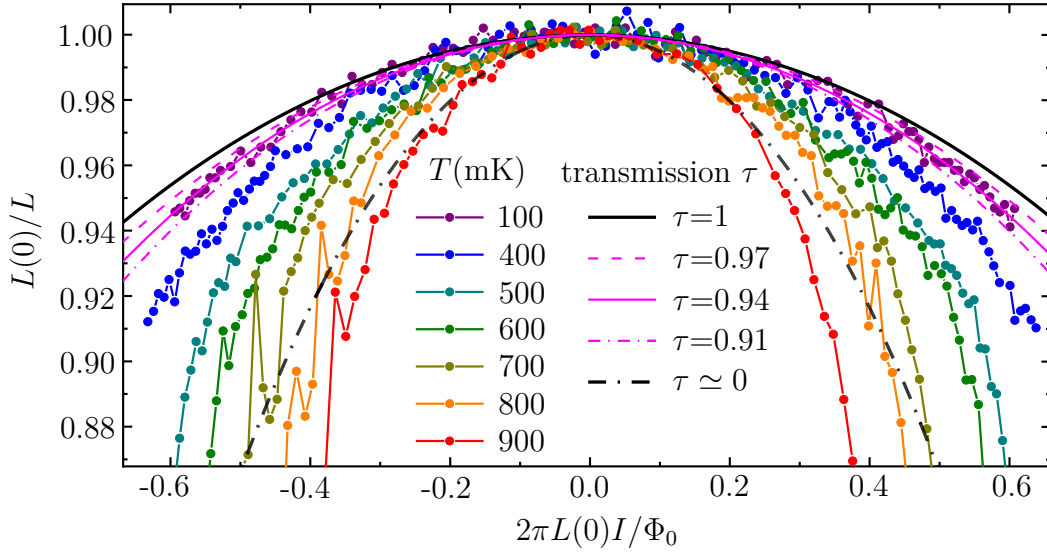
Figure 4.4: **Extraction of $\overline{\tau}$:** Normalised representation of the $L(I)$ curves from Fig. 4.3.

is shown in figure 4.4. To determine $\overline{\tau}$, we use the derivative of the function $f(\varphi)$ of the Beenakker-Furusaki equation 2.64 and plug it into $L^{-1}(\varphi) = 2\pi I_0 f'(\varphi)/\Phi_0$ (Eq. 2.62). The theoretical fits (highlighted in magenta) show how sensitive the curvature is to the transparency, and thus we can assign 0.94 to the average transparency $\overline{\tau}$ of the whole array.

Furthermore, we clearly observe an increase of the curvature with increasing temperature. The black solid and dashed lines show the theoretical limiting cases for $\overline{\tau} = 1$ and $\overline{\tau} = 0$, respectively.

The parameter $I_0 = 5.882\ \mu A$ is then determined by substituting $\overline{\tau}$ and $L(I = 0\ A, T{=}100\ \text{mK})$ into Eq. 2.62. The corresponding critical current $I_c = I_0 \max_\varphi f(\tau = 0.94, \varphi)$ is 4.41 μA, i.e. about $\approx 0.75\ I_0$.

The proximity effect is responsible for the emergence of the induced gap Δ^*, which does, however, not follow the BCS theory. As we have seen in section 2.4.5, for temperatures not too close to T_c, the gaps of the superconductor and the 2DEG are related via [129][99]

$$\Delta^*(T) \approx \frac{\Delta_{\text{Al}}(T)}{1 + \gamma_{\text{B}}\sqrt{\Delta_{\text{Al}}^2(T) - \Delta^{*2}(T)}/(\pi k_{\text{B}} T_{\text{c}})}, \tag{4.1}$$

where the relation between these gaps is determined by the dimensionless barrier

height γ_B. Using this equation, we can use the temperature dependent induced gap $\Delta^*(T)$ and plug it into the Beenakker-Furusaki formula 2.64. The resulting function $f(\varphi)$ together with the predetermined I_0 gives us via Eq. 2.62 the corresponding theoretical $L(T)$ values.

With this approach, we tried to fit the temperature dependent $L(0)$ values shown in Fig. 4.5. For $\gamma_B = 1.0$ and $\Delta_{Al} = 180$ μeV, the fit (red curve) matches all points. However, this fit is unrealistic, because the below in section 4.13 shown $R(T)$ measurement reveals a critical temperature of 1.44 K, to which a BCS gap $\Delta_{Al} = 220$ μeV can be assigned. That is why it is convenient to fix the Δ_{Al} parameter and try to fit
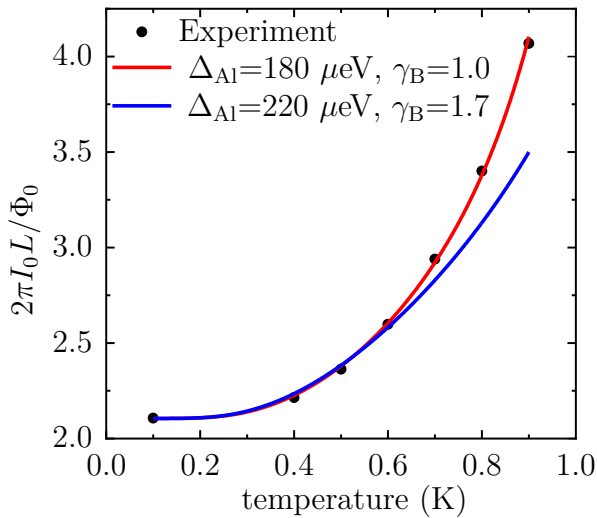
Figure 4.5

Temperature dependent zero bias inductance $L(0)$, normalised to $(2\pi I_0)/\Phi_0$, together with the fit results from the Eqs. 2.64 and 4.1 with $\Delta_{Al} = 180$ μeV and $\gamma_B = 1.0$ (red curve) and $\Delta_{Al} = 220$ μeV and $\gamma_B = 1.7$ (blue curve).

the $L(T)$ data by adjusting only γ_B, which shows the best result for 1.7 (blue curve). The blue curve does match the data points at lower temperatures.

For both fits, the induced gap is 130 μeV, which we can confirm with our tunnel spectroscopy experiments (described in section 3.4.4) and additionally with the $R_{N,1}I_0$ product ($\Delta^* = eR_{N,1}I_0/\pi = 125$ μeV). $R_{N,1}$ is defined as the normal resistance of a single Josephson junction (discussed below in section 4.2).

The reasons for the deviation between the data points and the blue fit at higher temperatures is not yet fully understood. Besides the unreliability of equation 4.1 towards T_c, the mentioned weak junctions could also be responsible, where the inductance of individual junctions start to dominate (see arrows in Fig. 4.3).

4.1.2 Gate Dependence

The array discussed in this chapter is completely covered with a topgate. In this way, we can tune the density of states in the normal conducting region. How the
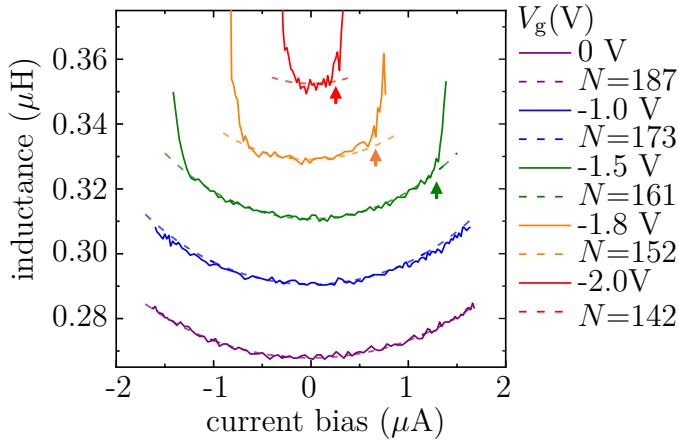
Figure 4.6
Gate dependence of $L(I)$ at $T=100$ mK. The experimental values (solid lines) are plotted together with the theoretical ones calculated from Eq. 2.64. The number of channels is determined with the help of Eq. 4.2.

gate voltage affects the $L(I)$ curves is shown in figure 4.6. At first glance, they resemble the temperature dependent $L(I)$ curves in Fig. 4.3. This time, however, the curvature does not change despite the increase in inductance. In other words, the average transparency $\overline{\tau}$ remains constant, but the prefactor I_0 changes and can be decomposed into

$$I_0(V_\mathrm{g}) = \frac{e\Delta^*}{\hbar}N(V_\mathrm{g}), \tag{4.2}$$

where $N(V_\mathrm{g})$ is the number of supercurrent-carrying transverse channels. Using Eqs. 4.2 and 2.64, the number of transverse channels $N(0)$ is 187 for $V_\mathrm{g} = 0$. This number can be compared with the Sharvin resistance, that is $R_\mathrm{sh} = R_\mathrm{N,1} = 66.8$ Ω. Inserted in equation $N = [(2e^2/h)/R_\mathrm{sh}]^{-1}$ gives a value of 193 for $N(0)$ [87]. This shows that almost all transverse channels are carrying a supercurrent.

Note the distiction from the number of channels estimated in the plain 2DEG hallbar characterisation (see Fig. 3.8 in section 3.4.2). The use of the Fermi wavelength from the 2DEG characterisation results in $N(0) = W/\lambda_\mathrm{F} = 700$. We conclude that in a Josephson junction the electrostatics in the vicinity of aluminium leads are not comparable to an extended aluminium-free 2DEG.

4.2 *I-V* Characteristics

When a new sample is mounted into the dilution refrigerator and cooled down, we obtain an initial overview with DC transport measurements. Figure 4.7 shows the
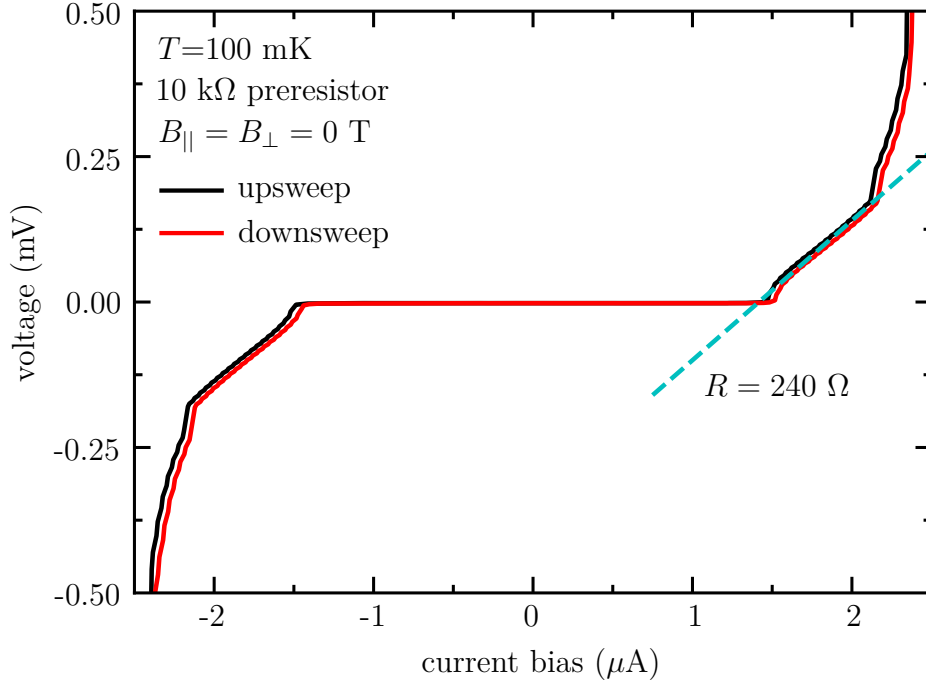

Figure 4.7: ***I-V* characteristics** of sample 1. Up- and downsweep show a tiny hysteresis. A reduced critical current at ± 1.6 μA stems from weaker junctions.

current-voltage curves of the sample 1 for an up- and downsweep (black and red curves). The current bias is defined by a 10 kΩ preresistor and the temperature was fixed to 100 mK. We observe a tiny hysteresis which we assign to heating effects and not to retrapping. In this kind of heterostructure, the capacitance of our Josephson junction is negligible and can therefore be regarded as an overdamped junction (described in section 2.3.3).

Additionally, a finite resistance of 240 Ω shows up at ± 1.6 μA (cyan dashed line). At this point the weakest junctions reach their critical current.

The current where the entire array switches to normal state is at 2.4 μA, whereby the critical current of the undamaged Josephson junctions is 4.41 μA, as we know from the inductance characterisation described in section 4.1.1, and goes along with the experience from single Josephson junction measurements. The discrepancy between

the critical currents we get from the normal state resistance and from the inductance measurements comes, according to our explanation, from weaker junctions that start to heat the entire array. The switching to normal resistance of the weak links goes rapidly, since the power increases with current according to $P = I^2 \cdot R$.

4.3 The Fraunhofer Diffraction Pattern

In this section, we discuss the modulation of the critical current and inductance by an external magnetic field acting on the array out-of-plane. The magnetic flux penetration into the Josephson junction leads to quantum interference that causes a variation of the supercurrent. The shape of the diffraction pattern depends on the form of the Josephson contact. Figure 4.8**a** shows a sketch of a single homogeneous and rectangular shaped S-N-S junction from above. The supercurrent across such a junction is given by the spatial integration of the supercurrent density:

$$I_{\mathrm{s}} = \int \int J_{\mathrm{s}}(x, y) dx dy \tag{4.3}$$

In the limit of small critical current densities J_{c}, where field screening effects over the junction area can be neglected, the supercurrent density $J_{\mathrm{s}} = J_{\mathrm{c}} \sin(x, y)$ oscillates sinusoidally as a function of position y, as exemplified in Fig. 4.8**b** for the flux $\Phi = \frac{5}{2}\Phi_0$. The net current is maximal for half cycles (as in the sketch) and zero for full cycles. If the supercurrent density is uniform across the junction, the maximum supercurrent can be written as follows:

$$I_{\mathrm{c}}(B_\perp) = I_{\mathrm{c}}(0) \left| \frac{\sin(\pi \Phi / \Phi_0)}{\pi \Phi / \Phi_0} \right| \tag{4.4}$$

with the flux $\Phi = awB_\perp$. This sinc function describes the so-called Fraunhofer pattern for a rectangular Josephson junction in analogy to optics.

The Fraunhofer pattern in Fig. 4.8**c** of our device with its 2250 junctions in series can be well fitted (yellow dashed line) by applying Eq. 4.4. We have to consider an extended area of $a = d + 2\lambda = 960$ nm to match the periodicity of the lobes, instead of the by lithography defined $d = 100$ nm. The size of this deviation was reported several times for this heterostructure [137][138] and was related to flux focussing, where the aluminium leads partially expel the magnetic field, thereby increasing the effective field in the junction. Our explanation is different. We claim that the magnetic field
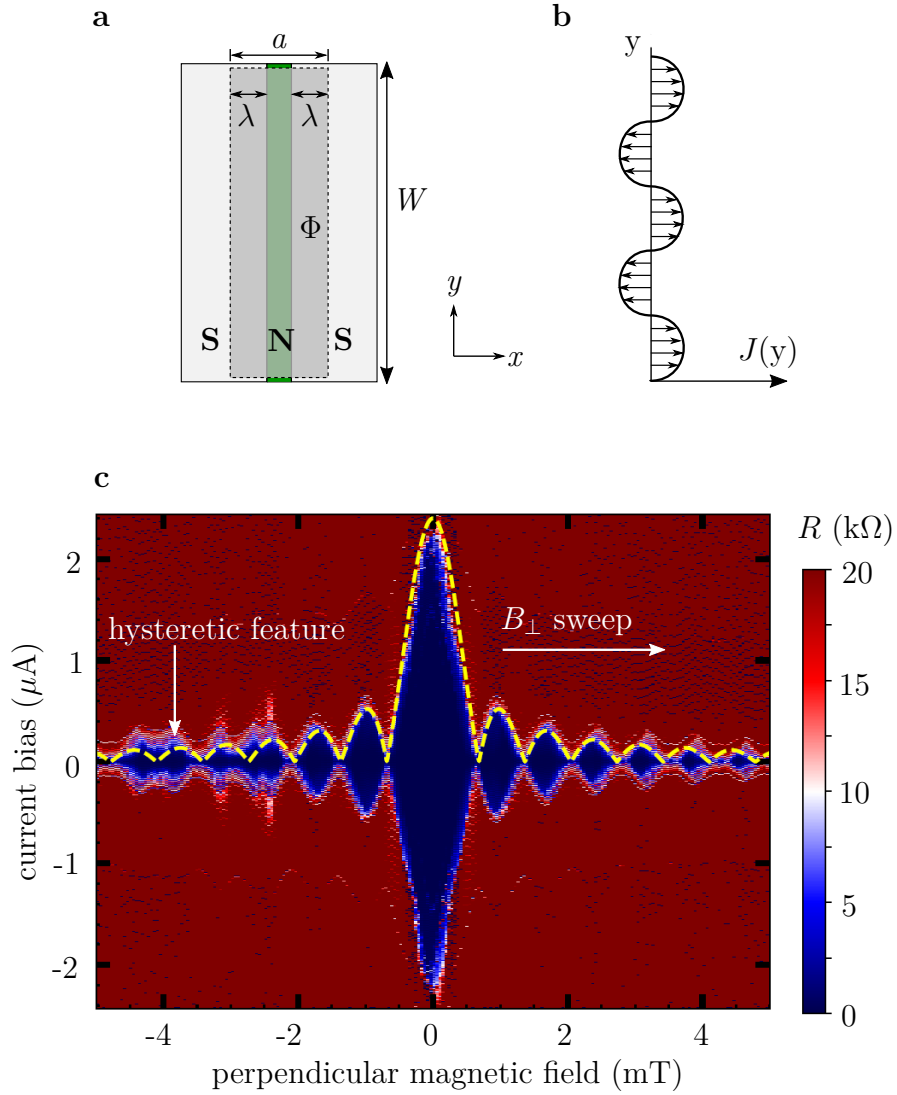
a

b

c

Figure 4.8: **Fraunhofer pattern: a,** Schematic top-view illustration of a single Josephson junction penetrated by flux Φ with λ being the London penetration depth. **b,** Current density distribution across a homogeneous junction. **c,** Calculated differential resistance of *I-V* curves show a Fraunhofer pattern, which follows the sinc function (yellow dashed line) of a rectangular junction. Figure **a,** and **b,** are inspired by [23].

almost completely penetrates the Al islands, which means that the effective area is much larger. In our wafer, the London penetration depth λ_L was determined to be 220 nm by kinetic inductance measurements performed by Lorenz Fuchs [126]. For large films, the field therefore penetrates up to $\Lambda_\perp = \lambda_L^2/d \approx 8~\mu$m.

Moreover, we observe some further puzzling features in the Fraunhofer pattern. For instance, in all three one-dimensional JJAs measured so far, we see a hysteretic distortion of the higher side lobes, indicated in Fig. 4.8**c** on the left side. This behaviour depends on the sweep direction of the out-of-plane field. However, since we see this hysteretic behaviour in other measurements as well [139][126], the origin could lie in glitches of the compensation coils.

In addition, we see a different hysteretic behaviour of low resistance within the main lobe, highlighted in Fig. 4.9**a** and **b**. The yellow marked area indicates this hysteretic feature, which might be caused by trapped vortices in the aluminium film. The green arrows in the discussed figures of 4.9 show a smaller critical current, which is unaffected by the sweeping direction of the perpendicular field. A plausible explanation are a few weaker junction with a non-rectangular and smaller area size. Both features in the main lobe are sample dependent and were not reproduced by sample 2 or sample 3. For this reason, no further analysis were considered.
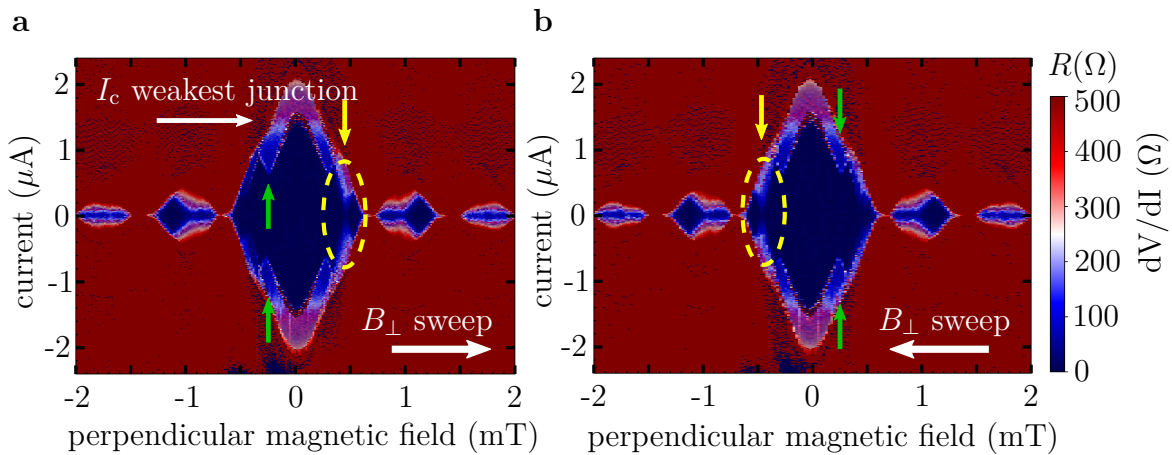
Figure 4.9: **Fine structure of critical current:** We observe a small resistance depending whether it is an up- **a,** or a downsweep **b,** of the out-of-plane field (yellow arrows). The green arrows mark another fine structure of the critical current in the main lobe, which is independent of the sweep direction. Both fine structures of I_c are an unique feature of sample 1.

As long as the device remains in the zero resistance state, we can measure the inductance with our RLC method. We characterised the dissipationless regime of the main lobe and performed an up- and downsweep with respect to the out-of-plane magnetic field. In contrast to the critical current $I_c(B_\perp)$ we obtain from the normal state resistance, the Josephson inductance shows a high sensitivity to $\overline{\tau}$, as shown in Fig. 4.10**a**. The experimental data points (black and grey symbols) match almost
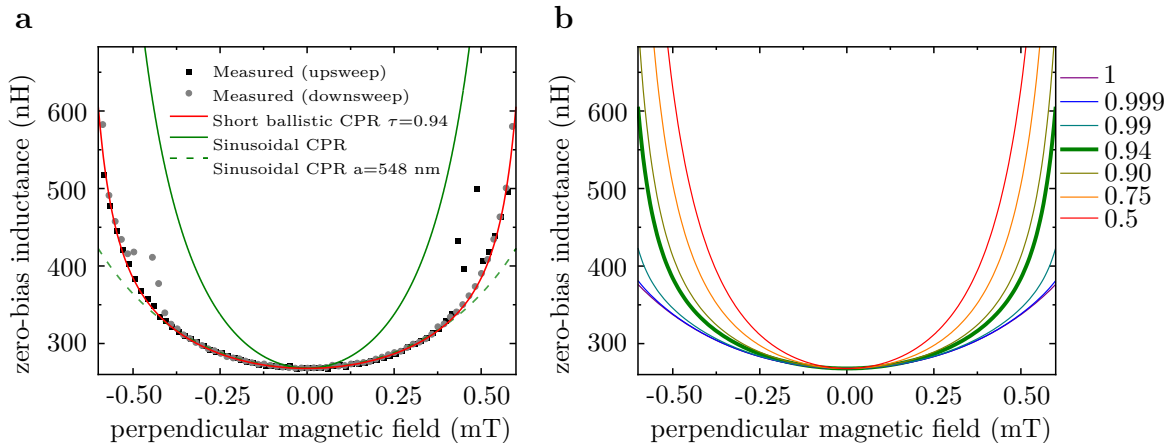

Figure 4.10: **Josephson inductance of the Fraunhofer pattern** at **a,** zero-bias for up- and downsweep. A few points scatter on each side. This is where the inner hysteretic feature with finite resistance kills the resonance (compare with Fig. 4.9). **b,** Calculated inductance as a function of the out-of-plane magnetic field. The intention of this plot is to emphasise the sensitivity of $L(B_\perp)$ to $\overline{\tau}$. The theoretical curves in both figures were rescaled to match the zero-field inductance. Analysis and theoretical curves made by Nicola Paradiso.

perfectly with the computed $L(B_\perp)$ values with the in section 4.1.1 predetermined parameters $I_0, \overline{\tau}, a$ (red solid curve).

The green curves represent the limiting cases of a tunnel junction ($\overline{\tau} \approx 0$). For the solid green curve, the same junction area ($a = (d + 2\lambda) \cdot w$=960 nm · 3.15 μm) was taken as for the red curve, while for the dashed green curve, the effective junction length $a = d + 2\lambda$ has been fixed to 548 nm in order to fit the data at low perpendicular magnetic fields from -0.4 to 0.4 mT.

Fig. 4.10**b** shows further theoretical curves in order to highlight the strong dependence of $L(B_\perp)$ on the shape of the CPR. To compute these curves, we have to take the CPR from Eq. 2.64: $I(\varphi) = I_0 f(\varphi)$. For a homogeneous rectangular junction, the local phase difference is given by [23]

$$\varphi(y) = \gamma + \left(\frac{2\pi a B_\perp}{\Phi_0}\right)y, \tag{4.5}$$

where γ is the gauge-invariant phase difference between the superconducting leads and x the position in the Josephson junction. The second term is the vector potential for a constant perpendicular field. The current I is given by the integral along the junction width w of the CPR

$$I = \int_0^w (I_0/w) f[\varphi(y)] dy = I_0 g(\gamma, B_\perp), \qquad (4.6)$$

where we can define a function $g(\gamma, B_\perp)$ as the average of f over the width w of our homogeneous junction. The current bias dependence of $\gamma = \gamma(I)$, given by the inverse of Eq. 4.6, allows us to calculate the inductance once again with Eq. 2.62. The inductance is therefore

$$L(B_\perp) = \frac{\Phi_0}{2\pi I_0 (\frac{\partial g}{\partial \gamma})_{\gamma = \gamma(I)}}, \qquad (4.7)$$

where the variation of $B_\perp$ is included in g and γ. To round off our analysis we also
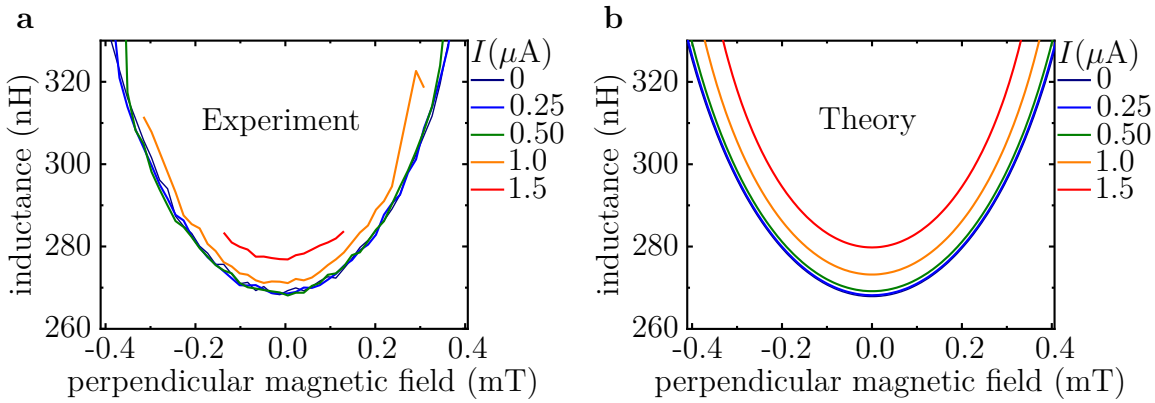
Figure 4.11: **Current bias dependence** of the Josephson inductance in the main lobe for **a,** measured and **b,** computed values. Theoretical $L(B_\perp)$ curves made by Nicola Paradiso.

measured the inductance of the main lobe of the Fraunhofer pattern at small and moderate current bias. The experimental data (see Fig. 4.11**a**) are again reproduced by the theory (compare with Fig. 4.11**b**).

Unlike the $B_\perp$-dependence of the Josephson inductance, the diffraction pattern is not affected at all by the transparency for short-ballistic junctions. Two cases, one for the obtained $\bar{\tau} = 0.94$ and one for a tunneling junctions $\bar{\tau} \to 0$, are depicted in 4.12. The former is calculated using Eq. 2.64, whereas the latter is replicated by

Figure 4.12
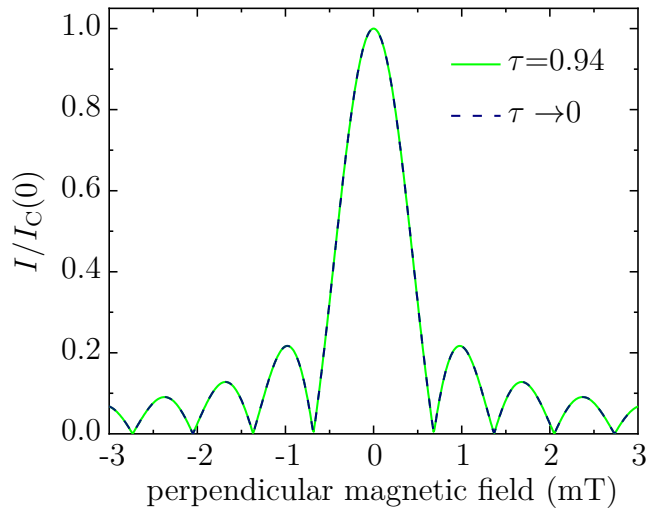
Critical current dependence of $\overline{\tau}$ at different perpendicular magnetic fields. Graphs and corresponding analysis made by Nicola Paradiso.

the sinc function $(I_c(B_\perp)/I_c(0) = |\sin(\pi\Phi/\Phi_0)/(\pi\Phi/\Phi_0)))$. Obviously, the curves are indistinguishable from each other and this counts for any value of $\overline{\tau}$.

4.4 Temperature Dependent Resistance

Another basic characterisation represent $R(T)$ curves. Besides the critical temperature, we obtain the total normal resistance R_N of the device, which is 157 kΩ in the case of the described sample 1. The $R(T)$ curve is plotted in Fig. 4.13**a**. The data was obtained by low-frequency lock-in technique using 1 MΩ as a preresistor in order to define 20 nA as current bias. The normal resistance $R_{N,1}$ of a single junction is 66.9 Ω, if we subtract 7 kΩ beforehand, which the aluminium islands and leads contribute to the total normal resistance R_N.

From the $R(T)$ curve we deduce for critical current $T_c = 1.44$ K with the criterion $R(T_c) = 0.5\, R_N$. Thus, the assumed BCS superconducting gap of the aluminium is:

$$\Delta_{Al} = 1.764 \cdot k_B T_c = 220 \ \mu eV \tag{4.8}$$

In figure 4.13**b**, we see the corresponding Arrhenius plot of the $R(T)$ measurement. Due to the exponential behaviour of the $R(T)$ curve, we can fit the slope and extract an activation energy E_A of 68 K $\cdot k_B$, that is $\simeq 5.9$ meV (the Ambegaokar Halperin theory to the activation energy is discussed in section 2.3.4). In section 6.4 we will discuss the activation energy E_A of sample 2 with respect to an in-plane field applied in different directions. There, we will see that E_A is slightly reduced by the field and

due to longer Josephson junctions of the array, whereby the average transparency $\overline{\tau}$ is smaller (i.e. $\simeq 0.75$ for sample 2) than it is for sample 1. Thus, in the image of the tilted washboard model (introduced in section 2.3.2) the potential barrier is smaller and less energy is necessary to activate the motion of the particle.
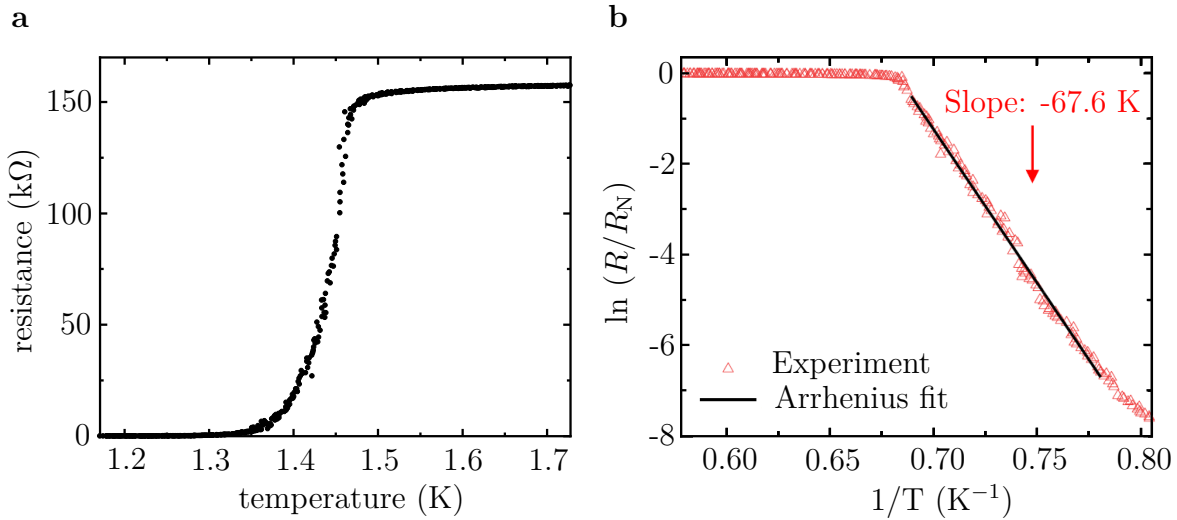
a

b

Figure 4.13: **Normal resistance a,** as a function of temperature. **b,** Corresponding Arrhenius plot. A few weaker junctions are responsible for the foot at lower temperatures.

5 Superconducting Diode Effect

Non-reciprocal charge transport is the basis of many important electronic components such as rectifiers, photosensors, solar cells, transistors or diodes [140][141]. Diodes, for example, are usually made of p- and n-doped semiconductors that form a p-n junction at the interface when brought together. In these type of junctions, the resistances for positive and negative currents are indeed different but finite, so energy losses cannot be avoided. A diode based on a superconductor would allow dissipationless charge

a   **b**
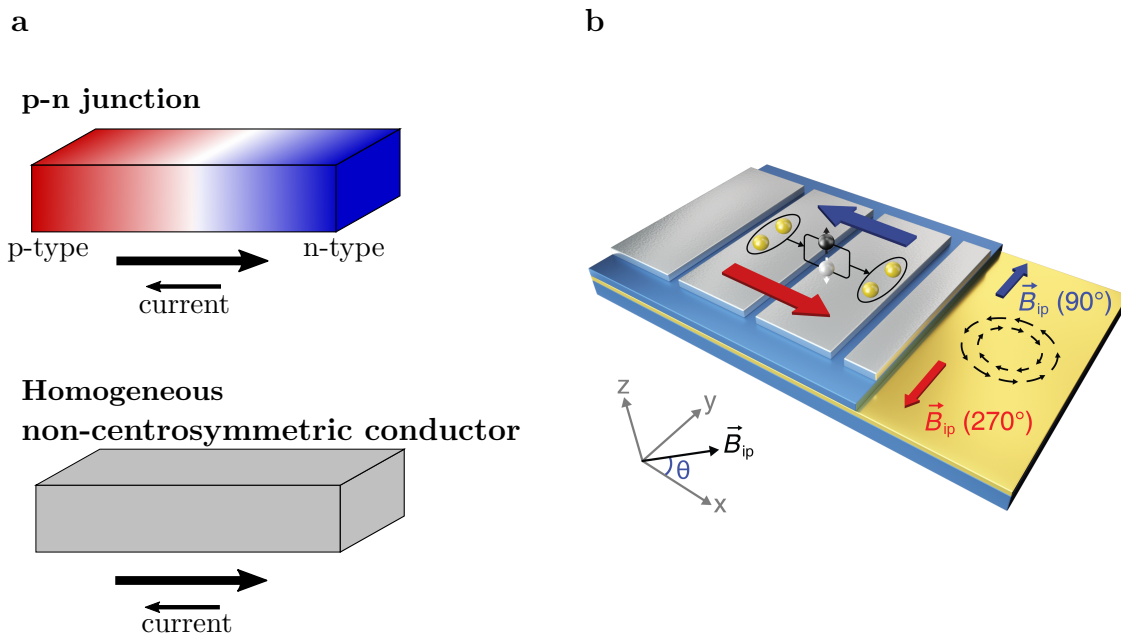
Figure 5.1: **Diode effect: a,** A diode normally consists of a p-n junction in which the atomic composition is spatially different. But homogeneous materials that are not centrosymmetric can also function as diodes if time-reversal symmetry is broken in addition. **b,** Illustration of diode effect in our one-dimensional Josephson junction array. Spontaneous supercurrents carried by spin-split pairs of Andreev bound states appear at zero phase difference. The amount and direction depend on the value and the polarity of the applied field $\vec{B}_{\mathrm{ip}}$. For $\theta = 0°$, the field is aligned parallel to the current direction and perpendicular for $\theta = 90°$ and $270°$.

transport in the forward direction and might open the door to new types of super-

conducting circuits.

In contrast to p-n junctions, where the non-reciprocal current is a consequence of spatial asymmetry, in *homogeneous* devices (see Fig. 5.1**a**) the inversion and time-reversal symmetries must be broken simultaneously to obtain a different current-voltage $I-V$ characteristic of the left and right moving charge carriers.

In 2020, Ando et al. [69] reported for the first time about the observation of a superconducting diode effect (SDE) in an artificial Nb/V/Ta superlattice.
In this chapter, we discuss the SDE that we observe in our one-dimensional superconducting array (here discussed for sample 1), if we apply an in-plane magnetic field perpendicular to the current direction. Figure 5.1**b** depicts this field-dependend diode behaviour schematically. Red and blue arrows indicate spontaneous supercurrents at zero phase difference, changing direction with the sign of the external in-plane field. The interplay of spin-orbit interaction and external magnetic field leads to the required breaking of the inversion and time-reversal symmetries.

Furthermore, we define a novel quantity, namely the magnetochiral anisotropy (MCA) coefficient γ_{L}, which we derive from the direct current dependend Josephson inductance. The MCA coefficient γ_{L} complements to the already existing MCA coefficient γ_{S}, which represents the non-reciprocal charge transport for the resistance in the superconducting phase fluctuation regime [142].
In addition to the reports from Ando et al. [69], our theory colleagues from the group of Prof. J. Fabian from the University of Regensburg provide a semi-quantitative model for the understanding of the underlying physics.

5.1 Non-Reciprocal Charge Transport in Non-Centrosymmetric Quantum Materials

Chirality, derived from the greek word $\chi\epsilon\iota\rho$ (hand), is an important type of broken symmetry in physics, chemistry and biology. A molecule or a system is chiral, when its mirror image is not identical to the original one. The symmetry group of chiral systems lacks inversion and mirror symmetry $\hat{I}$ and $\hat{M}$. $\hat{I}$ can be expressed by combination of a mirror operation $\hat{M}$ and a 180° rotation C_2 around the axis perpendicular to the mirror plane.

In our devices, inversion symmetry is broken in the z-direction due to the Zincblende structure and the asymmetric bandstructure of the 2DEG. A non-reciprocal response occurs when time-reversal symmetry $\hat{T}$ is broken in addition, for example, by a magnetic field.

The $\hat{T}$-symmetry in linear response theory is reflected by the Onsager's reciprocal theorem and it is given by [143][144]

$$K_{\mathrm{AB}}(q,\omega,B) = \epsilon_{\mathrm{A}}\epsilon_{\mathrm{B}}K_{\mathrm{BA}}(-q,\omega,-B), \tag{5.1}$$

where the function K_{AB} describes the linear response of the physical input observable A to the field coupled to the output observable B with the wave vector $\vec{q}$ and frequency ω. The factors ϵ_{A}, $\epsilon_{\mathrm{B}} = \pm 1$ indicate the even (1) and odd (-1) nature of the observable $A(B)$ with respect to the $\hat{T}$-operation [142][145].

Rikken et al. [146][147] extended this result into the non-linear response regime and to diffusive 2D conductors by using a heuristic argument. They replaced the wave vector $\vec{q}$ by the current $\vec{I}$, which leads to a resistance expressed by

$$R = R_0[1 + \gamma\hat{e}_{\mathrm{z}}(\vec{B} \times \vec{I})], \tag{5.2}$$

where the current $\vec{I}$, the magnetic field $\vec{B}$ and the electric field $\vec{E} = |\vec{E}|\hat{e}_{\mathrm{z}}$, caused by broken $\hat{I}$-symmetry, are orthogonal to each other. The coefficient γ represents the strength of the magnetochiral anisotropy.

In normal conducting metals, γ is rather small. Values in the order of 10^{-2} to 10^{-1} $\mathrm{T}^{-1}\mathrm{A}^{-1}$ are usually obtained. In superconducting regimes, however, γ reaches values up to 10^6 $\mathrm{T}^{-1}\mathrm{A}^{-1}$ (see sections 5.2 and 5.3).
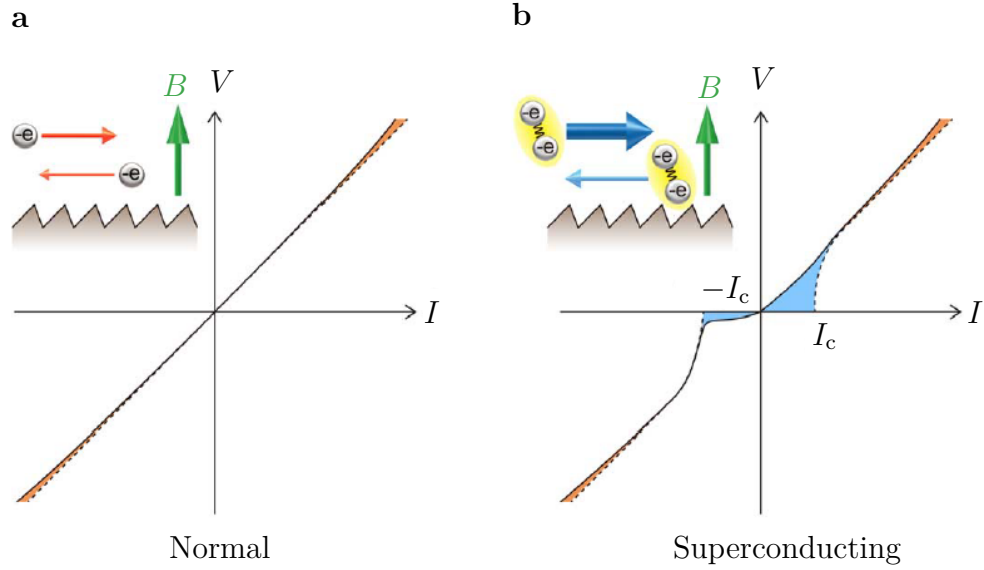
Figure 5.2: **Schematic illustration of non-reciprocal transport** in **a,** the normal and in **b,** the phase fluctuation regime. In both cases, the non-reciprocal current is small for larger I. But, when a critical current exists due to superconductivity, a much larger non-reciprocal current can be detected below I_c. The insets sketch the electron motion and the correlation of the Cooper pairs in a magnetic field B and in an asymmetric potential representing the lack of inversion symmetry. Image taken from [148].

The reason for difference between γ in normal and superconductors lies within the magnitude of the spin-orbit and Zeeman energies Δ_SO and E_Z. Both energies are small compared to the Fermi energy E_F and thus γ is small. In a superconducting regime, however, the reference energy changes from the Fermi energy E_F to the superconducting gap Δ, which is orders of magnitude smaller.

As a result, a large γ can be extracted from the resistance when superconductivity is added. The difference of the underlying regimes, i.e. the normal and the phase fluctuation regime, where superconductivity and a finite resistance are coexistent, is schematically illustrated in Fig. 5.2 [148][149]. Above the critical current, both I-V characteristics show a tiny non-reciprocal current (dashed line stands for a linear I-V). However, in the case of existing superconductivity (Fig. 5.2**b**), a much larger non-reciprocal current occurs below the critical current.

5.2 The Magnetochiral Anisotropy Coefficient γ_s for Dissipative Currents

So far, the magnetochiral anisotropy in superconducting materials was investigated in the superconducting phase fluctuation regime [69][150][151]. An established method are standard lock-in techniques to probe the first and the second harmonic of the resistance. The linear and the non-reciprocal magnetoresistance are represented in equation 5.2 by the first and second term in the bracket, where the latter and thus, the total resistance is proportional to B and I. Written as the output voltage, the equation reads as the following [150]:

$$V = R^{(1)}(I + \gamma_s B I^2). \tag{5.3}$$

An applied sinusoidal current excitation $I = I_0 \sin(\omega t)$, with the frequency ω (in our experiments 17 Hz), results in:

$$
\begin{aligned}
V &= R^{(1)} I_0 \sin(\omega t) + R^{(1)} \gamma_s B I_0^2 \sin^2 \omega t \\
&= R^{(1)} I_0 \sin(\omega t) + \frac{1}{2} \gamma_s R^{(1)} B I_0^2 \left\{ 1 + \sin\left(2\omega t - \frac{\pi}{2}\right) \right\}
\end{aligned} \tag{5.4}
$$

Accordingly, the first and second harmonic resistances can be written as:

$$R_\omega = \frac{V_\omega}{I_0} = R^{(1)} \tag{5.5}$$

and

$$R_{2\omega} = \frac{V_{(2\omega)}}{I_0} = \frac{1}{2} \gamma_s R^{(1)} B I_0 \tag{5.6}$$

The maximum strength of the non-reciprocal transport expressed by γ can be calculated with

$$\gamma_s = \frac{2 R_{2\omega}^{max}}{R_\omega B I_0}. \tag{5.7}$$

In this way, we can characterise non-reciprocity in our Josephson junction device in the phase fluctation regime.

Figure 5.3**a** and **b** show the first and second harmonic resistance with respect to temperature for different field directions in the plane, respectively. The outcome of equation 5.7 is shown in figure 5.4.
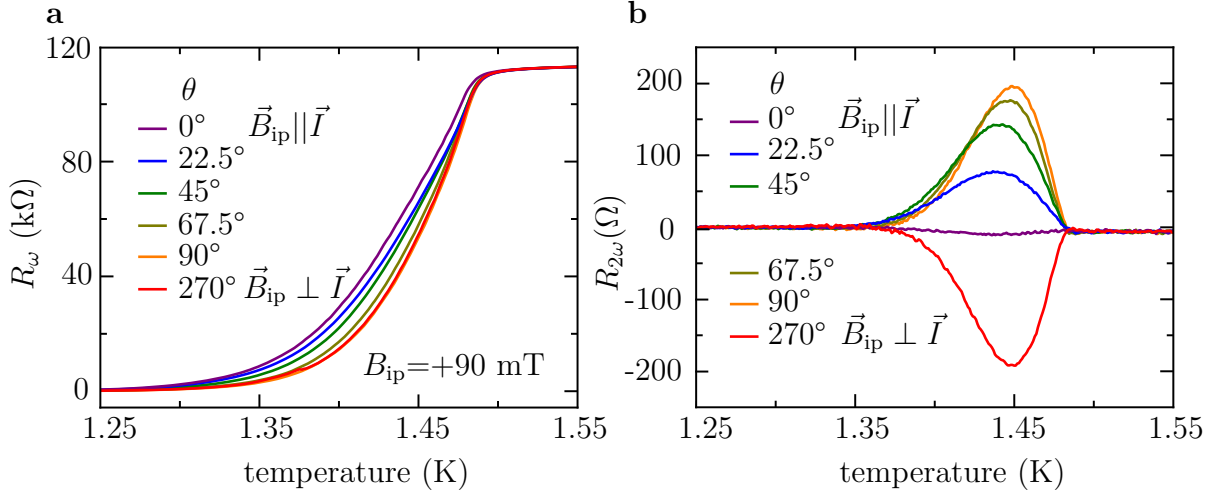
Figure 5.3: **Magnetochiral anisotropy in the fluctuation regime: a,** Normal resistance $R_\omega(T,\theta)$ curves measured with $\vec{B}_{\text{ip}}$ applied at different angles. **b,** Corresponding $R_{2\omega}(T,\theta)$ curves. The data presented here are from sample 2.

By applying a sine fit we extract the coefficient $\gamma_{\text{s}} \simeq 4.1 \cdot 10^6$ T^{-1}A^{-1} close to the transition temperature. The sinusoidal variation with the angle θ confirms the directional dependence of the in-plane field expected from Eq. 5.2. The product of γ_{s} and the sample width $w \approx 3.15$ μm with a value of $\gamma_{\text{s}} \cdot w \simeq 12.9$ T^{-1}A^{-1}m is similar to those quoted in the reports by Itahashi et al. from their artificial 2D superconductor [150].
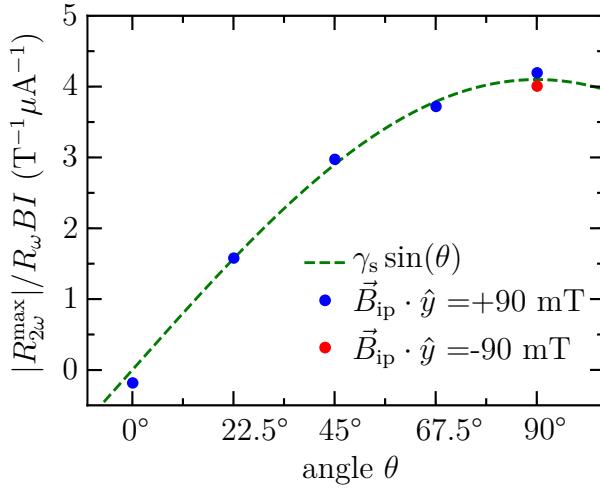
Figure 5.4

Magnetochiral anisotropy coefficient $\boldsymbol{\gamma_{\text{s}}}$: $R_{2\omega}^{\text{max}}$ is taken at the maximum in Fig. 5.3**b** together with the corresponding linear resistance R_ω in Fig.5.3**a** to calculate γ_{s} with Eq. 5.7.

5.3 The Magnetochiral Anisotropy Coefficient γ_L for Supercurrents

Now we come to the main result of this thesis. With our ability to measure the Josephson inductance L_J far below the transition temperature T_c, where the superfluid stiffness is constant and resistance absent, we are able to measure a magnetochiral anisotropy coefficient for a supercurrent. Here we introduce the new coefficient γ_L, which expresses a distortion of the $L(I)$ curves (the inverse CPR). In analogy to Eq. 5.2, the following equation

$$L = L_0[1 + \gamma_L \hat{e}_z(\vec{B} \times \vec{I})], \tag{5.8}$$

where the resistance is substituted by the Josephson inductance, describes non-reciprocal supercurrents. According to this Eq. 5.8, a finite γ_L should distort the $L(I)$ curves, if the magnetic field is aligned perpendicular to the current. To see whether a γ_L exists
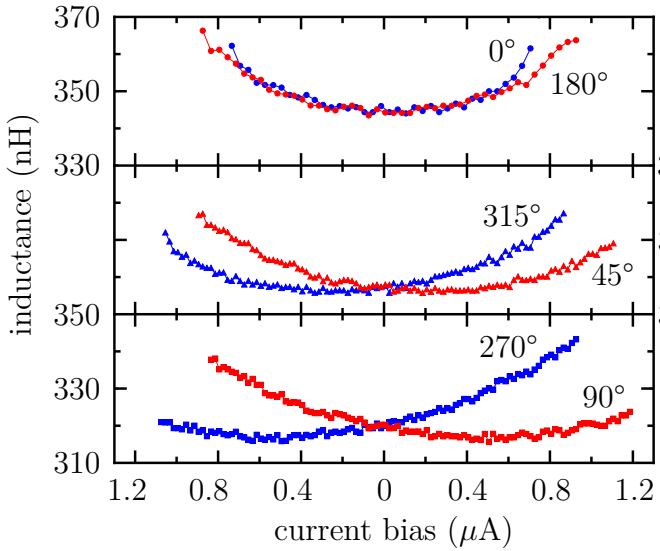
Figure 5.5

$L(I)$ data at $|\vec{B}_{ip}|=+100$ mT applied at different directions. From this data we substracted offsets from the horizontal and vertical axis. This procedure is explained in detail in the appendix B.

in our two-dimensional symmetric Josephson junctions, we measured $L(I)$ curves at $|\vec{B}_{ip} = B_x\hat{x} + B_y\hat{y}| = +100$ mT for various angles.

As figure 5.5 shows, the $L(I)$ curves in the top panel stay symmetric as expected for in-plane fields parallel to the current direction $\hat{x}$ (i.e. $B_y = 0$), because the vector product $\vec{B} \times \vec{I}$ is zero. However, the situation changes for $B_y \neq 0$. The curves become asymmetric, shift away from each other and the minima of the $L(I)$ curves occur at finite currents (mid and bottom panel).
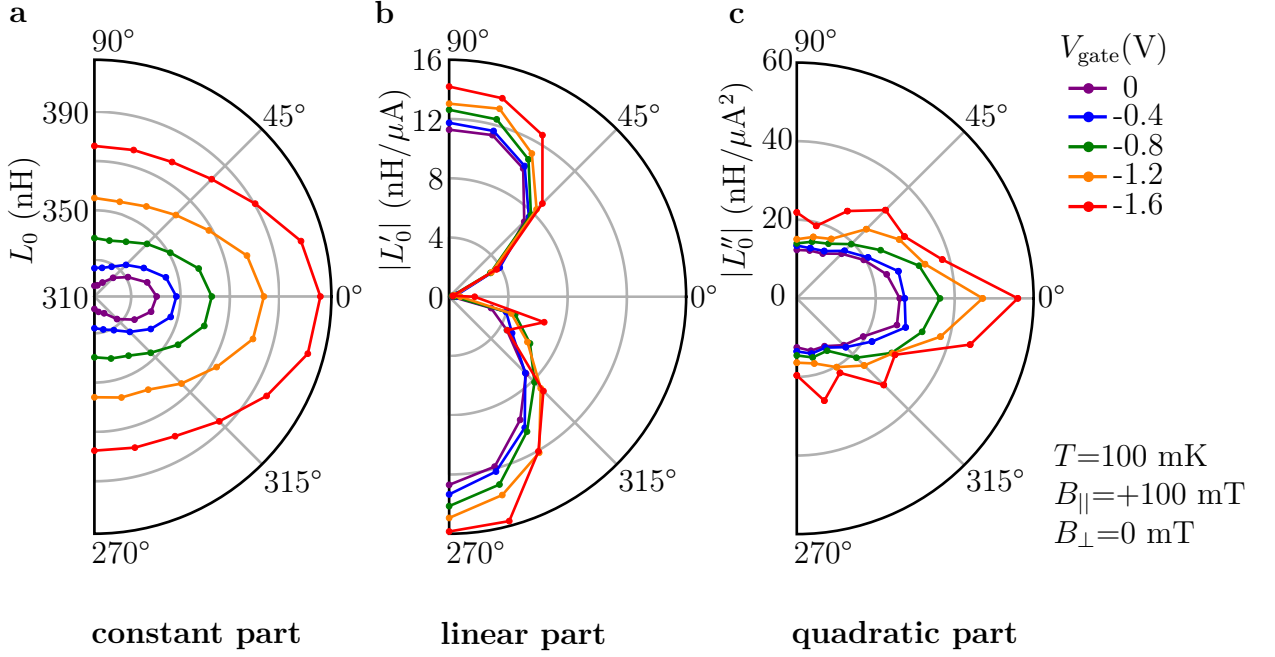
Figure 5.6: **Polynomial coefficients: a,** Extracted constant values L_0, **b,** linear values L_0' and **c,** quadratic values L_0'' for different in-plane field angles θ and topgate voltages. The data presented here were obtained from sample 1.

In order to evaluate this asymmetry in the $L(I)$ curves, we applied polynomial fits and extracted the leading parts of the polynomial expansion $\approx L_0 + L_0'I + L_0''I^2/2$, with $L_0' = \partial_I L|_{I=0}$ and $L_0'' = \partial_I L^2|_{I=0}$ around zero current.

Fig. 5.6**a**,**b** and **c** show the constant part L_0, the linear part L_0' and the quadratic part L_0'' in form of polar plots. The constant part, already slightly asymmetric with respect to the in-plane field direction, is maximal for $0°$ $(\vec{B}_{\text{ip}}||\hat{x})$ and minimal for $90°$ and $270°$ $(\vec{B}_{\text{ip}}||\hat{y})$. Decreasing the topgate voltage increases L_0, as it reduces the amount of supercurrent carrying channels an thus the critical current (discussed in the previous chapter 4.1.2).
But why the in-plane field affects L_0 asymmetrically is unclear. A plausible explanation is the warping of the Fermi surface in parallel magnetic fields, which influence the Fermi velocities of the two spin components.

The linear part L_0' in Fig. 5.6**b**, however, is highly anisotropic with respect to the in-plane field direction and L_0' mainly reflects the magnetochiral anisotropy of supercurrents. The gate voltage has little effect on the linear part in contrast to the
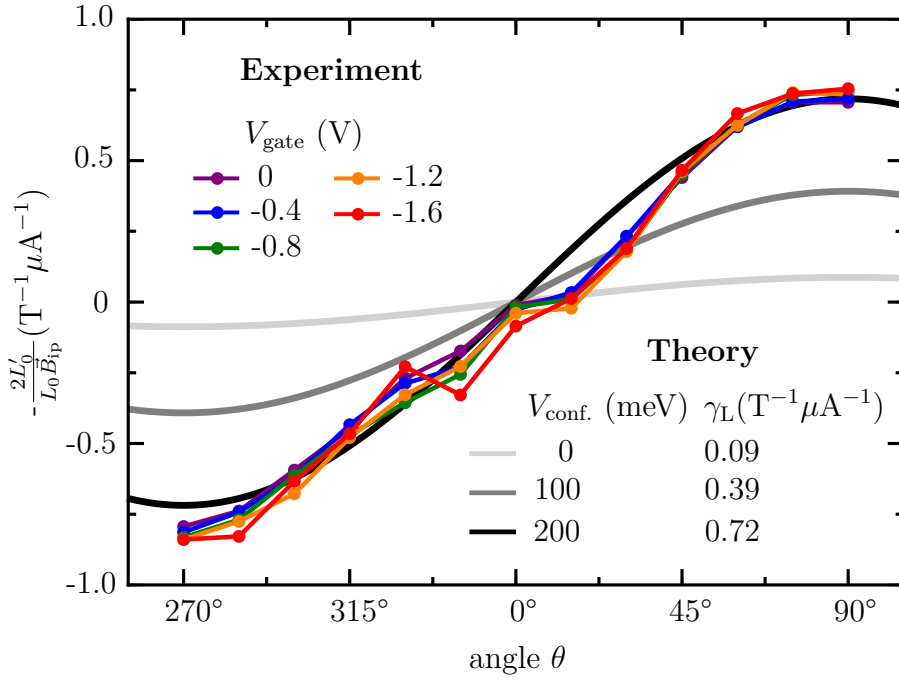
Figure 5.7: **Magnetochiral anisotropy coefficient γ_L** as a function of the in-plane field angle θ for $\vec{B}_{ip}$=+100 mT for different topgate voltages. From the sine fit, we extract the MCA coefficient $\gamma_L \cong 0.77 \cdot 10^6$ T^{-1}A^{-1}. This graph includes the theoretical results considering different confinement potentials V_{conf}, which are essentially sinusoids.

constant part.

The quadratic coefficient L_0'', displayed in Fig. 5.6c, shows a similar directional in-plane magnetic field behaviour as the constant part L_0.

In figure 5.7 we present the novel quantity $\gamma_L = -2L_0'/(L_0\vec{B}_{ip})$ as the magnetochiral anisotropy coefficient for the inductance. It follows sinusoidally the angle θ according to $(\vec{B} \times \vec{I}) \cdot \hat{z} = BI \sin\theta$. From the sine amplitude we take the value $\gamma_L = 0.77 \cdot 10^6$T^{-1}A^{-1}, which has the same order of magnitude we estimated for γ_s. The novel coefficient γ_L relates directly to the superfluid and cannot be obtained by resistance measurements. It is material-specific and geometry-independent.

Our observations are consistent with the theory. A. Costa and the group of Prof. J. Fabian from the University of Regensburg provided a semi-quantitative description by numerical simulations with the Python package KWANT [152]. For their realistic theoretical model, the following parameters were chosen: 15 meV nm for the Bychkov-

Rashba spin-orbit coupling strength, -10 for the in-plane *g*-factor in the quantum well, 0.02 m_0 for the effective mass and 239 meV for the Fermi energy μ.

In order to match the experimental data, a parabolic confinement potential along $\hat{z}$ has to be to be included in the simulations. The numerical results are also shown in Fig. 5.7 (grey lines). As we can see, the result without a confinement potential is off by one order of magnitude, while a confinement potential of $V_{\text{conf}} = 200$ meV can best reproduce our data. Such a value is realistic and a similar value of 150 meV was reported for the confinement in AlGa/GaAs/AlGa multilayers [153].

But since we cannot measure a φ_0-shift in the CPR with our RLC method, what is the reason for our observations? And why does the gate have little effect on γ_{L}, but a parabolic confinement potential does? As introduced in section 2.5, the presence of SOI and Zeeman field breaks Kramers degeneracy, which shows up as a φ_0-shift. This shift results from cosine contributions to the Fourier expansion of the 2π periodic function of the CPR, which is in most cases a sine. In our case, however, the CPR
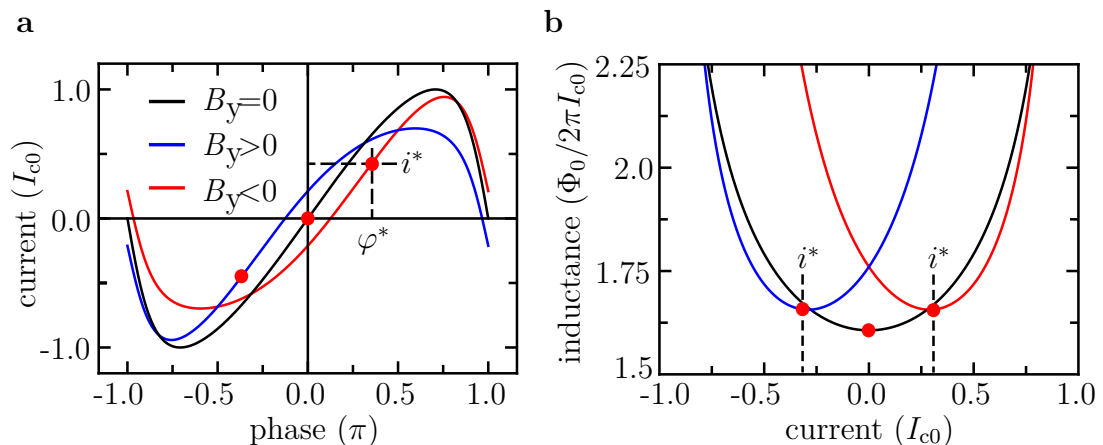
Figure 5.8: **Distorted CPR: a,** Magnetic fields cause cosine terms in the Fourier series which alter the shape of the CPR of short-ballistic Josephson junctions and shift therefore the inflection point to positive or negative i^* and φ^*. The results are finite currents at zero phase difference and the emergence of asymmetric critical currents. **b,** Corresponding $L(I)$ curves to emphasise the link to the experimental data in 5.5.

is skewed and non-sinusoidal due to the high transparency of the junctions. Therefore, the CPR is not only distorted by a mere phase shift φ_0. Here, the cosine terms

additionally lead to a shape exemplified in Fig. 5.8**a**. Depending on the direction of the magnetic field, the as red point indicated inflection point (i^*, φ^*) is shifted away either from zero to positive or negative currents. Moreover, we can see the difference in the extremal values for positive and negative phase differences that determine the critical currents I_c^+ and I_c^-. This behaviour is the reason why we observe the diode effect, i.e. supercurrent flow in one direction $(I < I_c^+)$, while in the other direction the system is resistive $(|I| > |I_c^-|)$ (discussed below in section 5.4). The corresponding $L(I)$ curves are shown in Fig. 5.8**b**. The shift of the inflection point is reflected in the inductance measurements.

We see, the diode effect of supercurrents and the anomalous φ_0-shift seem to have the same origin, but they do not always occur together. We can therefore use previous works from the latter effect for our purposes. A. Buzdin [105] concluded for a single ballistic mode, that $\varphi_0 = 4\alpha d |g^*| |\mu_B| |\vec{B}_{\mathrm{ip}}| \sin\theta / (\hbar v_{\mathrm{F,x}})^2$, with $v_{\mathrm{F,x}}$ being the Fermi velocity in $\hat{x}$ of the mode. The conduction band offsets of the quantum well are responsible for the formation of the confinement potential V_{conf}, which in turn lowers the Fermi energy μ and thus the Fermi velocity $v_{\mathrm{F,x}}$. Hence, the φ_0-shifts become more significant and the CPR asymmetry is enhanced.
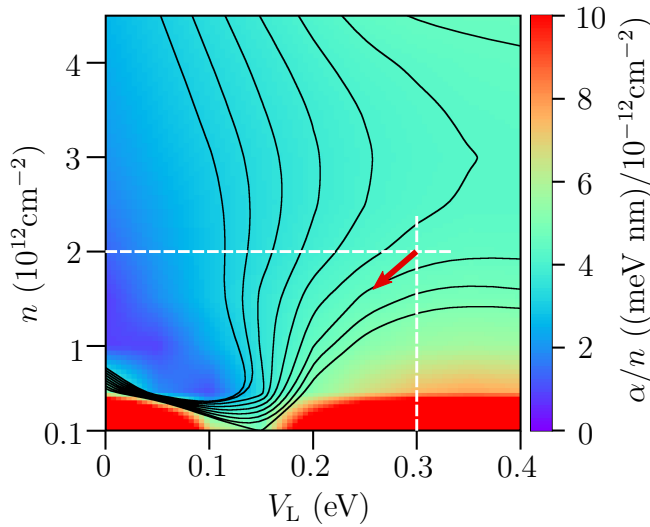
Figure 5.9

Gate dependence of α/n: The red arrow indicates approximately how a gate sweep from 0 to $-2\,V$ changes the charge carrier density n and the electrical potential V_L. The black contour lines show constant α/n traces. In order to increase the magnetochiral anisotropy, it is essential to increase the ratio α/n. Figure provided by P.E. Faria Junior.

The same formula from A. Buzdin can also explain the small impact of the topgate. The gate voltage changes not only the charge carrier density n and accordingly the Fermi velocity v_{F}, but also the Rashba parameter α.

Figure 5.9 shows the graph 2.5**a** from section 2.1.2, but here the Rashba parameter

is divided by the corresponding carrier density n. From the previous gate dependent $L(I)$ measurements in section 4.1.2, we can deduce a change of density $\Delta n \approx -0.2 \cdot 10^{12}$ cm^{-2}, when sweeping the topgate from 0 to -2 V. The electrical potential V_L simultaneously changes by a few tens of meV. The red arrow in Fig. 5.9 shows the corresponding change of the parameter in our data. It is roughly parallel to the constant α/n contour lines. However, for an effect of the gate on γ_L, the ratio α/v_F has to change.

5.4 Non-reciprocal Critical Current and Rectification

Finally, we will analyse the DC transport measurements and demonstrate the superconducting diode effect, which can be controlled by an in-plane magnetic field. In our superconducting system, this means that in one direction the current flows without dissipation, while in the other direction there is a resistance that depends on the sum of the normal resistances of the ensemble of the 2250 Josephson junctions in series.
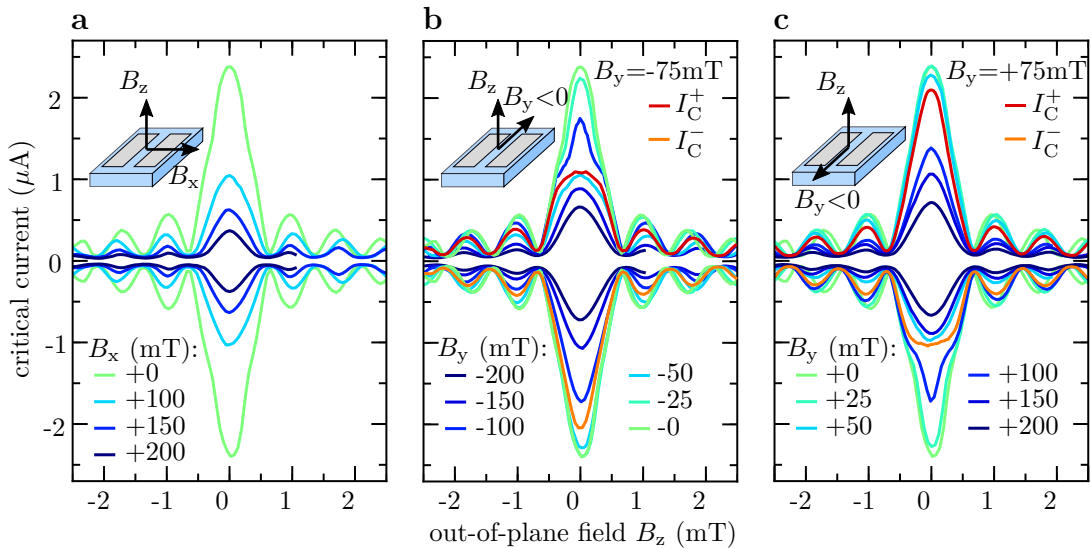
Figure 5.10: **Fraunhofer interference pattern** at different in-plane magnetic fields. **a,** B_x is parallel to the current direction and B_y is zero. **b,** Fraunhofer pattern for $B_\mathrm{y} < 0$ and $B_\mathrm{x}=0$. The asymmetry between the positive and negative critical currents reaches a maximum at $B_\mathrm{y}=$-75 mT and is highlighted in red and orange. **c,** The same graph as in panel **b,** but for positive fields in B_y. Temperature was fixed to $T=100$ mK for all measurements.

To get a complete overview, we again measured Fraunhofer interference patterns as we did in section 4.3. This time, however, with the coexistence of in-plane fields in

parallel and perpendicular directions. The current bias was swept from zero to finite positive or negative values, respectively. The voltage criterion for the critical current is 0.5 mV for the entire array.

As a reference, the green curve for B_x=0 mT is the same as in the previous chapter in section 4.3. Fig 5.10**a** shows that the application of an in-plane field in $\hat{x}$, i.e. parallel to the current, reduces the critical current and the induced gap likewise, but the symmetry between both current directions remains.

The figures 5.10**b** and 5.10**c** next to Fig. 5.10**a** clearly show an asymmetry between negative and positive critical currents. Here, the field is aligned parallel to $\hat{y}$. The curves for $B_y \simeq \pm 75$ mT are colorised in red and orange. The highlighted curves in 5.10**c** are again plotted in figure 5.11**a** as absolute values to emphasise the magnitude of the diode effect. Reflected in $\Delta I_c = I_c^+ - |I_c^-|$, the effect is mainly present in the inner half of the main lobe (see Fig. 5.11**b**).

Figure 5.11**c** and **d** show the rectification as a function of B_y at zero out-of-plane fields in absolute and difference values, respectively. The diode effect increases as expected linearly, but reaches a maximum at about $B_y \simeq \pm 75$ mT and decreases from that on until it is gone.

But why does the diode effect disappear? We see that both an out-of-plane field and an in-plane field suppress the effect. As we will see later, temperature is another way to remove the asymmetry between positive and negative critical currents.

Our phenomological explanation for the observation of the diode effect are higher order sine terms in the Fourier expansion of the CPR, which can be written as [154]

$$I(\varphi)/I_0 = a_0 + \sum_{n=1}^{\inf} [a_n \cos(n\varphi) + b_n \sin(n\varphi)], \tag{5.9}$$

where I_0 was determined in the previous chapter 4.1.1 as being 5.882 μA. It is important that the b_n coefficient is sizeable for n>1, otherwise the cosine contribution a_1 (only present in magnetic fields) will only cause an offset in the phase of the CPR, but no asymmetry between I_c^+ and I_c^-.

In chapter 4.3, it is described how a magnetic field in $\hat{z}$ affects the Beenakker-Furusaki formula (Eq. 2.64), which we used so far to analyse the CPR of our short-ballistic
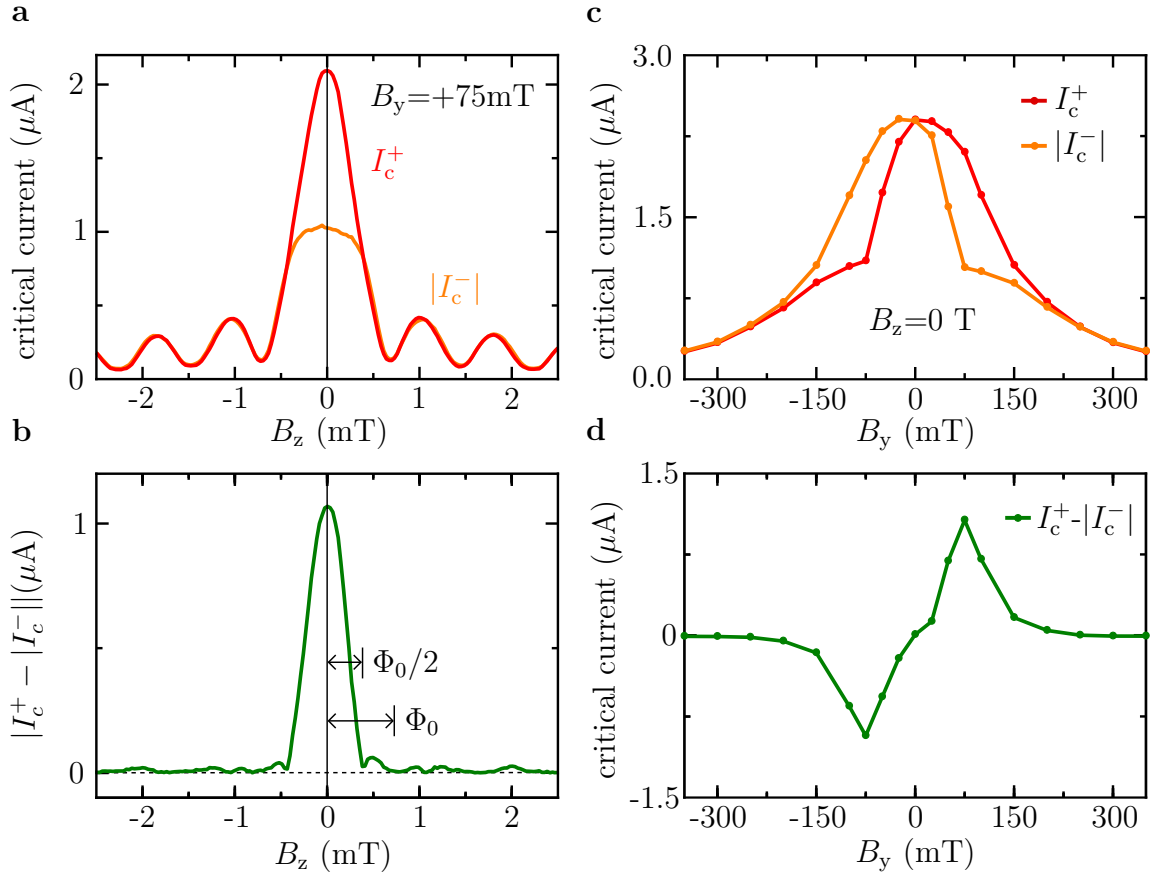
Figure 5.11: **Diode effect: a,** Illustrative comparison between I_c^+ and $|I_c^-|$ from the high-lighted curves in Fig. 5.10**c**, where the asymmetry is most pronounced. **b,** Corresponding $|\Delta I_c|$ from panel **a**. The diode effect mainly prevails in the inner half of the main lobe an gets suppressed for $\Phi_0/2 \simeq 0.37$ mT (see later in the text). **c,** B_y dependence of I_c^+ and $|I_c^-|$ at $B_z = 0$. **d,** Difference between I_c^+ and $|I_c^-|$ from panel **c**.

Josephson junctions. How the CPR evolves in B_z shows Fig. 5.12**a** for magnetic fields up to the first minimum in the Fraunhofer pattern. As expected, the maximum currents decrease within the main lobe as in Fig. 5.10**a**. Interestingly, a phase shift occurs at finite B_z. Since we just care about the sine terms in b_n, we substracted the phase offset. The following analysis was done by Nicola Paradiso.

Figure 5.12**b** displays the Fourier coefficients in zero field at $T=100$ mK, where the percentage in b_n decays exponentially with the order number of the harmonics. Therefore, we will focus on b_2 in relation to b_1, because the diode effect depends on the strength of the higher harmonics, which is mainly given by b_2.
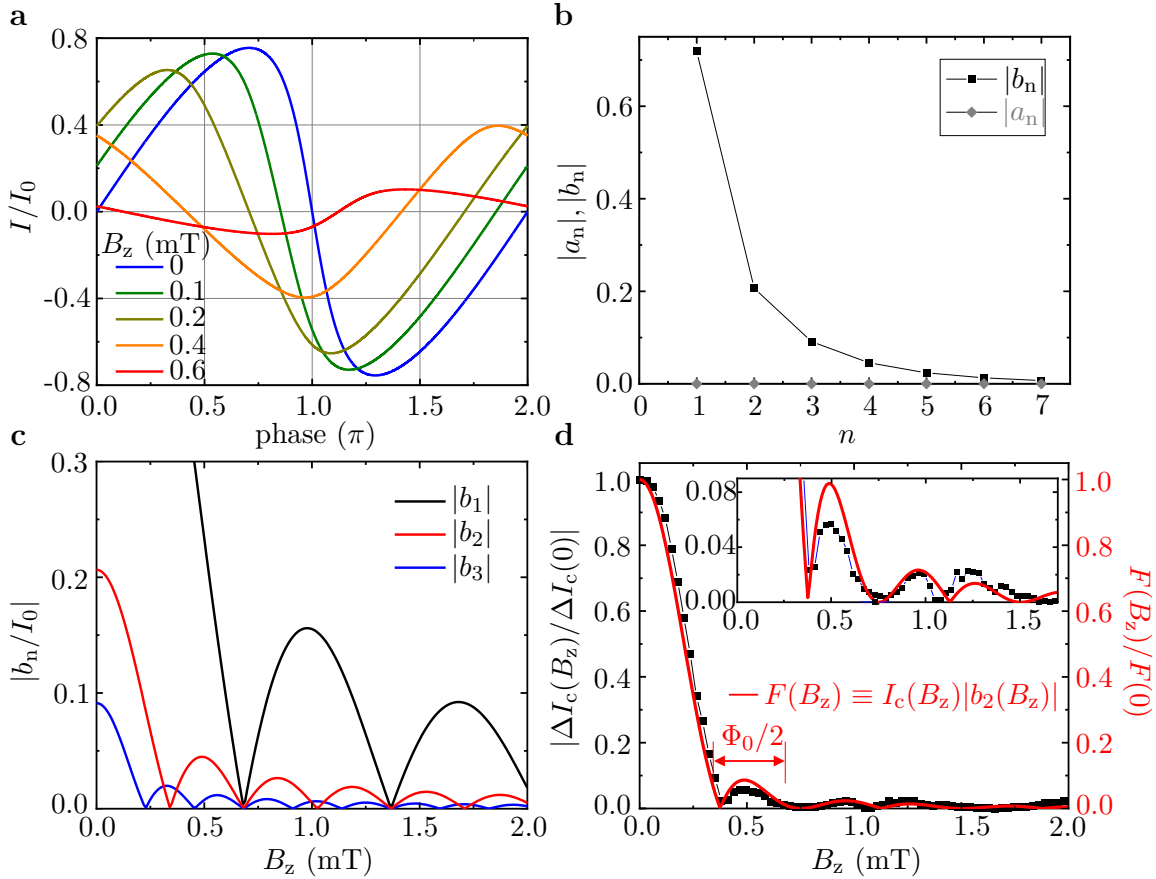
Figure 5.12: **Higher harmonics in B_z: a,** Calculated CPR for perpendicular magnetic fields up to the first minimum of the Fraunhofer pattern. Values are normalised by I_0. **b,** Fourier series coefficients a_n and b_n for the zero field CPR. **c,** Plotted interference pattern for the first three Fourier coefficients $b_{1,2,3}$ of the CPR. **d,** The black symbols show the difference between $I_c^+(B_z)$ and $|I_c^-(B_z)|$ as a function of B_z as in Fig. 5.11**b**, but normalised by $\Delta I_c(0)$. The red fit $F(B_z)$ is the product of $I_c(B_z)|b_2(B_z)|$. The inset is a zoom-in on the bottom part. Figures made by Nicola Paradiso.

Figure 5.12**c** shows the superconducting interference pattern in B_z for the first three Fourier coefficients in b_n, normalised to I_0. Here is vividly visible, that the minima of the n-th term are spaced by Φ_0/n. With this insight, it is possible to explain the $\Delta I_c(B_z)$ data in Fig. 5.11**b**, which is again plotted in Fig. 5.12**d** (black symbols). The red curve is the product of $I_c(B_z)$ and $b_2(B_z)$, which reveals a cusp-like (if b_n and $I_c = 0$) and quadratic (if only $b_2 = 0$) behaviour alternately. The red fit is stretched horizontally by 10 % in order to match the data points.

The periodicity of the higher harmonics explains quite well the evolution of the su-

perconducting diode effect with respect to the out-of-plane field B_z. But what about the in-plane field B_y and the temperature T? In this case we can again refer to the higher harmonics in the Fourier series.
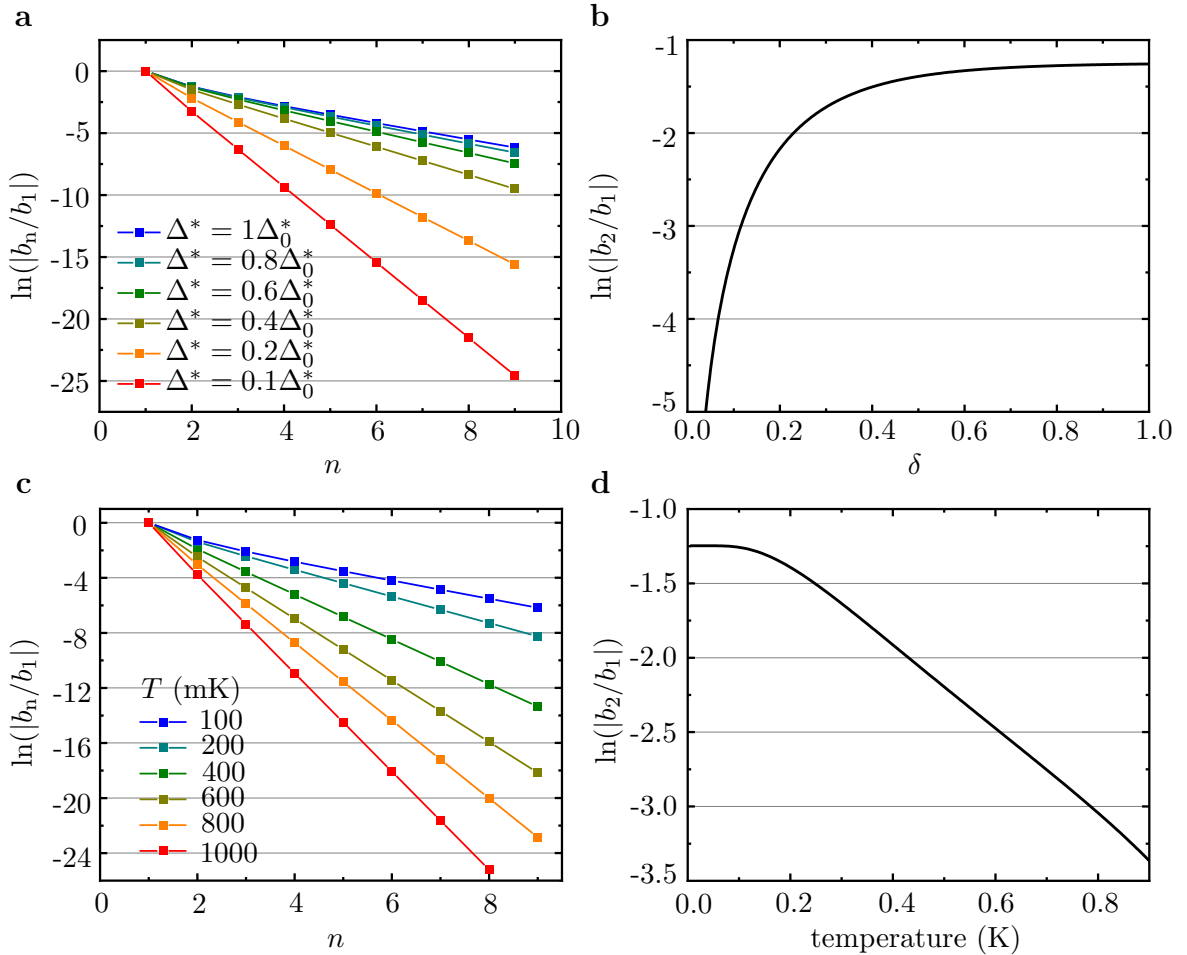
Figure 5.13: **Higher harmonics a,** of the sine Fourier coefficients for different pair-breaking values shown in a semi-log plot. **b,** Ratio b_2/b_1 plotted logarithmically as a function of $\delta = \Delta^*/\Delta_0^*$. **c,** Temperature dependence of the sine Fourier coefficients b_n. **d,** Corresponding T dependence of the natural logarithmic ratio b_2/b_1. Figures made by Nicola Paradiso.

In our heterostructure, an in-plane magnetic field weakens the induced gap by pair-breaking much more than it is the case for the superconducting gap of aluminium. For the suppression of the induced gap, we define the factor $\delta = \Delta^*/\Delta_0^*$. The question is what happens to b_n when one changes δ? The answer is presented in Fig. 5.13**a** on a semi-log plot, where the b_n coefficients are normalised by b_1. The blue curve corresponds to the curve presented in Fig. 5.12**b** and clarifies the exponential shape.

The logarithmic ratio between b_2/b_1 as a function of δ is shown in 5.13**b**. What we see is a moderate change of the ratio b_2/b_1 until Δ^* becomes comparable to $k_{\mathrm{B}}T$ (T=100 mK in our case). In other words, when the pair-breaking becomes to strong, higher harmonics vanish and the CPR reduces to a sine function and what remains is a φ_0-shift. This is what can be seen in the figures 5.11**c** and **d**, where the suppression of the induced gap Δ^* starts for $B_{\mathrm{y}} > 75$ mT.

For the disappearance of the diode effect with increasing temperature we can proceed similarly. Instead of the pair-breaking, we can control the temperature in the Beenakker-Furusaki formula and extract again the higher harmonics as depicted in the figures 5.13**c** and **d**. This time, however, $|b_2/b_1|$ decreases exponentially in T according to $|b_2/b_1| \cong e^{-\kappa T}$, with κ=2.8 K^{-1}. Panel **a** and **b** of Fig. 5.14 show experimental values of γ_{L} as a function of temperature. The figures 5.14**b** and **c** are normalised in the same fashion and demonstrate a good comparison.

a　　　　　　　　　　**b**　　　　　　　　　　**c**
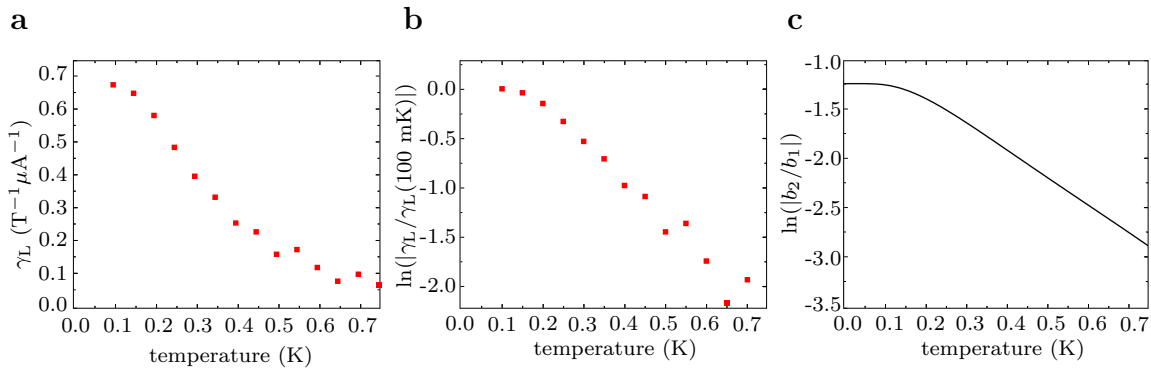
Figure 5.14: **Temperature dependence of higher harmonics: a,** Measured γ_{L} for different temperatures. **b,** Natural logarithmic of the values in **a** and normalised to γ_{L} (T=100 mK). **c,** Same graph as in Fig. 5.13**d**, but with adapted x-axis range. Figures made by Nicola Paradiso.

6 More on One-Dimensional Josephson Junction Arrays

Besides the superconducting diode effect and the magnetochiral anisotropy, we observed further physical properties in our one-dimensional JJA in the presence of in-plane magnetic fields. In addition to sample 1, which is described in chapter 4 and 5, we have fabricated sample 3, whose current direction is along the $[1\bar{1}0]$ crystal axis of the InAs. In this chapter, we present a comparison of L_0' between the two crystal orientations $[110]$ and $[1\bar{1}0]$, which allows us to determine the ratio of the Rashba and Dresselhaus components. Moreover, we observe in both samples a peculiar sign change of the magnetochiral anisotropy coefficient $\gamma_{\mathrm{L}}(B_{\mathrm{y}})$ for in-plane fields exceeding 200 mT. In addition, we determine the variation of the induced gap $\Delta^*(\vec{B}_{\mathrm{ip}})$ via the temperature dependent Josephson inductance. And finally, we present the in-plane field angle dependence of the Josephson coupling energies.

6.1 Disentangling Rashba and Dresselhaus SOI

For a conductor with pure Rashba SOI, the spin-split Fermi surfaces are isotropic. The situation changes for a finite Dresselhaus component β, as it is the case in our heterostructure. As discussed in the theory chapter 2.1.2, the Dresselhaus term causes anisotropic spin-orbit fields that are either enhanced or reduced with respect to pure Rashba in the $[110]$ and $[1\bar{1}0]$ directions. Figure 6.1**a** and **b** illustrate the different situations for sample 1 and sample 3, respectively.

In order to determine β, we performed $L(I)$ measurements to those of the previous chapter 5 for sample 3 (current flow in $[1\bar{1}0]$ as opposed to sample 1). The $L(I)$ curves in Fig. 6.2**a** show the same behaviour as it was the case for sample 1 (compare with Fig. 5.5), where the $L(I)$ curves become distorted when a magnetic field is applied in-plane at θ equal to 270° or 90°. Again, we extract the polynomial coefficients L_0, L_0'

a

Sample 1

$\beta < 0$

$[\bar{1}10]$

k_y

$+(\alpha - \beta)$

$-(\alpha + \beta)$

$[\bar{1}\bar{1}0]$ ——————— $[110]$

k_x

$+(\alpha + \beta)$

$-(\alpha - \beta)$

current

$[1\bar{1}0]$

b

Sample 3

$\beta < 0$

$[\bar{1}10]$

k_y

$+(\alpha - \beta)$

$-(\alpha + \beta)$

$[\bar{1}\bar{1}0]$ ——————— $[110]$

k_x

$+(\alpha + \beta)$

$-(\alpha - \beta)$

current

$[1\bar{1}0]$
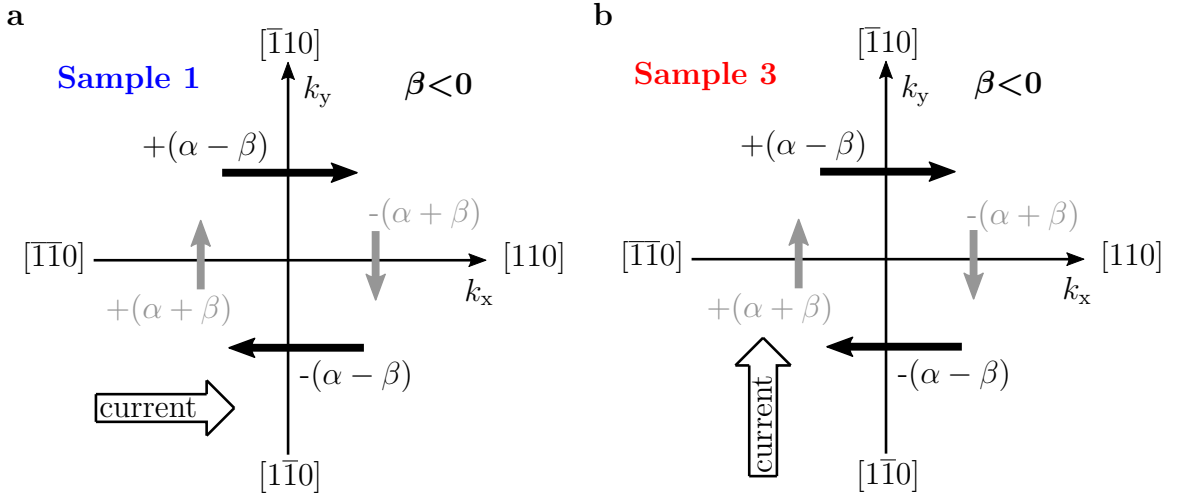
Figure 6.1: **SOI field:** Total spin-orbit fields (Rashba plus Dresselhaus) indicated by black and grey arrows for the corresponding $\vec{k}$-directions, where the current is **a,** horizontal (in direction [110]) for sample 1 and **b,** vertical (in direction [1$\bar{1}$0]) for sample 3.

and L_0'' by fitting the $L(I)$ curves approximately with a parabola at zero direct current.

The L_0 values of both samples (red and blue curves in Fig. 6.2**b**) indicate a good reproducibility of the fabrication process, because both samples have nearly the same L_0, when normalised by the corresponding Josephson junction widths.
In other words, the smaller inductance of sample 3 originates from a higher I_0, which in turn comes from a greater width of the Josephson junctions. The distinction in the widths between sample 1 and 3 is about 120 nm, which corresponds to a difference of 3%. Since the average transparency $\bar{\tau}$ of sample 1 and sample 3 are nearly equal (0.94 for sample 1 and 0.93[1] for sample 3), the width difference accounts for the different L_0 values of both samples (see Fig. 6.2**b**).

The MCA and thus the difference of the combined Rashba and Dresselhaus SOI is reflected in the zero-bias slope of the $L(I)$ curve, i.e. the L_0' coefficients, plotted in Fig. 6.2**c**. From the small but clearly discernible differences in L_0' for sample 1 and 3, we deduce the ratio $r = \frac{L_0'(sample\ 3)}{L_0'(sample\ 1)} = 0.854$.
A value r unequal to 1 implies a finite Dresselhaus term β. Numerical quantum transport simulations, performed by A. Costa using the KWANT package and the

---

[1]Obtained by an analysis analog to that in section 4.1.1.
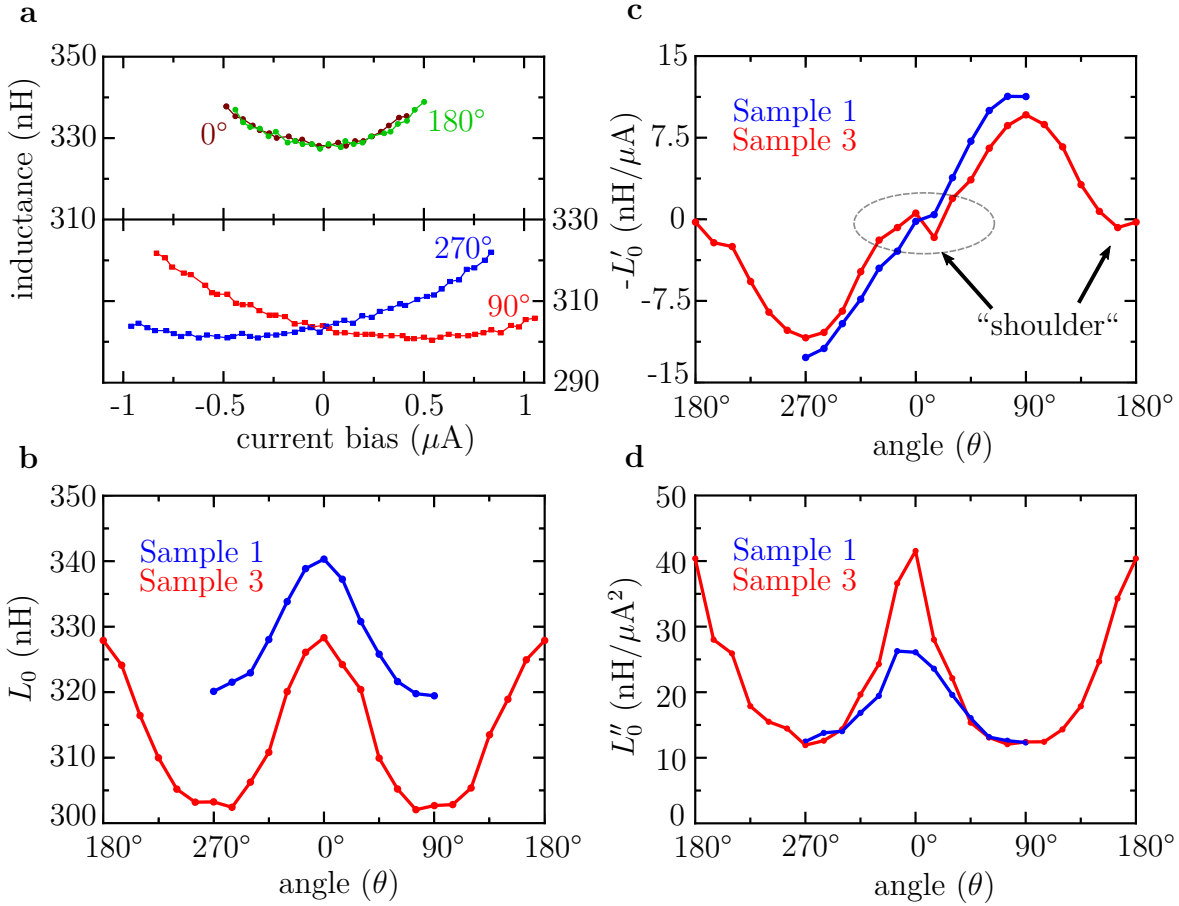
Figure 6.2: **$L(I)$ data: a,** obtained from sample 3 at $\vec{B}_{\mathrm{ip}}$=+100 mT and T=100 mK. **b,** Constant term L_0 for sample 1 (sample 3) in blue (red) as a function of θ. **c,** The corresponding linear part L_0' and **d,** the quadratic part L_0''.

methodology discussed in Ref. [32], revealed that $r(\beta)$ is given by [155]

$$r \approx 1.004 - 0.225|\beta|, \tag{6.1}$$

with β in units of meV nm. Solving $\beta(r)$, we obtain a Dresselhaus paramter of β=-0.67 meV nm, which is in agreement with the $\vec{k}\cdot\vec{p}$ simulations from P. E. Faria Junior, shown in Fig. 2.5 in section 2.1.2.

Another feature we observed in Fig. 6.2**c** is a shoulder in $L_0'(\vec{B}_{\mathrm{ip}})$ at θ=0° and 180°. Interestingly, the shoulder is less pronounced for sample 1, where the current direction is along [110]. Figure 6.2**d** shows the quadratic coefficient L_0''. In case of sample 3, the quadratic part varies much more, when the 100 mT in-plane magnetic field is applied

in $\hat{x}$ (θ=0°).
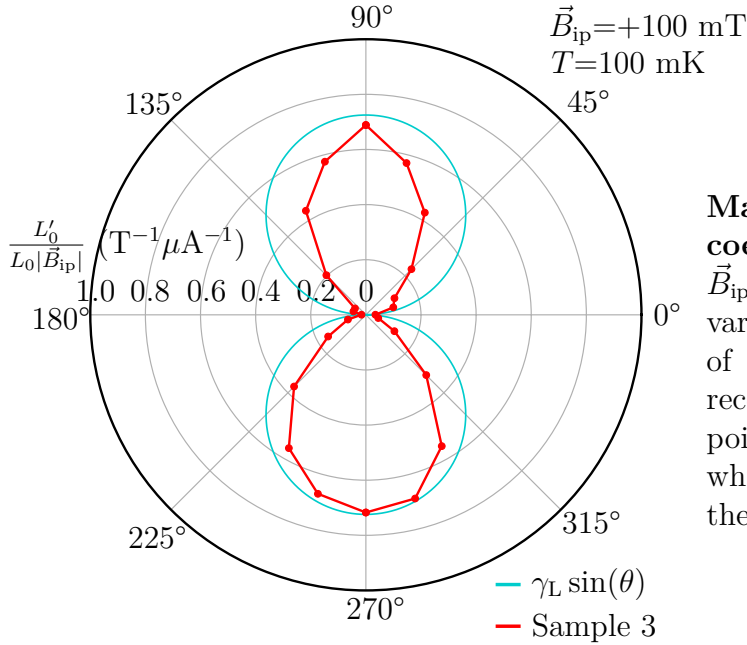
Figure 6.3

Magnetochiral anistropy coefficient $\boldsymbol{\gamma_L}$: Measured at $\vec{B}_{ip}$=+100 mT for sample 3 for various angles θ. A difference of the absolute values of γ_L is recognisable between the red data points and the blue sine curve, which emphasises the breaking of the C_{2v} symmetry.

A further interesting observation is a difference of the absolute values between $\gamma_L(\theta = 90°)$ and $\gamma_L(\theta = 270°)$ in the case of both samples 1 and 3. The polar plot of Fig. 6.3 displays the from Fig. 6.2 corresponding γ_L values. Sample 3 clearly shows a difference of the magnitude of the magnetochiral anisotropy between the angles around 90° and 270°. For these data we could exclude a dc-offset current as a possible cause of the asymmetry, as the current bias was directly measured. For sample 1 we have not measured the current bias directly.

The same asymmetry discussed here can be seen in the Fig. 5.6b for the linear part and in Fig. 5.7 for γ_L for different gate voltages. For three-terminal Josephson junctions (discussed in chapter 7.5.2), we will see a similar deviation from the expected C_{2v}-symmetry, which is there reflected in the critical currents.

A plausible explanation of a breaking of the C_{2v}-symmetry may result from the interface between the Al and the InAs. The aluminium has a fcc [111] lattice, which in combination with the [001] facet of the InAs breaks C_{2v}-symmetry [156]. Lorenz Fuchs discusses in his thesis [126] an interface spin-orbit texture originating from the Al/GaAs interface that is different from that of the InAs alone.

6.2 Sign Changes in Magnetochiral Anisotropy

According to the heuristic expression of the MCA for the Josephson inductance (Eq. 5.8), γ_L is expected to increase linearly with the magnetic field. To test this relationship, we measured the MCA for the inductance as a function of B_y for sample 1 and sample 3. Interestingly, we observe the expected linearity in B_y only up to about
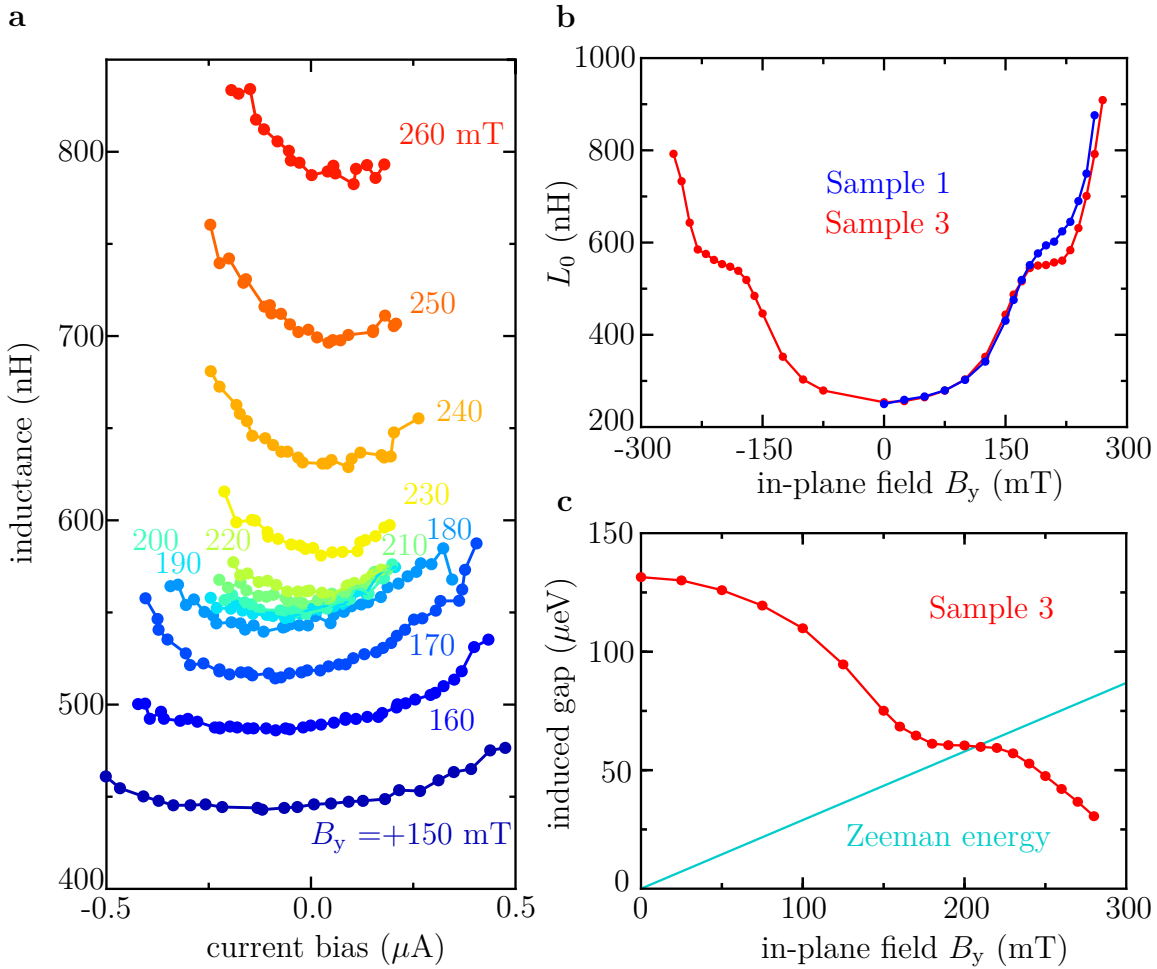
Figure 6.4: **Anomaly in $L(I)$ curves: a,** Measured $L(I)$ curves from sample 3 at in-plane magnetic fields applied perpendicular to the current direction (i.e $\theta=270°$). **b,** Extracted constant term L_0. **c,** Induced gap and Zeeman energy as a function of B_y. At $B_y \simeq +200$ mT, the via L_0 calculated induced gap matches with the Zeeman energy by considering a realistic g-factor of 10.

$B_y = \pm 150$ mT. The inspection of the measured $L(I)$ curves, plotted in Fig. 6.4**a**, shows an accumulation of traces around $B_y = +200$ mT and in addition, the tilt of the traces changes direction, which is connected to a shift of the inflection point from

negative to positive current bias.

The corresponding zero-bias part L_0 of the $L(I)$ curves is presented in Fig. 6.4**b**. For both samples, L_0 increases steadily and shows a plateau around $B_y \simeq +200$ mT, which reflects the observed accumulation of the $L(I)$ curves. This plateau appears in a specific B_y range, exactly when the Zeeman energy E_z and the via L_0 calculated induced gap Δ^* coincide (see Fig. 6.4**c**). If we assume that B_y affects the CPR solely via the induced order parameter $\Delta^*(B_y)$, we can extract the variation the induced gap Δ^* as a function of B_y from L_0 by using the equations 2.62 and 4.2, that is

$$L(\varphi) = \frac{V}{\frac{dI}{dt}} = \frac{\Phi_0}{2\pi I_0 f'(\varphi)} \quad \Rightarrow \quad I_0 = \frac{\Phi_0}{2\pi L_0 f'(0)}$$

and

$$I_0(V_g) = \frac{e\Delta^*}{\hbar} N(V_g) \quad \Rightarrow \quad \Delta^* = \frac{\hbar}{e} \frac{I_0(V_g)}{N(V_g)}.$$

For this approach, we in particular assumed that the average transmission coefficient $\bar{\tau}$ and the number of ABS channels $N(V_g)$ are independent of B_y. The plotted Zeeman energy in Fig.6.4**c** (cyan curve) was calculated with a g-factor of 10.

The extracted linear part L_0' is presented in Fig. 6.5**a** and shows the expected linear increase up to $B_y \simeq +150$ mT. Then comes a peak at $B_y = +190$ mT, followed by a strong decrease with a sign change of L_0' at $B_y=+220$ mT. For in-plane fields close to $+300$ mT, L_0' bounces back from the minimum at $+240$ mT towards zero. Further L_0' values for higher fields could not be obtained, because the Q-factor of the resonator was too strongly suppressed by the weakest link in the Josephson junction array.

The L_0' part of sample 3 reveals a deviation from point symmetry with respect to B_y. According to the phenomenological equation of the MCA for the inductance (Eq. 5.8), one would expect a point-symmetric relation through zero between $L_0'(B_y < 0)$ and $L_0'(B_y > 0)$. But, what we observe is that the $L_0'(B_y)$ values are point-symmetric only up to $B_y \simeq \pm 150$ mT. For higher (lower) in-plane fields, the linear coefficients differ from each other. Especially the dip of L_0' at $B_y=$-220 mT is with 150 nH/μA more than a factor of 3 bigger than the peak of L_0' at $B_y=+180$ mT. In contrast, the following peak at $B_y=$-250 mT is in absolute values smaller then the complementary dip at $B_y=+260$ mT.

If we decompose the $L_0'(B_y)$ data into an even and odd part (see Figs. 6.5**b** and **c**),

we cleary see that Eq. 5.8 loses its validity for $B_y \geq 150$ mT. The even part in panel **b** is approximately zero up to $B_y \simeq \pm 150$ mT, but starts then to have a peculiar course by going up, then down with a sign change and reaching a minimum at B_y=-220 mT. Then, the even part of L_0' goes up and down again.

The odd part of L_0' in panel **c** is nearly linear up to $B_y \simeq \pm 150$ mT, shows then a dip/peak at B_y at ± 220 mT, followed by a sign change and does then not bounce back again at higher B_y. The even part of L_0' could be a consequence of the broken C_{2v} symmetry (discussed at the end of section 6.1). For completion, Fig. 6.5**d** shows
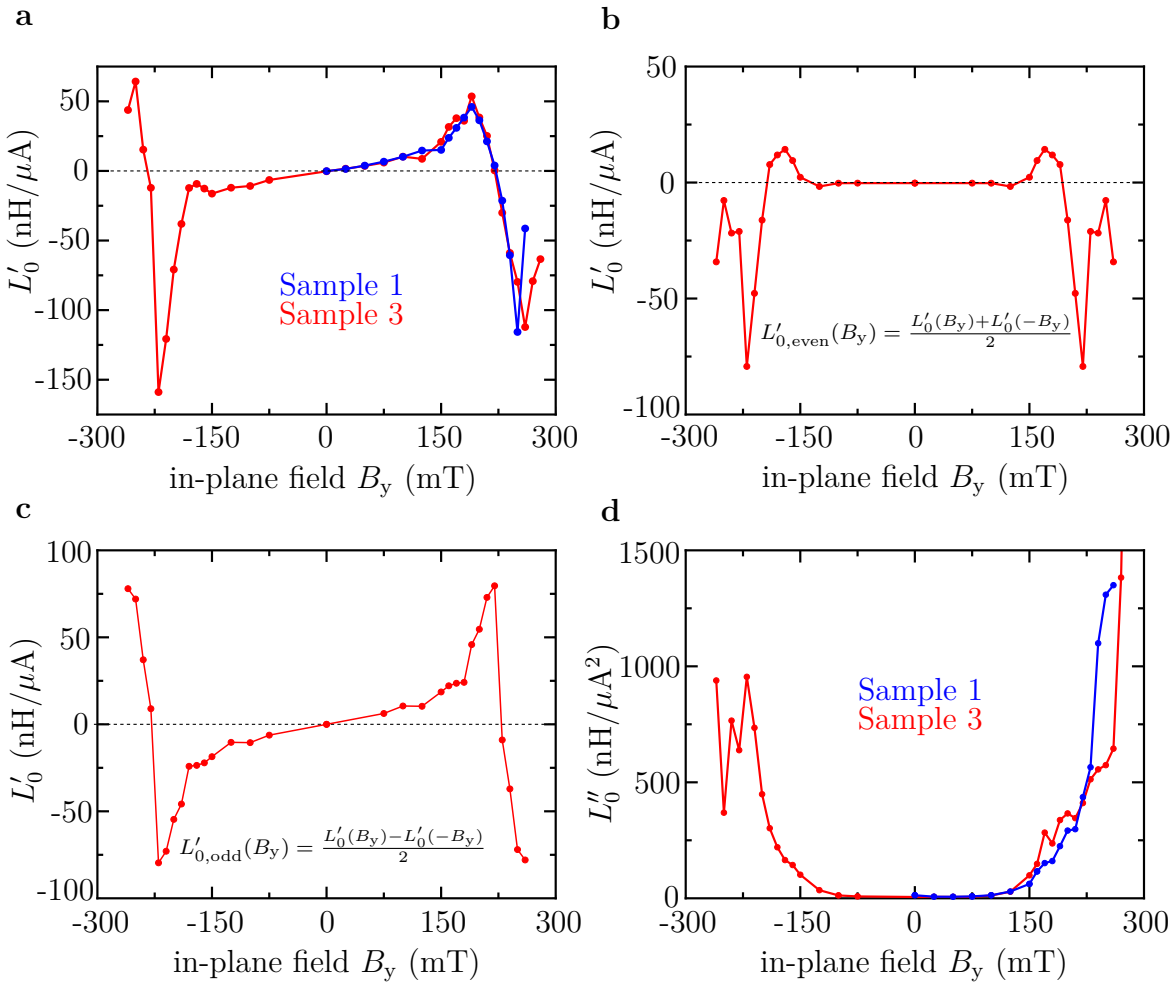
Figure 6.5: **Linear and quadratic coefficients** as a function of B_y. **a,** Linear part of sample 3 extracted from the $L(I)$ curves in Fig. 6.4**a**. **b,** Even and **c,** odd part of L_0'. **d,** Quadratic part of the $L(I)$ curves from the data shown in Fig. 6.4**a** and of data from sample 1.

the corresponding quadratic coefficient L_0'' of sample 1 and 3 of the data presented

in Fig. 6.4. The values of the quadratic term become inaccurate at higher in-plane magnetic fields, because the weaker Josephson junctions produce kinks in the $L(I)$ curves (see section 4.1.1), which can have a drastic impact on the L_0'' coefficient.

To date, we cannot provide a physical explanation for the plateau in the $L_0(B_y)$ and for the sign change in the $L_0'(B_y)$ data. This anomalous behaviour seems to be very robust as it was measured in two samples independently. Further KWANT simula-
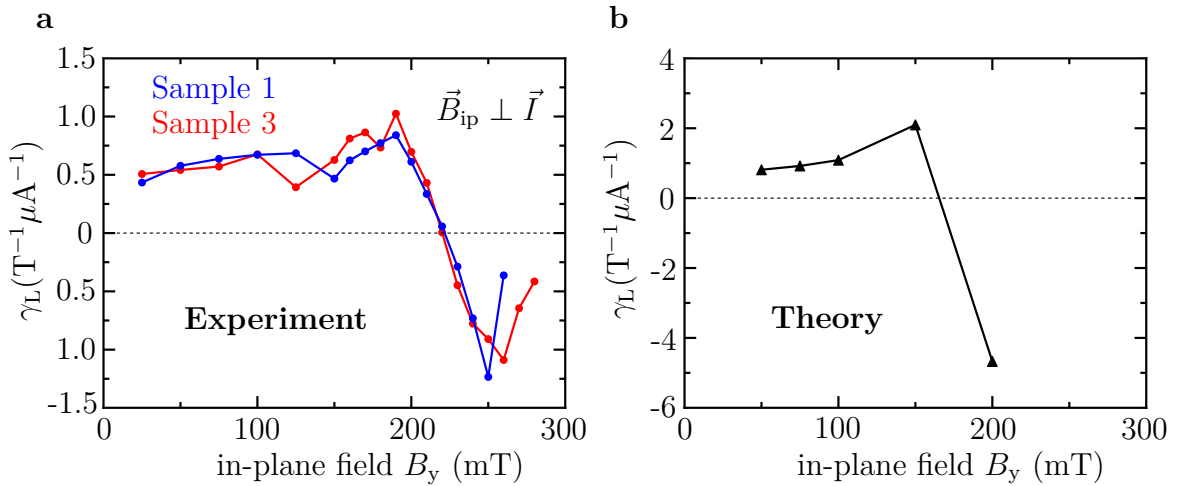
Figure 6.6: **Sign change reflected in γ_L: a,** Experimental obtained MCA coefficient γ_L plotted as a function of B_y. **b,** Corresponding computed γ_L from transport simulations performed with the help of the KWANT package. Since the simulation was fed with approximated parameters, the theoretical result is supposed to show a qualitative agreement.

tions by Andreas Costa show likewise the sign change of the MCA coefficient γ_L. The experimental and theoretical values of γ_L are plotted in figure 6.6**a** and **b**, respectively. Surprisingly, in the numerical simulation the sign change of γ_L exists also for vanishing SOI and depends on the Zeeman energy E_z only [A. Costa priv. comm.]. For the simulation, the setup from the previous chapter 5.3 was used, i.e. a g-factor of 10 and a confinement potential of 200 meV[2]. In addition, the simulation used the experimental determined values of the induced gap $\Delta^*(B_y)$ shown in Fig. 6.4**c**.

But what does this sign change of γ_L actually mean? Is it a topological transition which is predicted to occur when the induced gap has the same magnitude as the Zeeman energy in the case of low electron densities, as mentioned in Ref. [157]? Or

---

[2]also described in the supplement of Ref. [32]

does it simply reflect a 0-π transition in the CPR, which was a hint of a topological transition, as it was experimentally reported in a comparable system by M. Dartiailh et al. in Ref. [81]? In the latter case, a 0-π transition should be accompanied by a closing and reopening of the induced gap. Therefore, a minimum in the critical current should be visible. Furthermore, this effect should be highly anisotropic in $B_{\mathrm{ip}}(\theta)$ [80].

If we take a look at the in-plane field dependence of the critical currents, shown in the Figs. 6.7**a** and **b**, we observe a drastic difference of I_c between $B_\mathrm{x}(\theta =0°)$ and $B_\mathrm{y}(\theta =270°)$. Like in the inductance measurements[3], the I-Vs confirm the higher robustness of the superconducting state against magnetic fields applied perpendicular to the current direction in the plane.
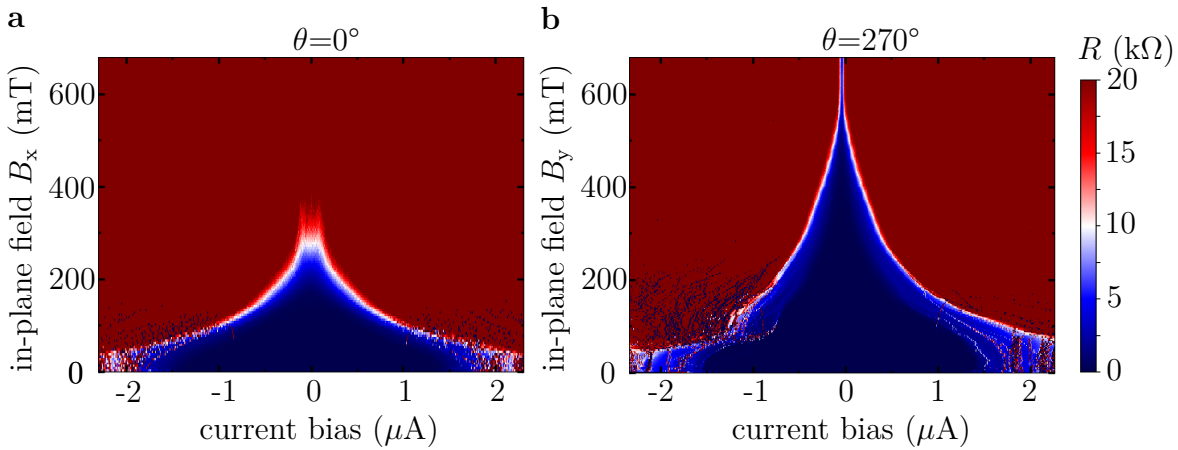
Figure 6.7: **Critical current evolution for finite in-plane fields** applied in the directions **a,** $\theta=0°$ and **b,** $\theta=270°$. The supercurrent shows a high anisotropic behavior in $B_{\mathrm{ip}}(\theta)$. Data obtained from sample 3.

A possible explanation for the difference in $I_\mathrm{c}(B_{\mathrm{ip}}(\theta))$ could be the distinct effective cross-sectional areas of the 2DEG, which are exposed to the in-plane magnetic field. In case of B_x, a larger part of the 2DEG is susceptible to the magnetic field per aluminium island and thus the suppression of Δ^* is higher than for an applied B_y. However, a minimum in I_c cannot be detected in Fig. 6.7**b** at the first glance. But if we change the scaling of the resistance on the z-axis, a peculiar course of the critical current appears. The transition from the superconducting to the resistive state starts to smear out for magnetic field above 200 mT and a waist appears at $B_\mathrm{y} \simeq 600$ mT.

---

[3]see the angle dependence of L_0 in Fig. 6.2

$\theta = 270°$
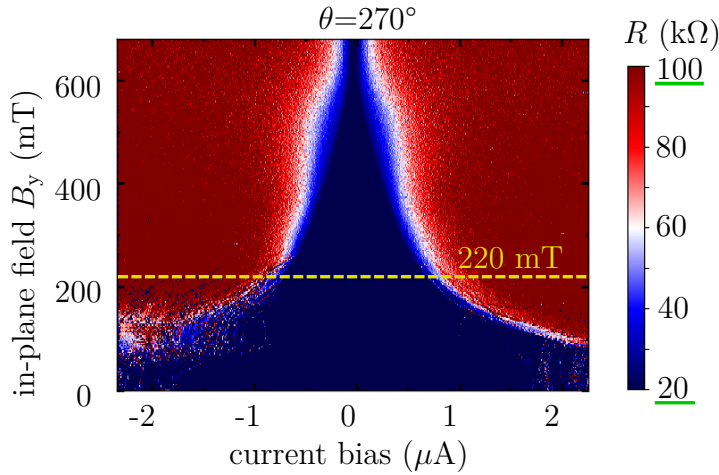
Figure 6.8

A different scale of the z-axis of Fig. 6.7**b** reveals a blurred critical current from $B_y \simeq +220$ mT on to higher fields of the ensemble of 2250 Josephson junctions in series.

At $B_y \simeq 600$ mT, M. Dartiailh et al. [81] observe the reported minimum of the critical current in a single Josephson junction.

Since we measure the accumulated resistance of 2250 Josephson junctions in series, this could mean that the individual criticial currents begin to spread out as the in-plane field increases. The main reason for this spreading comes from the out-of-plane magnetic field B_z, which is not perfectly homogeneous over the lengthscale of 3 mm of our Josephson junction array in contrast to the in-plane field $\vec{B}_{ip}$ (also discussed by L.Fuchs [126]). Therefore, the out-of-plane field cannot be optimally nulled at the outer parts of the array with our home-made compensation coils. However, whether the waist in Fig. 6.8 is related to a closing and opening the gap is questionable and cannot be answered within the scope of this work.

For a further analysis of the sign change of the supercurrent diode effect, we extracted the critical currents from Fig. 6.7**b**, calculated the difference $\Delta I_c(B_y) = I_c^+(B_y) - |I_c^-(B_y)|$ and plotted the result together with the obtained $\Delta I_c(B_y)$ from sample 1 (already shown in Fig. 5.11**d**) in figure 6.9. In this figure, $\Delta I_c(B_y)$ is normalised by $I_c(B_y = 0)$, because the critical currents of sample 1 and 3 differ due to individual defects, which are the reason for weaker junctions that start to heat the entire array at different currents. Thus, the critical currents of sample 1 and 3 differ. The insert in Fig. 6.9 shows a zoom-in of $\Delta I_c(B_y)$ for higher B_y and reveals a sign change of $\Delta I_c(B_y)$ for $B_y \simeq 270$ and $\simeq 330$ mT for sample 1 and 3, respectively. What we do not see in our data is an oscillating $\Delta I_c(B_y)$ around 0. However, during the measurement sessions we did not focus on obtaining the critical currents at high B_y. That is why the red curve (sample 3) becomes so fuzzy, which is due to the low amount of data points in the *I-V*s.
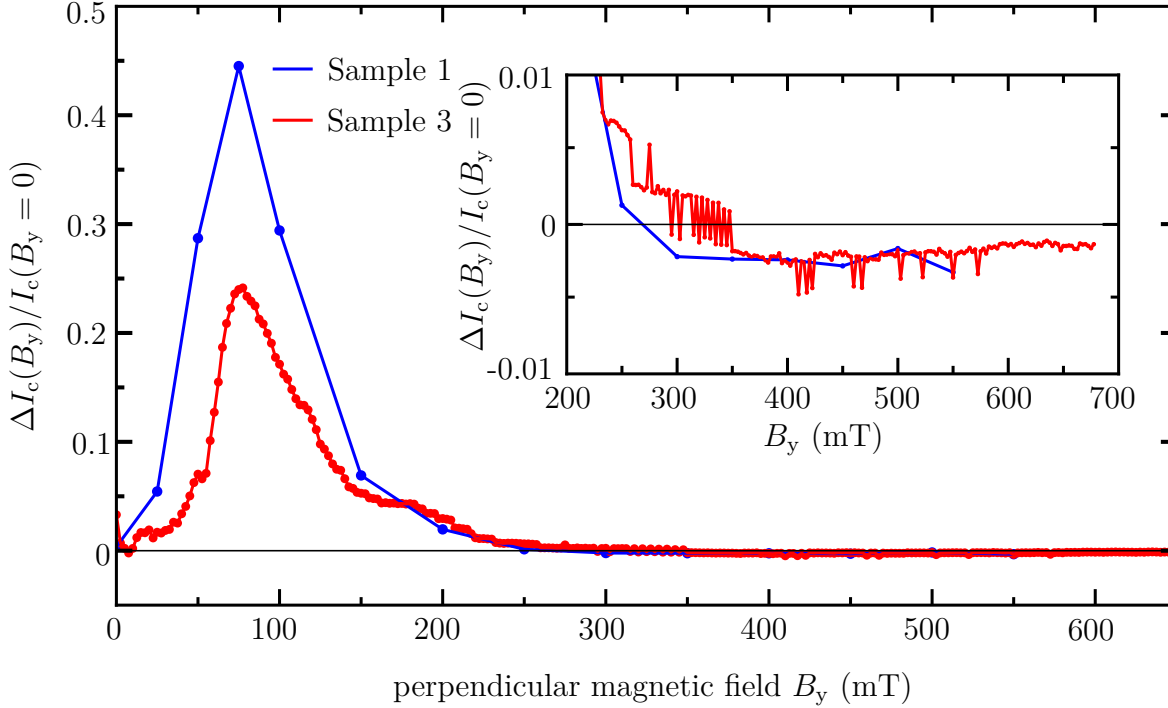
Figure 6.9: **Superconducting diode effect** in the critical currents as a function of B_y. Both samples show a sign change at higher fields, i.e. $B_y \simeq 250\text{-}350$ mT.

In order to further trace the angle dependence of the sign change of L_0', we performed in addition $L(I)$ measurements for in-plane fields in the directions 0° and 300°. The $L(I)$ curves, presented in the Figs. 6.10**a** and **b**, show no accumulation or a clear change of the tilt. The constant part L_0 in Fig. 6.10**c** shows no plateau. The linear part L_0' in Fig. 6.10**d** shows no clear sign change, but the extracted L_0' oscillate around zero with a huge error bar, because the data is difficult to fit accurately for higher in-plane fields. Furthermore, due to the reduced range in $\vec{B}_{\text{ip}}$, where we can access the Josephson inductance, we cannot clearly state that the sign change is anisotropic with respect to $\vec{B}_{\text{ip}}(\theta)$.

Recently, B. Pal et al. [158] and A. Daido et al. [159] reported about a sign change of the superconducting diode effect. B. Pal et al. observe this sign change in the difference of the critical currents and relate this behaviour to finite-momentum Cooper pairing derived from spin-helical topological surface states in their $NiTe_2$ device. In our case, the Josephson junction arrays with the InAs quantum well should not possess any spin-helical topological surface states. However, we also observe a sign change
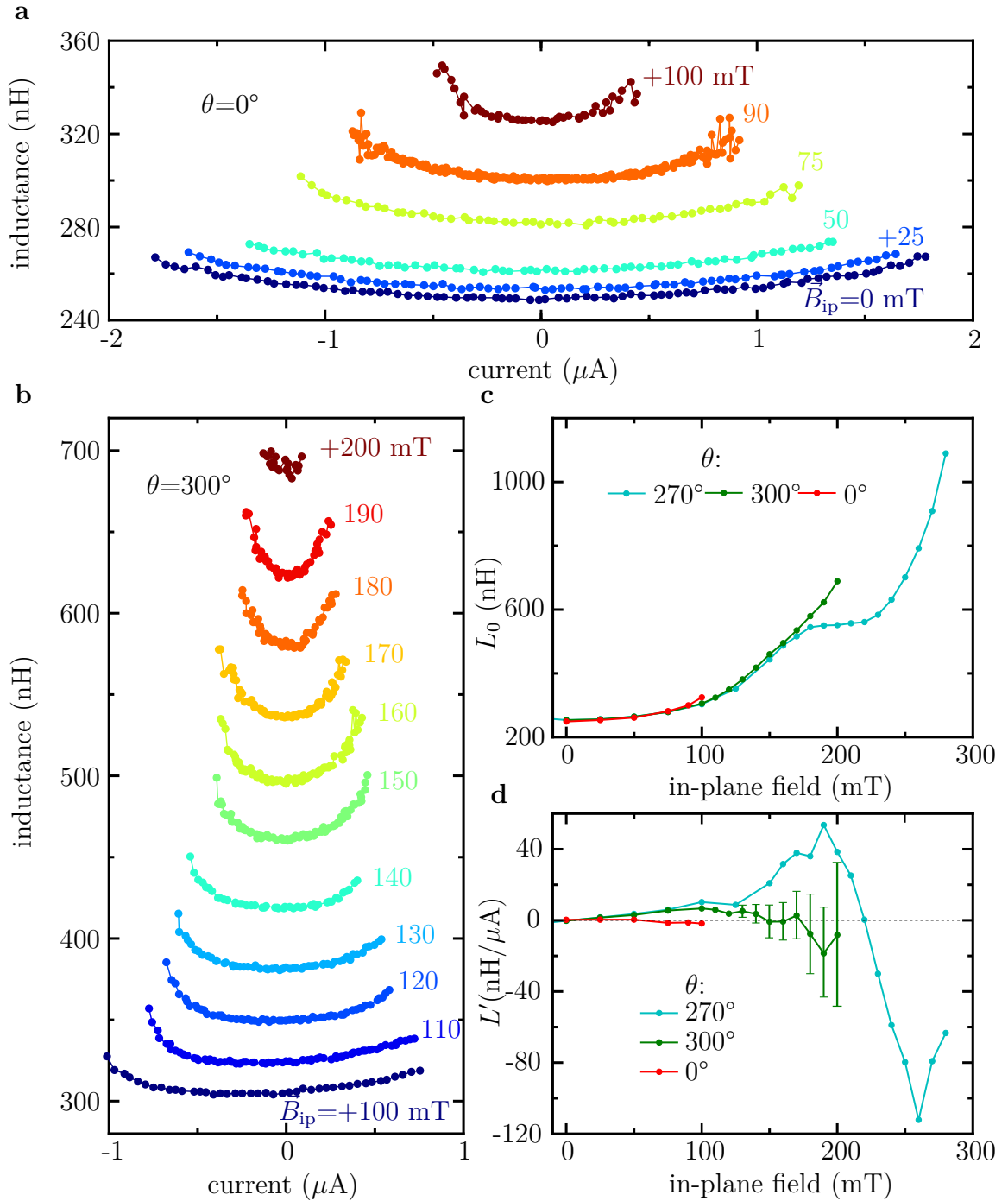
Figure 6.10: **Anisotropy in $\vec{B}_{ip}(\theta)$: a,** and **b,** show the $L(I)$ curves for different in-plane fields applied along 0° and 300°. The corresponding L_0 and L'_0 data are plotted in **c,** and **d**, respectively, together with the data obtained for $\theta = 270°$.

in the difference of the critical current, but no oscillations so far. In our devices, the

difference $\Delta I_c(B_y)$ is very small at higher B_y, due to the suppression of the higher harmonics in the current-phase relation by B_y.

Another interesting experiment for the investigation of the sign change of γ_L is to study a similar device like sample 1 or 3 again, but this time based on a heterostructure with InSb as the quantum well. In such a heterostructure, the SOI field is much higher and highly anisotropic with respect to the crystal lattice of the 2DEG due to the high Dresselhaus component [82]. Measuring $L(I)$ curves as a function of B_y for two different crystal orientations would reveal whether there is really no dependence of the sign change of L_0' on the spin-orbit field and could thus give a hint about topological states or not [160].

6.3 Peculiar Temperature Dependence of the Induced Gap at Finite In-Plane Fields

In the previous section, we have calculated the induced gap on the basis of L_0 with the assumption that $\bar{\tau}$ and $N(V_g)$ stay constant with increasing in-plane magnetic fields (compare with Fig. 6.4**c**). A different approach to extract Δ^* is by measuring the temperature dependence of $L(I = 0)$. We discussed this procedure already in section 4.1.1 for zero $\vec{B}_{ip}$. Fitting the $L(T)$ data at low temperatures with the help of the Furusaki-Beenakker equation 2.64, plus the Eq. 2.67 [4], allows us to extract the induced gap Δ^*.

Figure 6.11**a** and **b** show $L(T)$ curves for different in-plane magnetic fields applied in the directions 0° and 270°, respectively. The red lines indicate the applied fits.

What we see again is the higher robustness of the Andreev bound states against fields applied perpendicular to the array's orientation, expressed by the smaller Josephson inductance for the same magnitude of the magnetic field compared to the parallel configuration.
Furthermore, in the 270° direction we can access $L(0)$ for higher fields which in turn reveals a peculiar curve at $B_y=+150$ mT, highlighted by red arrows in figure 6.11**b**. In this curve, the $L(0)$ values increase less with temperature compared to the other

---

[4]This equation describes the relation between the superconducting gaps of the InAs and of the Al via γ_B. As we did in section 4.1.1, we set Δ_{Al} to 220 μeV.

a

b
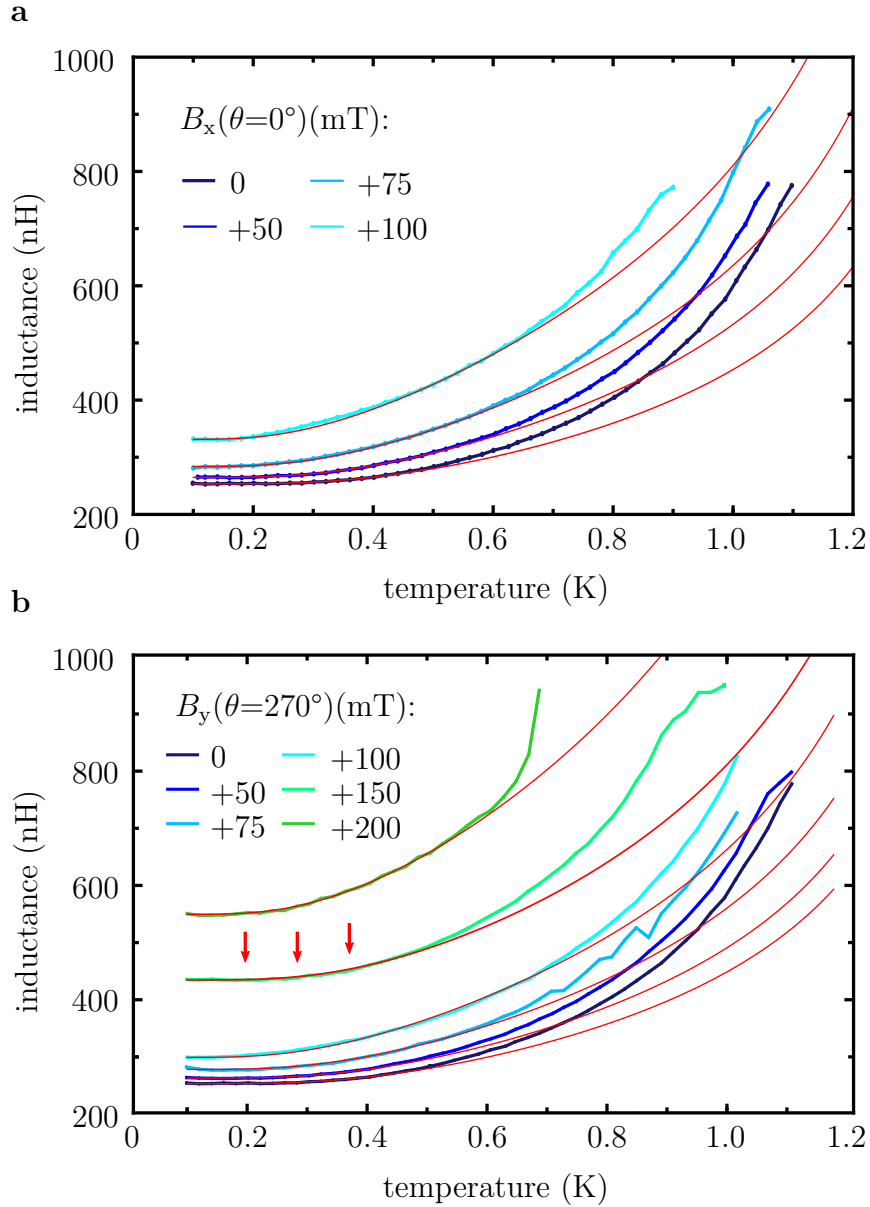
Figure 6.11: $\boldsymbol{L(I=0)}$ **vs** $\boldsymbol{T}$: Temperature dependence of the obtained Josephson inductance at zero current for different in-plane magnetic fields applied parallel **a,** and perpendicular **b,** to the array's orientation. The red lines show the applied fits. It was tried to match the data at low temperatures. Measurements performed on sample 3.

curves, i.e. for B_y=+100 or +200 mT.

This different behaviour of the $L(T, B_y$=+150 mT) curve leads to a puzzling fit result of the dimensionless parameter γ_B, shown in Fig. 6.12**a**. For the fitting routine, γ_B

was the only free parameter and Δ_{Al} was set to 220 μeV, as we did in section 4.1.1. Because a lower γ_{B} implies a higher Δ^*, the in Fig. 6.12**b** plotted corresponding induced gap Δ^* in red and blue shows this anomalous dependence in B_{y} too. For completeness, figure 6.12**b** shows the induced gap Δ^* calculated from solely $L(0, T = 100 \text{ mK})$ values (light blue and orange curve).
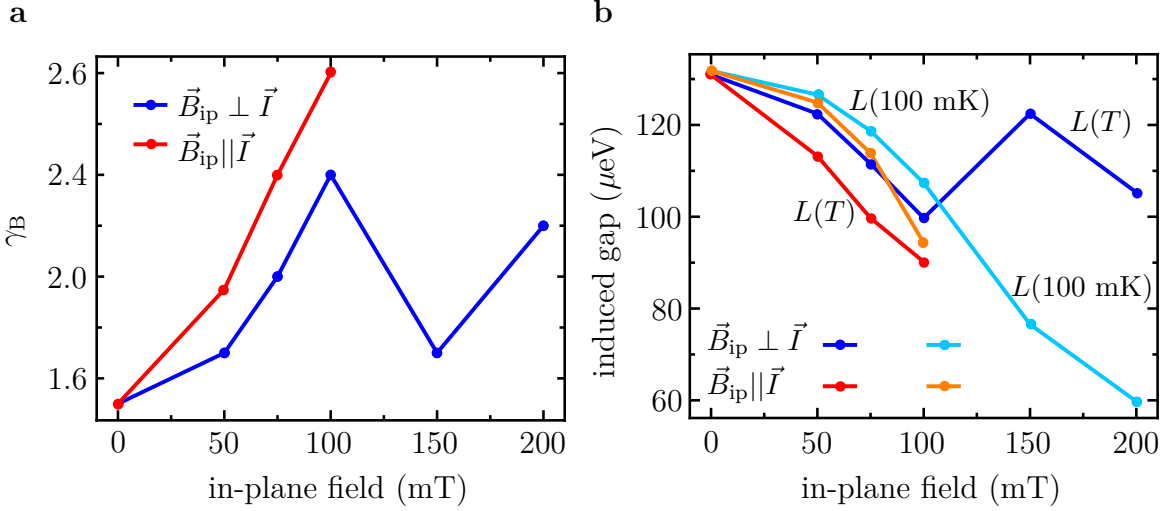
Figure 6.12: **Barrier strength $\gamma_{\mathbf{B}}$ and the related induced gap Δ^*** as a function of $\vec{B}_{\mathrm{ip}}$. The data points are obtained from the raw $L(T)$ data presented above in Fig. 6.11. The light blue and orange points, shown for comparison reasons, are determined from the same dataset by taking the $L(0)$ points at $T{=}100$ mK. As in Fig. 6.4**c**, the average transparency and the number of channels were assumed to stay constant for the calculation of the induced gap Δ^* via L_0.

The figure 6.12**a** (6.12**b**) shows a continuous increase (decrease) of γ_{B} (Δ^*) up to $\vec{B}_{\mathrm{ip}} \simeq 100$ mT. Then follows the deviation with a drastic decrease (increase) of γ_{B} (Δ^*).

Since we assume that $N(V_{\mathrm{g}})$, $\overline{\tau}$ and Δ_{Al} stay constant with increasing $\vec{B}_{\mathrm{ip}}$ and temperature T and the magnetochiral anisotropy for supercurrents as well as the sign change of L'_0 (discussed in the previous section 6.2) are not considered in the fitting model, the evaluation of γ_{B} and Δ^* with the help of Aminov's equation 2.67 and the Beenakker-Furusaki equation 2.64 seems to have reached its limits for $B_{\mathrm{y}} \geq 100$ mT. However, the intention of this section is to show this divergent increase of the $L(T)$ curves at $B_{\mathrm{y}} \geq 150$ mT. Further measurements of the $L(T)$ curves for different B_{y} are favorable for an analysis which could lead to a conclusion.

6.4 Activation and Josephson Energy

In section 5.3, we discussed the anisotropy of L_0' with respect to the external in-plane field for different angles, which mainly determines the MCA coefficient γ_L. In addition, we observed a smaller but still recogniseable anisotropy in L_0 (in Fig. 5.6). Because L_0 is linked to the critical current I_c, we expect an anisotropic Josephson energy $E_\mathrm{J} = \hbar I_\mathrm{c}/2e$, which in turn leads to an anisotropic activation energy for thermal phase slips in the Josephson junctions.

If we recall the model of the tilted potential from section 2.3.2, the activation energy E_A is the energy the particle needs to surpass the potential barriers. Here, a finite voltage appears and the junctions gradually become more and more resistive. A convenient method to obtain the activation energy E_A is to measure the temperature dependent resistance around T_c.
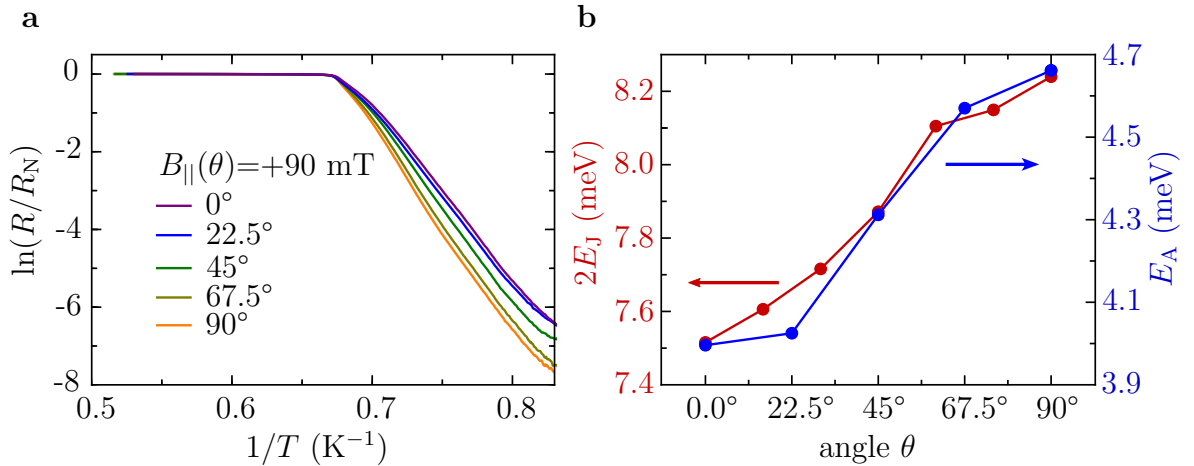
Figure 6.13: **Angle dependence of $E_\mathbf{A}$ and $E_\mathbf{J}$: a,** Arrhenius plots of the $R(T)$ curves obtained at $\vec{B}_\mathrm{ip}=+90$ mT applied at different angles θ. **b,** Corresponding activation and Josephson energies. The latter was calculated from L_0. All data shown here are from sample 2.

We measured $R(T)$ using standard low-frequency lock-in techniques. With a integration time of 75 ms at 21 Hz and a 1 MΩ preresistor defining 20 nA current bias, we obtained $R(T)$ at $\vec{B}_\mathrm{ip}=+90$ mT applied in difference angles. The curves are shown in figure 5.3 in section 5.2.

In this section, we show in Fig. 6.13**a** the corresponding Arrhenius plots, i.e. $\ln R$ vs. $1/T$.

We find an activated behaviour of the resistance, which we can clearly devote to thermal activation with an angle dependent activation energy E_A. This activation energy is shown in figure 6.13**b** (blue symbols) together with twice the calculated Josephson coupling energy $2E_J$[5] (red symbols). For the red symbols, we assumed a sinusoidal CPR ($f'(\varphi) = 1$) in order to use the simple relation $2E_J = 2\Phi_0 I_0/2\pi = E_A$. The result is a rough match up to a factor of $\simeq 2$ and the angle dependence of E_A and $2E_J$ matches very well. A possible reason for the deviation is the non-sinusoidal shape of the CPR ($\bar{\tau} \simeq 0.75$ for sample 2).

---

[5]According to Eq. 2.44, taken from Ref. [23], $2E_J$ is necessary to overcome the potential barrier.

7 Multiterminal Josephson Junction Array

The physics of Josephson junctions still seem to have a lot of unknown land that can be explored. New experimental avenues became accessible due to the rise of the two-dimensional superconductor-semiconductor platforms [22][161]. With these kind of heterostructures, we have the ability to flexibly design and fabricate different complex quantum circuits. For instance multiterminal Josephson junctions (MTJJs), where multiple superconducting leads are connected by a scattering region A. In such a region, the energies of the Andreev bound states are controlled by the macroscopic phase differences of the respective leads and may thus produce peculiar energy spectra. Due to the 2π periodicity in all phases of the ABS energies, we can draw an analogy to the band structures of natural solids.

Solids are limited to three dimensions. This does, however, not count for the quasi-band structures of multiterminal Josephson junctions, where $N+1$ superconducting leads correspond to the N-dimensions of the reciprocal space in solids [162]. For instance, an ordinary two-terminal Josephson junction corresponds to a one-dimensional solid or a three-terminal MTJJ to a two-dimensional solid.

7.1 Why Connect Several Superconducting Leads?

In condensed matter systems, single fermion states are a necessary condition for spin qubits [163], spintronics [164] or for topological superconductors, where states such as Majorana bound states or Weyl points are predicted to emerge. However, Kramers theorem says, that the energy eigenstates of fermions with half-integer spin are double degenerated, even in the presence of an electric field or when the spin-rotation is broken. The violation of Kramers theorem and creation of single state fermions requires the breaking of time-reversal symmetry [165]. In our case, we used an external mag-

netic field to break TRS in order to observe phenomena such as the superconducting diode effect among other things discussed in the chapters 5 and 6.

But there is another possibility than by using magnetic fields to break TRS in Josephson junctions. Theoretical reports (see Refs. [165][162][33][166]) propose a simple change of the device geometry by adding an extra superconducting lead, as illustrated in Fig. 7.1. With a third lead, TRS is broken by superconductivity only and the energy spectrum of the ABS changes crucially. Furthermore, if at least two of

Figure 7.1

Scheme of a three-multiterminal JJA:
Three superconducting banks, each with an independent macroscopic phase are connected via a scattering area A. Two leads are a part of a superconducting loop, where the phase can be controlled sensitively and locally with an external flux. The other control parameter is the current flow $\vec{I}$. Our sample, discussed below, is based on the layout shown here.
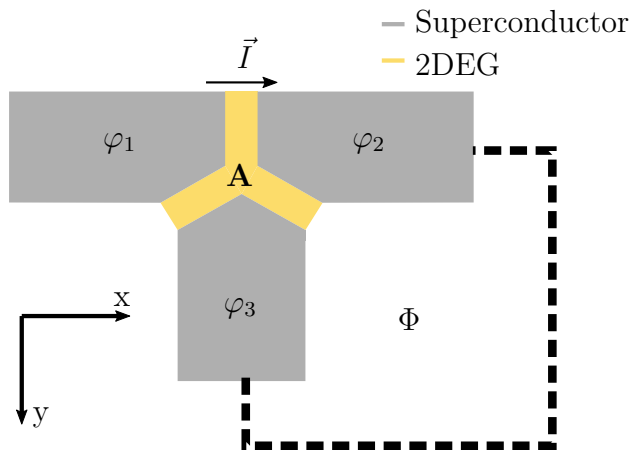
the three leads are embedded in a superconducting loop, we can manipulate the ABS states with a local flux through the loop without diminishing superconductivity in the leads. Our attempt is to use a current-carrying wire next to the addressed loop instead of the out-of-plane magnetic field in order to tune the phase difference between the leads.

7.2 Weyl Semi-Metals

In solids, (3D) Weyl-semi metals (WSM) lack either inversion or time-reversal symmetry and posses a strong spin-orbit interaction. Furthermore, WSM are characterised by surface states that are a consequence of the topology of the bulk band structure. The Berry curvature diverges in these surface states and the band gaps close in these called Weyl points. In the vicinity of such Weyl points, the dispersion relation satisfies a conical dispersion relation, as it is known from graphene [167]. But unlike in graphene, these isolated Weyl points are topologically protected and always occur in

pairs with an opposite chirality. The Berry flux between two Weyl pairs leads to a non-zero Chern number C and gives rise to chiral edge states. These edge states exist only between the corresponding Weyl points and cause the appearance of a Fermi arc (see Fig. 7.2**a**) [168][169][170]. The Fermi arcs are topologically protected by the Weyl points and can evoke fascinating transport phenomena, e.g. novel quantum oscillations in the density of states as a function of magnetic field [171][172]. In 2015,

a **b**
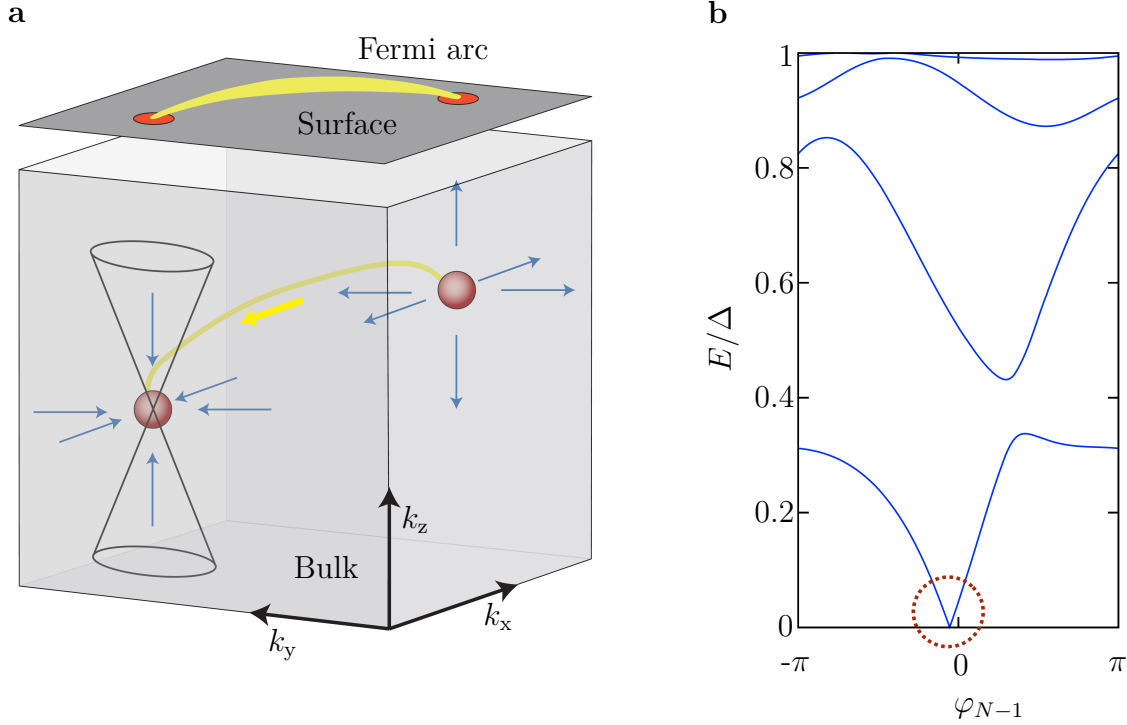
Figure 7.2: **Weyl points: a,** Two Weyl nodes in momentum space (red), with linear dispersions in the vicinity (black), are connected by a Fermi arc (yellow). The plane on the top shows the two-dimensional projection. **b,** ABS energy spectrum as a function of φ_{N-1}. A Weyl singularity (indicated by the red dashed circle) emerges in the phase difference φ_{N-1}, depending on the $N(=4,5...)$ lead's configuration. Images taken from [173] and [33].

Weyl points with the predicted Fermi arcs have been experimentally observed for the first time in a bulk material made of TaAs, by using angle-resolved photoemission spectroscopy (ARPES) (see Ref. [174]).

In short two-terminal Josephson junctions, the Andreev bound state levels reach zero energy when the phase difference is $\varphi = \pm\pi$ and the transmission coefficient of the normal region τ is unity. Riwar et al. [33] proposed in 2016 the existence of synthetic Weyl points in the pseudo-band structure of short multiterminal Josephson junctions,

as exemplified in Fig. 7.2**b**. For $N(= 4, 5...)$-terminal Josephson junctions, the ABS levels cross the zero energy level at various isolated points. The number of points depend on the N-1 dimensions in the phase space [162]. Unlike in solids, spin-orbit interaction and thus inversion symmetry breaking is not essential for existence of Weyl points, neither is Zeeman splitting. What is required is at least a four-terminal setup with a scattering area A. Numerical calculations with randomly generated scattering matrices revealed a chance of 5% for the manifestation of topologically non-trivial quasi-band structures.

We targeted the detection of these synthetic Weyl points in the ABS energy spectrum of a MTJJ experimentally via the Josephson inductance. A linear dispersion of a synthetic Weyl point in the energy spectrum should cause a significant decrease in the Josephson inductance. Although Riwar et al. [33] predicted the appearance of synthetic Weyl points for more than three superconducting leads, it might be possible that an in-plane magnetic field in the right direction could replace the fourth lead in our three-terminal Josephson junction layout.

7.3 What are the Goals of this Experiment?

To our knowledge, three and four-terminal Josephson junctions have been realised in graphene [175] and in the two-dimensional Al/InAs platform, as we use it [176][177]. However, these reports mainly focus on critical current contours (CCCs). Due to the lack of other experimental reports and with our experience acquired in the fabrication process of super-/semiconducting heterostructure arrays and the characterisation of such devices, it was appealing for us to start an experiment in the field of MTJJs. For the beginning, we set up the following goals:

1. Show that it is possible to fabricate an array consisting of multiterminal Josephson junctions.

2. DC transport characterisation with the sample exposed to magnetic fields out-of-plane and in-plane at different angles.

3. Demonstration of the possibility to perform inductance measurements on a MTJJA.

4. Manipulation of the ABS spectrum by using a superconducting loop, which is controlled by a flux line next to it.

7.4 The Sample MTJJA

Since the first experiment should have as simple a framework as possible, we decided to start with a three-terminal setup, including a well defined scattering region A. Fig. 7.3**a** shows a false color SEM image of the sample with the name MTJJA before the deposition of the AlOx. Figure 7.3**b** shows a zoom-in of the array.

a

b
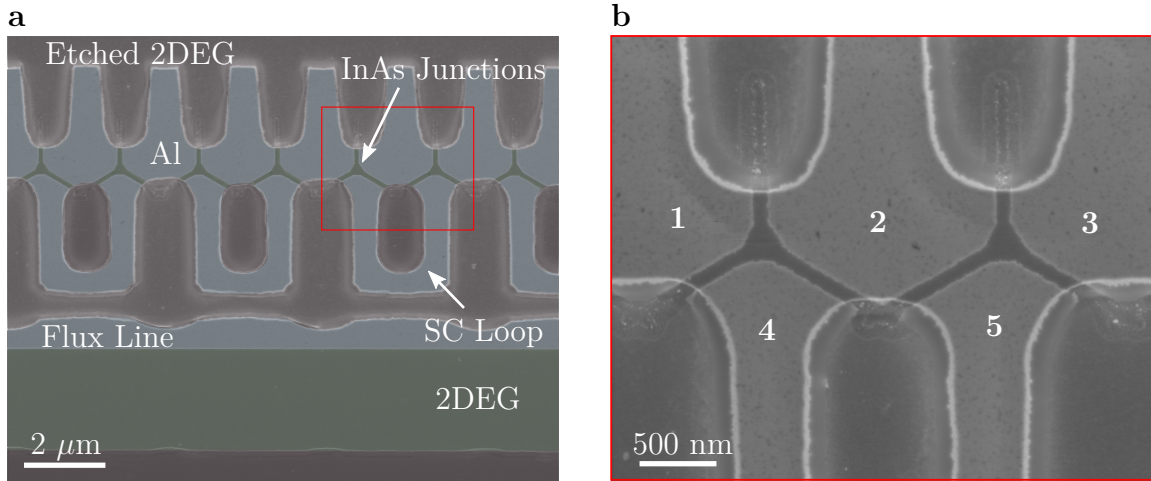
Figure 7.3: **False color SEM image of the sample MTJJA: a,** The current has to pass 400 three-terminal Josephson junctions in series. The ABS spectrum can be modulated by the attached superconducting loop, which is connected to two three-terminal Josephson junctions. **b,** Zoom on a similar area as framed in red in **a**. Three Josephson juctions tilted by 120° to each other are connected by a rectangular shaped area with a side length of $\simeq$400 nm.

The array has a total of 400 defect free[1] three-terminal Josephson junctions (3TJJ or trijunction) in series. Two 3TJJs are equipped with a superconducting loop. The ABS states between the lead 1,2 and 3 can be tuned by a current, while the other states between the leads 1,2,4 and 2,3,5 are phase biased by the attached superconducting loop. Below the loop is a flux line, consisting of the heterostructure's material, i.e. epitaxial Al on top of InAs. A broader strip of the 2DEG is left over due to fabrication reasons.

The layout and the corresponding geometric dimensions in this first sample are fabricated in such a way, that the resulting Josephson inductance of the entire array is large enough for the detection with our resonator technique. The fabrication steps are essentially the same as described in the fabrication section 3.2. Accordingly, we started to define and to etch the mesa first. Afterwards, the Josephson junctions and

---

[1]The inspection of the array by the SEM showed no defects.

the flux line were fabricated in the same step.

The whole structure is covered by 30 nm AlOx as a gate dielectric. A topgate with 5 nm Ti and 100 nm Au is deposited above the Josephson junction area and also covers about half the area of the loops. The flux line was kept free from the topgate to maintain the possibility to upgrade the sample with a flux line consisting of niobium or any similar superconducting material that can sustain a high current.

7.4.1 The Mesa

It turned out that the first etching step must be for patterning the mesa, otherwise the etching result is more than insufficient. Furthermore, this step can take place only once per chip. The reason why a sample exposed to a prior etching process shows such a different etching result, where the resist is underetched, etches are hardly to distinguish and defects are found everywere, is not understood.

We divided the sample into many smaller segments, each defined with 25 superconducting loops. The number of Josephson junctions per segment could be specified in the second etching step. There are two main reasons for this subdivision.

The first reason is the high demand on the positional accuracy of the components of the chosen layout. The superconducting loops, the flux line, the widths of the Josephson junctions and the alignment markers allow no shifts with respect to each other in the x- and y-directions in the 2D-plane. For larger structures, the stage of the SEM has to move mechanically and shifts are therefore unavoidable. This is one reason why smaller segments are beneficial. And secondly, we can choose the best segments and bypass those ones with defects.

For this sample, it took some time to elaborate a layout and a routine with a satisfying result, especially due to the strong proximity effect, where secondary electrons cause an overexposure of the resist. Any change on the layout entails various adjustments. For example, if one exposure area is increased, the nearby structures within several μm distance tend to be overexposed. By implication, their dose must be reduced. The crucial step here is hence the mesa etching. For etching the aluminium, the recipe described in section 3.2 must be applied rigidly and the alignment with the adjacent markers must work.

7.4.2 The Three-Terminal Josephson Junction

After fabricating the mesa, the next step is to etch the aluminium to define the Josephson junctions. Since we cannot control the resulting contact spacing of the junctions within a ±20-30 nm accuracy, the length of each of the three Josephson junctions is 120 nm instead of the predefined 100 nm for all 400 junctions in series. The three junctions are connected via the scattering region A, defined as a rectangle with a side-length of 400 nm.

In comparison to the one-dimensional Josephson junction arrays (i.e. sample 1-3, see overview in section 3.3), we downsized the width of the weak links[2] and put two 3TJJ per loop to achieve a sufficient high Josephson inductance. However, it is also interesting whether a sample with a single 3TJJ per SQUID reveals different results and if yes, what kind of differences.

7.4.3 Superconducting QUantum Interference Device (SQUID)

The loops in our MTJJA resemble a dc-SQUID (see Fig. 7.4**a**), where a superconducting loop has two point-like Josephson links and is distinct from a rf-SQUID, which is a superconducting loop interrupted by only one weak link.
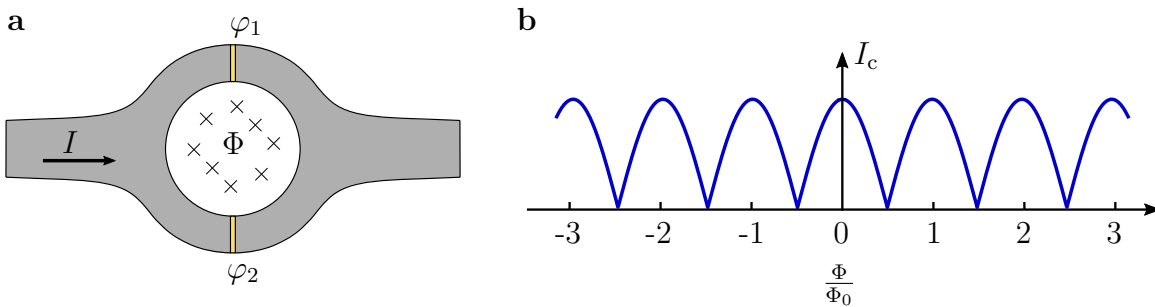
Figure 7.4: **SQUID: a,** Cartoon of a dc-SQUID. **b,** Flux dependence of the critical current of a dc-SQUID.

In order to derive the local phase difference between two points in an individual loop, we need to consider the vector potential A. In general, the gauge-invariant phase difference between a point A and B is described by [44][94]

$$\phi = \varphi_{\text{AB}} - \frac{2\pi}{\Phi_0} \int_A^B A \cdot d\vec{l}, \tag{7.1}$$

---

[2]The width of the Josephson junctions is defined by the mesa and by the position of the 3TJJ.

with

$$\Phi_0 = \frac{h}{2e} \tag{7.2}$$

being the flux quantum for Cooper pairs. Transferred to the SQUID, the magnetic flux is responsible for a phase gradient. This gradient gives rise to circulating supercurrents to screen the flux. The produced flux by the loop together with the external one gives the total flux Φ.

In textbooks as in the references [44][23][94], the derivation for the relation of the maximum current of a dc-SQUID as a function of flux can be found. The maximum current in the case of two identical critical currents of the weak links is:

$$I_{\mathrm{m}} = 2I_{\mathrm{c}} \left| \cos\left(\frac{\pi\Phi}{\Phi_0}\right) \right|. \tag{7.3}$$

This function is plotted in Fig. 7.4**b** and depicts the analog to the two-slit interference pattern in optics. In chapter 4.3, we discussed the Fraunhofer pattern, which is the analog to the single-slit case. Due to the relation to the flux, the SQUID finds application as an extremely sensitive magnetometer.

However, since the superconducting loop in our array has two weak links in form of trijunctions instead of symmetric rectangluar junctions, the approximation with equation 7.3 to describe the interference pattern of the critical current does not apply, as we will see in section 7.5.1.

7.4.4 Flux Line

It is desirable to modulate the phase differences between the three leads of the 3TJJs by an external field and by the loops separately. A simple but not ideal way is to upsize the area of the superconducting loops in relation to the area of the MTJJs, as it is the case in our sample MTJJA. The loops then show a higher periodicity to B_{z}, while the change of the critical currents of the 3TJJs due to the interference in the Josephson junctions caused by B_{z} can be assumed to be small.

The optimal way is to control the flux in the loops separately, especially in possible future devices where more than one superconducting loop is to be operated independently and at the same time.

Our approach to achieve this task is to use a current-carrying wire (flux line) next to the loops. The current that flows through the flux line induces a magnetic field

and can be regulated very gently by an external sourcemeter. However, in our arrays, the wire has to be positioned very precisely in order to tune all the loops equally. Furthermore, the flux line must have a high critical current to produce the required magnetic field. In our device, about 10 mA are required to induce a magnetic flux $\Phi_0 = h/2e$. In the non-superconducting state, the wire with its finite resistance represents a heater and thus raises the temperature of the whole sample.

For the first try, we used the Al/InAs heterostructure to fabricate the wire, because here we could define the wire together with the rest of the mesa in one fabrication step and avoid an alignment procedure. But as we expected, the Al film is not suitable to function as a flux line, because the critical current of the Al wire is too small.
The obstacle of establishing a reliable flux line has not yet been solved. In our opinion, the current sample MTJJA should not be risked for a further fabrication step, before most of the investigation is done.

7.5 DC Transport Characterisation

The results presented in this chapter are from the last experiment of this thesis, which was our first step into the large subject area of MTJJs. Further experiments are necessary for a deeper understanding of the data presented here. The following results are from measurements, which have been performed together with the master student Johanna Berger.

We mounted the sample MTJJA in our resonator (introduced in chapter 3.5.3) and cooled it down to 50 mK. The topgate was kept at zero voltage throughout this measurement session, since it had a finite resistance of 220 kΩ to the source electrode. At the beginning, we started with DC transport measurements for a first overview. Figure 7.5 shows current-voltage up- and downsweep curves at zero magnetic fields. As with sample 1 (compare with Fig. 4.7), we do not see any hysteresis either.
However, the *I-V* curves of sample 1 look different due to the individual Josephson junctions with a reduced critical current in the array, caused by defects. The sample discussed here has no defects along the array, but certain inaccuracies instead. One inaccuracy comes from the varying position of the 3TJJs from segment to segment (as we know from SEM examination), which is a consequence of the repeated alignment procedure of the SEM during fabrication. This means that the critical currents of the

individual junctions are expected to differ slightly from segment to segment. Another
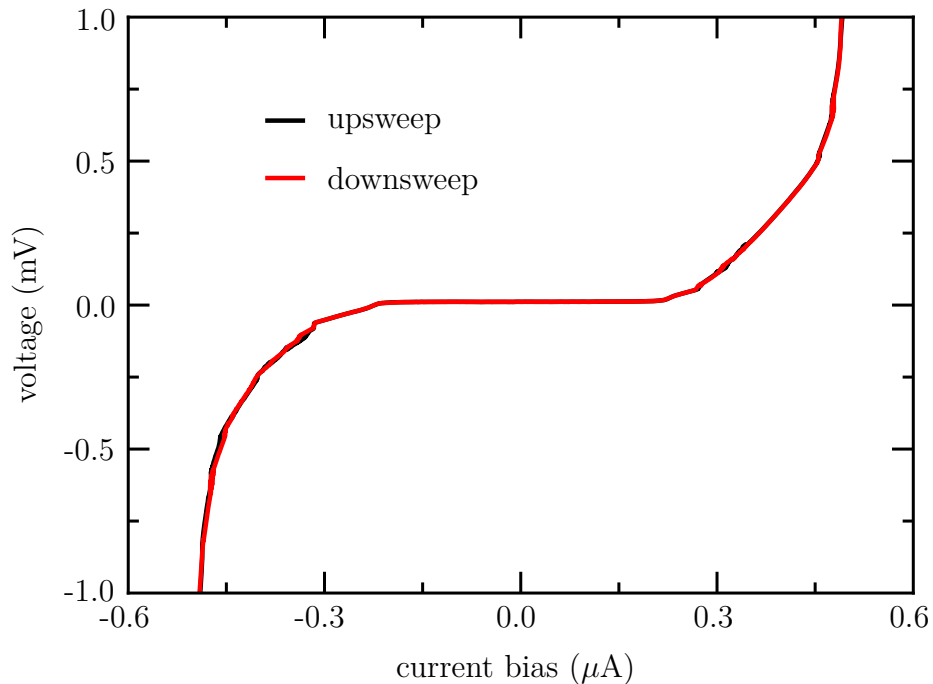
Figure 7.5: **Current-voltage curves** at zero magnetic fields at T=50 mK. As expected for a Josephson junction in the overdamped regime (see theory in section 2.3.3), we see no hysteresis between up- and downsweep.

inaccuracy can be attributed to the different effective areas of the loops. Not all loops of this sample have a perfect and consistent shape and since the modulation of the critical current by these loops is high, minor differences of the effective area can have a significant influence.

These inaccuracies can be a reason why a critical current of the array via the *I-V* curves cannot be exactly determined, but I_c seems to be about 470 nA for the whole array. Moreover, in the case of zero in-plane fields, we see finite resistance features inside the central lobe of the Fraunhofer pattern (shown and discussed below in section 7.12).

The total resistance R_N of sample MTJJA is $\simeq$105 kΩ, of which an estimated 15 kΩ comes from the aluminium leads and islands. This means that a single trijunction has a normal resistance $R_{N,1}$ of about 225Ω.

7.5.1 Out-of-Plane Magnetic Field

The modulation of the critical current $I_c(B_z)$ by quantum interference in an out-of-plane magnetic field can reveal a lot about the spatial distribution of the supercurrent J_s in a Josephson junction. In the colorplot in figure 7.6**a**, the shown diffraction
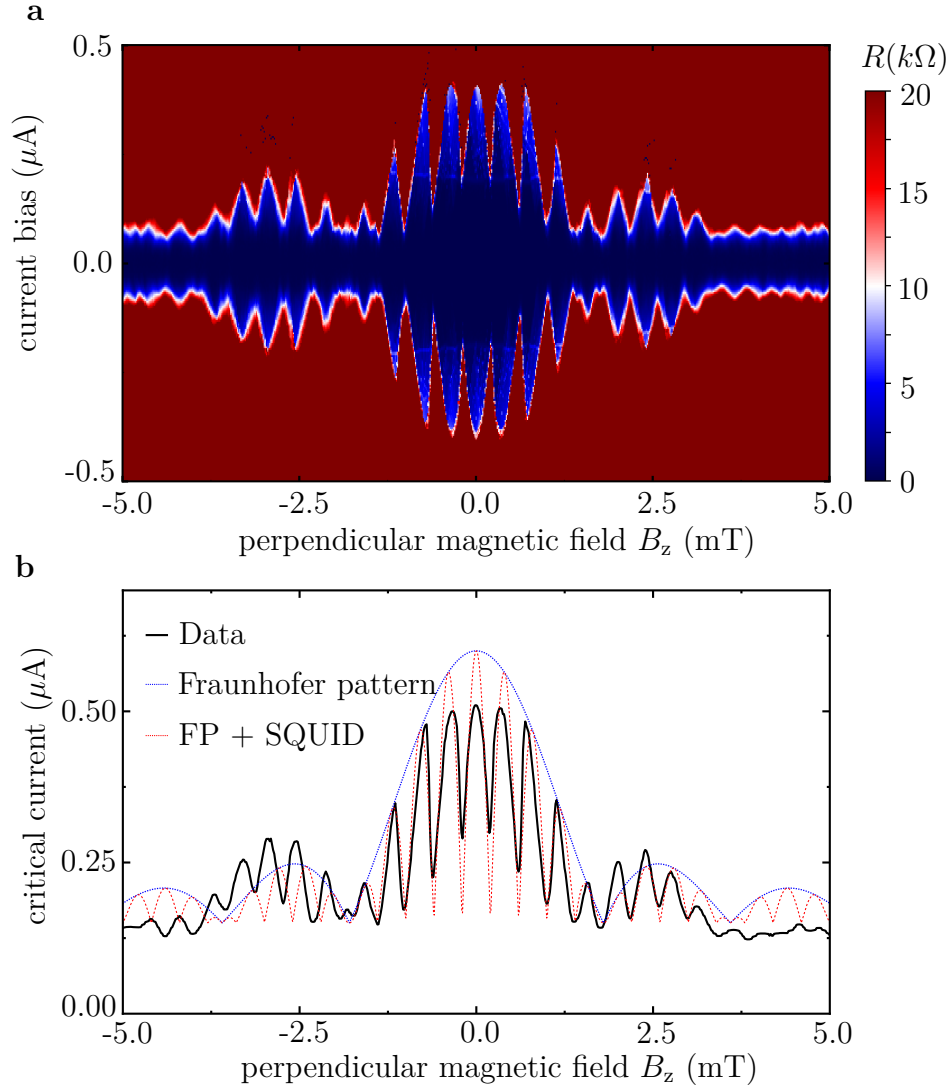
Figure 7.6: **Interference diffraction pattern of sample MTJJA: a,** Colorplot and **b,** corresponding critical currents with a sinc function fit (blue curve) and a fit with the product of a sinc function and SQUID modulation (red curve). An offset of +150 nA has been added to the critical current of the fits. The voltage condition for the critical current of the data was set to 2 mV, because of the sub-critical current features (described below in section 7.6). For all other critical currents, the voltage condition was set to 0.5 mV.

pattern appears to be a combination of a Fraunhofer pattern, as an envelope, and of

SQUID oscillations. To compare more precisely, we fitted the critical current $I_c(B_z)$ data with a sinc function (introduced in chapter 4.3). Furthermore, we tried to fit the data with the product of the envelope and the SQUID oscillations (introduced in section 7.4.3) according to

$$I_c(B_z) = I_c(0) \cdot \left| \frac{\sin(\pi B_z A_J / \Phi_0)}{\pi B_z A_J / \Phi_0} \right| \cdot \left| \cos\left(\frac{\pi B_z A_L}{\Phi_0} \right) \right| + I_{\text{offset}}, \qquad (7.4)$$

with $A_J = 1.15 \ \mu m^2$ and $A_L = 5.17 \ \mu m^2$ as the effective areas of the 3TJJ and the loop, respectively. The respective fits are plotted in Fig. 7.6**b**. What we observe is the matching of periodicity of the higher frequented oscilliations (red curve). The envelope (blue curve = Fraunhofer pattern) does also match the periodicity of the lower frequent enveloping oscillations.

However, the blue and consequently the red curve fail to fit the absolute values of the critical currents. The measured critical currents of the central lobe are too small, while for the side lobes, the measured critical currents are too big. This indicates a non-trivial current-phase dependence of the trijunctions, which thus needs a profound analysis. This analysis is part of the master thesis of Johanna Berger [178].

7.5.2 In-Plane Magnetic Field

The Superconducting Diode Effect (SDE)

The shape of the diffraction pattern becomes even more interesting in the presence of in-plane magnetic fields. Like with the simple Josephson junction arrays, we also observe in the MTJJA a diode effect of the critical currents in the central lobe (see Fig. 7.7). The critical current differences in the central lobe, i.e. $\Delta I_c^{\text{center}} = |I_c^+ - I_c^-|$,
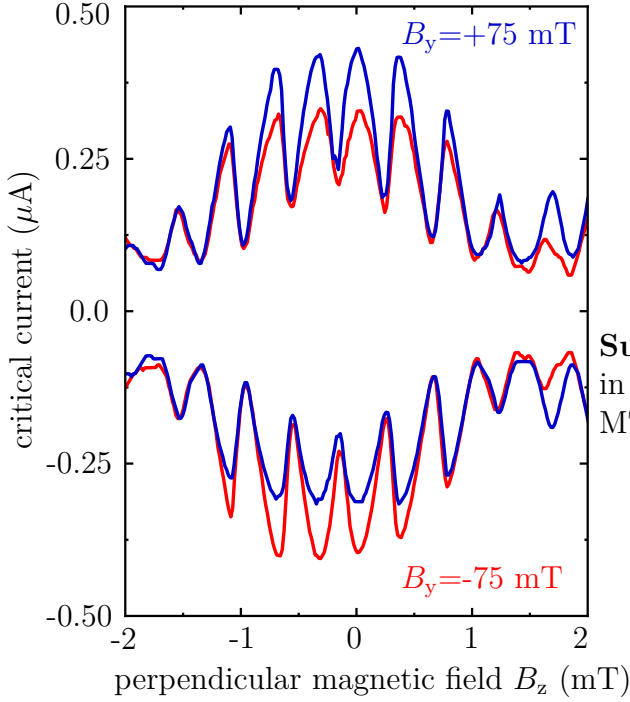
Figure 7.7
Superconducting diode effect in the central lobe of sample MTJJA.

show likewise for the sample 1 (discussed in section 5.4) and for sample MTJJA (discussed here) a similar B_y dependence, as it is shown in Fig. 7.8**a**. The values are normalised to 1 by the data point $\Delta I_c^{\text{center}}$ at $B_y = +75$ mT for comparison reasons and is necessary due to the different sample geometries.

Both curves show an absolute maximum of $\Delta I_c^{\text{center}}$ at $B_y = \pm 75$ mT. For increasing B_y, the diode effect begins to vanish, what we relate to the disappearence of the higher harmonics in the current-phase relation (described in section 5.4).

To see whether our 120° geometry of our three-terminal Josephson junction has an influence on the diode effect and thus reflected in $\Delta I_c^{\text{center}}(\theta)$, we measured diffraction patterns for in-plane field orientations from 270° to 90° at $\vec{B}_{\text{ip}} = \pm 75$ mT. Figure 7.8**b** presents the angle dependence of $\Delta I_c^{\text{center}}$. The result shows a similar angle dependence as we have seen from the magnetochiral anisotropy effect of the two-terminal

a

b
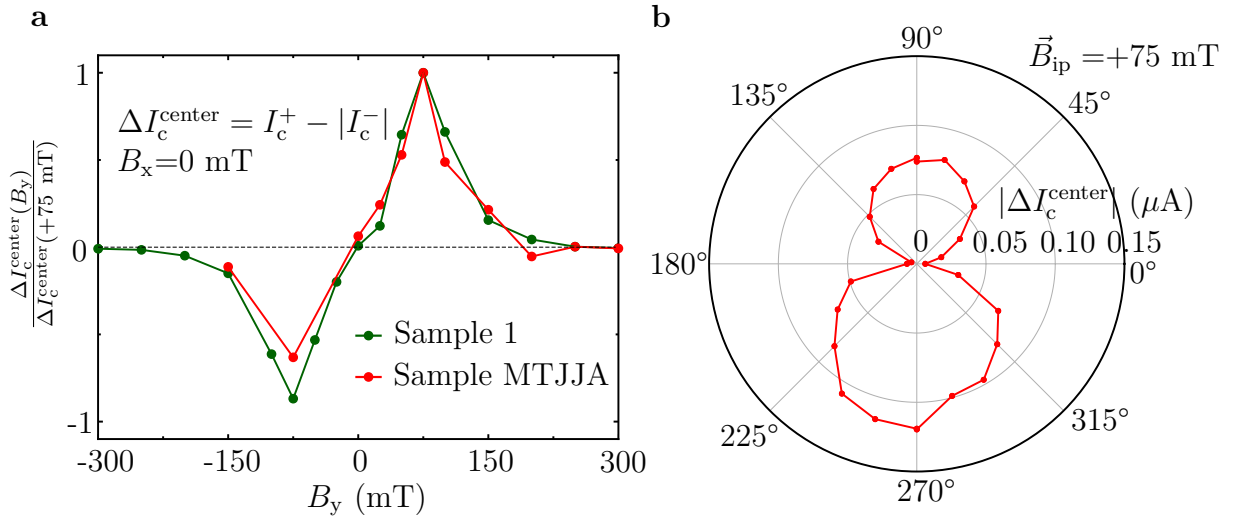
Figure 7.8: **Superconducting diode effect a,** of sample 1 and MTJJA as a function of B_y ($\theta=270°$) normalised by $\Delta I_c(B_y=+75 \text{ mT})$. **b,** Angle dependence of the critical current difference $\Delta I_c(\theta)$ at $B_z=0$ T and $\vec{B}_{ip}=+75$ mT for sample MTJJA.

Josephson junctions (compare sections 5.3 and 6.1) and from the Fraunhofer diffraction pattern of sample 1 (compare appendix C). Indeed, ΔI_c^{center} seems to be stronger in one direction (i.e. $\theta=270°$), as we have also observed for the MCA effect of sample 1 and 3, shown in Fig. 6.3 in the previous chapter.

Interestingly, this asymmetric angle depende of ΔI_c^{center} does not apply for the following effect we have noticed in this 3TJJ device.

Asymmetry of ΔI_c between Positive and Negative B_z

In the presence of an in-plane magnetic field in y-direction (i.e. $\theta=90°$ or $270°$), a peculiar effect appears in our three-terminal Josephson junction device. The critical currents between positive and negative perpendicular magnetic fields become asymmetric with respect to each other, as figure 7.9 shows. The asymmetric effect is particularly noticeable in the side lobes and therefore it is temporarily called side lobe effect (SLE) in this work. That is why we have chosen to use the maximum critical currents $I_c^{max,left}$ and $I_c^{max,right}$ for further analysis. As an example for the definition, $I_c^{max,left}$ and $I_c^{max,right}$ are drawn into Fig. 7.9 bottom.

The direction of the current does not play a role in this side lobe effect, because it applies: $I_c^+(B_z) = |I_c^-(B_z)|$. In other words, by mirroring the critical currents on the
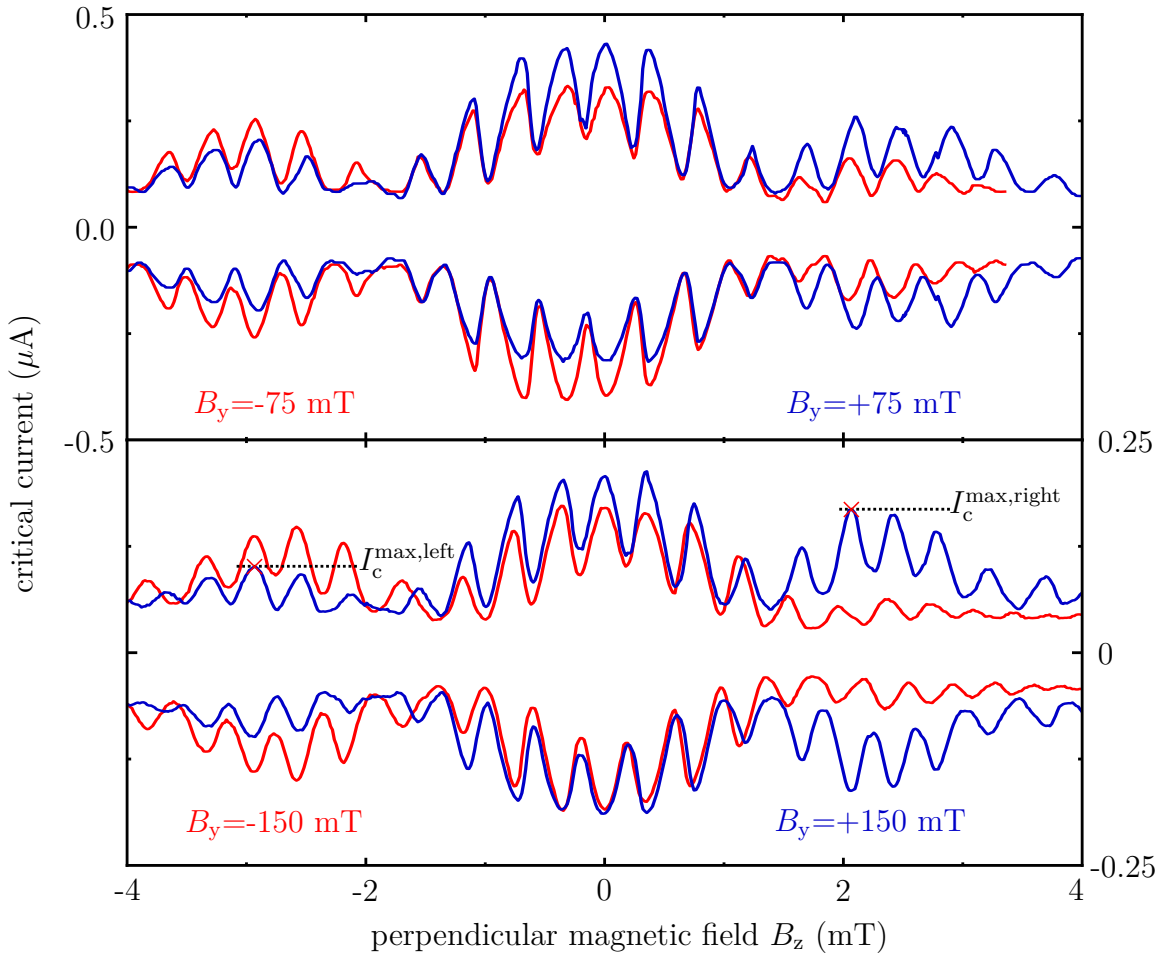
Figure 7.9: **Asymmetric critical currents** between positive and negative out-of-plane fields $\vec{B}_z$. The effect is especially recogniseable in the side lobes of the envelope. That is why $I_c^{\text{max,left}}$ and $I_c^{\text{max,right}}$ has been defined as the maximum critical current of the left and right side lobe.
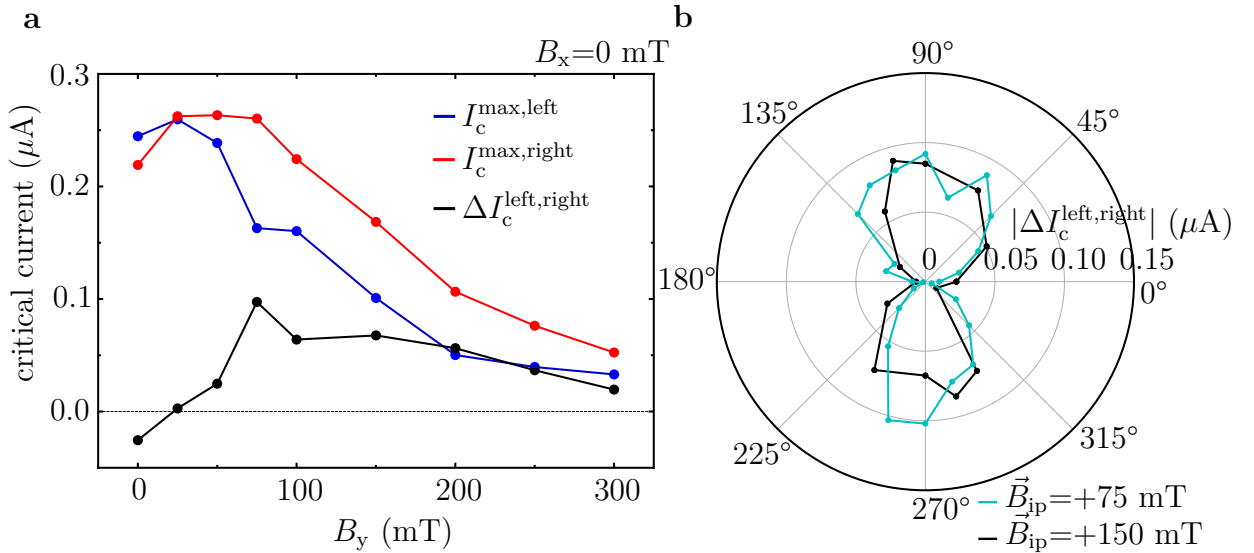
Figure 7.10: $I_c^{\text{max,left}}$ **and** $I_c^{\text{max,right}}$ **dependence: a,** as a function of the in-plane field for $\theta=270°$. In contrast to the SDE, the difference $\Delta I_c^{\text{left,right}}$ does not disappear with increasing B_y, but becomes smaller due to the suppression of the induced gap and thus the critical currents themselves become smaller. **b,** Angle dependence of $\Delta I_c^{\text{left,right}}$ for $\vec{B}_{\text{ip}}=+75$ and $+150$ mT.

horizontal axis does not alter the shape of the $I_c(B_z)$ curves.

Such a mirror operation does, however, not work on the y-axis, which means that the $I_c^{\pm}$ values are not symmetric with respect to B_z, i.e. $I_c^{\pm}(B_z < 0) \neq I_c^{\pm}(B_z > 0)$, and neither are the $I_c^{\pm}(B_z)$ values symmetric with respect to B_y, i.e. $I_c^{\pm}(B_z, B_y < 0) \neq I_c^{\pm}(B_z, B_y > 0)$. But inverting both, B_z and B_y, leads to the original form of the traces.

Another interesting observation, which is different to the superconducting diode effect in our samples, is the persistence of the SLE with increasing B_y. Fig. 7.10**a** presents the absolute values of $I_c^{\text{max,left}}$, $I_c^{\text{max,right}}$ and the difference of both. Similar to the SDE, the difference $\Delta I_c^{\text{left,right}}$ increases up to $B_y=+75$ mT, but $\Delta I_c^{\text{left,right}}$ remains for increasing B_y. We measured diffraction pattern up to $B_y=300$ mT, where the critical currents of the side lobe become equally big as the critical currents from the central lobe. Figure 7.10**b** shows the in-plane field angle dependence of $\Delta I_c^{\text{left,right}}$ at $\vec{B}_{\text{ip}}=$ $+75$ and $+150$ mT in a polar plot. Both curves have a similar magnitude and angle dependence. We see a two-fold symmetry of the side lobe effect similar to the superconducting diode effect and no reflection of the 120° geometry from the trijunctions.

If we compare this side lobe effect with the superconducting diode effect (see Fig.

7.11), we see that the absolute values of the ΔI_c are about the same size at $\vec{B}_{ip}=+75$ mT. Moreover, an enhanced effect of the SLE in one direction (e.g. $\theta=270°$) seems not to
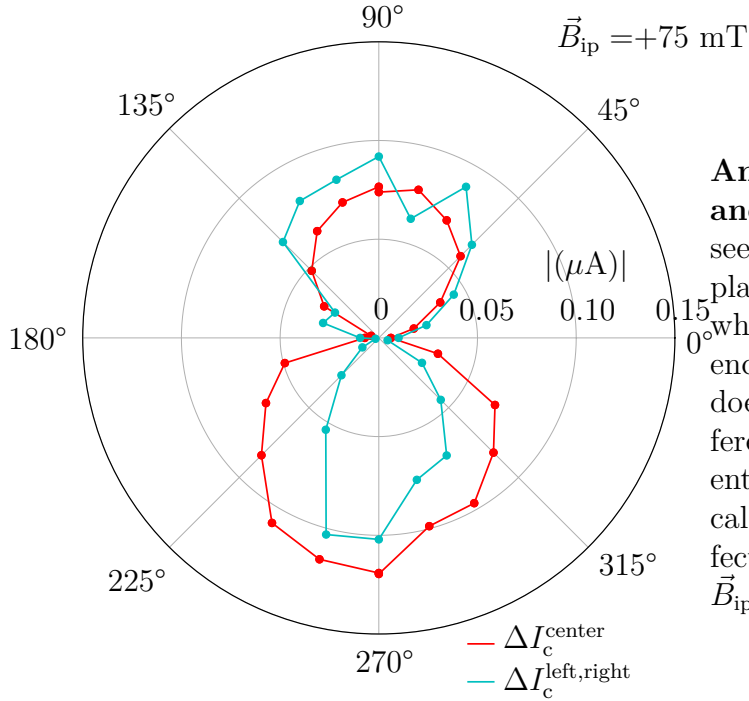
Figure 7.11
Angle dependence of SDE and SLE: The SDE (red curve) seems to be stronger if the in-plane field is applied in $\theta=270°$, while the critical current difference of the side lobes (cyan curve) does not show a pronounced difference between 270° and 90° orientation. Interestingly, the critical current difference of both effects have a similar magnitude at $\vec{B}_{ip}=+75$ mT.

exist, which is in contrast to the SDE. But how isotropic the SLE between 270° and 90° really is, is difficult to tell since this data obtains a certain scattering amplitude.

7.6 Josephson Inductance

In addition to the observations we made from the sample MTJJA from the DC transport characterisation, we obtained the Josephson inductance as a function of B_z. The following graph in 7.12**a** shows the central lobe of the diffraction pattern presented in Fig.7.6**a**, but this time with a smaller range on the z-scale (i.e. $R=10$ kΩ). Below the critical current, finite resistance features appear for current biases greater than $\pm \simeq 200$ μA. Figure 7.12**b** shows the corresponding Josephson inductance for zero current bias and zero in-plane magnetic fields.

a

b
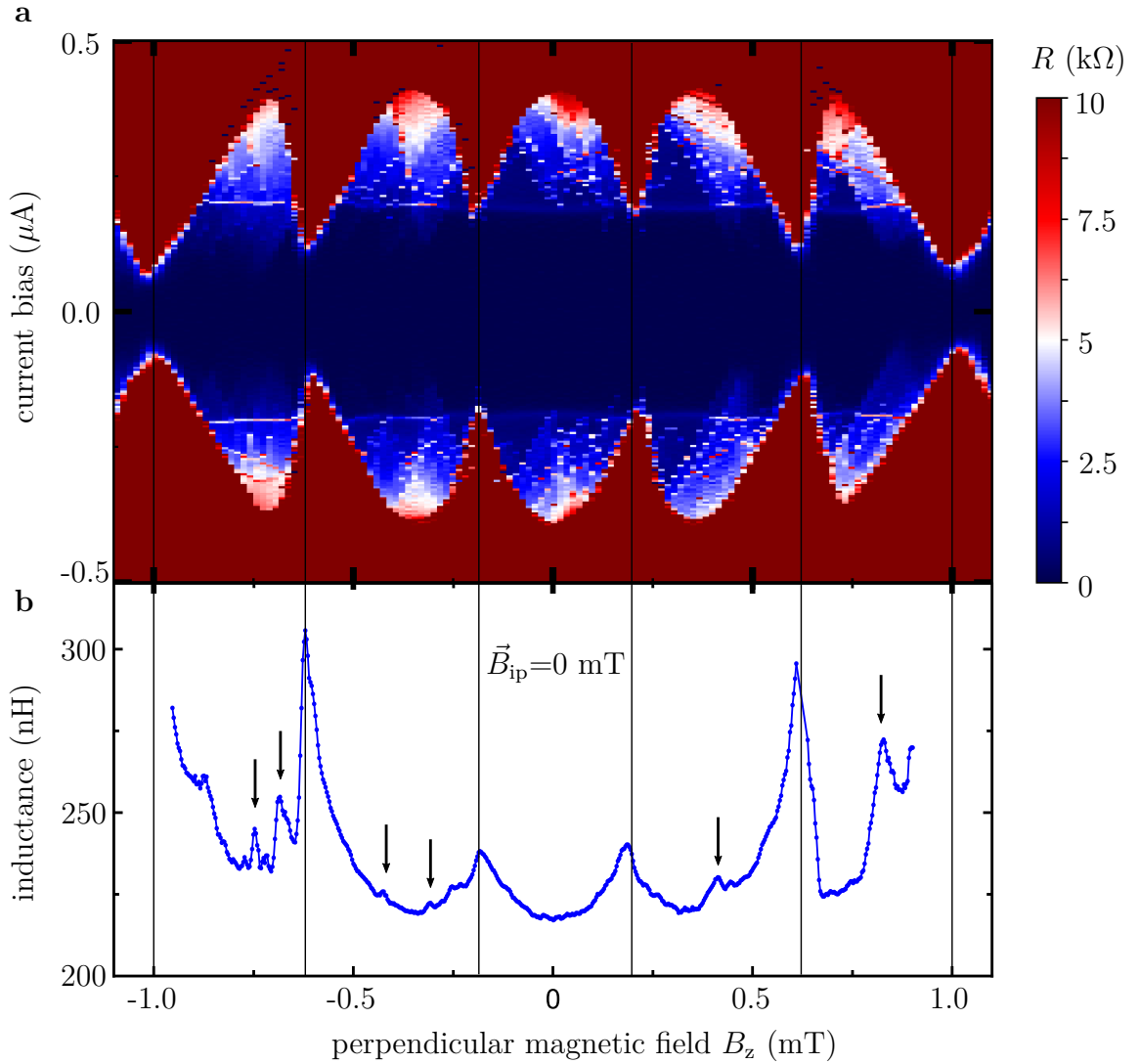
Figure 7.12: **Diffraction pattern for $\vec{B}_{\text{ip}}$=0 T: a,** Zoom-in of Fig. 7.6. In the central lobe of the envelope we observe sub-critical current features which also show up in the Josephson inductance in **b**, indicated by black arrows. **b,** The corresponding Josephson inductance obtained at zero current bias.

The Josephson inductance reproduces the smaller oscillations of the central lobe of the envelope caused by the attached superconducting loop. The inner sub-critical current features are responsible for an overall reduced I_{c} of the array. Therefore, these features seem to be reflected in the $L(B_{\text{z}})$ curve. The most prominent peaks are highlighted by the black arrows.

a

b
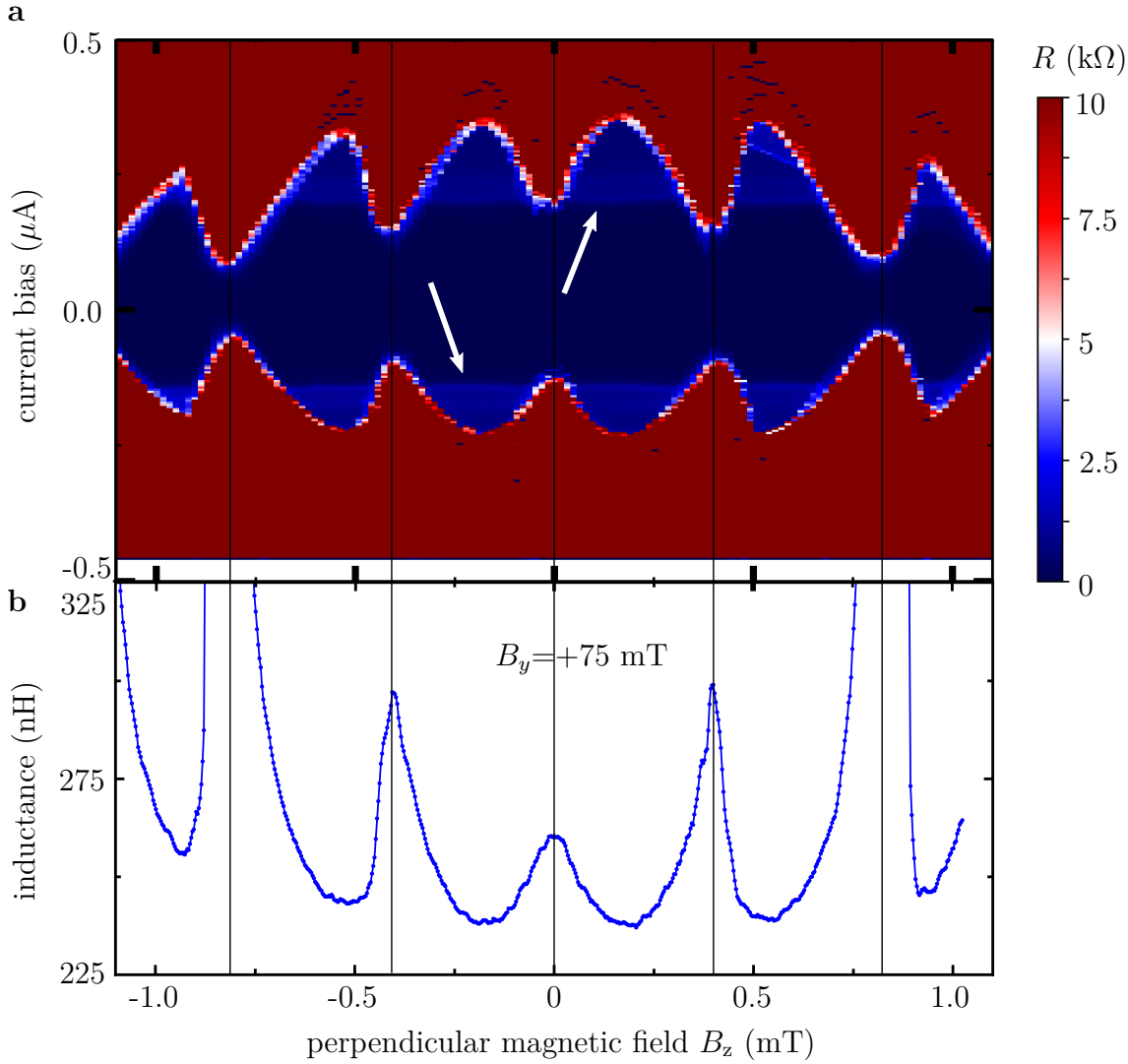
Figure 7.13: **Diffraction pattern for B_y=75 mT: a,** The sub-critical current features (mentioned in Fig. 7.12) disappear at finite in-plane fields. Except a from B_z nearly independent resistance remains, in this colorplot at $+\simeq$-0.2μA and $\simeq$-0.13μA (indicated by white arrows). **b,** Corresponding Josephson inductance, measured at zero current bias. The maximum critical current goes over to a minimum at zero out-of-plane field. The offset on the x-axis was removed manually in order to compensate the misalignment of the in-plane field.

Moreover, we observe a phase shift of the loop oscillations with respect to B_y. The center of the central lobe has a maximum of the critical current around B_z=0 and thus a minimum in the inductance. When an in-plane field B_y is added, for instance of B_y=+75 mT, the situation is reversed. The plots in figure 7.13 show a mininum/maximum of the critical current/Josephson inductance. This B_y dependent

phase shift is studied by Johanna Berger and will be discussed in her thesis [178].

Another finding is the simultaneously disappearance of the sub-critical current features at finite in-plane fields in the *I-V* characteristics and in the Josephson inductance (compare Figs. 7.12 and 7.13). However, a small resistance remains, which is highlighted in Fig. 7.13 by white arrows. The resistance occuring here at $I_{\mathrm{dc}} \simeq +0.2$ μA and -0.13 μA seems to be independent from B_{z}, but not from B_{y}, since it shows a diode behavior. Furthermore, this resistance feature shows a negative differential resistance, which ranges from $\approx$900 to $\approx$600 kΩ (see appendix E).

Both, the origin of the remaining and of the vanishing resistance features are not understood and might be sample dependent. More experiments on new samples will show whether this is the case or not.

So far, we performed mainly DC transport measurements in the first measurement session, because the *Q*-factor of our resonator was far to low (Q<7). Therefore, especially the $L(I)$ curves had an insufficient quality for a meaningful evaluation. The reason for this low *Q*-factor could have been the cold ground, which the flux line and the resonator shared together in order to save a wire against which our piezo-rotator would have had to work. But, by sharing the cold ground, the resonator might have seen the cable inductance of the flux line source connection.

7.7 Discussion

The experiment of our first multiterminal Josephson junction device showed first promising and exciting results. It is possible to produce and to obtain the Josephson inductance from a homogeneous MTJJ array. The sample MTJJA has 400 3TJJs in series, which have a sufficient high inductance ($\simeq$220 nH). This means that using the same layout for future samples, 200 3TJJs in series will produce at least >100 nH Josephson inductance - sufficient for a good sample characterisation. The attached superconducting loops can serve as a knob to tune the phase difference, which we controlled with an global out-of-plane magnetic field. To install a superconducting flux line, which runs accross the entire array with the same distance to the loops with a sufficient high critical current, has not yet been attempted.

The appearing asymmetries between the critical currents of positive and negative B_z, which appear at finite B_y, deserve a deeper analysis. The side lobe effect (SLE) seems to mainly be present in the envelope of the diffraction pattern. In order to examine if this impression is true, a quick and easily realisable experiment could be carried out. Because the SLE is a signature in the envelope, the loops are probably unimportant for the effect and thus the loops can be just removed. The simplest way is to fabricate a new sample, where multiple (e.g. 10) 3TJJs of the same 120° geometry of sample MTJJA are etched in series into an Al/InAs strip. So far, we measured the SLE via dc current-voltage curves and thus an array is obsolete for a quick validation. But, about ten 3TJJs in series ensure that unique signatures of an individual 3TJJ, caused by a defect for instance, are smoothed out by the number of junctions in series.
Another experiment building upon the described one above, is to fabricate a device similar to the sample MTJJA, but with a different Josephson junction geometry. Using a 90°, 90° and 180° layout, which means that one junction is arranged perpendicular to the two other ones, should reveal whether the 120° geometry plays any role for the SLE.

These two experiments would be a quick and easy way to check if the loop or the layout of the 3TJJ are important for the SLE or not. Both devices can be put on a single chip and be characterised in one measurement session. Step by step, insights into the physics of the 3TJJs can be gathered for a more and more clear picture. Overall, further experiments are necessary to have sufficient information for a theoretical analysis.

8 Summary

In this thesis, a study of superconductor-seminconductor weak links in the presence of spin-orbit and Zeeman fields is presented. Besides the standard *I-V* characteristics, we have measured the Josephson inductance, whose current bias dependence is a direct mirror of the current-phase relation. This allowed us to study the response of the Andreev bound states to various physical quantities, e.g. temperature, magnetic and electric fields or current.

After elaborating a fabrication procedure and performing measurements to precharacterise the Al/InAs heterostructure, we installed a RLC resonator technique to determine the Josephson inductance. With this resonator, we have shown that it is possible to investigate a Josephson junction device in the resistive and non-resistive state in the same cooldown. Characterising both states together can provide an comprehensive picture of the Josephson physics of a device, which in our case is based on a two-dimensional Al/InAs heterostructure.

The first part for drawing an all-encompassing picture of a Josephson device is presented in chapter 4. We conducted an experiment on an array made of 2250 two-terminal Josephson junctions in series. The result of the Josephson inductance measurements include i.a. the determination of the average transmisison coefficient of the ABS $\overline{\tau}$, the maximum current I_0, the number of ABS carrying channels N, the induced gap in the proximitised InAs Δ^* and the barrier parameter γ_{B}.
Direct current-voltage curves revealed an uniform Fraunhofer diffraction pattern confirming the homogeneity of the ensemble of rectangular Josephson junctions. The shape of this pattern is independent of the value of $\overline{\tau}$, while in contrast, the diffraction pattern in the inductance is strongly influenced by $\overline{\tau}$.

The main goal of this thesis was to study the Josephson effect of two-terminal Josephson junctions in the presence of spin-orbit and Zeeman fields. If both fields are present, inversion and time-reversal symmetry are broken at the same time and we observe a

rectification effect of the supercurrent. The observations are described in chapter 5 and 6.

Non-reciprocal behaviour shows up in the difference of the positive and negative critical currents, if a magnetic field is applied perpendicular to the current direction. This superconducting diode effect (SDE) reaches an absolute maximum at $B_\mathrm{y} \simeq \pm 75$ mT and starts to vanish for higher magnetic fields. We relate the suppression of the SDE with the disappearence of higher harmonics in the current-phase relation, since the distortion of the CPR is a consequence of a cosine term.

Furthermore, we studied the magnetochiral anisotropy for resistances in the dissipative fluctuation regime. In analogy, we introduced the magnetochiral anisotropy coefficient for supercurrents γ_L, which we studied for all three magnetic field directions via the Josephson inductance. Our theory colleagues from the group of Prof. J. Fabian confirm our observations with a semi-quantitative model (see supplementary information in [32]).

With these findings, we make an important contribution to the possible future implementation of superconducting components, e.g. a Josephson rectifier for microwave quantum electronic circuits or novel superconducting computing devices.

Moreover, the magnetochiral effect deep in the superconducting regime shows a sign change for increasing magnetic fields at $B_\mathrm{y} \simeq 200$ mT. Such a sign change is also reflected in the difference of the critical currents. However, in contrast to other works [159][158] we do not observe a reappearance of the sign change, neither in the critical currents nor in the MCA coefficient γ_L so far.

The Josephson inductance further allowed us to determine the influence of the intrinsic spin-orbit Dresselhaus term, which originates from the Zincblende crystal structure of the InAs. For this purpose, we produced the to sample 1 identical sample 3, but with the current flowing in the $[1\bar{1}0]$ crystal lattice direction of the InAs. By comparing the mangetochiral anisotropy coefficients for supercurrents of both samples, we can assign a value 0.67 meV nm to β.

In our last experiment, we extended the Josephson junctions by a third superconducting lead and performed a first experiment on multiterminal Josephson junction devices, which have, according to theory, the potential to accomodate synthetic Weyl singularities.

In chapter 7, we present the results of a characterisation measurement of a multiterminal Josephson junction array. This array has 400 three-terminal Josephson junctions

in series, whereby two of three leads are part of a superconducting loop. The attached loop makes it possible to vary the phase difference between the leads of the trijunctions independently.

In this multiterminal Josephson junction device, the superconducting diode effect is equally present as it is the case in the two-terminal Josephson junction arrays.

The envelope of the diffraction pattern, however, cannot be simply fitted with a mere Fraunhofern pattern function. The smaller oscillations in the diffraction pattern can be attributed to the loops, but the product of a sinc function and of SQUID oscillations does not match the critical currents of the experimental data.

Furthermore, we obtained an asymmetry of the critical currents between positive and negativ out-of-plane magnetic fields, if an in-plane field is applied in y-direction. This asymmetry, particularly noticeable in the side lobes, behaves different than the superconducting diode effect. Although the SDE and SLE (side lobe effect) have same magnitude at B_y=+75 mT, the SLE does, in contrast to the SDE, not disappear with increasing in-plane magnetic fields. Moreover, we observe a different in-plane field angle dependence between the SLE and the SDE.

Overall, this work establishes the Josephson inductance as a striking diagnostic tool for unconventional Josephson junctions. Many further experiments are conceivable with our methods, and questions remain to be answered, such as the sign change of the magnetochiral anisotropy γ_L.

There is great potential in studying multiterminal Josephson junctions, which could give rise to topological protected states or things that no one has thought of yet. With this work, we have fundamentally deepened the understanding of the building blocks of semiconductor-superconductor devices, which is essential for further research and future applications.

Appendices

A Fabrication Recipe

Cleaving and Cleaning

1. Cleaving:

   a) Spin optical resist (e.g. S1318) at 1000 rpm on wafer.

   b) Bake out at 80°C for 5 mins

   c) Cleave long parts with the use of hand diamond scriber and two tweezers - size depends on the planed device (3-4.5 mm)

   d) Cleave short edges with scriber, power = 5, one time

   e) Check in optical microscope the surface and note the crystallographic axis

2. Cleaning:

   a) Sonicate in acetone for 10 s

   b) Clean sample in two beakers for 1.5 mins with acetone in each, IPA 1 min

   c) Blow dry with N_2 pistol

Mesa Etch

1. Resist:

   a) Spin PMMA 950 K 4 % (Anisol) @ 4000 rpm

   b) Bake out at 120°C for 10 mins

2. Exposure and Develop:

   a) Auriga SEM: aperture: 30 μm , EHT: 30 kV , area dose: 200 μC, spacing: 10 nm

   b) Develop: swirl 60 s in MIBK 1:3, 30 s in IPA, blow dry with N_2 pistol

3. Al Etch:

   a) Preparation: Insert 3 ml Etchant Type D from Transene company via glas pipette into beaker and thermalise it to $\approx 50°C\pm2°C$ on the hot plate together with a second beaker filled with distilled water. Prepare third beaker with distilled water at room temperature

    b) Etching: Swirl sample for 7 s in Transene Al etch

    c) Stop process: 20 s in H_2O @ 50°C and 40 s in H_2O @ RT

4. Mesa Etch:

    a) Preparation: Dilute 20 g citric acid in 20 ml water. Fill large beaker with: H_2O : $C_6H_8O_7$: H_3PO_4 : H_2O_2 (88 : 22 : 1.2 : 2) and use a magnetic stirrer

    b) Turn off magnetic stirrer. Put sample into solution for 5 mins ($\approx$ 300 nm etching depth)

    c) Stop process: 20 s in H_2O and 40 s in second beaker with H_2O @ RT each

    d) Wash off resist @ 3 min in Aceton, 1 min in IPA, blow dry with N_2

Al Etch

1. Resist:

    a) Spin PMMA 950 K4 % (Anisol) @ 4000 rpm

    b) Bake out at 120°C for 10 mins

2. Exposure:

    a) Auriga SEM: aperture: 30 μm , EHT: 30 kV, area dose: 350 μC, spacing: 5 nm

    b) Develop: swirl 60 s in MIBK 1:3, 30 s in IPA, blowdry with N_2 pistol

3. Etch resist residues

    a) Either by RIE: duration: 10 s, gas: O_2[20 sccm], pressure: 100 mTorr, power: 5 W

    b) Or new plasma asher: duration: 10 s, gas: O_2, pressure: 3 mbar, power: 12 %,

4. Al etch:

    a) Preparation: Insert 3 ml Etchant Type D from Transene company via glas pipette into beaker and thermalise it to $\approx$ 50°C$\pm$2°C on the hot plate together with second beaker filled with distilled water. Preparde third beaker with distilled water at RT

    b) Etching: Swirl sample for 2 s in Transene Al etch

    c) Stop process: 20 s in H_2O @ 50°C and 40 s in H_2O @ RT

    d) Wash off resist @ 3 min in Aceton, 1 min in IPA, blow dry

    e) Check result in SEM

Atomic Layer Deposition

1. Resist:

   a) Spin PMMA 950 K 4 % (Anisol) @ 4000 rpm

   b) Bake out @ 120°C for 10 mins

   a) Spin PMMA 200 K 9 % (Anisol) @ 4000 rpm

   b) Bake out @ 120°C for 10 mins

2. Exposure:

   a) Auriga SEM: aperture: 120 μm , EHT: 30 kV , area dose: 280 μC, spacing: 40 nm

   b) Develop: swirl 60 s in MIBK 1:3, 30 s in IPA, blow dry with N_2 pistol

3. ALD:

   a) Grow desired thickness of AlOx at 80°C. 10 h preconditioning. Start with TMA.

   b) After process has finished: Put sample in lift-off beaker filled with acetone and put beaker on hot plate (60°C) for several hours.

   c) Lift-off in Acetone. Put sample into IPA and check result in the optical microscope. Use injection if necessary. Blow dry with N_2 pistol.

Topgate Deposition

1. Resist:

   a) Spin PMMA 950 K 4 % (Anisol) @ 4000 rpm

   b) Bake out at 120°C for 10 mins

2. Exposure:

   a) Auriga SEM: aperture: 30 μm , EHT: 30 kV , area dose: 200 μC, spacing: 10 nm

   b) Develop: swirl 60 s in MIBK 1:3, 30 s in IPA, blowdry with N_2 pistol

3. Evaporation:

   a) Evaporate 5 nm Ti, xx nm Au in Univex B.

4. Lift-off

   a) Acetone bath overnight at 60°C

   b) Lift-off in Acetone. Put sample into IPA and check result in the optical microscope. Use injection if necessary. Blow dry with N_2 pistol.

B Offset in Data of Sample 1

When we investigated sample 1, described in chapter 4, 5 and 6, we were confronted with certain offsets in the $L(I)$ data on the vertical and horizontal scale. Figure B.1 shows the $L(I)$ curves from Fig. 5.5 in chapter 5. This time, however, without the substraction of the offsets in the current bias and inductance values. The reason for the discrepancy on
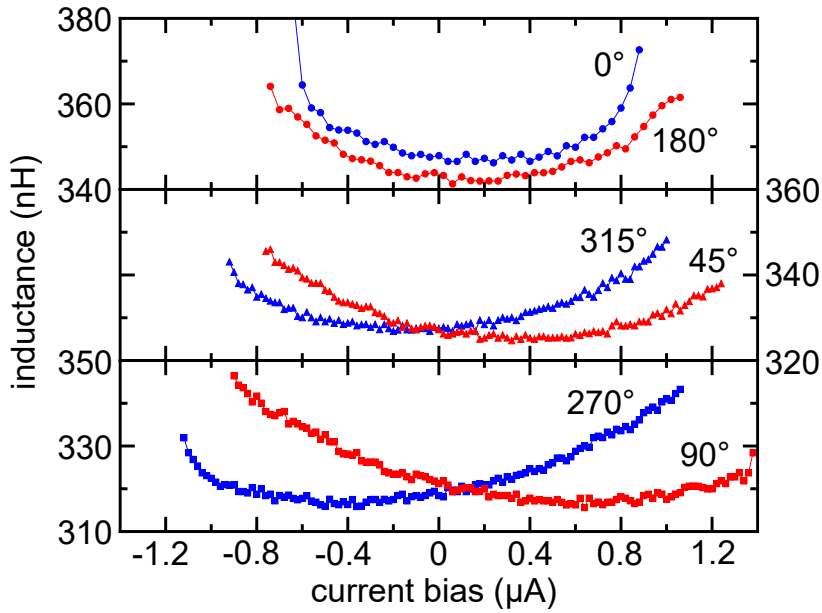
Figure B.1: Raw data from sample 1 from Fig. 5.5 plotted without applied offset.

the y-scale was a small residual field in the superconducting coil of the big 8 T magnet, caused by trapped vortices. These vortices contributed a few mT to the total in-plane magnetic field. If one nominally applies ±100 mT, the actual applied field was therefore in the order of +98/-102 mT. This results in a recogniseable difference in L_0 of a few percent.

For the whole dataset of sample 1 discussed in chapter 4 and 5, we substracted a constant current offset of +130 nA. Such an offset comes from voltage differences between the MFLI lock-in (our current source instrument) and the cold ground of the resonator. The current is defined by the voltage difference and the 1 kΩ decoupling resistor R_{D1} of the RLC circuit.

For the subsqeuent measurements after sample 1,i.e. sample 2, sample 3 and the multiterminal Josephson junction array, we solved the problem for the vertical offset by warming up the magnetic coils before a new measurement session or by a demagnitisation procedure. We got rid off the horizontal offset by measuring the current bias directly with a 100 Ω preresistor.

C Further Data of the Fraunhofer Pattern of Sample 1

In this section, we present additional Fraunhofer diffraction pattern data from sample 1, complementing the data shown in chapter 5.4.

C.1 Gate and Angle Dependence of the Diode Effect

Figure C.1**a** shows the gate dependence of the superconducting diode effect for different magnetic fields along $\hat{y}$-direction. The difference between I_c^+ and I_c^-, normalised by the

a **b**
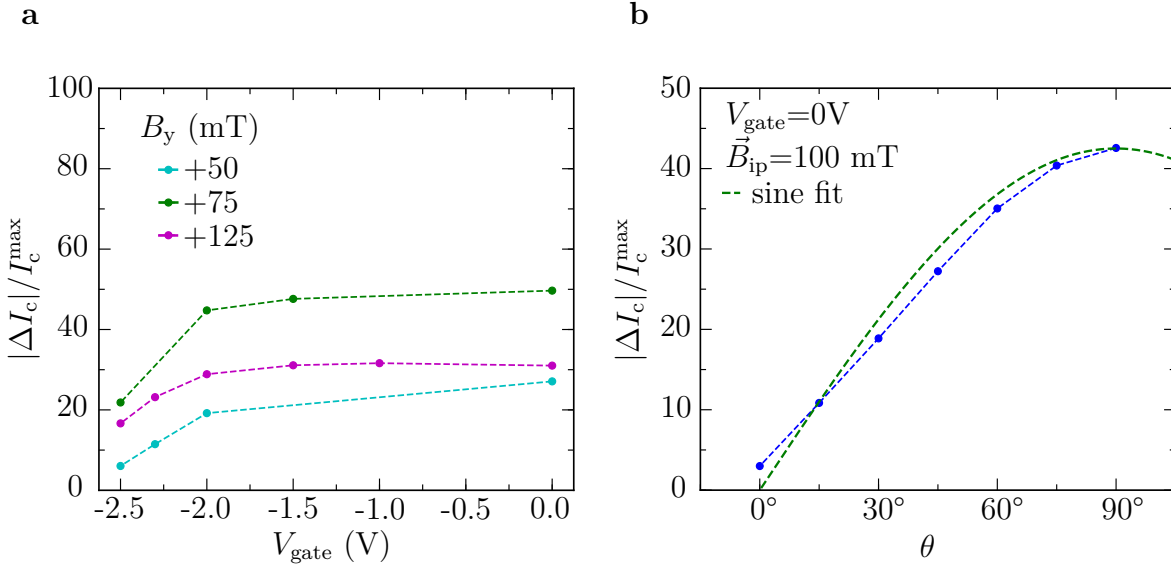
Figure C.1: **a,** Gate dependence of the non-reciprocal current at B_y =+50,+75 and +125 mT. **b,** Angle dependence of the diode effect at $\vec{B}_{ip}$=+100 mT together with a sine fit.

maximum value of I_c^+, is nearly independent of the gate what confirms the observations made by the gate dependent magnetochiral anisotropy coefficient γ_L (see section 5.3). Below -2 V, we observe a breakdown due to the depletion of the 2DEG.

In Fig. C.1**b**, the angle dependence of the non-reciprocal current at $\vec{B}_{ip}=+100$ mT is shown, extracted from the main lobe of the measured Fraunhofer patterns. Here we see again the expected sinusoidal shape.

C.2 Periodicity of the Lobes

In the interference pattern, shown in chapter 5.4, we observe a change of the periodicity of the lobes with increasing in-plane fields. This effect seems to occur regardless of whether the field is applied in $\hat{x}$ or in $\hat{y}$-direction. Figure C.2**a** shows a zoom-in of Fig. 5.10**a** with focus on the main and the first side lobe of the diffraction pattern. The deviatiaons lie within 10 % (see Fig. C.2**b**). Interestingly, if we take a closer look on the in-plane field angle
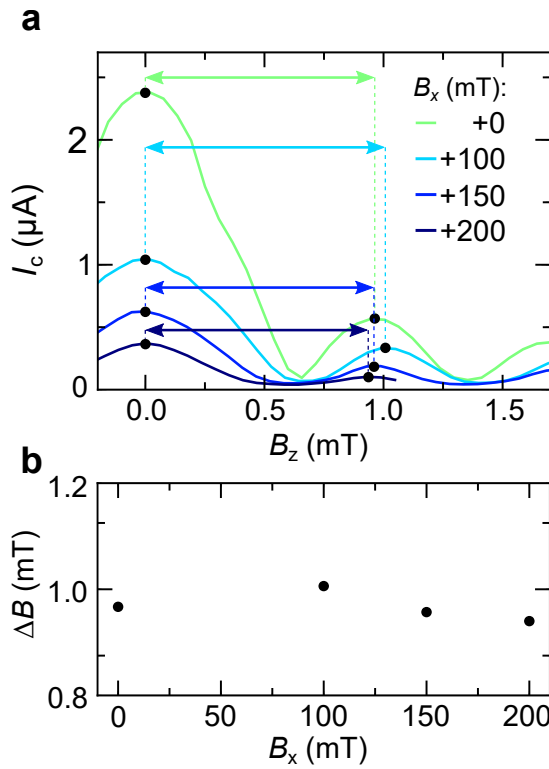
Figure C.2
a, Zoom-in on the interference pattern for different B_x discussed in chapter 5.4. **b,** Period between main and first side lobe B_z as a function of B_x.

dependence of the Fraunhofer pattern for $\vec{B}_{ip}=+100$ and $+150$ mT (Figs. C.3**a** and **c**), we see a different behaviour. The corresponding figures C.3**b** and **d** illustrate the positional change of the side lobes with respect to the angle of the applied magnetic field. In case of $\vec{B}_{ip}=+100$ mT the periodicity follows no distinct pattern, whereas for $\vec{B}_{ip}=+150$ mT, a clear angle dependence is observed.

So far, we have no explanation for these observations. Studies of Josephson junctions exposed to in-plane fields or next to Abrikosov vortex affecting the shape of the Fraunhofer

pattern have been reported in [137] and [179]. However, effects such as flux focussing, suppression of the superfluid stiffness or the influence of vortices in the film are so far not suitable for an adequate explanation. Furthermore, the facts described here go beyond the relevant research topics of this thesis.
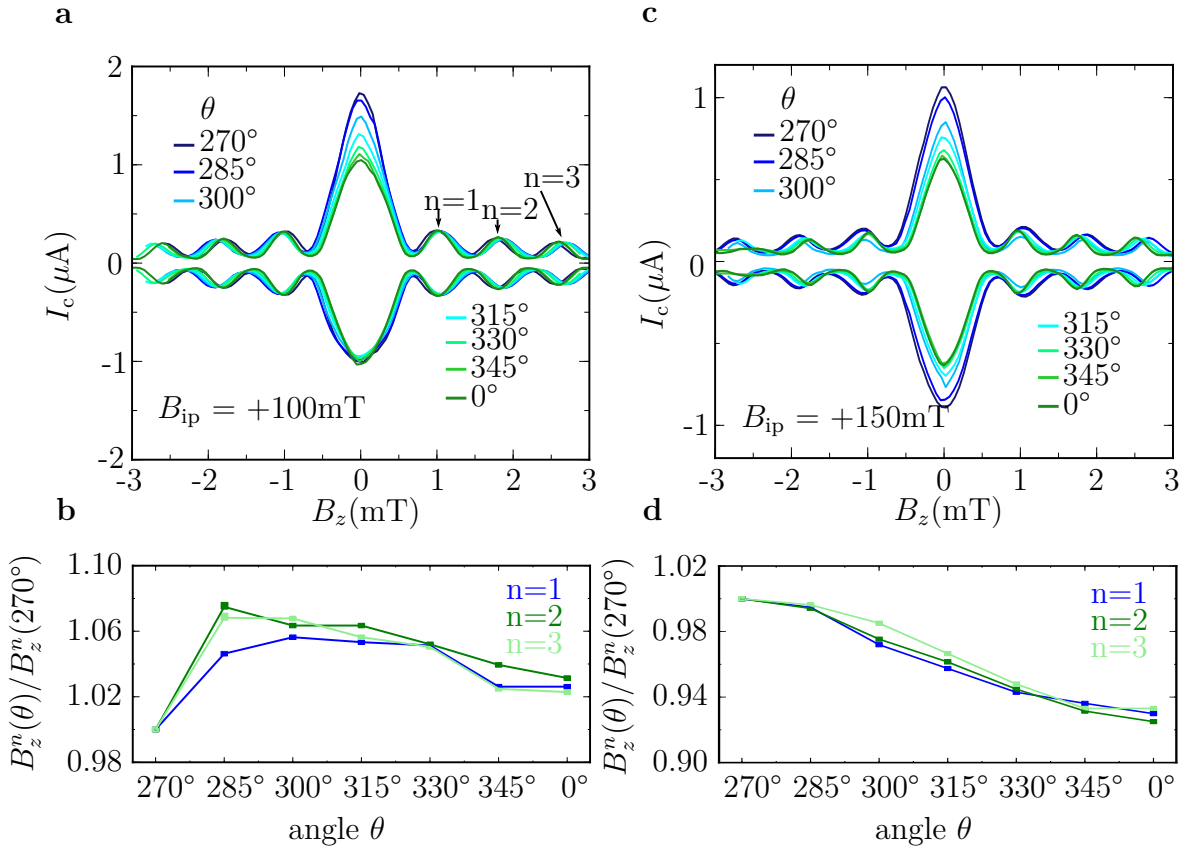
Figure C.3: Evaluation of the FP side lobe positions in B_z. **a,** Fraunhofer pattern obtained for $\vec{B}_{ip} = +100$ mT applied in different angles. **b,** This panel shows how the first, second and third side lobe of the FP change the relative position for fields applied in different angles in-plane normalised to the FP side lobe positions for $B_{ip}(\theta=270°)$.

D Magnetochiral Anisotropy in the Normal State

To see whether and how the magnetochiral anisotropy looks like above the critical temperature, we took the experimental data from the $R(T)$ measurements of sample 2 (shown in chapter 5.2) and averaged the values from 2.4 to 3 K. The result is plotted in D.1 on the left y-axis together with theoretical results from tight-binding simulations from A. Costa. The experimental and theoretical results show an extremely small MCA effect in the order
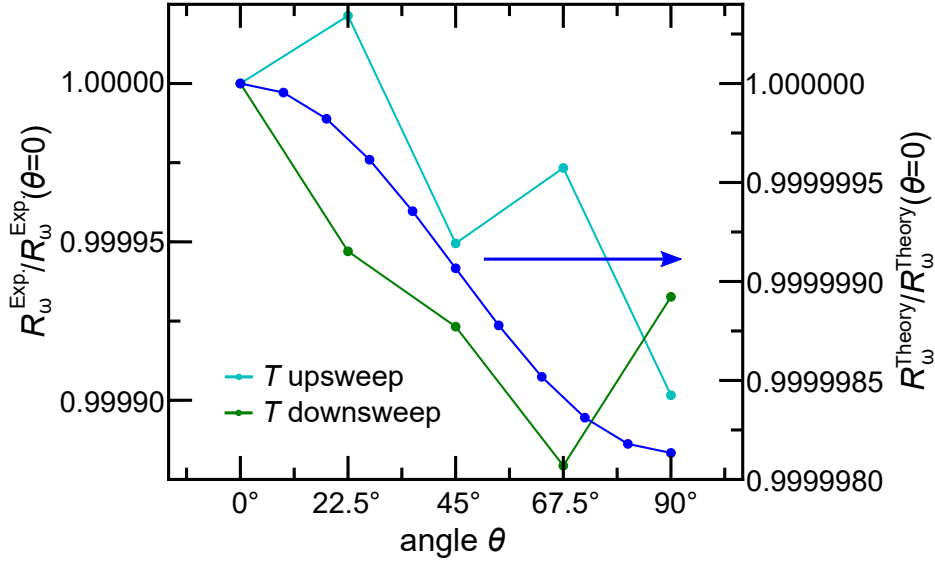
Figure D.1: **MCA above T_c**: Experimental (left-) and theoretical (right axis) normalised resistances at in-plane fields of +90 mT.

of 10^{-5}, much smaller than the magnetochiral coefficient γ_L and is close to the limit of the resolution of our measurement devices.

E Fine Structures in the Diffraction Pattern of Sample MTJJA

The colorplot in E.1**a,** shows the same data as in 7.13, but here for a smaller z-scale range (i.e. 0-1.6 kΩ). The white arrows highlight a from $B_\perp$ independent feature, whose resistance becomes smaller for increasing current bias. This feature, omnipresent in all diffraction pattern measurements, becomes smaller with increasing in-plane magnetic fields, probably due to the suppression of the induced gap in the InAs. Moreover, it shows a small tilt along B_z (not shown here), if $\vec{B}_{ip}$ is applied in $\hat{x}$. This tilt is inverted by inverting B_x.

Another interesting observation are small resistances in the main lobe of the envelope, where no dissipation should be present. These features (indicated by white arrow in Fig. E.1**b**) show a regular pattern and appear only for positive and negative in-plane magnetic fields applied between θ=45° to 315° (i.e. $\vec{B}_{ip}$ parallel to $\hat{x}$). If the in-plane field is applied in $\hat{y}$, as in Fig. E.1**a**, the subcritical currents are featureless. We made the observation of these features for $\vec{B}_{ip}$=75 mT, other measurements where not accurate enough. Because this pattern depends on the orientation of $\vec{B}_{ip}$ and shows a robust regularity, this feature might not be caused by a defect or by an unregular three-terminal Josephson junction. Experiments on new samples can give an answer whether this pattern originates from an individual 3TJJ or not.
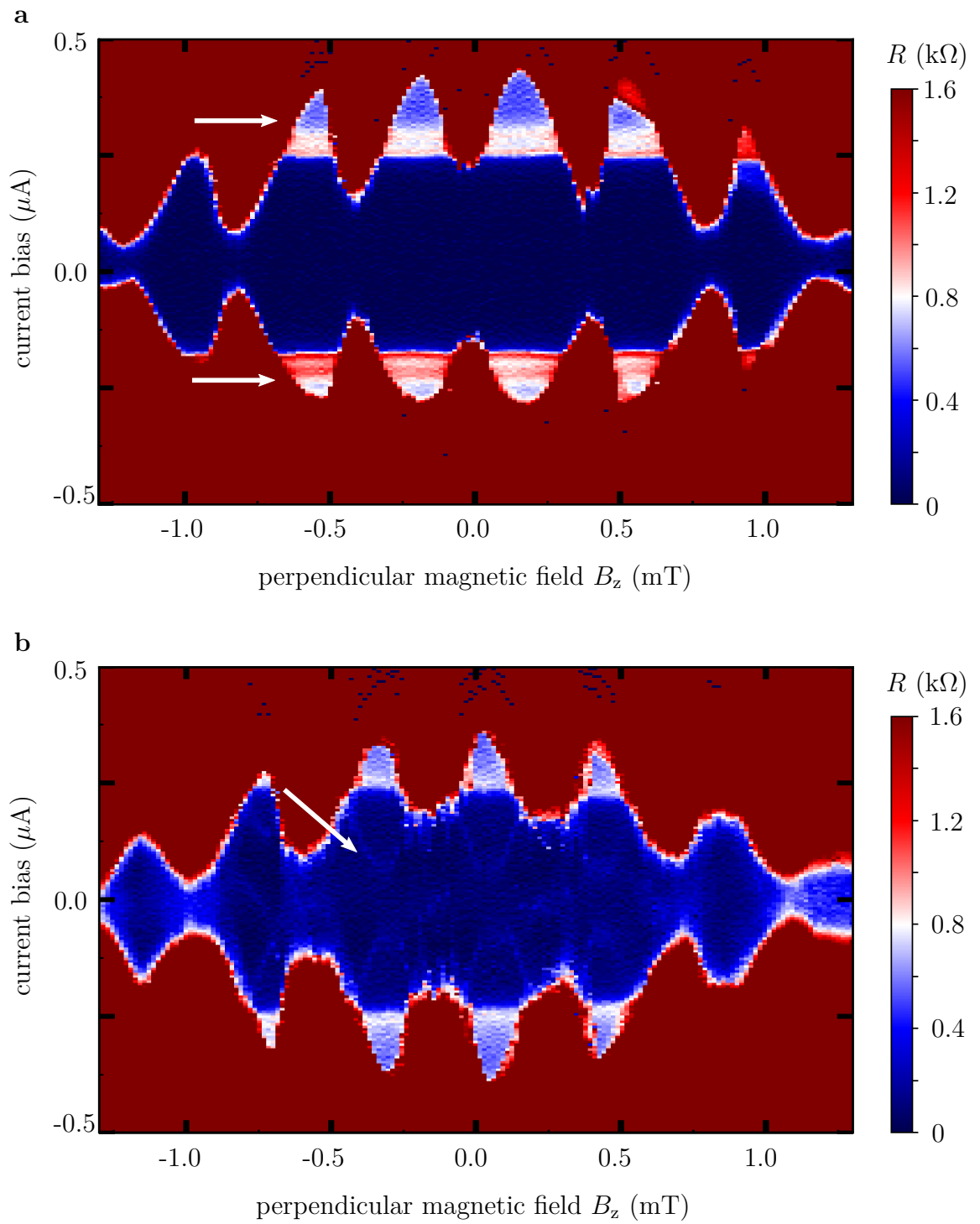
Figure E.1: **Diffraction pattern of Sample MTJJA** at $\vec{B}_{\mathrm{ip}}$=+75 mT applied **a,** parallel to $\hat{y}$ (i.e. θ=270°) and **b,** parallel to $\hat{x}$ (i.e. θ=0°).

Bibliography

1. Feynman, R. P. Simulating Physics with Computers. *International Journal of Theoretical Physics* **21,** 467–488. doi:10.1007/BF02650179 (1982).

2. Hassija, V. *et al.* Present landscape of quantum computing. *IET Quantum Communication* **1,** 42–48. doi:10.1049/iet-qtc.2020.0027 (2020).

3. Kjaergaard, M. *et al.* Superconducting Qubits: Current State of Play. *Annual Review of Condensed Matter Physics* **11,** 369–395. doi:10.1146/annurev-conmatphys-031119-050605 (2020).

4. Arute, F. *et al.* Quantum supremacy using a programmable superconducting processor. *Nature* **574,** 505–510. doi:10.1038/s41586-019-1666-5 (2019).

5. Preskill, J. Quantum computing in the NISQ era and beyond. *Quantum Journal* **2,** 1–20. doi:10.22331/q-2018-08-06-79 (2018).

6. Majorana E. Teoria simmetrica dell'elettrone e del positrone. *Nuovo Cimento* **14,** 171. doi:10.1007/BF02961314 (1937).

7. Das Sarma, S., Freedman, M. & Nayak, C. Topological quantum computation. *Physics Today* **59,** 32–38. doi:10.1063/1.2337825 (2006).

8. Beenakker, C. W. J. Search for Majorana Fermions in Superconductors. *Annu. Rev. Condens. Matter Phys.* **4,** 113–136. doi:10.1146/annurev-conmatphys-030212-184337 (2013).

9. Kitaev, A. Y. Unpaired Majorana fermions in quantum wires. *Phys.-Usp.* **44,** 131–136. doi:10.1070/1063-7869/44/10s/s29 (2001).

10. Fu, L. & Kane, C. L. Superconducting Proximity Effect and Majorana Fermions at the Surface of a Topological Insulator. *Phys. Rev. Lett.* **100,** 96407. doi:10.1103/PhysRevLett.100.096407 (2008).

11. Alicea, J. Majorana fermions in a tunable semiconductor device. *Phys. Rev. B* **81,** 125318. doi:10.1103/PhysRevB.81.125318 (2010).

12.   Lutchyn, R. M., Sau, J. D. & Das Sarma, S. Majorana Fermions and a Topological Phase Transition in Semiconductor-Superconductor Heterostructures. *Physical Review Letters* **105,** 077001. doi:`10.1103/PhysRevLett.105.077001` (2010).

13.   Oreg, Y., Refael, G. & Von Oppen, F. Helical Liquids and Majorana Bound States in Quantum Wires. *Physical Review Letters* **105,** 177002. doi:`10.1103/PhysRevLett.105.177002` (2010).

14.   Scharf, B., Pientka, F., Ren, H., Yacoby, A. & Hankiewicz, E. M. Tuning topological superconductivity in phase-controlled Josephson junctions with Rashba and Dresselhaus spin-orbit coupling. *Physical Review B* **99,** 214503. doi:`10.1103/PhysRevB.99.214503` (2019).

15.   Mourik, V. *et al.* Signatures of Majorana Fermions in Hybrid Superconductor-Semiconductor Nanowire Devices. *Science* **336,** 1003–1007. doi:`10.1126/science.1222360` (2012).

16.   Assouline, A. *et al.* Spin-Orbit induced phase-shift in Bi_2Se_3 Josephson junctions. *Nature Communications* **10,** 126. doi:`10.1038/s41467-018-08022-y` (2019).

17.   Bäuml, C. *et al.* Supercurrent and Phase Slips in a Ballistic Carbon Nanotube Bundle Embedded into a van der Waals Heterostructure. *Nano Letters* **21,** 8627–8633. doi:`10.1021/acs.nanolett.1c02565` (2021).

18.   Ren, H. *et al.* Topological superconductivity in a phase-controlled Josephson junction. *Nature* **569,** 93–98. doi:`10.1038/s41586-019-1148-9` (2019).

19.   Nakamura, J., Liang, S., Gardner, G. C. & Manfra, M. J. Direct observation of anyonic braiding statistics. *Nature Physics* **16,** 931–936. doi:`10.1038/s41567-020-1019-1` (2020).

20.   Frolov, S. M., Manfra, M. J. & Sau, J. D. Topological superconductivity in hybrid devices. *Nature Physics* **16,** 718–724. doi:`10.1038/s41567-020-0925-6` (2020).

21.   Krogstrup, P. *et al.* Epitaxy of semiconductor-superconductor nanowires. *Nature Materials* **14,** 400. doi:`10.1038/NMAT4176` (2015).

22.   Shabani, J. *et al.* Two-dimensional epitaxial superconductor-semiconductor heterostructures: A platform for topological superconducting networks. *Phys. Rev. B* **93,** 155402. doi:`10.1103/PhysRevB.93.155402` (2016).

23. Tinkham, M. *Introduction to Superconductivity* 2nd ed. (Dover Publications, 2004).

24. Kjaergaard, M. *et al.* Quantized conductance doubling and hard gap in a two-dimensional semiconductor-superconductor heterostructure. *Nature Communications* **7,** 12841. doi:`10.1038/ncomms12841` (2016).

25. Whiticar, A. M. *et al.* Coherent transport through a Majorana island in an Aharonov–Bohm interferometer. *Nature Communications* **11,** 3212. doi:`10.1038/s41467-020-16988-x` (2020).

26. Fornieri, A. *et al.* Evidence of topological superconductivity in planar Josephson junctions. *Nature* **569,** 89–92. doi:`10.1038/s41586-019-1068-8` (2019).

27. Lee, E. J. *et al.* Spin-resolved Andreev levels and parity crossings in hybrid superconductor-semiconductor nanostructures. *Nature Nanotechnology* **9,** 79–84. doi:`10.1038/nnano.2013.267` (2014).

28. Valentini, M. *et al.* Nontopological zero-bias peaks in full-shell nanowires induced by flux-tunable Andreev states. *Science* **373,** 82–88. doi:`10.1126/science.abf1513` (2021).

29. Yu, P. *et al.* Non-Majorana states yield nearly quantized conductance in proximatized nanowires. *Nature Physics* **17,** 482–488. doi:`10.1038/s41567-020-01107-w` (2021).

30. Baumgartner, C. *et al.* Josephson Inductance as a Probe for Highly Ballistic Semiconductor-Superconductor Weak Links. *Physical Review Letters* **126,** 037001. doi:`10.1103/PhysRevLett.126.037001` (2021).

31. Szombati, D. B. *et al.* Josephson φ_0-junction in nanowire quantum dots. *Nat Phys* **12,** 568–572. doi:`10.1038/NPHYS3742` (2016).

32. Baumgartner, C. *et al.* Supercurrent rectification and magnetochiral effects in symmetric Josephson junctions. *Nature Nanotechnology* **17,** 39–44. doi:`10.1038/s41565-021-01009-9` (2021).

33. Riwar, R. P., Houzet, M., Meyer, J. S. & Nazarov, Y. V. Multi-terminal Josephson junctions as topological matter. *Nature Communications* **7,** 11167. doi:`10.1038/ncomms11167` (2016).

34. Sato, M. & Ando, Y. Topological superconductors: A review. *Reports on Progress in Physics* **80,** 076501. doi:`10.1088/1361-6633/aa6ac7` (2017).

35. Mackenzie, A. P. & Maeno, Y. The superconductivity of Sr_2RuO_4 and the physics of spin-triplet pairing. *Reviews of Modern Physics* **75,** 657–712. doi:`10.1103/RevModPhys.75.657` (2003).

36. Mackenzie, A. P., Scaffidi, T., Hicks, C. W. & Maeno, Y. Even odder after twenty-three years: The superconducting order parameter puzzle of Sr_2RuO_4. *npj Quantum Materials* **2,** 40. doi:`10.1038/s41535-017-0045-4` (2017).

37. Hor, Y. S. *et al.* Superconductivity in CuxBi2Se3 and its implications for pairing in the undoped topological insulator. *Physical Review Letters* **104,** 057001. doi:`10.1103/PhysRevLett.104.057001` (2010).

38. Butch, N. P., Syers, P., Kirshenbaum, K., Hope, A. P. & Paglione, J. Superconductivity in the topological semimetal YPtBi. *Phys. Rev. B* **84,** 220504. doi:`10.1103/PhysRevB.84.220504` (2011).

39. Brydon, P. M., Wang, L., Weinert, M. & Agterberg, D. F. Pairing of j=3/2 Fermions in Half-Heusler Superconductors. *Physical Review Letters* **116,** 177001. doi:`10.1103/PhysRevLett.116.177001` (2016).

40. Klitzing, K. V., Dorda, G. & Pepper, M. New Method for High-Accuracy Determination of the Fine-Structure Constant Based on Quantized Hall Resistance. *Physical Review Letters* **45,** 494–497. doi:`10.1103/PhysRevLett.45.494` (1980).

41. Van Wees, B. J. *et al.* Quantized Conductance of Point Contacts in a Two-Dimensional Electron Gas. *Physical Review Letters* **60,** 848–850. doi:`10.1103/PhysRevLett.60.848` (1988).

42. Ihn, T. *Semiconductor Nanostructures* (Oxford University Press, 2010).

43. Gross, Rudolf Marx, A. *Festkörperphysik* (De Gruyter Oldenbourg, 2010).

44. Heikkilä, T. T. *The Physics of Nanoelectronics* (Oxford University Press, 2013).

45. Schäpers, T. *Superconductor/Semiconductor Junctions* (Springer, 2001).

46. Vurgaftman, I., Meyer, J. R. & Ram-Mohan, L. R. Band parameters for III-V compound semiconductors and their alloys. *Journal of Applied Physics* **89,** 5815–5875. doi:`10.1063/1.1368156` (2001).

47. Schmidt-Böcking, H. *et al.* The Stern-Gerlach experiment revisited. *European Physical Journal H* **41,** 327–364. doi:`10.1140/epjh/e2016-70053-2` (2016).

48. Dresselhaus, G. Spin-Orbit Coupling Effects in Zinc Blende Structures. *Phys. Rev.* **100,** 580–586. doi:`10.1103/PhysRev.100.580` (1955).

49. Bychkov, Y. A. & Rashba, E. I. Oscillatory effects and the magnetic suscepti-bility of carriers in inversion layers. *Journal of Physics C: Solid State Physics* **17,** 6039–6045. doi:`10.1088/0022-3719/17/33/015` (1984).

50. Bychkov, Y. A. & Rashba, E. I. Properties of a 2D electron gas with lifted spectral degeneracy. *JETP letters* **39,** 78–83 (1984).

51. Ganichev, S. D. *et al.* Experimental Separation of Rashba and Dresselhaus Spin Splittings in Semiconductor Quantum Wells. *Physical Review Letters* **92,** 256601. doi:`10.1103/PhysRevLett.92.256601` (2004).

52. Ho Park, Y. *et al.* Separation of Rashba and Dresselhaus spin-orbit interactions using crystal direction dependent transport measurements. *Applied Physics Let-ters* **103,** 252407. doi:`10.1063/1.4855495` (2013).

53. Winkler, R. *Spin–Orbit Coupling Effects in Two-Dimensional Electron and Hole Systems* **3,** 278. doi:`10.1787/9789264059597-8-en` (2003).

54. Mayer, W. *et al.* Superconducting Proximity Effect in InAsSb Surface Quantum Wells with In Situ Al Contacts. *ACS Applied Electronic Materials* **2,** 2351. doi:`10.1021/acsaelm.0c00269` (2020).

55. H. K. Onnes. Further experiements with liquid helium. D. On the change of the elctrical resistance of pure metals at very low tem- peratures, etc. V. The disappearance of the resistance of mercury. *Leiden Comm.* **122b,** 264 (1911).

56. Ginzburg, V.L. and Landau, L. On the Theory of Superconductivity. *Soviet Physics JETP* **20,** 1064 (1950).

57. J. Bardeen, L. N. Cooper, J. S. Theory of superconductivity. *Phys. Rev.* **108,** 1175. doi:`10.1201/9780429495700` (1957).

58. Kjaergaard, M. *Proximity Induced Superconducting Properties in One and Two Dimensional Semiconductors* PhD thesis (2015).

59. C. Enss, S. H. *Low-Temperature Physics* **4613** (Springer, 2005).

60. Gor'kov, L. P. Microscopic Derivation of the Ginzburg-Landau Equations in the Theory of Superconductivity. *Soviet Physics JETP* **36,** 1364–1367 (1959).

61. Singh, N. P., Gupta, S. C. & Sood, B. R. An experiment to determine the skin depth and Fermi velocity in metals. *American Journal of Physics* **70,** 845–846. doi:`10.1119/1.1485716` (2002).

62. Rainis, D. & Loss, D. Majorana qubit decoherence by quasiparticle poisoning. *Physical Review B* **85,** 1–10. doi:`10.1103/PhysRevB.85.174533` (2012).

63. Albrecht, S. M. *et al.* Exponential protection of zero modes in Majorana islands. *Nature* **531,** 206–209. doi:`10.1038/nature17162` (2016).

64. O'Farrell, E. C. *et al.* Hybridization of Subgap States in One-Dimensional Superconductor-Semiconductor Coulomb Islands. *Physical Review Letters* **121,** 256803. doi:`10.1103/PhysRevLett.121.256803` (2018).

65. Wallraff, A. *et al.* Strong coupling of a single photon to a superconducting qubit using circuit quantum electrodynamics. *Nature* **431,** 162–167. doi:`10.1038/nature02851` (2004).

66. Walsh, E. D. *et al.* Josephson junction infrared single-photon detector. *Science* **372,** 409–412. doi:`10.1126/science.abf5539` (2021).

67. Bal, M., Deng, C., Orgiazzi, J. L., Ong, F. R. & Lupascu, A. Ultrasensitive magnetic field detection using a single artificial atom. *Nature Communications* **3,** 1324. doi:`10.1038/ncomms2332` (2012).

68. Clarke, J. Josephson Junction Detectors. *Science* **184,** 1235–1242. doi:`10.1126/science.184.4143.1235` (1974).

69. Ando, F. *et al.* Observation of superconducting diode effect. *Nature* **584,** 373–376. doi:`10.1038/s41586-020-2590-4` (2020).

70. Lyu, Y. Y. *et al.* Superconducting diode effect via conformal-mapped nanoholes. *Nature Communications* **12,** 2703. doi:`10.1038/s41467-021-23077-0` (2021).

71. Aguado, R. A perspective on semiconductor-based superconducting qubits. *Applied Physics Letters* **117,** 240501. doi:`10.1063/5.0024124` (2020).

72. Josephson, B. D. Supercurrents through barriers. *Advances in Physics* **14,** 419–451. doi:`10.1080/00018736500101091` (1965).

73. Alidoust, M., Shen, C. & Žutić, I. Cubic spin-orbit coupling and anomalous Josephson effect in planar junctions. *Physical Review B* **103,** L060503. doi:`10.1103/physrevb.103.1060503` (2021).

74. Stewart, W. C. Current-Voltage Characteristics of Josephson Junctions. *Appl. Phys. Lett.* **12,** 277. doi:`https://doi.org/10.1063/1.1651991` (1968).

75. McCumber, D. E. Effect of ac Impedance on dc Voltage-Current Characteristics of Superconductor Weak-Link Junctions. *Journal of Applied Physics* **39,** 3113–3118. doi:`10.1063/1.1656743` (1968).

76. Barone, A. & Paternò, G. *Physics and Applications of the Josephson Effect* doi:`10.1002/352760278x` (John Wiley & Sons, Inc., 1982).

77. Ambegaokar, V. & Halperin, B. I. Voltage Due to Thermal Noise in the dc Josephson Effect. *Phys. Rev. Lett.* **22,** 1364–1366. doi:`10.1103/PhysRevLett.22.1364` (1969).

78. Thouless, J. T. E. & J., D. Numerical studies of localization in disordered systems. *Journal of Physics C: Solid State Physics* **5,** 807–820. doi:`10.1143/JPSJ.37.904` (1972).

79. Altland, A., Gefen, Y. & Montambaux, G. What is the Thouless Energy for Ballistic Systems? *Physical Review Letters* **76,** 1130–1133. doi:`10.1103/PhysRevLett.76.1130` (1996).

80. Pientka, F. *et al.* Topological Superconductivity in a Planar Josephson Junction. *Phys. Rev. X* **7,** 21032. doi:`10.1103/PhysRevX.7.021032` (2017).

81. Dartiailh, M. C. *et al.* Phase Signature of Topological Transition in Josephson Junctions. *Physical Review Letters* **126,** 036802. doi:`10.1103/PhysRevLett.126.036802` (2021).

82. Ke, C. T. *et al.* Ballistic superconductivity and tunable π–junctions in InSb quantum wells. *Nature Communications* **10,** 3764. doi:`10.1038/s41467-019-11742-4` (2019).

83. Andreev, A. F. Thermal Conductivity of the Intermediate State of Superconductors. *Soviet Physics JETP* **20,** 1490–1493. doi:`10.1088/0022-3719/1/3/323` (1965).

84. Drachmann, A. C. C. *Enhancing transparent superconductor-semiconductor hybrids* PhD thesis (2020).

85. Blonder, G. E., Tinkham, M. & Klapwijk, T. M. Transition from metallic to tunneling regimes in superconducting microconstrictions: Excess current, charge imbalance, and supercurrent conversion. *Phys. Rev. B* **25,** 4515–4532. doi:`10.1103/PhysRevB.25.4515` (1982).

86. C. W. J. Beenakker. Universal Limit of Critical-Current Fluctuations in Mesoscopic Josephson Junctions. *Physical Review Letters* **67,** 3836–3839. doi:`10.1103/PhysRevLett.67.3836` (1991).

87. Klapwijk, T. M. Proximity Effect From an Andreev Perspective. *Journal of Superconductivity* **17,** 593–611. doi:`10.1007/s10948-004-0773-0` (2004).

88.   Kulik, I. Macroscopic Quantization and the Proximity Effect in S-N-S Junctions. *Soviet Physics JETP* **30,** 944 (1970).

89.   B. Pannetier and H. Courtois. Andreev Reflection and Proximity effect. *Journal of Low Temperature Physics* **118,** 599–615. doi:10.1023/A:1004635226825 (2000).

90.   Golubov, A. A., Kupriyanov, M. Y. & E. Il'chev. The current-phase relation in Josephson junctions. *Rev. Mod. Phys.* **76,** 411–469. doi:10.1103/RevModPhys.76.411 (2004).

91.   Della Rocca, M. L. *et al.* Measurement of the current-phase relation of superconducting atomic contacts. *Physical Review Letters* **99,** 127005. doi:10.1103/PhysRevLett.99.127005 (2007).

92.   Beenakker, C. W. & Van Houten, H. Josephson current through a superconducting quantum point contact shorter than the coherence length. *Physical Review Letters* **66,** 3056–3059. doi:10.1103/PhysRevLett.66.3056 (1991).

93.   Furusaki, A. & Tsukada, M. DC Josephson Effect and Andreev Reflection. *Solid State Communications* **78,** 299–302. doi:10.1016/0038-1098(91)90201-6 (1991).

94.   Waldram, J. *Superconductivity of Metals and Cuprates* (Routledge, 1996).

95.   Eilenberger, G. Transformation of Gorkov's equation for Type II Superconductors into Transport-Like Equations. *Zeitschrift für Physik* **214,** 195–213. doi:10.1007/BF01379803 (1968).

96.   Usadel, K. D. Generalized Diffusion Equation for Superconducting Alloys. *Physical Review Letters* **25,** 507–509. doi:10.1103/PhysRevLett.25.507 (1970).

97.   Belzig, W., Wilhelm, F. K., Bruder, C., Schön, G. & Zaikin, A. D. Quasiclassical Green's function approach to mesoscopic superconductivity. *Superlattices and Microstructures* **25,** 1251–1288. doi:10.1006/spmi.1999.0710 (1999).

98.   Aminov, B., Golubov, A. & Kupriyanov, M. Y. Quasiparticle current in ballistic constrictions with finite transparencies of interfaces. *Physical Review B* **53,** 365–373. doi:10.1103/PhysRevB.53.365 (1996).

99.   Chrestin, A., Matsuyama, T. & Merkt, U. Evidence for a proximity-induced energy gap in Nb/InAs/Nb junctions. *Physical Review B* **55,** 8457–8465. doi:10.1103/PhysRevB.55.8457 (1997).

100. Cherkez, V. *et al.* Proximity Effect between Two Superconductors Spatially Resolved by Scanning Tunneling Spectroscopy. *Physical Review X* **4,** 011033. doi:`10.1103/PhysRevX.4.011033` (2014).

101. Le Sueur, H., Joyez, P., Pothier, H., Urbina, C. & Esteve, D. Phase Controlled Superconducting Proximity Effect Probed by Tunneling Spectroscopy. *Phys. Rev. Lett.* **100,** 197002. doi:`10.1103/PhysRevLett.100.197002` (2008).

102. Bergeret, F. S. & Tokatly, I. V. Theory of diffusive φ_0 Josephson junctions in the presence of spin-orbit coupling. *EPL* **110,** 57005. doi:`10.1209/0295-5075/110/57005` (2015).

103. Konschelle, F., Tokatly, I. V. & Bergeret, F. S. Theory of the spin-galvanic effect and the anomalous phase shift φ_0 in superconductors and Josephson junctions with intrinsic spin-orbit coupling. *Phys. Rev. B* **92,** 125443. doi:`10.1103/PhysRevB.92.125443` (2015).

104. Silaev, M. A., Tokatly, I. V. & Bergeret, F. S. Anomalous current in diffusive ferromagnetic Josephson junctions. *Phys. Rev. B* **95,** 184508. doi:`10.1103/PhysRevB.95.184508` (2017).

105. Buzdin, A. Direct Coupling Between Magnetism and Superconducting Current in the Josephson φ_0 Junction. *Phys. Rev. Lett.* **101,** 107005. doi:`10.1103/PhysRevLett.101.107005` (2008).

106. Yokoyama, T., Eto, M. & Nazarov, Y. V. Anomalous Josephson effect induced by spin-orbit interaction and Zeeman effect in semiconductor nanowires. *Phys. Rev. B* **89,** 195407. doi:`10.1103/PhysRevB.89.195407` (2014).

107. Mayer, W. *et al.* Gate controlled anomalous phase shift in Al/InAs Josephson junctions. *Nature Communications* **11,** 212. doi:`10.1038/s41467-019-14094-1` (2020).

108. Strambini, E. *et al.* A Josephson phase battery. *Nature Nanotechnology* **15,** 656–661. doi:`10.1038/s41565-020-0712-7` (2020).

109. Rohlfing, F. *et al.* Doppler shift in Andreev reflection from a moving superconducting condensate in Nb/InAs Josephson junctions. *Phys. Rev. B* **80,** 220507. doi:`10.1103/PhysRevB.80.220507` (2009).

110. Chang, W. *et al.* Hard gap in epitaxial semiconductor-superconductor nanowires. *Nature Nanotechnology* **10,** 232–236. doi:`10.1038/NNANO.2014.306` (2015).

111. Krizek, F. *et al.* Field effect enhancement in buffered quantum nanowire networks. *Physical Review Materials* **2,** 093401. doi:`10.1103/PhysRevMaterials.2.093401` (2018).

112. Vaitiekenas, S. *et al.* Selective-Area-Grown Semiconductor-Superconductor Hybrids: A Basis for Topological Networks. *Physical Review Letters* **121,** 147701. doi:`10.1103/PhysRevLett.121.147701` (2018).

113. Carrad, D. J. *et al.* Shadow Epitaxy for In Situ Growth of Generic Semiconductor/Superconductor Hybrids. *Advanced Materials* **32,** 1908411. doi:`10.1002/adma.201908411` (2020).

114. Kanne, T. *et al.* Epitaxial Pb on InAs nanowires for quantum devices. *Nature Nanotechnology* **16,** 776–781. doi:`10.1038/s41565-021-00900-9` (2021).

115. Pendharkar, M. *et al.* Parity-preserving and magnetic field–resilient superconductivity in InSb nanowires with Sn shells. *Science* **372,** 508–511. doi:`10.1126/science.aba5211` (2021).

116. Bjergfelt, M. *et al.* Superconducting vanadium/indium-arsenide hybrid nanowires. *Nanotechnology* **30,** 294005. doi:`10.1088/1361-6528/ab15fc` (2019).

117. Meservey, R. & Tedrow, P. M. Properties of Very Thin Aluminum Films. *Journal of Applied Physics* **42,** 51–53. doi:`10.1063/1.1659648` (1971).

118. Hieke, S. W., Breitbach, B., Dehm, G. & Scheu, C. Microstructural evolution and solid state dewetting of epitaxial Al thin films on sapphire (α-Al2O3). *Acta Materialia* **133,** 356–366. doi:`10.1016/j.actamat.2017.05.026` (2017).

119. Pauka, S. J. *et al.* Repairing the surface of InAs-based topological heterostructures. *Journal of Applied Physics* **128,** 114301. doi:`10.1063/5.0014361` (2020).

120. Krizek, F. *et al.* Growth of InAs Wurtzite Nanocrosses from Hexagonal and Cubic Basis. *Nano Letters* **17,** 6090–6096. doi:`10.1021/acs.nanolett.7b02604` (2017).

121. Gazibegovic, S. *et al.* Epitaxy of advanced nanowire quantum devices. *Nature* **548,** 434–438. doi:`10.1038/nature23468` (2017).

122. Khan, S. A. *et al.* Highly transparent gatable superconducting shadow junctions. *ACS Nano* **14,** 14605–14615. doi:`10.1021/acsnano.0c02979` (2020).

123. Drachmann, A. C. *et al.* Anodic oxidation of epitaxial superconductor-semiconductor hybrids. *Physical Review Materials* **5,** 013805. doi:`10.1103/PhysRevMaterials.5.013805` (2021).

124. Frész, L. *Fabrication and measurements of Josephson junction chains on epitaxial Al-InAs heterostructures* (University of Regensburg, 2020).

125. Romijn, J., Klapwijk, T. M., Renne, M. J. & Mooij, J. E. Critical pair-breaking current in superconducting aluminum strips far below T_c. *Physical Review B* **26,** 3648–3655. doi:10.1103/PhysRevB.26.3648 (1982).

126. Fuchs, L. Interplay of Spin-Orbit Interaction and Two-Dimensional Superconductivity in Al / InAs Heterostructures. *PhD Thesis* (2021).

127. Hatke, A. T., Wang, T., Thomas, C., Gardner, G. C. & Manfra, M. J. Mobility in excess of 10^6 cm^2/Vs in InAs quantum wells grown on lattice mismatched InP substrates. *Applied Physics Letters* **111,** 142106. doi:10.1063/1.4993784 (2017).

128. Wickramasinghe, K. S. *et al.* Transport properties of near surface InAs two-dimensional heterostructures. *Applied Physics Letters* **113,** 262104. doi:10.1063/1.5050413 (2018).

129. Kjaergaard, M. *et al.* Transparent Semiconductor-Superconductor Interface and Induced Gap in an Epitaxial Heterostructure Josephson Junction. *Phys. Rev. Applied* **7,** 34029. doi:10.1103/PhysRevApplied.7.034029 (2017).

130. Wharam, D. A. *et al.* One-dimensional transport and the quantisation of the ballistic resistance. *Journal of Physics C: Solid State Physics* **21,** L209–L214. doi:10.1088/0022-3719/21/8/002 (1988).

131. Beenakker, C. W. J. Quantum transport in semiconductor-superconductor microjunctions. *Phys. Rev. B* **46,** 12841–12844. doi:10.1103/PhysRevB.46.12841 (1992).

132. Gül, Ö. *et al.* Ballistic Majorana nanowire devices. *Nature Nanotechnology* **13,** 192–197. doi:10.1038/s41565-017-0032-8 (2018).

133. Zhang, H. *et al.* Ballistic superconductivity in semiconductor nanowires. *Nature Communications* **8,** 16025. doi:10.1038/ncomms16025 (2017).

134. Dynes, R. C., Narayanamurti, V. & Garno, J. P. Direct measurement of quasiparticle-lifetime broadening in a strong-coupled superconductor. *Physical Review Letters* **41,** 1509–1512. doi:10.1103/PhysRevLett.41.1509 (1978).

135. Meservey, R; Tedrow, P. M. Measurements of the Kinetic Inductance of Superconducting Linear Structures. *Journal of Applied Physics* **40,** 2028. doi:10.1063/1.1657905 (1969).

136. *https://lmfit.github.io/lmfit-py/builtin_models.html#lmfit.models.BreitWignerModel* Mar. 28, 2022.

137. Suominen, H. J. *et al.* Anomalous Fraunhofer interference in epitaxial superconductor-semiconductor Josephson junctions. *Phys. Rev. B* **95,** 35307. doi:`10.1103/PhysRevB.95.035307` (2017).

138. Dartiailh, M. C. *et al.* Missing Shapiro steps in topologically trivial Josephson junction on InAs quantum well. *Nature Communications* **12,** 78. doi:`10.1038/s41467-020-20382-y` (2021).

139. Hüttner, N. *ongoing PhD thesis* (University of Regensburg).

140. Scaff, J. H. and Ohl, R. S. Development of silicon crystal rectifiers for microwave radar receivers. *The Bell System Technical Journal* **26,** 1–30. doi:`10.1002/j.1538-7305.1947.tb01310.x` (1947).

141. Shockley, W. The theory of p-n junctions in semiconductors and p-n junction transistors. *The Bell System Technical Journal* **28,** 435–489. doi:`https://doi.org/10.1002/j.1538-7305.1949.tb03645.x` (1949).

142. Hoshino, S., Wakatsuki, R., Hamamoto, K. & Nagaosa, N. Nonreciprocal charge transport in two-dimensional noncentrosymmetric superconductors. *Physical Review B* **98,** 054510. doi:`10.1103/PhysRevB.98.054510` (2018).

143. Onsager, L. Reciprocal Relations in Irreversible Processes. *Physical Review* **37,** 405. doi:`10.1142/9789814293273_0013` (1931).

144. Ryogo Kubo. Statistical-mechanical Theory of Irreversible Processes. *Journal of the Physical Society of Japan* **12,** 570. doi:`10.1143/JPSJ.12.570` (1957).

145. Tokura, Y. & Nagaosa, N. Nonreciprocal responses from non-centrosymmetric quantum materials. *Nature Communications* **9,** 3740. doi:`10.1038/s41467-018-05759-4` (2018).

146. Rikken, G. L., Fölling, J. & Wyder, P. Electrical Magnetochiral Anisotropy. *Physical Review Letters* **87,** 236602. doi:`10.1103/PhysRevLett.87.236602` (2001).

147. Rikken, G. L. & Wyder, P. Magnetoelectric Anisotropy in Diffusive Transport. *Physical Review Letters* **94,** 016601. doi:`10.1103/PhysRevLett.94.016601` (2005).

148. Wakatsuki, R. *et al.* Nonreciprocal charge transport in noncentrosymmetric superconductors. *Science Advances* **3,** e1602390. doi:`10.1126/sciadv.1602390` (2017).

149. Wakatsuki, R. & Nagaosa, N. Nonreciprocal Current in Noncentrosymmetric Rashba Superconductors. *Physical Review Letters* **121,** 026601. doi:`10.1103/PhysRevLett.121.026601` (2018).

150. Itahashi, Y. M. *et al.* Nonreciprocal transport in gate-induced polar superconductor SrTiO$_3$. *Science Advances* **6.** doi:`10.1126/sciadv.aay9120` (2020).

151. Ideue, T. *et al.* Bulk rectification effect in a polar semiconductor. *Nature Physics* **13,** 578–583. doi:`10.1038/nphys4056` (2017).

152. Groth, C. W., Wimmer, M., Akhmerov, A. R. & Waintal, X. Kwant: A software package for quantum transport. *New Journal of Physics* **16,** 063065. doi:`10.1088/1367-2630/16/6/063065` (2014).

153. Seraide, R. M. & Hai, G. Q. Low-Temperature Electron Mobility in Parabolic Quantum Wells. *Brazilian Journal of Physics* **32,** 344–346. doi:`10.1590/S0103-97332002000200026` (2002).

154. Yamakage, A., Sato, M., Yada, K., Kashiwaya, S. & Tanaka, Y. Anomalous Josephson current in superconducting topological insulator. *Physical Review B* **87,** 100510. doi:`10.1103/PhysRevB.87.100510` (2013).

155. Baumgartner, C. *et al.* Effect of Rashba and Dresselhaus spin–orbit coupling on supercurrent rectification and magnetochiral anisotropy of ballistic Josephson junctions. *Journal of Physics: Condensed Matter* **34,** 154005. doi:`10.1088/1361-648x/ac4d5e` (2022).

156. Wang, T. *et al.* The dependence of aluminum lattice orientation on semiconductor lattice parameter in planar InAs/Al hybrid heterostructures. *Journal of Crystal Growth* **535,** 125570. doi:`10.1016/j.jcrysgro.2020.125570` (2020).

157. Aguado, R. & Kouwenhoven, L. P. Majorana qubits for topological quantum computing. *Physics Today* **73,** 44–50. doi:`10.1063/pt.3.4499` (2020).

158. Pal, B. *et al.* Josephson diode effect from Cooper pair momentum in a topological semimetal. *arXiv,* 1–14 (2021).

159. Daido, A., Ikeda, Y. & Yanase, Y. Intrinsic Superconducting Diode Effect. *Physical Review Letters* **128,** 37001. doi:`10.1103/physrevlett.128.037001` (2022).

160. Pekerten, B., Pakizer, J. D., Hawn, B. & Matos-Abiague, A. Anisotropic topological superconductivity in Josephson junctions. *Physical Review B* **105,** 054504. doi:10.1103/physrevb.105.054504 (2022).

161. Moehle, C. M. *et al.* InSbAs Two-Dimensional Electron Gases as a Platform for Topological Superconductivity. *Nano Letters* **21,** 9990–9996. doi:10.1021/acs.nanolett.1c03520 (2021).

162. Yokoyama, T. & Nazarov, Y. V. Singularities in the Andreev spectrum of a multiterminal Josephson junction. *Physical Review B* **92,** 155437. doi:10.1103/PhysRevB.92.155437 (2015).

163. Vandersypen, L. M. & Eriksson, M. A. Quantum computing with semiconductor spins. *Physics Today* **72,** 38–45. doi:10.1063/PT.3.4270 (2019).

164. Igor Žutić Jaroslav Fabian, S. D. S. Spintronics: Fundamentals and applications. *Reviews of Modern Physics* **76,** 323–410. doi:10.1103/RevModPhys.76.323 (2004).

165. Heck, B. V., Mi, S. & Akhmerov, A. R. Single fermion manipulation via superconducting phase differences in multiterminal Josephson junctions. *Physical Review B* **90,** 155450. doi:10.1103/PhysRevB.90.155450 (2014).

166. Nowak, M. P., Wimmer, M. & Akhmerov, A. R. Supercurrent carried by nonequilibrium quasiparticles in a multiterminal Josephson junction. *Physical Review B* **99,** 075416. doi:10.1103/PhysRevB.99.075416 (2019).

167. Yan, B. & Felser, C. Topological Materials : Weyl Semimetals. *Annu. Rev. Condens. Matter Phys.* **8,** 337–354. doi:10.1146/annurev-conmatphys-031016-025458 (2017).

168. Armitage, N. P. Weyl and Dirac semimetals in three-dimensional solids. *Reviews of Modern Physics* **90,** 15001. doi:10.1103/RevModPhys.90.015001 (2018).

169. Hosur, P. & Qi, X. Recent developments in transport phenomena in Weyl semimetals. *Comptes Rendus Physique* **14,** 857–870. doi:10.1016/j.crhy.2013.10.010 (2013).

170. Bansil, A., Lin, H. & Das, T. Colloquium: Topological band theory. *Reviews of Modern Physics* **88,** 1–37. doi:10.1103/RevModPhys.88.021004 (2016).

171. Potter, A. C., Kimchi, I. & Vishwanath, A. Quantum oscillations from surface Fermi arcs in Weyl and Dirac semimetals. *Nature Communications* **5,** 5161. doi:10.1038/ncomms6161 (2014).

172. Moll, P. J. *et al.* Transport evidence for Fermi-arc-mediated chirality transfer in the Dirac semimetal Cd_3As_2. *Nature* **535,** 266–270. doi:10.1038/nature18276 (2016).

173. Bernevig, B. A. It's been a Weyl coming. *Nature Physics* **11,** 698–699. doi:10.1038/nphys3454 (2015).

174. Xu, S. Y. *et al.* Discovery of a Weyl fermion semimetal and topological Fermi arcs. *Science* **349,** 613–617. doi:10.1126/science.aaa9297 (2015).

175. Draelos, A. W. *et al.* Supercurrent Flow in Multiterminal Graphene Josephson Junctions. *Nano Letters* **19,** 1039–1043. doi:10.1021/acs.nanolett.8b04330 (2019).

176. Graziano, G. V., Lee, J. S., Pendharkar, M., Palmstrøm, C. J. & Pribiag, V. S. Transport studies in a gate-tunable three-terminal Josephson junction. *Physical Review B* **101,** 054510. doi:10.1103/PhysRevB.101.054510 (2020).

177. Pankratova, N. *et al.* Multiterminal Josephson Effect. *Physical Review X* **10,** 31051. doi:10.1103/physrevx.10.031051 (2020).

178. Berger, J. *ongoing Master thesis* (University of Regensburg).

179. Golod, T., Rydh, A. & Krasnov, V. M. Detection of the phase shift from a single Abrikosov vortex. *Physical Review Letters* **104,** 227003. doi:10.1103/PhysRevLett.104.227003 (2010).